

DISS. ETH NO. 23507

***Understanding and improving gold-catalyzed formic acid decomposition for application in the SCR process***

A thesis submitted to attain the degree of  
DOCTOR OF SCIENCES of ETH ZURICH  
(Dr. sc. ETH Zurich)

presented by

**MANASA SRIDHAR**

*M. Sc. in Chemical Engineering, University of Cincinnati*

born on 12.12.1987  
citizen of India

accepted on the recommendation of

Prof. Dr. Jeroen A. van Bokhoven, *examiner*

Prof. Dr. Oliver Kröcher, *co-examiner*

Prof. Dr. Christoph Müller, *co-examiner*

2016



*“anything can happen, in spite of what you’re pretty sure should happen.”*

– Richard Feynman



---

## Table of content

<b>Abstract</b> .....	II
<b>die Zusammenfassung</b> .....	VI
<b>Chapter 1</b> Introduction.....	1
<b>Chapter 2</b> Methods.....	15
<b>Chapter 3</b> Unique selectivity of Au/TiO <sub>2</sub> for ammonium formate decomposition under SCR-relevant conditions .....	25
<b>Chapter 4</b> Effect of ammonia on the decomposition of ammonium formate and formic acid on Au/TiO <sub>2</sub> .....	33
<b>Chapter 5</b> Promotion of ammonium formate and formic acid decomposition on Au/TiO <sub>2</sub> by support basicity .....	53
<b>Chapter 6</b> Water-assisted oxygen activation during gold-catalyzed formic acid decomposition under SCR-relevant conditions .....	73
<b>Chapter 7</b> Numerical modeling of hydroperoxyl–mediated oxidative dehydrogenation of formic acid .....	103
<b>Chapter 8</b> From mechanism to catalyst design: Fine tuning the basicity of Au/TiO <sub>2</sub> for formic acid decomposition .....	119
<b>Chapter 9</b> Conclusion and Outlook.....	137
<b>Publications and presentations</b> .....	143
<b>Curriculum Vitae</b> .....	145
<b>Acknowledgments</b> .....	146
<b>References</b> .....	A-II

---

## Abstract

Selective catalytic reduction (SCR) is one of the most successful and widely implemented technologies for the abatement of nitrogen oxide emissions from stationary and mobile sources. Since the storage and handling of ammonia is perilous in automotive applications, urea is used as the ammonia storage compound in the form of aqueous solutions that are sprayed and decomposed on-demand to produce ammonia for the SCR process. However, the application of urea is in practice impeded by various issues which has fueled growing interests in replacing this compound with alternative ammonia precursors. In this context, concentrated guanidinium formate, ammonium formate and methanamide solutions are more thermally stable, freeze at lower temperatures, have higher ammonia storage capacities, and decompose more selectively. Most of these precursors undergo thermolysis in the hot exhaust feed to produce ammonia and formic acid in the gas phase. Hence, the successful application of these formate-based compounds in the SCR process relies on the development of dedicated catalysts that rapidly decompose the acid to prevent formic acid emissions and side reactions with ammonia, while remaining inactive for ammonia oxidation.

Chapter 1 reviews the existing literature on formic acid decomposition. Besides the fundamental studies unravelling the acid-base characteristics of metal and metal oxide surfaces and the catalytic links with water gas shift, most of the research works focus on the use of formic acid as a convenient hydrogen source which can selectively release hydrogen (and carbon dioxide) upon stoichiometric dehydrogenation. The general consensus is that a formate-type intermediate is formed and that its C-H bond cleavage constitutes the kinetically relevant step in the decomposition mechanism. Apart from the studies on the promotional effect of water on formate decomposition during water gas shift, reports on the influence of oxygen and water on the formic acid decomposition chemistry are scarce. In this work, catalytic formic acid decomposition is investigated in the starkly different context of SCR where oxygen and water are ubiquitously present and exert significant effects on the decomposition chemistry.

Chapter 2 describes the experimental procedures for the synthesis, characterization and testing of the catalysts. Several characterization techniques such as X-ray diffraction (XRD), nitrogen physisorption, X-ray photoelectron spectroscopy, electron microscopy and infrared spectroscopy were applied. The catalysts were tested after coating on inert cordierite monoliths.

Ammonium formate is an experimentally simple compound to study the formate decomposition behavior of catalysts under SCR-relevant conditions. In Chapter 3, the remarkable activity and selectivity of titania-supported gold catalyst ( $\text{Au/TiO}_2$ ) for ammonium formate decomposition is reported. Under the highly oxidizing conditions of the simulated exhaust feed,  $\text{Au/TiO}_2$

---

decomposed ammonium formate to carbon dioxide without oxidizing the co-evolved ammonia. The inactivity for ammonia oxidation is a crucial aspect for the design of dedicated hydrolysis catalysts since it ensures that a reliable supply of ammonia is available for the downstream SCR process.

Ammonium formate undergoes non-catalytic thermolysis in the exhaust feed to produce close to 100% yields of ammonia and formic acid. Chapter 4 presents a systematic investigation of the influence of ammonia on formic acid decomposition revealing its beneficial influence on the carbon dioxide yield. Activity testing of bare titania revealed an inhibitory effect of ammonia on formic acid decomposition to carbon monoxide. Overall, it is concluded that the presence of gold is critical for the realization of the ammonia-induced activity-enhancement.

Chapter 5 demonstrates the realization of the observed gas-phase promotional effect of ammonia as a catalytic effect. Modification of titania by lanthanum prior to gold deposition entailed highly improved catalytic activities for ammonium formate and formic acid decomposition under SCR-relevant conditions stemming from dual phenomena. There is a particle size effect and a base effect. Smaller gold particles were stabilized and there was higher uptake of carbon dioxide and formic acid as demonstrated by in situ diffuse reflectance infrared Fourier transform spectroscopy (DRIFTS) studies. A higher apparent activation energy alongside a higher pre-exponential factor, describe an underlying compensation phenomenon originating from the contribution of enthalpy associated with the desorption of the strongly adsorbed formate, which is consistent with the highly negative formic acid orders and high steady state formate coverage observed in the case of the lanthanum-modified catalysts under reaction conditions. The introduction of lanthanum to the catalytic system preferentially promoted the carbon dioxide formation mechanism, enabling complete decomposition of formic acid selectively to carbon dioxide at significantly lower gold loading and lower contact times.

Chapter 6 reports the findings from the kinetic and mechanistic investigation of formic acid decomposition in the presence of oxygen and water. Oxygen activation over unmodified and lanthanum-modified titania supported gold catalysts was greatly enhanced in the presence of water resulting in a significant increase in carbon dioxide production from formic acid decomposition. Carbon dioxide was formed only in the presence of gold. In the absence of gold, the metal oxide supports produced only carbon monoxide and their activity was independent of oxygen and inhibited by water. Monodentate formates and bidentate formates are the precursors for carbon monoxide and carbon dioxide, respectively. The support acts as a reservoir storing bidentate formates that do not react at steady state when formic acid and oxygen (and water) are co-fed. However, during transient experiments, when the feed is switched from formic acid to oxygen (and water), they are reactivated upon reverse-spillover to

---

the active site (associated with gold) where they decompose to carbon dioxide. In the presence of oxygen and water, carbon monoxide oxidation and WGS reaction do not produce carbon dioxide, and instead, a direct oxidative-dehydrogenation-type (ODH) pathway proceeds. This strongly differs from stoichiometric formic acid decomposition reported in the absence of oxygen and water. Hydroperoxy species are proposed to form from energetically more favorable water-assisted oxygen activation. A kinetically consistent mechanism is proposed in which the hydroperoxy species facilitate the C-H bond cleavage of formates to release carbon dioxide and water in the rate determining step. The promotional roles of ammonia and lanthanum must relate to the acceleration of the formate decomposition step.

In Chapter 7, the validity of the ODH mechanistic model is tested against the experimental data. Using the surface perfectly stirred reactor (SPSR) model, the ODH mechanism is demonstrated to satisfactorily predict the experimentally observed conversions. The single-site mechanistic model accurately captured the negative trend in conversion with increasing formic acid concentrations, which originates from the extensive blockage of the active sites by formates. This in turn rendered a majority of active sites unavailable for the formation of the active hydroperoxy species required for the rate-determining-step of C-H bond scission of formates. The positive order dependence on oxygen concentrations and the promotional effect of water are qualitatively and semi-quantitatively described by the model. Predicted trends in the relative surface coverages of different reaction intermediates are in agreement with the kinetic and spectroscopic measurements.

Chapter 8 presents a systematic investigation of incremental addition of lanthanum to Au/TiO<sub>2</sub>. An optimum in the base-induced promotional effect is revealed. Bidentate formates, the kinetically relevant intermediates for carbon dioxide formation are formed as the dominant surface species and experience C-H bond weakening upon base-modification. At already one atomic % surface lanthanum concentration, monodentate formates were substantially suppressed leading to ~85% reduction in carbon monoxide production. Very high lanthanum surface concentrations lowered the relative coverage of oxygen-derived surface species that are crucial for the decomposition of the abundantly present formates. The linearity of the Constable-Cremer relationship between the apparent activation energy and the natural log of the pre-exponential factor indicates the mechanistic commonality in formic acid decomposition on gold supported on unmodified and lanthanum-modified titania catalysts.

Chapter 9 summarizes the findings from this research and also presents an outlook for future work. The research reported in this thesis contributes mechanistic insights into the roles of oxygen-water synergy and structural-modification on gold-catalyzed formic acid decomposition. The findings from this thesis are important on a fundamental level as well as in practice for the

---

design of a dedicated hydrolysis catalyst for the decomposition of alternative formate-based ammonia precursors in the SCR process.

---

## Die Zusammenfassung

Die selektive katalytische Reduktion (SCR) ist eine der meist verwendeten und effizientesten Methoden zur Bekämpfung von Stickoxiden im Abgas von stationären und mobilen Anlagen. Die direkte Verwendung von giftigem Ammoniak birgt jedoch grosse Risiken, insbesondere für automobiler Anwendungen. Als Alternative wird eine wässrige Harnstofflösung als Ammoniak-Vorläufersubstanz verwendet, die durch Einspritzen ins heisse Abgas und Zersetzung den nötigen Ammoniak für den SCR-Prozess zur Verfügung stellt. In der Praxis birgt die Zersetzung von Harnstoff mehrere Probleme, was zu wachsendem Interesse an alternativen Ammoniak-Vorläufersubstanzen, wie z.B. Guanidiniumformiat, Ammoniumformiat und Methenamid führt. Diese Substanzen zeigen grössere thermische Stabilität, gefrieren bei tieferen Temperaturen, haben eine höhere Ammoniak-Speicherkapazität und zersetzen sich mit höheren Selektivitäten zu Ammoniak. Die meisten dieser Vorläufersubstanzen zersetzen sich mittels Thermolyse im heissen Abgas zum gewünschten Ammoniak und unerwünschter Ameisensäure. Die erfolgreiche Applikation dieser Formiat-basierenden Substanzen im SCR-Prozess hängt deshalb von der Entwicklung geeigneter und effizienter Katalysatoren für die Zersetzung von Ameisensäure ab, um allfälligen Säureemissionen und anderen Nebenreaktionen mit Ammoniak vorzubeugen.

Kapitel 1 fasst den Stand des Literaturwissens über die Ameisensäurezersetzung zusammen. Neben Studien, welche die grundsätzlichen katalytischen Zusammenhänge von Säure-Base-Eigenschaften von Metall- und Metalloxydoberflächen und der sogenannten Wassergas-Shift-Reaktion (WGS) aufzeigen, fokussiert sich der grösste Teil der aktuellen Forschung auf die Verwendung von Ameisensäure als bequeme Wasserstoffquelle, welche selektiv Wasserstoff (und Kohlenstoffdioxid) durch stöchiometrische Dehydrierung freisetzen kann. Es besteht Konsens in der Literatur, dass dabei ein Formiat-ähnliches Zwischenprodukt gebildet wird. Die Spaltung der C-H-Bindung ist der geschwindigkeitsbestimmende Schritt im Zersetzungsmechanismus. Neben dem angeblich beschleunigenden Effekt von Wasser auf die Zersetzung von Ameisensäure während der WGS sind Informationen über den Einfluss von Wasser und Sauerstoff auf die Chemie der Ameisensäurezersetzung sehr rar. Kapitel 1 fasst den Stand des Wissens über die Zersetzung von Ameisensäure und die WGS zusammen. Die vorliegende Arbeit untersucht erstmalig die katalytische Zersetzung von Ameisensäure im Kontext der selektiven katalytischen Reduktion, bei welcher Wasser und Sauerstoff omnipräsent sind, die die Zersetzungschemie signifikant beeinflussen.

Kapitel 2 beschreibt die experimentellen Methoden für die Synthese, Charakterisierung und Tests der Katalysatoren. Es wurden verschiedene Charakterisierungstechniken, wie z.B. Röntgenbeugung (XRD), Stickstoff-Physisorption, Röntgen-Photoelektronenspektroskopie und

---

Infrarotspektroskopie eingesetzt. Die Katalysatoren wurden getestet nachdem sie auf inerte Cordierit-Monolithe beschichtet wurden.

Ammoniumformiat ist ein chemisch einfacher Stoff, um die Formiat-Zersetzung auf Katalysatoren unter SCR-relevanten Bedingungen zu untersuchen. In Kapitel 3 dieser Arbeit wird die aussergewöhnliche Aktivität und Selektivität von Gold-Titanoxid-Katalysatoren für die Zersetzung von Ammoniumformiat vorgestellt. Unter stark oxidierenden Bedingungen im simulierten Abgasstrom wurde Ammoniumformiat über Au/TiO<sub>2</sub> zersetzt, ohne dass der dabei produziert Ammoniak oxidiert wurde. Diese Inaktivität gegenüber der Oxidation von Ammoniak ist eine wichtige Katalysatoreigenschaft, da nur so sichergestellt wird, dass genügend Ammoniak für den nachgelagerten SCR-Prozess zur Verfügung steht.

Ammoniumformiat zersetzte sich via Thermolyse bereits im heissen Abgas zu nahezu 100% Ammoniak und Ameisensäure, ohne dass ein Katalysator nötig wäre. Kapitel 4 zeigt die Ergebnisse einer systematischen Untersuchung des Einflusses von Ammoniak auf die Zersetzung der Ameisensäure. Es zeigte sich, dass Ammoniak einen stark positiven Einfluss auf die Kohlenstoffdioxidausbeute und -selektivität der Reaktion hat. Aktivitätsbestimmungen von reinem Titanoxid zeigten einen hemmenden Effekt von Ammoniak auf die Zersetzung von Ameisensäure zu Kohlenstoffmonoxid. Die wichtigste Schlussfolgerung daraus ist, dass Gold zwingend vorhanden sein muss, um den positiven Effekt von Ammoniak auf die Reaktion zu erzielen.

Kapitel 5 zeigt, dass sich der beobachtete positive Effekt in der Gasphasen-Reaktion auch auf katalytische Prozesse übertragen lässt. Titanoxid, welches vor der Golddeposition mit Lanthan modifiziert wurde, zeigte eine höhere katalytische Aktivität aufgrund von zwei Phänomenen – einer verringerten Partikelgrösse und höherer Oberflächenbasizität. Kleinere Partikel wurden durch Gold stabilisiert und die Adsorption von Kohlenstoffdioxid und Ameisensäure verstärkt, wie Messungen der Fourier-Transformations-Infrarotspektroskopie im Reflexionsmodus (DRIFTS) belegten. Formiat wurde als relevantes Reaktionsintermediat identifiziert. Die Aktivität des Lanthan-modifizierten Katalysators wurde bei Gleichgewichtsbedeckung des Katalysators mit Formiat und unter Reaktionsbedingungen untersucht. Höhere gemessene Aktivierungsenergien zusammen mit einem höheren präexponentiellen Faktor zeigten ein Kompensationsphänomen, welches von der hohen Desorptionenthalpie der stark gebundenen Formiate herrührt. Dies ist in Übereinstimmung mit der negativen Reaktionsordnung für Ameisensäure, welche beim Lanthan-modifizierten Katalysator gemessen wurden. Die Anwesenheit von Lanthan auf dem Katalysator beschleunigte selektiv den Kohlenstoffdioxid-Mechanismus, was zu kompletter Zersetzung von Ameisensäure zu Kohlenstoffdioxid bei signifikant tieferen Goldbeladungen und Kontaktzeiten führte.

---

Kapitel 6 zeigt die Ergebnisse der kinetischen und mechanistischen Untersuchung der Ameisensäurezersetzung in der Gegenwart von Sauerstoff und Wasser. Die Sauerstoff-Aktivierung wurde auf unmodifizierten und Lanthan-modifizierten Gold-Titanoxid Katalysatoren in der Gegenwart von Wasser verstärkt. Dies führte zu signifikant höherer Kohlenstoffdioxidproduktion während der Zersetzung von Ameisensäure. Zusätzlich wurde gezeigt, dass Kohlenstoffdioxid lediglich in der Gegenwart von Gold gebildet wird. Die Metalloxid-Trägermaterialien produzieren lediglich Kohlenstoffmonoxid und dies unabhängig von der Gegenwart von Wasser. Die Vorläuferstoffe für Kohlenstoffmonoxid und Kohlenstoffdioxid waren monodentate resp. bidentate Formiate. Das Trägermaterial fungiert als Reservoir für die Speicherung bidentater Formiate, die bei Abwesenheit von Gold oder Sauerstoff nicht reagieren können, in deren Anwesenheit aber zu Kohlendioxid zerfallen. Bei Anwesenheit von Sauerstoff und Wasser wurde weder Kohlenmonoxid-Oxidation noch WGS zu Kohlendioxid beobachtet. Stattdessen folgte die Reaktion einer direkten oxidativen Dehydrierung (ODH), welche stark von der bisher bekannten direkten Zersetzung von Ameisensäure bei Abwesenheit von Sauerstoff und Wasser abweicht. Hierfür wird ein kinetisch konsistenter Mechanismus vorgeschlagen, in welchem Hydroperoxy-Spezies, die durch Wasser-assistierte Aktivierung von Sauerstoff gebildet werden, die C-H-Spaltung von Formiaten als geschwindigkeitsbestimmenden Schritt beschleunigen. Die promotierende Wirkung von Ammoniak und Lanthan muss mit der Beschleunigung des Formiat-Zersetzungsschritts verknüpft sein.

In Kapitel 7 wird die Gültigkeit des ODH-Mechanismus durch Vergleich mit den experimentellen Daten untersucht. Es konnte mittels des sogenannten „surface perfectly stirred reactor“ (SPSR) Modells gezeigt werden, dass der ODH-Mechanismus die beobachteten Reaktionsumsätze befriedigend beschreibt. Das sogenannte „single site“ mechanistische Modell konnte den beobachteten negativen Trend bei den Reaktionsumsätzen für erhöhte Ameisensäurekonzentrationen akkurat beschreiben. Dieser rührt daher, dass die aktiven Zentren stark durch Formiate blockiert werden. Dies wiederum deaktiviert den Grossteil der aktiven Zentren für die Bildung der benötigten aktiven Hydroperoxy-Spezies. Der positive Einfluss von Sauerstoff auf die Reaktionsordnung und der promotierende Effekt von Wasser werden qualitativ und semi-quantitativ durch das Modell beschrieben. Vorhergesagte Trends für die relative Oberflächenbedeckung durch verschiedene Reaktionsintermediate sind in Übereinstimmung mit kinetischen und spektroskopischen Messungen.

Kapitel 8 zeigt die Ergebnisse der systematischen Untersuchungen der Zugabe von Lanthan zu Au/TiO<sub>2</sub>. Es wurde ein Optimum des baseninduzierten positiven Effekts gefunden werden. Auf der Katalysatoroberfläche werden überwiegend bidentate Formiate gebildet, welche kinetisch relevante Intermediate für die Kohlenstoffdioxidbildung sind. Deren C-H-Bindung wird durch die Modifizierung des Trägermaterials mit einer Base geschwächt. Bei einer Lanthan-

---

Oberflächenkonzentration von 1 Atom% werden monodentate Formiate, die Vorläufer für Kohlenstoffmonoxid, substanziell unterdrückt. Dies führt zu einer Reduktion der Kohlenstoffmonoxidbildung von ~85%. Hohe Lanthan-Konzentrationen lösen eine Verarmung an Sauerstoff-Oberflächenspezies aus, welche aber für die Zersetzung der Formiate nötig wären. Die Linearität des Constable-Cremer-Zusammenhangs zwischen der scheinbaren Aktivierungsenergie und dem natürlichen Logarithmus des präexponentiellen Faktors deutet auf eine mechanistische Ähnlichkeit der Ameisensäurezersetzung auf unmodifizierten und Lanthan-modifizierten Au/TiO<sub>2</sub>-Katalysatoren hin.

Kapitel 9 fasst die Ergebnisse der gesamten Studie zusammen und stellt mögliche zukünftige Forschungsarbeiten auf diesem Gebiet vor. Die Arbeit trägt zum allgemeinen mechanistischen Verständnis der Gold-katalysierten Zersetzung der Ameisensäure bei und zeigt den Einfluss der Basizität und der Sauerstoff-Wasser-Synergie auf die Zersetzungsreaktion auf. Die Resultate dieser Arbeit sind wichtig für das grundlegende Verständnis der ablaufenden Chemie, aber auch für die Praxis, da sie wertvolle Informationen für die Entwicklung von aktiven Hydrolysekatalysatoren für alternative Formiat-basierende Ammoniakvorläufersubstanzen im SCR-Verfahren liefern.



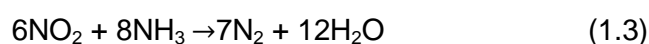
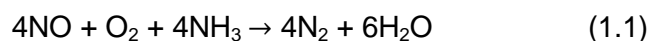
# **Chapter 1**

## **Introduction**

## 1.1 Selective catalytic reduction technology: Challenges of Urea-DeNO<sub>x</sub>

Over the recent years, the world has witnessed an increasing awareness on the dire need for processes that have minimal environmental impact. The laws and regulations on environmental protection are tending to be more stringent demanding rigorous treatment of process effluents to achieve negligible levels of hazardous contaminants. In the context of air pollution, combustion processes associated with operation of power plants and vehicles are the major culprits. Sulfur oxide (SO<sub>2</sub>), particulate matter, carbon monoxide, volatile organic compounds and nitrogen oxides (NO<sub>x</sub>) are some of the key combustion-generated air pollutants. Among these NO<sub>x</sub> are primary pollutants which are responsible for the formation of photochemical smog, acid rain and ground-level ozone. They are suggested to cause destruction of the stratospheric ozone layer and contribute to global warming.<sup>[1-4]</sup> NO<sub>x</sub> are liberated from stationary and mobile sources. NO<sub>x</sub> abatement strategies can be implemented at three levels: Pre-combustion control, combustion-modification and post-combustion control.<sup>[1,2]</sup> The first two categories involving fuel purification and alteration of operational conditions of combustion, respectively, offer insufficient NO<sub>x</sub> emission reduction by less than 50% and often result in a penalty on the fuel efficiency.<sup>[1,2]</sup> On the other hand, post-combustion measures provide a higher degree of control accompanied with the necessary reduction in NO<sub>x</sub> levels in compliance with the emission standards.

Selective catalytic reduction (SCR) is a leading technology used worldwide that is proven for its high efficiency, selectivity and economics in stationary as well as mobile applications.<sup>[5]</sup> It has been widely applied in fossil fuel-based power plants, industrial heaters and several chemical manufacturing plants. An important market domain for the SCR technology is the diesel vehicle industry. Diesel engines typically operate under lean conditions and use highly compressed hot air to ignite the fuel. At high temperature ( $\geq 1600$  °C), NO<sub>x</sub> formation occurs upon reaction between nitrogen and oxygen. It is estimated that diesel engines account for more than 85% NO<sub>x</sub> emissions from mobile sources.<sup>[6,7]</sup>



SCR utilizes a reducing agent such as ammonia to convert NO<sub>x</sub> to harmless nitrogen and water (Eq. 1.1-1.3). Though the use of ammonia is feasible in stationary applications, the dangers in handling compressed or liquefied ammonia render it unsuitable for carrying it onboard vehicles. Aqueous solutions of urea are commonly applied as the ammonia source in diesel vehicles. Urea is safe, non-toxic and since it is produced in large-scale as a bulk commodity by fertilizer industry, it is readily available in large quantities. Urea solutions are typically eutectic mixtures

composed of 32.5 % urea by mass and traded by the names AdBlue<sup>®</sup> or Diesel Exhaust Fluid (DEF) or Aqueous Urea Solution (AUS).



In the current state of the art diesel exhaust after-treatment system, the solution of urea is directly sprayed into the hot exhaust duct. The decomposition of the solid or molten urea follows immediately after the evaporation of water from the spray.<sup>[8]</sup> Urea decomposition involves two steps: (i) thermolysis to equimolar amounts of ammonia and isocyanic acid and (ii) hydrolysis of the isocyanic acid to form carbon dioxide and one more molecule of ammonia (Eq. 1.4 and Eq. 1.5). The former reaction is highly endothermic ( $\Delta H^0 = 185.5 \text{ kJ}$ ) while the latter reaction is exothermic ( $\Delta H^0 = -95.9 \text{ kJ}$ ).<sup>[9]</sup> Hence, the rates of these reactions are highly dependent on the exhaust gas temperature and their conversion efficiency can drop below 50% in the absence a dedicated hydrolysis catalyst.<sup>[8,10-12]</sup> Even in the presence of a hydrolysis catalyst, when the temperatures drop below 200 °C or space velocities are too high, urea decomposition is incomplete leading to the formation of many undesirable side products such as cyanuric acid, cyanamide, hydrogen cyanide, biuret, melamine, etc.<sup>[13]</sup> These products accumulate in the exhaust pipe and ultimately clog the catalyst. Additionally, large excess of ammonia emissions (ammonia slip) in the exhaust can result if the urea dosing system is unable to rapidly synchronize with sudden changes in the load during engine operation.<sup>[8]</sup> This complicates the discrete mixing and design of the exhaust packaging and the urea injection system. Another critical limitation of urea solutions (Adblue) is that they freeze at temperatures as high as -11 °C. For operation in colder climates, this necessitates the use of additional heating in order to sustain it in the liquid state suitable for spraying. Furthermore, urea solutions suffer from poor thermal stability and their durability is restricted to 6 months when stored at temperatures in the range 30-35 °C.<sup>[14]</sup>

## 1.2 Proposal for alternative precursors

The aforementioned limitations associated with urea-DeNO<sub>x</sub> have stimulated growing interest in the scientific community to explore the prospects of alternative ammonia storage compounds that can potentially replace urea. In this context, formate-based ammonia precursor compounds such as guanidinium formate (GuFo), ammonium formate (AmFo) and methanamide are promising candidates.<sup>[15-20]</sup> They present multitude of advantages that can potentially overshadow the higher capital costs associated with their use. They freeze at temperatures as low as -30 °C, have higher thermal stability, durability and similar or even higher ammonia storage capacity as urea. Additionally, they exhibit excellent solubility in water which enables the

use of highly concentrated solutions of these precursors, thus, reducing the energy expense in evaporating the water from the spray.<sup>[11]</sup>

AmFo is already commercially applied as an antifreeze additive to urea which causes freezing point depression without compromising on the ammonia storage capacity. It is sold under the names Denoxium-20<sup>®</sup> or Denoxium-30<sup>®</sup> with freezing points lowered down to -20 °C and -30 °C, respectively or as TerraCairPlus<sup>®</sup> in Canada, the USA and Mexico.<sup>[21,22]</sup> Contrary to AmFo which can be easily integrated into the existing SCR technology, bulky molecules such as GuFo strictly require temperatures higher than 200 °C for their complete decomposition.<sup>[23]</sup> In view of this, an alternative configuration for diesel exhaust after-treatment proposed by Hammer and coworkers<sup>[18,24]</sup> can be highly suitable for achieving selective and efficient decomposition of such high molecular weight precursors (Figure 1.1). In the traditional exhaust treatment architecture, the ammonia precursor compound is directly sprayed into the main exhaust duct and hence, the extent of decomposition is contingent on the inherent exhaust gas conditions. In the proposed modified design,<sup>[18,24]</sup> a separate side stream reactor housing the dedicated hydrolysis catalyst is placed in parallel to the main exhaust. In this way the decomposition can be carried out at higher temperatures and/or lower space velocities so as to accomplish complete decomposition of the ammonia precursor and ensure the reliable release of a clean and concentrated stream of ammonia upstream of the SCR catalyst.<sup>[15,16,18]</sup>

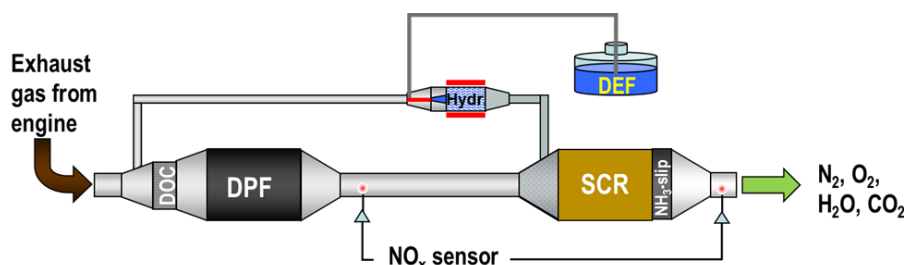
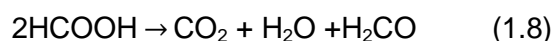
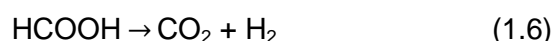


**Figure 1.1** Illustration of the proposed alternative configuration for diesel exhaust after-treatment housing a separate side stream reactor for ammonia precursor hydrolysis.

Preliminary investigations revealed that these formate-based ammonia precursors undergo non-catalytic thermolysis in the hot exhaust and liberate formic acid.<sup>[23,25]</sup> Hence, the rapid removal/decomposition of formic acid is essential for the efficient utilization of these precursors. Formic acid is highly reactive and corrosive and its elimination entails two benefits: (i) destabilization of the cationic moiety, and (ii) the formate anion is made unavailable for side product formation from undesired reactions with co-evolved ammonia.<sup>[23]</sup> Earlier works identified that titania supported gold catalyst is active for the decomposition of the formate-based compounds while maintaining high selectivity against the formation of toxic side products.<sup>[15]</sup>

### 1.3 Formic acid decomposition on metals and metal oxides

Since a high formic acid decomposition activity is intrinsic to the efficiency of a dedicated hydrolysis catalyst for the decomposition of formate-based ammonia precursors, it is essential to be primed with the existing literature on formic acid decomposition chemistry. The first studies on formic acid were performed by Mailhe and Sabatier<sup>[26]</sup> with the objective of differentiating the formic acid decomposition selectivity of the metal and metal oxide catalysts (Eq. 1.6-1.8). Following these works, the relatively facile nature of this reaction was appreciated and became to be extensively studied for distinguishing the acid-base characteristics of catalysts.<sup>[27-29]</sup> A general consensus was reached regarding the selectivity of metals and metal oxides, wherein the former were observed to almost exclusively drive dehydrogenation-type reaction (Eq. 1.6), while the latter displayed a switch-over from dehydrogenation to dehydration-type reaction (Eq. 1.7) with increasing acidity. However, such a relationship between the catalytic selectivity and actual state of the metal oxide surface is made ambiguous when there is a possibility of several oxidation states.<sup>[27]</sup> Traces of formaldehyde was also found to occur via the bimolecular reaction (Eq. 1.8) on specific dehydrating metal oxide surfaces (eg: manganese oxide).<sup>[28,30,31]</sup>



Identification of the nature and reactivity of the intermediates is of immense interest in relation to the catalytic decomposition of formic acid. Numerous studies in this direction have concluded that, with few exceptions (e.g.: silica) formate is the relevant reaction intermediate formed instantaneously upon exposure of catalysts to the acid itself.<sup>[32-36]</sup> Deficiently coordinated cations and surface hydroxyls act as the sites for the dissociative adsorption of formic acid which in turn behaves as a Lewis base.<sup>[32,37]</sup> On the other hand, the strong Brønsted acidity and the absence of exposed  $\text{Si}^{4+}$  ions are proposed to invoke this behavior of silica which shows only molecular adsorption.<sup>[38]</sup> Kinetic investigations on silica revealed that a first order in formic acid characterizes a small energy of formate-metal bond wherein the overall rate is determined by the dissociative adsorption of formic acid. However, when the formates exhibit sufficient stability, which is the case with most other metal oxides, then the reaction is zero order in formic acid and limited by the subsequent steps of formate decomposition and product desorption.

Sachtler and Fahrenfort put forth the classic “volcano curve” (Figure 1.2 (top left)) as a validation for Sabatier’s hypothesis on the relationship between the catalytic activity and the binding strength of the reaction intermediate complex.<sup>[39]</sup> The formic acid decomposition temperature ( $T_d$ ) was plotted as a function of the thermodynamic heat of formation of bulk formate for various

transition metal powders (Figure 1.2 (top left)). The former quantity is an index of the intrinsic kinetics while the latter is representative of the stability of formate. Despite wide acceptance, the Sachtler-Fahrenfort volcano curve suffers several shortcomings. Wachs and coworkers<sup>[40]</sup> pointed out that the plot does not consider an appropriate reactivity parameter (eg: turn over frequency) as a normalized measure of the specific reaction rates among the metal catalysts; the heat of formation represented the stability of the bulk metal formates (bulk  $\Delta H_f$ ) instead of the surface metal formates ( $\Delta H_{ads}$ ) and the plot employed data derived from several research lab thus lacking consistency in measurements. These drawbacks were considered in constructing a more realistic picture where the  $\Delta H_{ads}$  values derived from the density function theory (DFT)-calculated binding energies of formate on the (111) metal surfaces were compared against the experimentally obtained turn over frequency (TOF) for formic acid adsorption on the metal powders (Figure 1.2 (top right)).

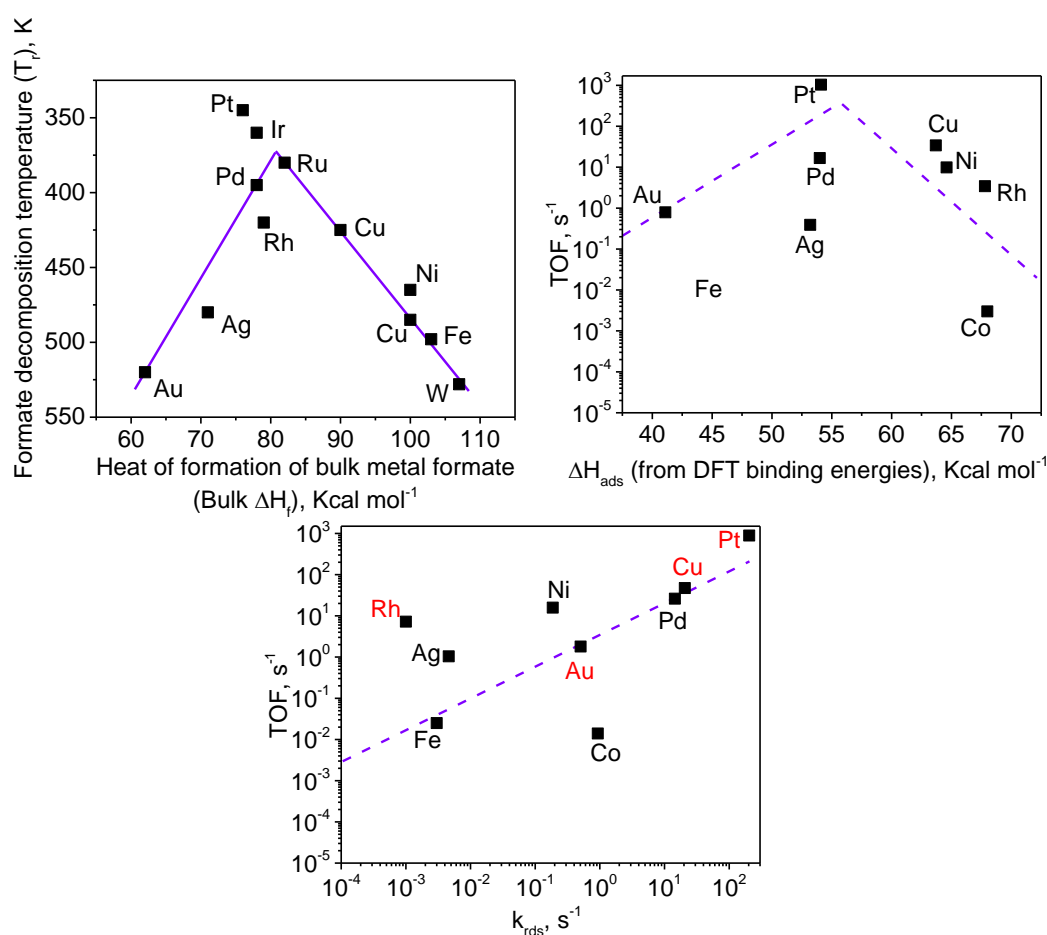
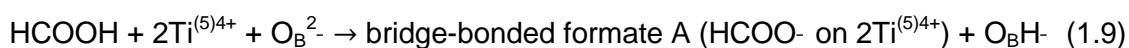


**Figure 1.2** The original Sachtler–Fahrenfort volcano curve (top left), the plot of steady-state specific catalytic activity (TOF) for formic acid decomposition versus  $\Delta H_{ads}$  for surface formate from DFT calculations of formate binding energies on metal (111) surfaces (top right), and the plot of steady-state specific catalytic activity (TOF) for formic acid decomposition versus kinetics for surface formate decomposition ( $k_{rds}$ ) bottom). Metals in black form monodentate surface formates and metals in red form bidentate/bridged surface formate. Adapted from Reference<sup>[40]</sup>, Copyright (2016), with permission from Elsevier.

The revised plot exhibited a weaker trend which paralleled the trend obtained from plotting the TOFs as a function of the first order kinetic constant ( $k_{\text{rds}}$ ) determined from temperature programmed desorption (TPD) experiments (Figure 1.2 (bottom)). In agreement with Madix's work,<sup>[41]</sup> it was concluded that both  $\Delta H_{\text{ads}}$  and  $k_{\text{rds}}$  influence the overall steady state activity of the metal catalysts. Hence, even though the surface properties may be incidentally manifest in the bulk properties, the classic volcano curve cannot substitute as the *priori* evidence for their relationship.<sup>[40]</sup>

The formic acid decomposition mechanism can follow either a decarbonylation (dehydration) route to produce carbon monoxide or a decarboxylation (dehydrogenation) pathway to form carbon dioxide. For instance, Munuera employed TPD to deduce that the activation energy ( $E_a$ ) of formic acid dehydration on titania correlates with that for surface formate decomposition into carbon monoxide and water. Moreover, it was equal to the  $E_a$  for elimination of surface hydroxyl-groups by water condensation. This explained the water-induced inhibition observed in formic acid dehydration of titania. These findings reconcile with the reports of Iwasawa and coworkers who combined in situ scanning tunneling microscopy and first-principle DFT calculations to follow formic acid dehydration on titania (110).<sup>[42,43]</sup> They observed that a bridging oxygen anion ( $\text{O}_\text{B}^{2-}$ ) abstracts a proton of formic acid to form bridge-bonded formate (A) on two neighboring 5-fold coordinated  $\text{Ti}^{4+}$  (Eq. 1.9). This formate can in turn be transformed to another configuration (B) in which one oxygen atom is located on a 5-fold coordinated  $\text{Ti}^{4+}$  and the other oxygen atom of the formate adsorbs at an oxygen vacancy site on a bridging oxygen row (Eq. 1.11). The latter bridge bonded formate (B) which can also be formed upon direct collision of a gas phase formic molecule with the oxygen vacancy site ( $\eta$ ) is then converted into the less stable monodentate formate (C) (Eq. 1.12). The decomposition of the monodentate formate to carbon monoxide and  $\text{O}_\text{B}\text{H}^-$  (Eq. 1.13) is said to constitute the rate-determining-step (RDS).<sup>[42]</sup> Water is released upon condensation of two  $\text{O}_\text{B}\text{H}^-$  and thus, the oxygen vacancy is replenished (Eq. 1.10). This was backed by computational studies<sup>[44]</sup> which showed carbon monoxide formation by such a bimolecular mechanism to be more energetically favorable compared with previously proposed<sup>[45]</sup> unimolecular mechanisms.



Similar to the dehydration mechanism, formic acid dehydrogenation also proceeds via a formate intermediate. In a study over zinc oxide and manganese oxide, infrared spectroscopy combined with isotopic labelling studies established that decomposition of formate to carbon dioxide via C-H bond breakage was the RDS.<sup>[46]</sup> Studies on formic acid decomposition selectivity on several metal oxides including titania and chromium oxide, demarcated the existence of two different active sites responsible for dehydration and dehydrogenation-type reactions and ascertained that the acid-base interactions, rather than the electric properties govern the dehydrogenation activity of metal oxides.<sup>[28]</sup> Contrary to the dehydration tendency of polycrystalline titania powders, single crystal studies on rutile titania (110) showed that the participation of molecularly adsorbed formic acid species promoted a new reaction pathway leading to bimolecular formic acid dehydrogenation to produce hydrogen at temperatures lower than 500 K.<sup>[47]</sup> Molecular evidence supplemented by DFT calculations showed that dehydrogenation proceeds via a bimolecular pathway involving acid-base interactions between a bridging formate on two  $2\text{Ti}^{(5)4+}$  and a formic acid molecule weakly adsorbed at the adjacent  $\text{Ti}^{4+}$  on rutile titania (110).<sup>[48]</sup>

Analogous to the observations on metal oxides, metal-catalyzed dehydrogenation of formic acid is also reported to operate via formates as intermediates. Computational calculations using DFT consent bidentate (bridging) formate with its two oxygen atoms interacting with two equivalent surface sites of the metal, as the most important surface-bonded intermediate formed during formic acid adsorption on metal surfaces.<sup>[44]</sup> In line with these theoretical predictions, an X-ray photoelectron spectroscopy (XPS) study of formic acid adsorption on copper (110) surface revealed an O1s linewidth corresponding to the presence of only one type of oxygen.<sup>[49]</sup> More importantly, the presence of co-adsorbed species, namely oxygen, exerted a strong influence on the configuration and the activation energies associated with formic acid adsorption and decomposition, respectively. For instance, the co-presence of adsorbed oxygen species significantly increased formate formation on copper (110) and in its absence, only molecular adsorption of formic acid occurred on silver (110) and gold (110) surfaces.<sup>[50,51]</sup> Using temperature programmed reaction spectroscopy, Outka and Madix observed a Brønsted acid-base type mechanism in which oxygen adsorbed on gold (110) facilitated formate formation in a kinetically important step preceding decarboxylation to carbon dioxide.<sup>[51]</sup> Furthermore, the exclusive formation of water was linked to the weak gold-hydrogen bond strength which favors direct hydrogen transfer to other surface species such as oxygen adatoms rather than to surface which would have then lead to recombination to form hydrogen.

### **1.3.1 Application of formic acid decomposition: Analogy with water gas shift and relevance in hydrogen generation**

In the past decades, the mechanistic influence of water on formic acid dehydrogenation to carbon dioxide (and hydrogen) has garnered special attention owing to the putative link with

water gas shift (WGS)<sup>[52–59]</sup> and in the context of sustainable hydrogen production and carbon dioxide valorization<sup>[60–66]</sup> using (aqueous) formic acid fuel cells. One of the first studies establishing the interrelation between WGS and formic acid decomposition was performed on zinc oxide and magnesium oxide.<sup>[67]</sup> In subsequent studies, de Jong and coworkers examined the kinetics of WGS and formic acid decomposition on Cu/ZnO and concluded that both the reactions proceeded via the same surface intermediate whose decomposition (formate dehydrogenation) limited the rates. This was deduced from the identical temperature dependence and the high carbon dioxide selectivity for formic acid dehydrogenation which correlated with the value (50) for the ratio between the rates of the forward and the reverse shift reactions.<sup>[68,69]</sup> Formates could be readily formed upon flowing carbon monoxide over partially hydrated surfaces (magnesium oxide,  $\gamma$ -Alumina) or by flowing carbon dioxide and hydrogen.<sup>[68,70]</sup> Furthermore, the temperature and the density of formate formation from carbon monoxide were observed to decrease and increase, respectively, with increasing hydroxyl concentration on the surface.

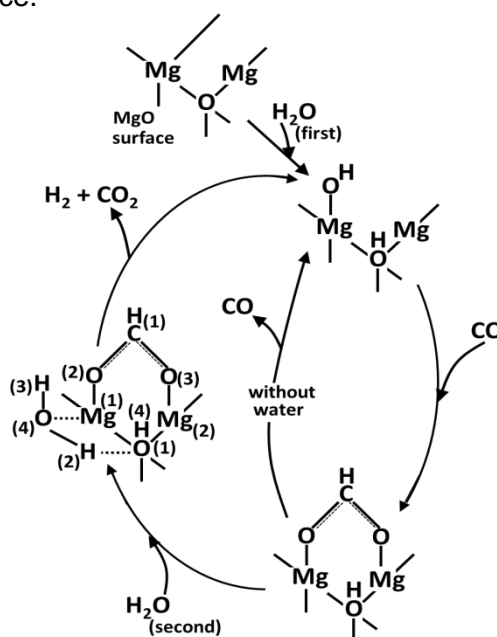


**Figure 1.3** Proposed mechanism for WGS on magnesium oxide. Adapted from Reference<sup>[54]</sup>, Copyright (1990), with permission from Elsevier.

Following these works, Iwasawa and coworkers performed in-depth studies of the interrelationship between the two reactions and coined the phrase ‘reactant-promoted reaction mechanism’ in relation to WGS on bare metal oxides and metal oxide supported catalysts.<sup>[53,54,56]</sup> Using FT-IR, the hydroxyl groups on top of coordinatively unsaturated magnesium atoms were observed to react with carbon monoxide to produce surface formates that were uni-, bridge-bonded or bidentate in configuration.<sup>[54]</sup> The unidentate formates that were readily produced at room temperatures transformed to bridge-bonded formates upon heating to higher temperatures (>450 K) and in the co-presence of adsorbed water. Furthermore, it was

revealed that the formate decomposition to carbon dioxide and water was initiated only in the presence of co-adsorbed water, while dry conditions triggered the reverse reaction to form carbon monoxide and hydroxyl. It was proposed that both electron-donation and withdrawal between water and a magnesium oxide pair facilitated the formate conversion from unidentate to bridge-bonded configuration, the decrease in the rate constant for the reverse reaction and promotion of the forward reaction (Figure 1.3).

The decomposition of the surface formate was explained from a stereochemical perspective as follows: (a) the delocalization of the electrons through the O-C-O bond in the formate at/near the transition state diminishes the bond order to ~one, (b) rotation and torsion around C-O(2), C-O(3) and C-H(1) bonds occur (c) interaction between H(1) (with  $\delta^-$  charge) and H(4) (with  $\delta^+$  charge), and (d) finally, dissociation of C-H(1) bond upon tilting of bridge-bonded formate to form hydrogen (H(1)H(4)) accompanied with carbon dioxide and dissociation of adsorbed water to form Mg(1)-O(4)H and O(1)-H(2) bonds. Isotopic labelling studies using DCOOH/HCOOH determined that the RDS must involve C-H bond dissociation of the bridge-bonded formate in the transition state. However, fast hydrogen exchange between surface water and hydroxyls disallowed the identification of the origin of hydrogen deuteride (HD) which could arise from the deuterium of formate and hydrogen of hydroxyl or from the deuterium of formate and hydrogen of water. Along these lines, Davis and coworkers<sup>[58,71]</sup> reported that the formates arising from the adsorption of formic acid and D-formic acid (DCOOH) were identical to those arising from the adsorption of carbon monoxide to bridging OH and OD groups, respectively. Moreover, a normal kinetic isotope effect was observed upon switching from water to deuterium oxide (D<sub>2</sub>O) which was consistent with a link between the RDS of WGS and surface formate decomposition.<sup>[72,73]</sup> Hence, with the existence of a common kinetically relevant intermediate (formate) between formic acid decomposition and the WGS, the activity of the catalysts for C-H bond cleavage became an important descriptor for the design of WGS catalysts.<sup>[74,75]</sup>

Another area of extensive formic acid decomposition research is founded on the promising potential of formic acid as a convenient 'in situ' source of hydrogen for fuel cells. Formic acid offers high energy density while being non-toxic and safe to be handled in aqueous solution.<sup>[76]</sup> It can be facilely stored in a disposable or recyclable cartridge that is readily available for on-demand release of hydrogen and easily replaced.<sup>[77]</sup> Moreover, a reversible cycle of hydrogen supply and storage based on formic acid decomposition and reverse hydrogenation of carbon dioxide is a highly attractive sustainable energy concept.<sup>[78-80]</sup> Homogeneous catalysts based on iridium or platinum phosphine complexes, dinuclear ruthenium complexes, etc, have been demonstrated to show high activity for formic acid decomposition at close to ambient conditions.<sup>[81-85]</sup> However, as with many homogeneous catalysts, their practical application is impeded by the difficulties in separation and the use of organic solvents, ligands and additives

that complicate device fabrication. The development of heterogeneous (solid) catalysts is mainly centered on selective formic acid dehydrogenation to carbon dioxide and water while restricting carbon monoxide formation to negligible levels so as to prevent poisoning of fuel cell catalysts. Further on, their low temperature (<50 °C) activity was crucial in view of the high volatility of formic acid/water mixtures and the complexity of heat management that forbids miniaturization.<sup>[86]</sup> Noble metal-based catalysts have been reported to show exciting potential in fulfilling these criteria as summarized in the extensive review by Grasmann and Laurency (Table 1.1). In line with earlier studies,<sup>[33,51]</sup> a (bidentate) formate intermediate formed on the large terrace sites of metal were identified to be the kinetically-relevant precursors for carbon dioxide formation (Figure 1.4) on palladium<sup>[87]</sup> and platinum<sup>[88]</sup>. On the other hand, the linear (monodentate formate) mode on surface-unsaturated metal sites (corners, steps, kinks) were predisposed to form carbon monoxide.

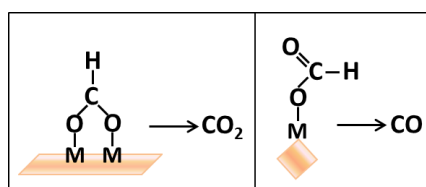


**Figure 1.4** Dependence of formic acid decomposition selectivity on the surface structure of the metal particle. Adapted by permission from Macmillan Publishers Ltd: Nature Nanotechnology Reference<sup>[86]</sup>, copyright (2011).

**Table 1.1** Noble metal-based catalysts for the decomposition of formic acid. In part from Reference<sup>[77]</sup> with permission of The Royal Society of Chemistry.

Active phase/support	Solvent	Performance	Temperature	Reference
0.61% Au/Al <sub>2</sub> O <sub>3</sub>	He/gas phase	TOF = 25600 h <sup>-1</sup> , ~10 ppm CO	353 K	[89]
20 wt% PdAu/C–CeO <sub>2</sub>	Aqueous	TOF = 832 h <sup>-1</sup> , <140 ppm CO	375 K	[90]
1% Pd/C	He/gas phase	TOF = 255 h <sup>-1</sup> , S <sub>H<sub>2</sub></sub> ≈ 99%	373 K	[63]
PdAu@Au/C (core–shell)	Aqueous	30 ppm CO	356 K	[64]
5% Au/CeO <sub>2</sub>	Ar/gas phase	TOF = 295 h <sup>-1</sup> , S <sub>H<sub>2</sub></sub> = 100% <sup>a</sup>	473 K	[91]
Ir/C	Ar/gas phase	TOF = 960 h <sup>-1</sup> , S <sub>H<sub>2</sub></sub> ≈ 99%	373 K	[92]
Ag@Pd/C (core–shell)	Aqueous	TOF = 125 h <sup>-1</sup> , S <sub>H<sub>2</sub></sub> = 100%	293 K	[86]
		TOF = 626 h <sup>-1</sup> , 84 ppm CO	363 K	
Pd-S-SiO <sub>2</sub>	Aqueous	TOF = 803 h <sup>-1</sup> , S <sub>H<sub>2</sub></sub> = 100%	358 K	[93]

### 1.3.2 Catalysis by gold: Relevance and importance in formic acid decomposition

Ever since the discovery of the remarkable chemical activity of nanoparticulate gold,<sup>[94–97]</sup> extensive research efforts have been dedicated towards the exploration of gold chemistry and catalysis. The first report of supported gold-catalyzed olefin hydrogenation by Bond et al.<sup>[98]</sup> was followed by the demonstration of gold's exceptional ability to oxidize carbon monoxide at low temperatures by Haruta et al.<sup>[96]</sup> and Hutchings's<sup>[94]</sup> report on gold catalyzed hydrochlorination of alkynes to vinyl chloride. Now, gold-based catalysts are common place owing to their versatility and selectivity in catalyzing oxidation as well as hydrogenation-type reactions and it is only a matter of time before they make a foray into industry.<sup>[99–102]</sup>

One of the first fundamental studies of formic acid decomposition on gold was conducted by Outka and Madix who explored the adsorption of the acid on clean and oxidized Au(110) surface.<sup>[51,103]</sup> They found that while weak molecular adsorption took place on the clean Au(110) surface, on the oxidized surface, oxygen acted as a Brønsted base in abstracting the proton from formic acid. This was followed by hydrogen transfer from the adsorbed formate to gold which constituted the RDS. The weak Au-H bond necessitated the transfer of hydrogen to other surface species like hydroxyls to form water rather than recombination with another hydrogen atom to form hydrogen.<sup>[103]</sup> Isotopic studies confirmed that the oxygen in carbon dioxide exclusively arose from the dosed formic acid and not from the oxygen in the gas phase.

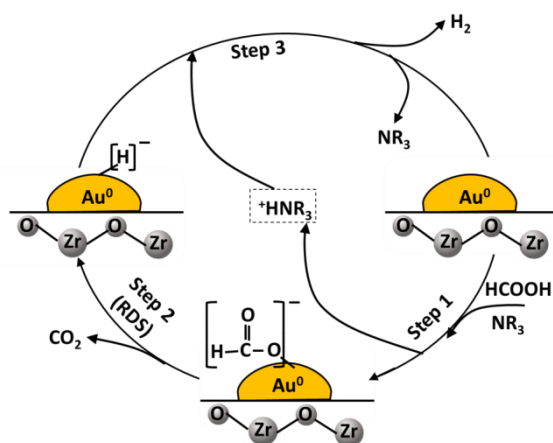


**Figure 1.5** Proposed mechanism for hydrogen evolution from decomposition of formic acid/amine mixtures on Au/ZrO<sub>2</sub>. Adapted with permission from Reference<sup>[66]</sup>. Copyright (2012) American Chemical Society.

Recently, many studies have demonstrated the excellent potential of supported gold catalysts for selective formic acid decomposition to hydrogen and carbon dioxide.<sup>[63,66,89,91]</sup> Ojeda and Iglesia reported that TEM-invisible gold clusters supported on alumina were responsible for the unprecedentedly high activity for formic acid decomposition, while the TEM visible clusters catalyzed carbon monoxide oxidation. Furthermore, using H/D kinetic isotope effects, the C-H bond cleavage of formate was identified as the RDS. Along these lines, Au/ZrO<sub>2</sub> was reported to

show high activity for formic acid dehydrogenation particularly when formic acid/amine mixtures were used.<sup>[66]</sup> The amine was proposed to facilitate the formation of the Au-formate complex, the relevant reaction intermediate, by acting as a proton scavenger in facilitating the O-H bond breakage (Figure 1.5). The resulting alkyl ammonium ion ( $^+\text{HNR}_3$ ) promoted further dehydrogenation of the formate to produce hydrogen and carbon dioxide via a  $\beta$ -elimination pathway.<sup>[83,104,105]</sup>

In parallel to the gas phase studies, adsorbed formate is reported to be the relevant surface-bonded intermediate during electrochemical oxidation of formic acid on gold.<sup>[106]</sup> Using surface-enhanced Raman spectroscopy, the RDS was demonstrated to involve formate dehydrogenation to carbon dioxide on gold electrodes with the aid of water. Consistent with these studies, DFT studies on gold surfaces reported that gold exclusively catalyzed formic acid dehydrogenation and that the mechanism was mediated by a formate intermediate.<sup>[107]</sup> With the purported mechanistic links between formic acid decomposition and WGS, it is no surprise that gold-based catalysts have also shown high WGS activity.<sup>[108–113]</sup> Gold's inability to activate water, one of the most important steps of reaction is said to be overcome by the formation of oxidic gold species ( $\text{Au-O-MO}_x$ ) upon strong-metal-support-interaction with metal oxides such as titania or ceria.<sup>[114,115]</sup> An extensive kinetic and mechanistic study by Behm and coworkers on low temperature WGS on  $\text{Au/CeO}_2$  catalysts revealed that the ionic gold species ( $\text{Au}^{\delta+}$ ) at the metal-support interface are the likely active sites that catalyze the reaction of adsorbed carbon monoxide and hydroxyl to form surface formates and their subsequent decomposition to carbon dioxide and hydrogen.

With oxidic gold species proposed as the active centers for formate decomposition, it is essential to understand the oxidative chemistry on gold. Oxygen activation on gold has been a highly debated subject in literature spanning from a Mars van-Krevelen type pathway<sup>[116]</sup> involving lattice oxygen and its replenishment by gaseous oxygen to a Langmuir-Hinshelwood type pathway<sup>[117]</sup> involving molecularly or dissociatively adsorbed oxygen. Since oxygen and water are both ubiquitously present in the simulated exhaust feed employed in this study, it is highly interesting to consider the implications of water on oxygen activation. Several works point towards the direct participation of water as a promoter in opening up new, energetically more favorable pathways for oxygen activation.<sup>[118–120]</sup> Furthermore, strong indications of the temperature-sensitive role of moisture in oxidation reactions exist in literature.<sup>[121]</sup> At high temperatures, oxygen molecules were activated directly over the  $\text{Au/TiO}_2$  (110) surface, whereas moisture participated in the activation at low temperatures. Hydroperoxy species ( $\text{HOO}^*$ ) that are readily produced in aqueous environments by proton shift equilibrium between adsorbed oxygen ( $\text{O}_2^*$ ) and water ( $\text{H}_2\text{O}^*$ ) are proposed as the active oxygen species on gold

(Eq. 1.14).<sup>[119,122,123]</sup> Such species have often been invoked in oxidation mechanisms necessitating C-H bond activation of alkoxy groups.<sup>[123–129]</sup>



#### 1.4 Rationale of the work

The aim of this thesis is to develop mechanistic understanding of formic acid decomposition on titania-supported gold catalysts under SCR-relevant conditions and to use the gained insights towards rational design of better catalyst systems. Formic acid decomposition which is commonly studied under stoichiometric conditions was explored in a wholly different context where significant influence of gas phase oxygen and water exists. The mechanistic insights gained from this study are important in furthering the knowledge on gold catalysis and formic acid decomposition chemistry as well as in practice for the rational design of dedicated hydrolysis catalysts for the decomposition of formate-based ammonia precursors in the SCR process.

Chapter 2 describes the experimental methodologies employed in this work which includes the details of the synthesis, characterization and the testing of the catalysts. Chapter 3 presents the first findings which demonstrate the high activity and selectivity of Au/TiO<sub>2</sub> for the decomposition of ammonium formate without oxidizing the co-evolved ammonia. Chapter 4 reports the promotional effect of gas phase ammonia on formic acid decomposition. Chapter 5 describes the realization of the aforementioned gas phase effect as a catalytic effect by modification of Au/TiO<sub>2</sub> with a basic metal oxide. Chapter 6 is devoted to the kinetic and mechanistic investigation of gold-catalyzed formic acid decomposition in the presence of oxygen and water. A kinetically-consistent hydroperoxyl-mediated mechanism is proposed for the oxidative dehydrogenation of formic acid to carbon dioxide and water. Chapter 7 presents the validity of the proposed mechanism as tested by numerically modelling. Chapter 8 shows the optimization of the lanthanum effect to achieve the highest activity and selectivity for formic acid decomposition to carbon dioxide. Chapter 9 presents the conclusions and discusses the outlook of the work.

# **Chapter 2**

## **Methods**

## 2.1 Catalyst synthesis

Titania is the most common hydrolysis catalyst in the SCR process.<sup>[130]</sup> It also offers good thermal stability and high surface area making it a convenient support for dispersion of active components. For the works reported in Chapters 3-7, commercial anatase titania (DT51, Cristal Global) and lanthana-modified titania with 10 wt% lanthana (DT57, Cristal Global) were used as the supports for depositing gold. In Chapter 8, the surface basicity was systematically tuned by varying the lanthana content of Au/TiO<sub>2</sub>. Lanthana was introduced by two methods: wet impregnation and coprecipitation. In the first technique, the desired amount of lanthana was precipitated on the surface of anatase titania (DT51, Cristal Global). The latter method by which titania and lanthana are precipitated together guaranteed a more intimate contact between the two components.

Instead of the solvent-intensive and tedious deposition-precipitation method, a facile modified incipient wetness impregnation technique<sup>[131]</sup> was followed to deposit gold on the supports. By adding a simple washing step with ammonia, the chloride ligands are replaced from the coordination sphere of gold (III) precursor to form ammino-hydroxo or ammino-hydroxo-aquo gold complex. This way, the gold catalysts were almost completely rid of chlorine which is known to cause metal sintering.

In this work, the catalyst powders were washcoated on cordierite monoliths before testing. Monolithic catalysts consist of zigzag, or as in this work, narrow parallel straight channels forming continuous unitary structures. In contrast to the pellets or fixed beds with small catalyst particles, monolithic catalysts offer lower pressure drop, higher external surface area, lower diffusional resistances and smaller attrition or erosion.<sup>[132,133]</sup> For these reasons, extruded high-strength cordierite monolith honeycombs are extensively used in the industry and are particularly popular in automobile applications.

### 2.1.1 Synthesis of wet-impregnated lanthana-modified titania supports

The wet-impregnated lanthana-modified titania supports of different lanthana contents were synthesized in accordance with a previously published procedure.<sup>[134]</sup> An aqueous slurry consisting of calculated amounts of lanthanum nitrate (La(NO<sub>3</sub>)<sub>3</sub>·6H<sub>2</sub>O, Fluka) and anatase titania (DT 51, Cristal Global) in 50 ml water was stirred for 1 h at room temperature and then left to dry under vacuum. This was followed by a second drying step at 105 °C for 12 h. Finally, the dried powder was ground and calcined at 500 °C for 5 h in air.

### 2.1.2 Synthesis of coprecipitated lanthana-modified titania supports

The coprecipitated lanthana-modified titania supports were prepared by modifying the procedure described by Sang and coworkers.<sup>[135]</sup> Lanthanum nitrate (La(NO<sub>3</sub>)<sub>3</sub>·6H<sub>2</sub>O, Fluka) was dissolved

in 30 ml water and subsequently added under vigorous stirring to a calculated amount of metatitanic acid  $\text{TiO}(\text{OH})_2$  suspension (29.97 wt % titania, Treibacher). The obtained solution was adjusted to  $\text{pH} > 9.3$  using aqueous ammonia solution (2 M  $\text{NH}_4\text{OH}$ ) in order to ensure complete precipitation of the lanthanum ions and was kept under stirring for 30 min at room temperature. The precipitated solids were separated by centrifuging and washed three times with water in order to remove the ammonium ions. The resulting solids were dried and calcined under identical conditions as the wet-impregnated lanthana-modified titania supports. In order to investigate the whole range of lanthanum loading, pure lanthana support was also synthesized in the same manner without the addition of titanium precursor. Additionally, a pristine titania sample was prepared as reference using metatitanic acid as the precursor.

### 2.1.3 Synthesis of supported gold catalysts

Deposition of gold on the supports was carried out following a previously published procedure based on incipient wetness impregnation.<sup>[131]</sup> The support was impregnated with a solution of the gold precursor, tetrachloroauric (III) acid ( $\text{HAuCl}_4$ , Sigma), of 0.032 M in gold, calculated on the basis of the desired gold loading and the volume of water equivalent to the pore volume of the support. The sample was aged for 1 h at room temperature. Washing with aqueous ammonia (1M) twice followed by distilled water ensured effective removal of chloride from the samples (less than 0.07 wt% as estimated by XPS). Calcination was performed at 400 °C for 5 h in air. ICP-OES analysis indicated that the actual gold loadings were close to the nominal values with a maximum standard deviation of  $\pm 0.04$  wt%.

### 2.1.4 Preparation of catalyst coated monoliths

The ceramic monoliths were cut to desired size and shape out of large (10.5", 400 cpsi, Corning) honeycomb samples. The monolith material ( $2 \text{MgO} \cdot 2\text{Al}_2\text{O}_3 \cdot 5\text{SiO}_2$ ) was by itself catalytically inert. The catalyst powders were coated on the monoliths following a previously reported procedure.<sup>[136]</sup> An aqueous suspension consisting of the catalyst powder and colloidal silica (Ludox AS-40, Sigma) as the binder was prepared. The pH was adjusted close to the isoelectric point so that the catalyst particles do not agglomerate. The ceramic monoliths were dipcoated with the catalyst suspension, then dried using a hot gun and finally calcined in air at 400 °C for 5 h.

## 2.2 Catalyst characterization

Characterization is an essential step in the rational design of catalysts. It allows understanding the structural and physicochemical properties that may be the potential descriptors of catalytic activity. Besides several ex situ techniques, in situ diffuse reflectance infrared spectroscopy (DRIFTS) was also applied to study the catalyst under reaction conditions.

### 2.2.1 X-ray diffraction

Diffraction effects are encountered when electromagnetic radiation impinges on periodic structures that possess geometric variations in the same length scale as the wavelength of the radiation. X-rays are generated by a cathode ray tube, filtered to produce monochromatic radiation and collimated to concentrate and directed towards the sample. When X-rays with photon energies in the range 3 to 8 keV are used, their wavelengths correspond to the interatomic distances in crystals and molecules. Thus, the interaction between X-rays and the electron density around an atom causes the atom to elastically scatter radiation at the same frequency as the incoming X-rays. While the amorphous materials produce only broad background bumps as a result of destructive interference from scattering X-rays in all directions, the ordered planes of a crystalline material produce distinct diffraction patterns characterized by constructive interference from scattering X-rays coherently in a few directions. The condition for the constructive interference can be described by the Bragg's law (Eq. 2.1):

$$n\lambda = 2d \sin\theta \quad (2.1)$$

where, the integer  $n$  represents the reflection order,  $\lambda$  is the wavelength of the X-rays,  $d$  is the spacing between the crystallographic lattice planes and  $\theta$  is the scattering angle at which the X-rays impinge on the lattice planes. A diffraction pattern is obtained by plotting the intensity of the diffracted radiation as a function of  $2\theta$ .

In this work, XRD was employed to assess the crystallinity of the supports. The small particle sizes, high dispersion and low loading of gold (<2 wt%) obscured any chances of its detection. X-ray diffraction measurements were performed on a D8 Advance Bruker AXS diffractometer with Cu K $\alpha$  radiation (1.5418 Å, 8.048 keV) in a  $2\theta$  range of 10° to 70° with a step size of 0.01. Prior to measurement, the samples were evenly pressed in a silicon sample holder that is equipped to rotate during measurements to reduce preferential orientation effects.

### 2.2.2 Nitrogen physisorption

The porous properties of catalysts are important aspects that often determine their activity. The supports should ideally offer high surface areas for ensuring good dispersion of the active components. Nitrogen physisorption is the most widely used technique for evaluating the porosity of materials. Physisorption measurements are generally undertaken under isothermal conditions, thus giving rise to an 'adsorption isotherm'. The adsorption isotherm (Eq. 2.2) plots the amount of gas adsorbed ( $v$ ) as a function of the equilibrium relative pressure  $\left(\frac{p}{p^0}\right)$ .<sup>[137]</sup>

$$v = f\left(\frac{p}{p^0}\right)_T \quad (2.2)$$

At very low partial pressure, the adsorption begins as a monolayer. The molecules of the first layer act as sites for adsorbing a second layer and so on. Such a multilayer adsorption at intermediate partial pressure is followed by sudden filling of pores by capillary condensation at high partial pressure. The shape of the isotherm and the presence or absence of the hysteresis loop provides vital information on the pore characteristics such as size and shape. There are six IUPAC classifications of the adsorption isotherms (Figure 2.1).<sup>[137]</sup>

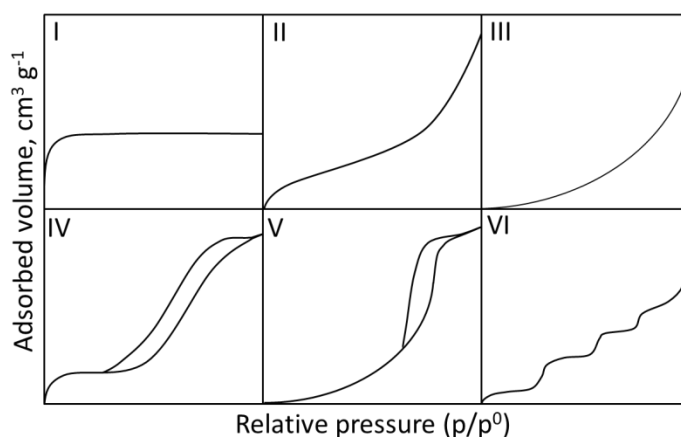


**Figure 2.1** BET N<sub>2</sub>-adsorption isotherms

The Type I isotherm is characteristic of micropore filling taking place at lower  $p/p^0$ . Type II isotherm is the result of monolayer-multilayer adsorption in nonporous or macroporous solids and indicative of high energy of adsorption. Type III isotherms are exhibited when the adsorbent-adsorbate interactions are weak and the adsorbates preferentially occupy favorable sites instead of forming a monolayer. Type IV isotherms showing hystereses are displayed by mesoporous solids. Type V isotherms are produced by materials showing lower energy of adsorption than in Type III and in addition exhibit mesopore filling at high partial pressure. Type VI isotherms signify layer by layer adsorption (like epitaxial growth) on highly uniform surfaces. The steps at lower relative pressure are indicative of distinct energies of adsorption while those at higher pressures may be due to sharp steps on the adsorbate surface.<sup>[138]</sup>

The Brunauer-Emmett-Teller (BET) method is a reliable method for estimating the surface area of narrow pore networks of molecular dimensions. It assumes that monolayer adsorption occurs on equivalent sites, no adsorbate-adsorbent interactions exist, the adsorbed molecules are immobile and all layers succeeding the first monolayer are identical.<sup>[139]</sup> By plotting the linear BET equation (Eq. 2.3), the monolayer capacity ( $v_m$ ) can be determined from the value of the intercept ( $\frac{1}{v_m C}$ ) of the line. The specific surface area ( $S_{BET}$ ) is derived using the monolayer capacity in Eq. 2.4.

$$\frac{p}{[v(p^0-p)]} = \left(\frac{1}{v_m C}\right) + \left[\frac{C-1}{v C}\right] \left(\frac{p}{p^0}\right) \quad \text{Eq. 2.3}$$

$$S_{\text{BET}} = v_m N \sigma \quad \text{Eq. 2.4}$$

Where  $v$  is the measured gas uptake at the relative pressure  $\left(\frac{p}{p^0}\right)$ ,  $C$  is the BET constant,  $N$  represents the Avagadro constant and  $\sigma$  is the area covered by a single molecule of nitrogen ( $\sigma = 0.162 \text{ nm}^2$ ).

In this work, a Micromeritics Tristar 3000 instrument cooled with liquid nitrogen at 77 K was used to perform nitrogen physisorption. All samples were pretreated at 150 °C for 1 h under a continuous flow of nitrogen to remove volatile impurities.

### 2.2.3 Electron microscopy

Scanning transmission electron microscopy (STEM) coupled with high angle annular dark field detector (HAADF) allowed distinguishing the gold particles from the support using  $z$  (atomic number) –contrast.<sup>[140–142]</sup> This way, the heavier gold particles ( $Z_{\text{Au}} = 79$ ) appeared as bright spots on a relatively dark background of lighter titania ( $Z_{\text{Ti}} = 22$ ) matrix. In STEM, a finely focused electron beam is scanned over the sample and the resulting transmitted or scattered electrons are collected to form the image of the spot. In addition to the imaging, electrons bombarding the sample also cause it to emit X-rays that are characteristic of its elemental composition. An energy-dispersive X-ray (EDX) spectrometer counted and sorted the characteristic X-rays according to their energy which enabled the determination of the chemical composition of a selected spot of the sample. In this work, STEM and EDX spectroscopy measurements were performed on a Hitachi HD2700CS aberration-corrected scanning transmission electron microscope equipped with a cold field emission gun operating at an acceleration voltage of 200 kV. Prior to measurement, the catalyst powders were dispersed in ethanol and deposited onto a perforated carbon–copper grid.

### 2.2.4 Elemental analysis

To determine the actual gold and lanthana loading in the synthesized catalysts, inductively coupled plasma optical emission spectroscopy (ICP-OES) was employed. The samples were subjected to hot digestion in a mixture of 96 %  $\text{H}_2\text{SO}_4$  and 30 %  $\text{H}_2\text{O}_2$  (Sigma-Aldrich) and subsequently diluted in distilled water prior to analysis. About 2 ml of the diluted solution is introduced at the center of an inductively coupled argon plasma at high temperature. ICP-OES measurements were performed on Varian, type VISTA Pro AX instrument.

### 2.2.5 X-ray photoelectron spectroscopy

X-ray photoelectron spectroscopy operates on the principle of the photoelectric effect. When the sample is irradiated with X-rays of known energy, photoelectrons are ejected. By measuring the kinetic energy of the photoelectrons, their binding energy can be determined (Eq. 2.5) which is in turn characteristic of the electron orbital in an atom.<sup>[143,144]</sup> This way the energy at which the photoelectron peak appears divulges information on the atomic composition while the area under peak can be used for quantification.

$$KE = h\nu - BE \quad (2.5)$$

where KE and BE represent the kinetic energy and the binding energy of the photoelectron, respectively and  $\nu$  is the frequency of the incident radiation.

In this work, XPS was performed to measure the surface concentrations of gold, lanthanum and chlorine (if any) in the catalyst samples. Before the analysis, the powder samples were pressed into copper adhesive tape. The XPS chamber was kept at pressure in the order of  $10^{-10}$  mbar during the measurement. The samples were irradiated by monochromatized Al K-alpha source at a power of 400 W. Sample charging was compensated by low energy electron flood gun. The binding energies were referenced to carbon 1s peak from a commercial anatase titania sample at 285.25 eV (Ti 2p<sub>3/2</sub> at 458.85 eV). The amount of each element has been calculated from the normalized area of the respective XPS peak. Peak fitting and deconvolution was performed using UniFit 2013 (UniFit Scientific Software GmbH, Leipzig, Germany).

### 2.2.6 In situ diffuse reflectance infrared Fourier transform spectroscopy

Diffuse reflectance infrared Fourier transform spectroscopy (DRIFTS) is a surface localized spectroscopy that is highly suitable to rapidly and non-destructively analyze powder samples. Rough surfaces of powder samples reflect light in all directions; the resulting diffuse reflection can be collected by an ellipsoid or paraboloid mirror and relayed to an infrared detector.<sup>[145-147]</sup> In this work, the in situ DRIFTS study of carbon dioxide and formic acid adsorption under steady state and transient conditions was conducted using a Bruker Vertex 70 spectrometer equipped with a liquid nitrogen cooled MCT detector and a Praying Mantis mirror accessory (Harrick). A homemade in situ cell with a flat calcium fluoride window was used. The homemade cell was specially designed to perform gas pulses and exhibited a faster exchange rate by 3.6 times compared to the commercial Harrick cell (Figure 2.2). The 95% decay time was 15 s in the homemade cell against 54 s of the commercial one. The feed gases were introduced into the in situ DRIFTS cell as shown in Figure 2.3. The total flow rate was set at  $50 \text{ ml min}^{-1}$ . The gas exiting the cell was analyzed by a Fourier transform infrared (FT-IR) spectrometer (Bruker Alpha equipped with a 7 cm gas cell).

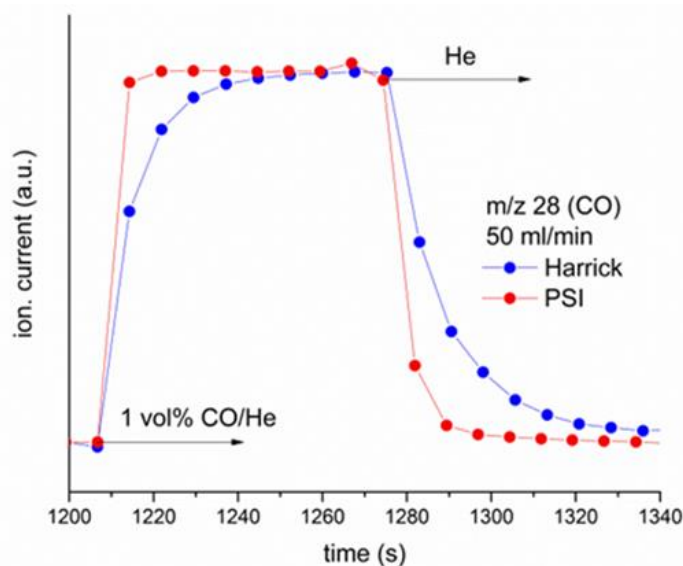


**Figure 2.2** Mass spectrometer traces of carbon monoxide during exchange in a commercial Harrick cell and the homemade cell employed in this work.

Prior to each experiment, the sample was pretreated at 400 °C for 0.5 h in a flow of nitrogen containing 10 vol.% oxygen and 5 vol.% water to remove any carbonate residues that may be present on the catalyst surface. Then, the sample was cooled to 200 °C and 260 °C in flowing nitrogen, at which point the background spectrum was collected. For steady state experiments, formic acid or carbon dioxide (1120 ppm, unless otherwise stated) was flowed in the desired feed gas containing only nitrogen, 10 vol% oxygen, 5 vol% water or a mixture comprising of 10 vol% oxygen and 5 vol% water and the adsorption was monitored for 17 min. For the transient experiments, formic acid adsorption in nitrogen was followed by a rapid switch of the feed gas to nitrogen, oxygen, water or oxygen-water mixture in nitrogen. All DRIFT spectra were collected by accumulating 100 scans at 4  $\text{cm}^{-1}$  resolution and a scanner velocity of 80 kHz.

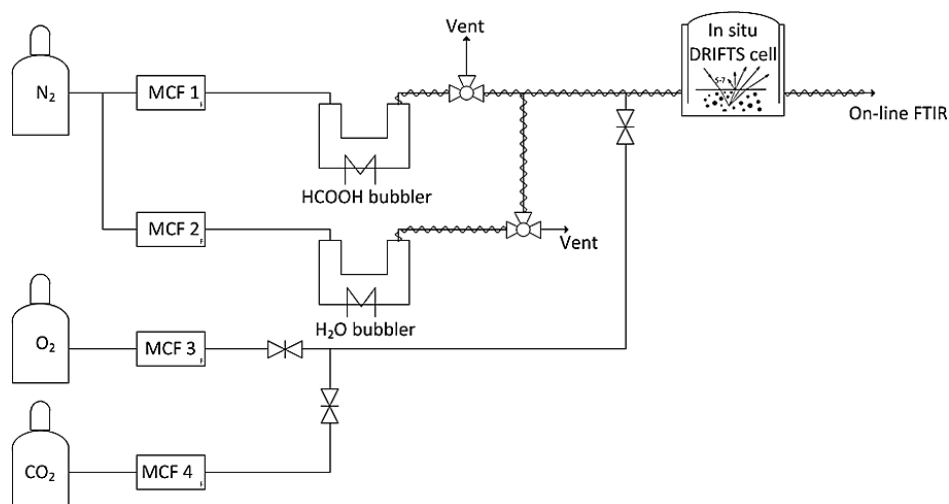


**Figure 2.3** Schematic of in situ DRIFTS setup.

### 2.3 Catalytic experiments

In the experimental setup, 0.05 ml min<sup>-1</sup> flow of 40 wt% ammonium formate (Sigma) solution or 30 wt% formic acid solution in water was pumped using a Shimadzu LC-20 AD HPLC pump and sprayed by means of a nebulizer (e-pond) on the catalyst-coated monolith in a flow of model exhaust gas.<sup>[148]</sup> Feed gas containing 10 vol% oxygen, 5 vol% water and balance nitrogen was set to flow at a rate of 500 to 750 L h<sup>-1</sup> in order to realize very GHSVs in the range 20,000 h<sup>-1</sup> to 300,000 h<sup>-1</sup>. The cylindrical monolithic catalysts were wrapped around with ceramic fiber mats before being placed inside the reactor in order to prevent bypass of the reactant gas mixture. The contact time was varied by changing the number of monoliths stacked along the axis of the reactor while keeping the total catalyst concentration per unit volume constant. The temperatures up- and downstream of the catalyst-coated monoliths were controlled using K-type thermocouples. Gaseous reaction products at the reactor outlet were quantified by FTIR spectroscopy (Antaris, Thermo Nicolet).<sup>[149]</sup> For experiments determining the kinetic orders, the concentrations of formic acid, carbon monoxide, oxygen, carbon dioxide and water were varied in the range 0-2200 ppm, 0-750 ppm, 0.25-4.00 vol%, 0-750 ppm and 0.01-1.50 vol%, respectively. In all the experiments, the C-balance was closed within an accuracy of ±3% by summing up carbon monoxide, carbon dioxide and formic acid. Moreover, temperature programmed oxidation experiments on the used catalysts in feed containing 10% oxygen and 5% water at temperatures up to 500 °C showed that no oxidation products (carbon monoxide and carbon dioxide) were formed. This way, the formation of coke deposits on the catalysts was ruled out. The very low washcoat loadings used in the study resulted in washcoat thicknesses of 0.5-3 µm (assuming homogeneous washcoat loading), in which case, the existence of internal mass transport regime can be ruled out.<sup>[150,151]</sup> Carberry number ( $\eta_{\text{ext}}\text{Dall}$ ) is a good measure for evaluating the external mass transfer limitation.  $\eta_{\text{ext}}\text{Dall}$  was calculated by taking into account that the diffusivity of formic acid in air at 290 K is 0.129 cm<sup>2</sup>.s<sup>-1</sup>.<sup>[152,153]</sup> The values of  $\eta_{\text{ext}}\text{Dall}$  were always  $\ll 0.1$  indicating that the contribution of external mass transfer limitation under the investigated conditions is negligible.

Assuming first order kinetics,<sup>[19,152,154]</sup> mass based rate constants were calculated using Eq. 2.6

$$k_m = -\frac{V^*}{m} \ln(1 - X) \quad (2.6)$$

where  $k_m$  is the mass based pseudo first order rate constant in L g<sup>-1</sup> s<sup>-1</sup>,  $V^*$  is the gas flow under reaction conditions in L s<sup>-1</sup>,  $m$  is the catalyst mass (mass of the washcoat present on the monolith) in g, and  $X$  is the fractional conversion, given by Eq. 2.7.

$$X = \frac{\text{ppmHCOOH}_{\text{in}} - \text{ppmHCOOH}_{\text{out}}}{\text{ppmHCOOH}_{\text{in}}} \quad (2.7)$$

The yield and selectivity of carbon dioxide and carbon monoxide are calculated as follows:

$$Y_{\text{CO}_2} = \frac{\text{ppmCO}_2}{\text{ppmHCOOH}_{\text{in}}} * 100, \% \quad (2.8)$$

$$Y_{\text{CO}} = \frac{\text{ppmCO}}{\text{ppmHCOOH}_{\text{in}}} * 100, \% \quad (2.9)$$

$$S_{\text{CO}_2} = \frac{\text{ppmCO}_2}{\text{ppmHCOOH}_{\text{in}} - \text{ppmHCOOH}_{\text{out}}} * 100, \% \quad (2.10)$$

$$S_{\text{CO}} = \frac{\text{ppmCO}}{\text{ppmHCOOH}_{\text{in}} - \text{ppmHCOOH}_{\text{out}}} * 100, \% \quad (2.11)$$

# Chapter 3

## Unique selectivity of Au/TiO<sub>2</sub> for ammonium formate decomposition under SCR-relevant conditions

Based on:

Sridhar, M.\*; Peitz, D.\*; van Bokhoven, J. A.; Kröcher, O. *Chem. Commun.* **2014**, 50(53), 6998–7000.

\*Equal contribution from M.S and D.P: experiments, analysis and write-up

### 3.1 Introduction

As stated in the Chapter 1, the application of formate-based ammonia precursors is contingent on the development of highly active and robust dedicated hydrolysis catalysts that selectively hydrolyse the precursors and release ammonia without oxidation.<sup>[16,155,156]</sup> Besides being an attractive choice of precursor, ammonium formate is also experimentally the simplest choice to study the activity and behaviour of the hydrolysis catalysts towards selective ammonia release and side product suppression under realistic conditions.<sup>[23]</sup> In this chapter, analogous to the extraordinary selectivity of finely dispersed gold for preferential carbon monoxide oxidation (PROX) in hydrogen-rich stream,<sup>[157–160]</sup> another phenomenological observation is reported, wherein, titania-supported gold catalysts are found to show absolute selectivity for AmFo decomposition in the presence of excess oxygen, yielding close to 100% ammonia up to temperatures as high as 300 °C.

### 3.2 Experimental

*Catalyst preparation and testing:* Au/TiO<sub>2</sub> was prepared by a modified incipient wetness impregnation technique according to a previously published method<sup>[131]</sup> and tested following the procedure described in Chapter 2.

### 3.3 Results and Discussion

Anatase Au/TiO<sub>2</sub> catalysts were synthesised via a facile modified incipient wetness impregnation method<sup>[131]</sup> as described in Chapter 2. Figure 3.1 presents the XRD patterns of the fresh and 10 h hydrothermally aged catalyst which had been exposed to 10 vol% water at 800 °C. Both the catalysts exhibited peaks corresponding to anatase phase. The low loading (0.5 wt%) and small particle size (5-7 nm) of gold rendered its detection impractical. There was a slight anatase peak broadening which corresponded to an increase in the anatase crystallite size from 25 nm to 32 nm. However, no phase transformation of titania from anatase to rutile was evident from the XRD patterns. The BET surface areas of the fresh, 5 h and 10 h hydrothermally aged catalysts are presented in Table 3.1. A gradual decrease in surface area was witnessed with increasing hydrothermal aging time. After 10 h of hydrothermal aging, the BET surface area dropped by ca. 35% to 49 m<sup>2</sup> g<sup>-1</sup>. Figure 3.2 depicts the nitrogen sorption isotherms of the fresh and 10 h hydrothermally aged catalysts. Both the catalysts exhibited Type IV isotherms characteristic of H<sub>2</sub>-hysteresis loops associated with capillary condensation taking place in mesopores. The hydrothermally aged catalyst exhibited sintering-induced lowering of adsorbed volume. Figure 3.3 presents the SEM and STEM images of the fresh and 10 h hydrothermally aged catalyst. It appears that while the support (titania) morphology exhibited signs of sintering upon 10 h hydrothermal aging at 800 °C, the particle sizes of the visible gold particles were only subtly

affected. Titania particles of the aged catalyst are in an aggregated state upon sintering which is in consensus with the lowering of BET surface area.

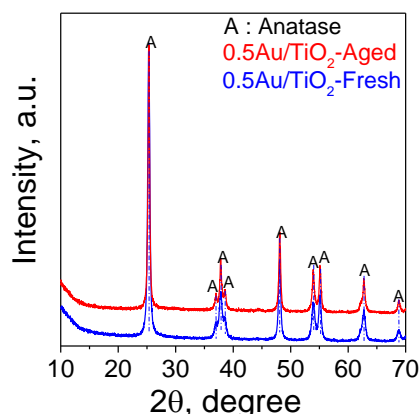


**Figure 3.1** XRD patterns of fresh and 10 h hydrothermally aged 0.5 wt% Au/TiO<sub>2</sub> catalysts showing the absence of any major peaks associated with the rutile phase. The TiO<sub>2</sub> crystallite sizes were determined to be 25 nm and 32 nm in the fresh and 10 h hydrothermally aged samples, respectively.

**Table 3.1** BET surface area of fresh and hydrothermally aged 0.5 wt% Au/TiO<sub>2</sub> catalysts.

Sample	BET Surface Area (m <sup>2</sup> g <sup>-1</sup> )
Fresh	75
5 h Aged	51
10 h Aged	49

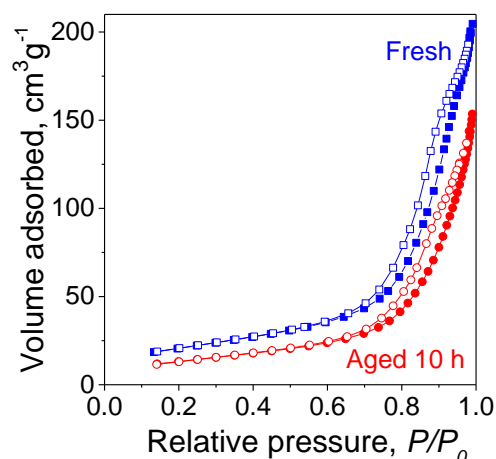


**Figure 3.2** Nitrogen sorption isotherms of fresh and 10 h hydrothermally aged 0.5 wt% Au/TiO<sub>2</sub> catalysts. Closed symbols indicate the adsorption branch while the open symbols represent the desorption branch.

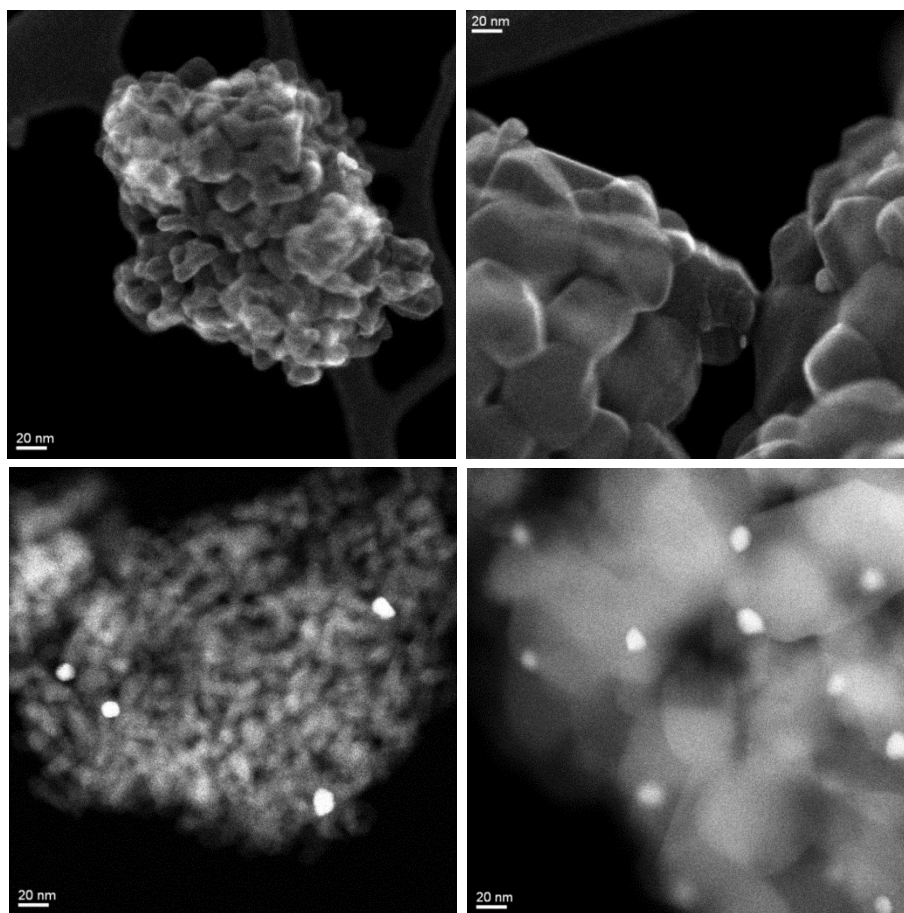


**Figure 3.3** SEM and HAADF-STEM images of 0.5 wt% Au/TiO<sub>2</sub>, fresh (left column) and 10 h hydrothermally aged (right column) catalysts, showing sintering of TiO<sub>2</sub> particles upon aging without any significant change in Au particle size.

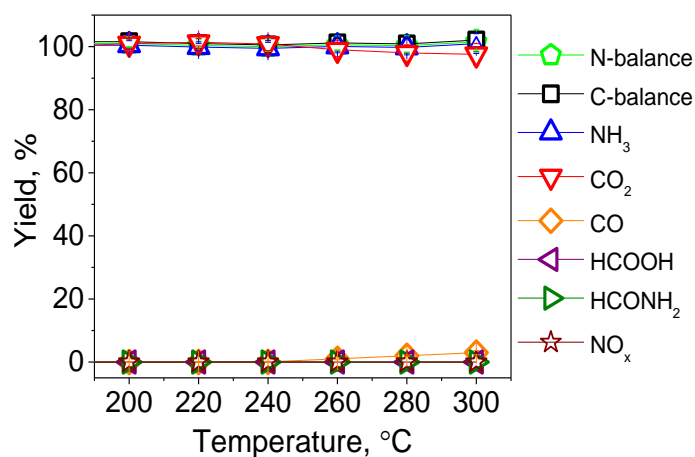


**Figure. 3.4** Product yields for carbon dioxide, carbon monoxide, ammonia, formic acid, methanamide and nitrogen oxide (NO+NO<sub>2</sub>) yields obtained upon the complete decomposition of 40% AmFo over 0.5 wt% Au/TiO<sub>2</sub>. (0.5 g·L<sup>-1</sup> washcoat loading on the monolith, GHSV = 19,490 h<sup>-1</sup>; feed gas: 5 vol% water, 10 vol% oxygen, 85 vol% N<sub>2</sub> and 0.05 mL·min<sup>-1</sup> liquid spray of 40 wt% AmFo).

The carbon and nitrogen balances were closed using the molar feed and reactor outlet concentrations as quantified by FT-IR spectroscopy.<sup>[149]</sup> Washcoat loading refers to the amount of the catalyst deposited on the monolith per unit volume.<sup>[162]</sup> At a 100 g·L<sup>-1</sup> washcoat loading, which is approximately two-thirds of the typical catalyst loadings in automobiles, Au/TiO<sub>2</sub> reliably converted AmFo into ammonia and carbon dioxide in feed containing 10 vol% oxygen and 5 vol% water (Figure 3.4). Ammonia did not react under such conditions rendering negligible NO<sub>x</sub> and methanamide yields, the latter being a side-product arising from the reaction between formic acid and ammonia.<sup>[23]</sup> Methanamide may dehydrate further to form hydrogen cyanide (HCN); however, under these reaction conditions, no HCN was formed over Au/TiO<sub>2</sub>. To determine the stability of the catalysts at partial conversion, the washcoat loading was reduced by 99.5% and tested under identical conditions of GHSV and feed composition. Additionally, the fresh catalyst was subjected to two incremental hydrothermal aging steps each lasting for 5 h at 800 °C in air containing 10% water, and the activity tests were repeated.

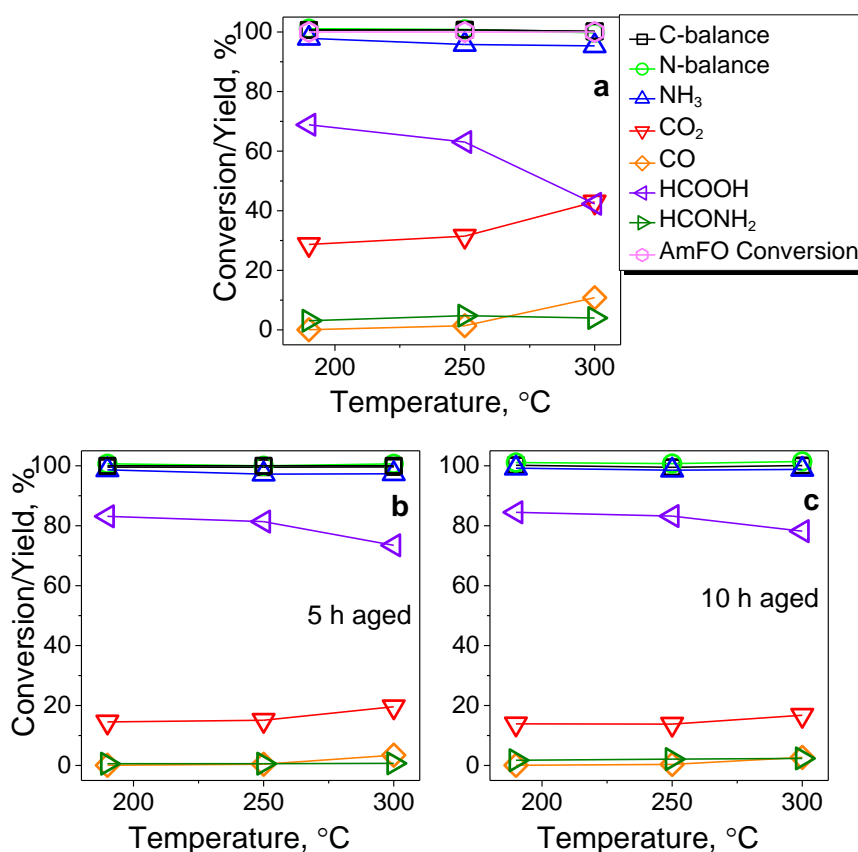


**Figure 3.5** Product yields and AmFo conversion during AmFo decomposition over (a) fresh (b) 5 h aged, and (c) 10 h aged 0.5 wt% Au/TiO<sub>2</sub> catalysts (0.5 g·L<sup>-1</sup> washcoat loading, GHSV = 19,490 h<sup>-1</sup>; feed gas: 5 vol% water, 10 vol% oxygen, 85 vol% N<sub>2</sub> and 0.05 mL·min<sup>-1</sup> liquid spray of 40 wt% AmFo), showing nearly 100% ammonia yields between 200 °C and 300 °C.

Figures 3.5 (a), (b) and (c) depict the yield of all products formed from the decomposition of 40 wt% AmFo over fresh, 5 h and 10 h hydrothermally aged 0.5 wt% Au/TiO<sub>2</sub>, respectively. 100% conversion for AmFo decomposition was achieved with all catalysts. Ammonia, formic acid and

carbon dioxide were the major products, while carbon monoxide and methanamide formed in low yields. The carbon monoxide yield decreased from ~10% over fresh catalyst to ~3% over aged catalysts. Methanamide, which was not observed in the case of 100 g·L<sup>-1</sup> catalyst, started to appear when using 0.5 g·L<sup>-1</sup> catalyst and accounted for ~3% yield or lesser over both the fresh and aged catalysts across all temperatures. Carbon dioxide yields were decreased due to aging from ~43% over the fresh catalyst to ~20% and ~17% over 5 h and 10 h aged catalysts, respectively, at 300 °C. The product yield patterns over the 5 h and 10 h aged catalysts suggest a kind of stabilisation of the catalytic activity after the first aging step. Moreover, ammonia yields always remained close to 100%, which further reiterates the discriminative oxidation behaviour of our catalyst, and contrasts the typical ammonia oxidation behaviour of precious metal containing catalysts.<sup>[163,164]</sup>

**Table 3.2** Mass-based rate constants at various reaction temperatures calculated using pseudo-first-order kinetics.

Catalyst sample	Temperature (K)	Rate constant $k_{\text{mass}}$ (L·g <sup>-1</sup> s <sup>-1</sup> )
Fresh	300	12.5 ± 0.03
	250	6.1 ± 0.01
	190	4.4 ± 0.02
5 h Aged	300	4.4 ± 0.02
	250	2.7 ± 0.01
	190	2.0 ± 0.02
10 h Aged	300	3.7 ± 0.03
	250	2.4 ± 0.02
	190	2.0 ± 0.01
Bare titania	300	3.2 ± 0.04
	250	0.8 ± 0.04
	190	0.3 ± 0.03

Pseudo-first-order kinetic constants were calculated to assess the relative activities of catalysts tested under identical operating conditions.<sup>[19,152,154]</sup> Table 3.2 lists the mass based rate constants calculated for the fresh, 5 h aged, 10 h aged 0.5 wt% Au/TiO<sub>2</sub> and fresh bare titania catalysts. The rate constants progressively decreased for all catalysts with decreasing temperature, indicative of generic Arrhenius behaviour. Hydrothermal aging at 800 °C for 5 h decreased the rate constants by over 60%, while 5 h further treatment resulted in a marginal drop of ~15% when comparing the activities at 300 °C. At lower temperatures, the rate constants tend to nearly identical values for 5 h and 10 h aged catalysts. To elucidate the influence of gold, a control experiment using similar washcoat loading of bare titania was performed under identical conditions. The resultant rate constants were found to be a magnitude of at least 4 lower than that of the fresh Au/TiO<sub>2</sub> catalysts. Importantly, over bare titania, the conversion of formic acid selectively produced carbon monoxide; there is no carbon dioxide formation, under these conditions.

Because, formic acid undergoes secondary reactions to form carbon monoxide and carbon dioxide, the evolution of their selectivities as a function of temperature over the fresh and aged catalysts is interesting. Figure 3.6 (a) and (b) show that the temperature dependence of the selectivities for carbon monoxide and carbon dioxide formation and formic acid conversion remained essentially unchanged even after 10 h aging. A decrease in carbon dioxide selectivity was accompanied by an increase in the carbon monoxide selectivity with increasing temperature for all catalysts. Formic acid conversion was significantly affected by the hydrothermal aging translating to a drop in conversion from ~57% to ~17% after 10 h treatment in 10% water.

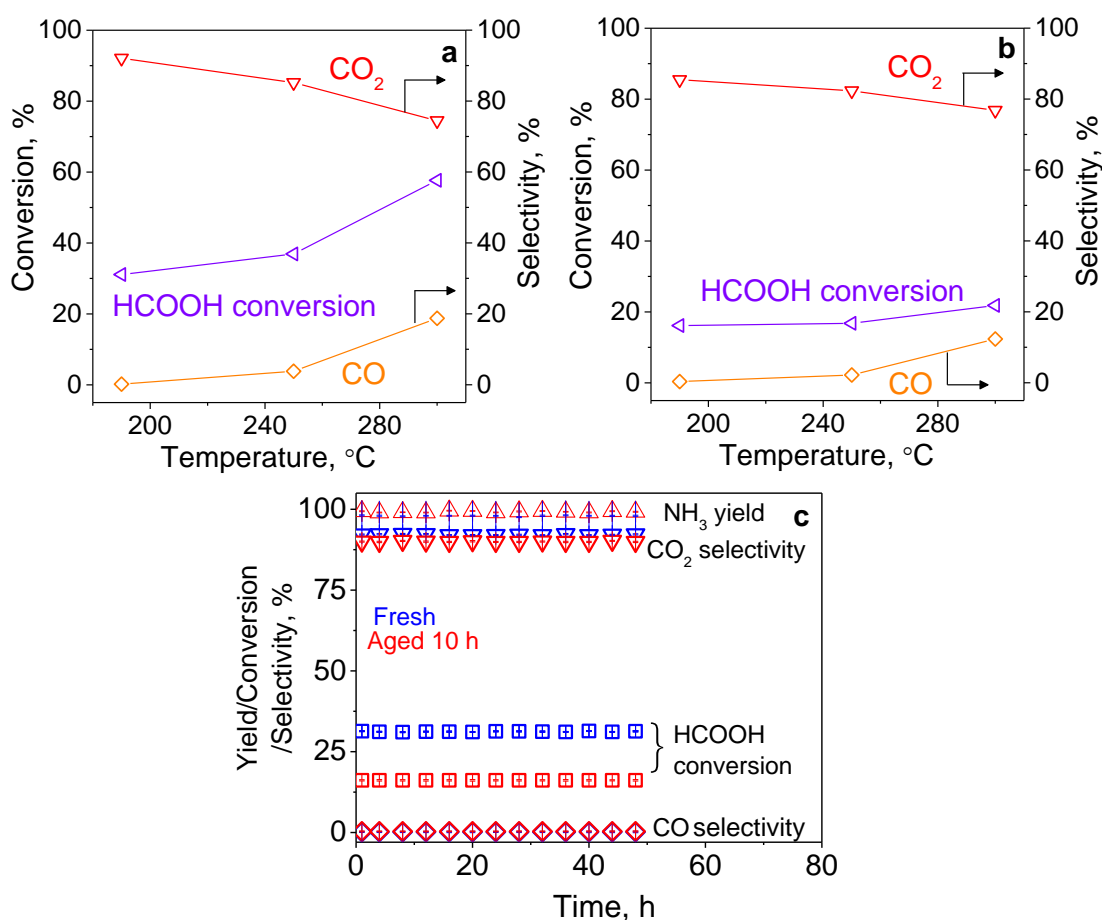


**Figure 3.6** Relationship between selectivity and conversion with temperature for fresh (a) and 10 h aged (b) 0.5% Au/TiO<sub>2</sub> catalysts and (c) Time on stream plot portraying long term stability of fresh (blue) and 10 h hydrothermally aged (red) catalysts at 190 °C (0.5 g·L<sup>-1</sup> washcoat loading on the monolith, GHSV = 19,490 h<sup>-1</sup>; feed gas: 5 vol% water, 10 vol% oxygen, 85 vol% N<sub>2</sub> and 0.05 mL·min<sup>-1</sup> liquid spray of 40 wt% AmFo).

The time on stream activities of the fresh and 10 h hydrothermally aged catalysts were evaluated over 48 h (Figure 3.6 (c)). A low temperature (190 °C) was chosen to examine the low conversion stability. Both the fresh and aged catalysts exhibited stable activities, selectivities and nearly 100% ammonia yields with no signs of deactivation with time-on-stream.

### **3.4 Conclusions**

Au/TiO<sub>2</sub> catalysts demonstrating unique selectivity against ammonia oxidation in a highly oxidizing environment during ammonium formate decomposition is reported in this chapter. The catalysts display excellent stability giving close to 100% ammonia yields for 48 h of time on stream showing no signs of deactivation. The observations evidenced in this work, reflecting the exceptional selectivity against ammonia oxidation could entail new applications of monometallic gold in exhaust gas catalysis.

# Chapter 4

## Effect of ammonia on the decomposition of ammonium formate and formic acid on Au/TiO<sub>2</sub>

Based on:

Sridhar, M.; van Bokhoven, J. A.; Kröcher, O. *Appl. Catal. A Gen.* **2014**, *486*, 219–229.

M.S. contributions: experimental, analysis and write-up

## 4.1 Introduction

In Chapter 3, Au/TiO<sub>2</sub> was demonstrated to be a highly active and uniquely selective catalyst for AmFo decomposition without ammonia oxidation. To optimize the catalyst and the process, it is critical to understand the influence of ammonia on formic acid decomposition under oxidizing conditions relevant to SCR. Loges and coworkers investigated the controlled generation of hydrogen by decomposition of formic acid amine adducts using ruthenium-based homogeneous complexes.<sup>[81]</sup> They found a linear correlation between the amine concentration and the volume of hydrogen produced. In one of the very few demonstrations using heterogeneous catalysts, Bi et al. achieved TOFs up to 1,590 h<sup>-1</sup> over nanocrystalline Au/ZrO<sub>2</sub> at 50 °C for dehydrogenation of formic acid-amine mixtures, which was proposed to stem from the proton scavenging ability of NEt<sub>3</sub> (triethylamine).<sup>[66]</sup> However, there are scarcely any reports that describe the influence of ammonia on heterogeneous catalytic decomposition of formic acid in the gas phase. In this chapter, varying ammonia to formic acid molar ratios ranging from sub-stoichiometric to super-stoichiometric ammonia concentrations have been employed to investigate the effect on formic acid conversion and product selectivity at different temperatures and space velocities over heterogeneous Au/TiO<sub>2</sub> monolithic catalysts. Oxygen and water were employed in excess to simulate exhaust gas conditions in Diesel engines. A significant enhancement of formic acid decomposition rate was observed in the presence of ammonia which was in turn contingent on the presence of gold. In the absence of gold, ammonia induced an inhibitory effect on formic acid decomposition to carbon monoxide over bare titania. Addition of ammonia over Au/TiO<sub>2</sub> selectively improved carbon dioxide yield while the carbon monoxide formation remained disfavored.

These findings can be extrapolated to other ammonia precursor compounds such as guanidinium formate which could release 3 molecules of ammonia per molecule of formic acid. As stated in the Introduction, fast decomposition of the formate part of alternative ammonia precursor compounds presents two fold advantages: (1) it can be expected that the anionic part is destabilized and (2) formic acid is no longer available to form side products like methanamide or HCN.<sup>[23]</sup> With the observed rate enhancement in the presence of ammonia, it could be expected that a basic support or the presence of a basic dopant may also accelerate the decomposition of formic acid. Hence, this marks an important step towards optimization of a more efficient dedicated hydrolysis catalyst.

## 4.2 Experimental

*Catalyst preparation and testing:* Au/TiO<sub>2</sub> was prepared by a modified incipient wetness impregnation technique according to a previously published method<sup>[131]</sup> and tested following the procedure described in Chapter 2. In the experimental setup, 0.05 mL.min<sup>-1</sup> flow of 40 wt%

ammonium formate (AmFo) (Sigma) solution or 30 wt% formic acid solution in water was pumped using a Shimadzu LC-20 AD HPLC pump and sprayed by means of a nebulizer (e-pond) on the catalyst-coated monolith<sup>[148]</sup> in a flow of feed gas containing excess of oxygen (10 vol%), water (5 vol%) and balance nitrogen to emulate the highly oxidizing conditions observed in automobile exhaust. The composition of the precursor solutions were chosen so as to produce isoconcentrations of formic acid in the gas phase. The flow rate was set at 750 L h<sup>-1</sup> in order to realize very high GHSVs in the range 57,000 h<sup>-1</sup> to 300,000 h<sup>-1</sup>. Step-wise increase in contact time was achieved by adding monoliths of identical dimension and washcoat loadings along the reactor axis thus keeping the total catalyst concentration per unit volume constant along the total length of the monolith stack.

### 4.3 Results and Discussion

#### 4.3.1 Homogeneous gas phase experiments

Table 4.1 lists the conversions, product selectivities and yields obtained with the empty reactor for different reactants, namely, AmFo, stoichiometric ammonia- formic acid mixture, and formic acid. The reported values were obtained when the reactor was maintained at 300 °C under identical feed gas and flow conditions as the catalytic runs. Homogeneous gas phase reactions are crucial to identify the thermal decomposition products that are formed before reaching the frontal area of the catalyst. In all cases, the conversions displayed weak dependence on temperature and flow rate of carrier gas. AmFo and stoichiometric ammonia- formic acid mixture exhibited identical gas phase decomposition behavior. In both cases, the ammonia yield was close to 100%, confirming that there is no gas phase reaction taking place between ammonia and formic acid. The formic acid conversion was ~2%, from which carbon dioxide was selectively formed, while, the rest was emitted as unreacted formic acid. This preferential formation of carbon dioxide under the SCR-relevant conditions which included 5 vol% water is in agreement with previous findings that explained the role of water as a homogeneous co-catalyst in the decarboxylation of formic acid.<sup>[165–167]</sup> Formation of methanamide was negligible under the investigated conditions. When formic acid was used as the reactant, decomposition occurred to a low extent and was selective towards carbon dioxide formation. Independent measurements employing mass spectrometry excluded the evolution of any significant amounts of hydrogen for all experiments under the reaction conditions. Close to 30 % drop in conversion was observed upon temperature reduction from 300 °C to 160 °C. Independent measurements checking the effect of varying gas phase ammonia concentrations on formic acid decomposition revealed no such influence and the conversion remained constant at ~2%.

### 4.3.2 Catalytic experiments

The catalyst characterization is described in Chapter 3. Figure 4.1 depicts the kinetic traces derived from the decomposition of AmFo, formic acid, and stoichiometric ammonia-formic acid mixture over 0.5 wt% Au/TiO<sub>2</sub> between 160 °C and 300 °C. W/F is used to denote the contact time, which was calculated by dividing the weight of the catalyst with the total volumetric gas flow. The catalytic formic acid conversion obtained using AmFo, stoichiometric ammonia-formic acid mixture and formic acid were the same at 300 °C. The agreement between AmFo and the stoichiometric ammonia-formic acid mixture at all contact times and temperatures reconciles with the homogeneous gas phase experiments in which AmFo was found to thermally decompose to 100% ammonia and 97.8% formic acid with the residual amount converted to carbon dioxide (Table 4.1).

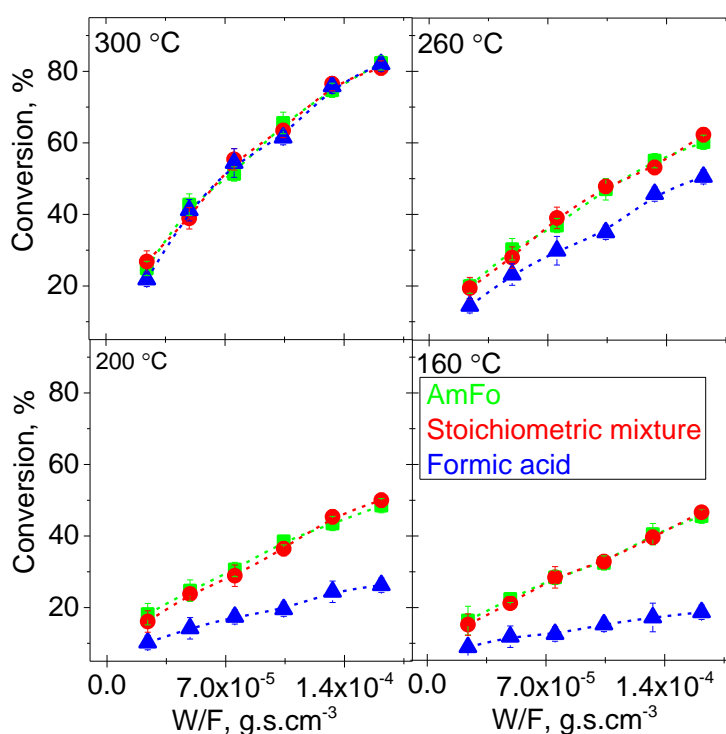
**Table 4.1** Empty tube reaction conversions and products yields for different precursors, namely, AmFo, stoichiometric ammonia-formic acid mixture, and formic acid\*

Precursor	Conversion (%)	$S_{CO_2}$ (%)	$Y_{CO_2}$ (%)	$Y_{HCOOH}$ (%)	$Y_{NH_3}$ (%)	$Y_{HCONH_2}$ (%)	$Y_{HCHO}$ (%)
AmFo	100	-	2.1	97.8	100	0.1	0
Stoichiometric ammonia-formic acid mixture	-	-	-	-	-	0.1	0
Formic acid	1.9	100	-	-	-	-	-
Ammonia	0	-	-	-	-	-	-
Formic acid	2.1	100	-	-	-	-	0

\* Reaction temperature = 300 °C, 750 L.h<sup>-1</sup> flow, feed gas contained 10 vol% oxygen, 5 vol% water, 85 vol% nitrogen to simulate exhaust gas composition and 0.05 ml min<sup>-1</sup> liquid spray of 30 wt% formic acid, 40 wt% AmFo. Stoichiometric amount of ammonia corresponding to formic acid concentration was dosed for the experiments corresponding to the 2<sup>nd</sup> row.

The slopes of the curves, which are indicative of the rates, showed significant differences at lower temperature. At 160 °C, the pseudo-first-order rate constant for formic acid decomposition using AmFo was 6.7 L g<sup>-1</sup> s<sup>-1</sup>, which was nearly 3.5 times higher than the rate obtained using formic acid as the reactant. This suggests a promotional role of ammonia in formic acid decomposition. Literature on such ammonia-induced rate enhancement in gas phase is rare if not absent, however, recently various papers explored the prospects of amine-assisted homogeneous formic acid decomposition for fuel cell applications.<sup>[61,66,76,81,82]</sup> Loges et al. pioneered the use of formic acid amine adducts for hydrogen generation over homogeneous phosphine-based ruthenium complexes. They found an increase in the activity with increasing amine concentration in the reactant mixture, divulging no further mechanistic insight.<sup>[76,81]</sup> In a following work, Bi et al.<sup>[66]</sup> demonstrated that formic acid amine adducts can be efficiently decomposed over heterogeneous catalysts, particularly, nanocrystalline gold supported on

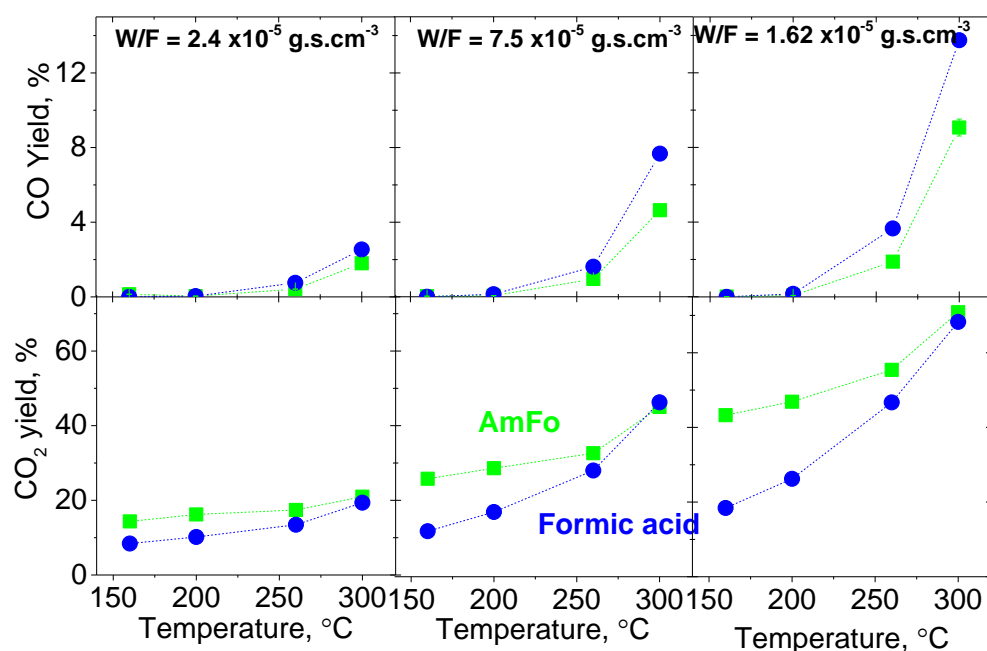
zirconia catalysts. The TOF after the initial 20 min of reaction increased from 15 h<sup>-1</sup> to 250 h<sup>-1</sup> upon addition of about 0.5 molar equivalents of NEt<sub>3</sub> during the aqueous phase decomposition of formic acid at 40 °C. They hypothesized that the amines, being strong bases, assist in the deprotonation of OH of formic acid which leads to accelerated rates. Along the same lines, ammonia being a strong Brønsted base can be construed to aid hydrogen abstraction from formic acid in a kinetically relevant step.



**Figure 4.1** Kinetic traces depicting formic acid conversion as a function of contact time, expressed as W/F (g cat s cm<sup>-3</sup>) obtained over 0.5 wt% Au/TiO<sub>2</sub> by using AmFo, formic acid and stoichiometric ammonia-formic acid mixture at different temperatures.

To fully understand the influence of ammonia, the product yields (Figure 4.2) and the selectivities at different level of conversion (Figure 4.3) have been determined. Interestingly, in the case of AmFo, the carbon dioxide yield was higher at all temperatures below 300 °C, and the difference tended to be of greater magnitude at higher contact times and lower temperatures. For W/F = 1.62\*10<sup>-4</sup> g s cm<sup>-1</sup>, the carbon dioxide yield obtained at 160 °C with AmFo is 45%, while with formic acid, only 18% carbon dioxide yield can be achieved. As expected, the carbon monoxide yield followed an opposite trend. Interestingly, at 300 °C, even though the formic acid conversion rates were closely similar for AmFo and formic acid, there exists a significant difference in the corresponding carbon monoxide yields: 14% for formic acid decomposition and 9% for AmFo. At 260 °C, the carbon monoxide yields were 4% and 2%, respectively. Below 200 °C, no carbon monoxide was detected in either case.

Further insight into the evolution of product selectivities during the decomposition of formic acid and AmFo was deduced by plotting selectivities as a function of conversion obtained isothermally at different GHSVs (Figure 4.3). When only formic acid was used as the precursor, the carbon monoxide selectivity increased in parallel with decreasing carbon dioxide selectivity and increasing conversion. This can be explained by the fact that titania requires higher contact times to decompose formic acid to carbon monoxide, since its rate constants were at least five orders of magnitude lower than that of 0.5 wt% Au/TiO<sub>2</sub> (Table 4.2). Thus, the carbon monoxide selectivity steadily increased at the expense of carbon dioxide selectivity with increasing formic acid conversion. In the case of AmFo, there was an increase in carbon dioxide and carbon monoxide selectivities with increasing conversion offset by a proportionate decrease in methanamide selectivity. Methanamide is an amidation product formed by dehydration reaction between ammonia and formic acid.<sup>[168]</sup>



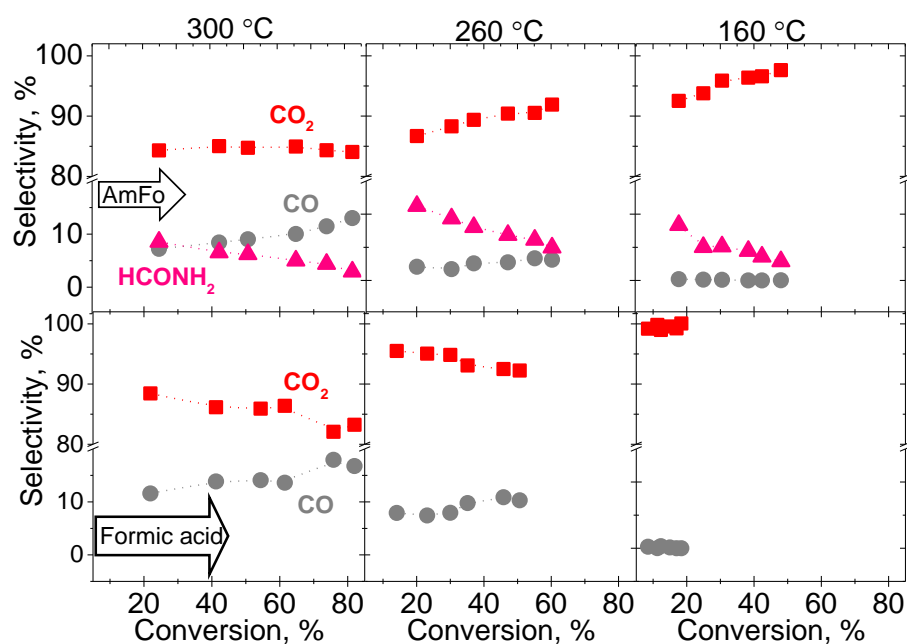
**Figure 4.2** Evolution of carbon monoxide yields (top row) and carbon dioxide yields (bottom row) with temperature for different W/F upon decomposition of AmFo (green) and formic acid (blue) over 0.5 wt% Au/TiO<sub>2</sub>.

Figure 4.4 depicts the effect of contact time on methanamide emission during AmFo decomposition. At lower contact time, formic acid and ammonia evolved from the gas phase thermolysis of AmFo, may not sufficiently interact to form methanamide, however, at higher contact times, the formed methanamide increasingly re-hydrolyzes to formic acid and ammonia. Separate experiments probing methanamide decomposition over 0.5 wt% Au/TiO<sub>2</sub> catalyst exposed the formation of formic acid and ammonia as primary products, where, the former subsequently decomposed to carbon monoxide and mainly carbon dioxide with increasing

contact time (Figure 4.5). The hydrolysis and formation of methanamide can be represented as an equilibrium reaction (Eq. 4.1).



This reaction is endergonic with  $\Delta G = 2.175 \text{ kJmol}^{-1}$  at 150 °C, turning exergonic only above 450 °C. However, due to the small positive value of the free enthalpy change, law of mass action dictates the thermodynamic equilibrium. Hence the concentration of the reactants bears a pronounced influence on the extent of hydrolysis or amidation.<sup>[169]</sup>



**Figure 4.3** Selectivity versus conversion in the range 160 °C ≤ T ≤ 300 °C upon decomposition of AmFo (top) and formic acid (bottom) over 0.5 wt% Au/TiO<sub>2</sub>.

**Table 4.2** Mass-based-pseudo-first-order rate constants for carbon monoxide production and amidation reaction during AmFo decomposition over bare titania.

Ammonia: formic acid molar ratio	300 °C		260 °C		160 °C	
	$K_{\text{CO}}$	$k_a$	$k_{\text{CO}}$	$k_a$	$k_{\text{CO}}$	$k_a$
	(L g <sup>-1</sup> s <sup>-1</sup> )					
0	5.6	0.0	1.5	0.00	0	0.00
0.25	4.8	0.1	1.2	0.2	0	0.2
0.5	4.5	0.2	1.1	0.3	0	0.3
1	4.1	0.4	1.0	0.6	0	0.4
2	3.6	0.8	0.9	1.0	0	0.4
3	3.3	1.1	0.8	1.5	0	0.5
5	2.9	1.9	0.7	2.5	0	0.6
9	2.4	2.6	0.6	3.2	0	0.8
12	2.0	2.8	0.4	3.5	0	0.8

Experiments involving step-wise increase in the gas phase ammonia concentration during formic acid decomposition were conducted to systematically probe the influence of ammonia on conversion and product distribution (Figure 4.6). Ammonia to formic acid molar ratios ranging from 0 to 12 were employed. The influence of ammonia was more pronounced at lower temperatures and higher contact times. At higher contact times and lower temperature ( $W/F > 2.4 \cdot 10^{-5} \text{ g s cm}^{-3}$ ,  $T = 160 \text{ }^\circ\text{C}$ ), the carbon dioxide yield and the conversion almost doubled with 0.25 molar equivalents of ammonia in the gas phase.

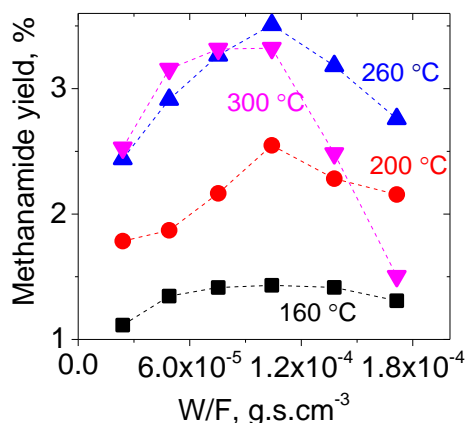


**Figure 4.4** Evolution of methanamide yield as a function of contact time at different temperatures during AmFo decomposition over 0.5 wt% Au/TiO<sub>2</sub>.

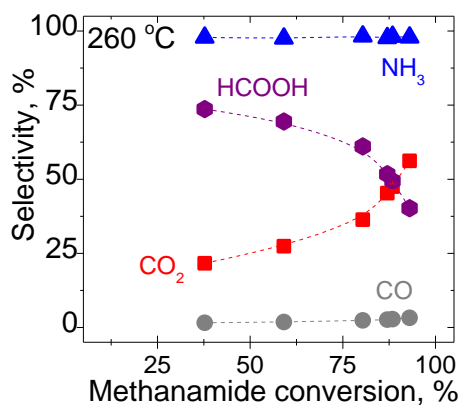


**Figure 4.5** Selectivity versus conversion plot at 260 °C upon decomposition of 30% methanamide over 0.5 wt% Au/TiO<sub>2</sub> showing the formation of ammonia and formic acid as primary products upon methanamide hydrolysis followed by formic acid decomposition to carbon monoxide and carbon dioxide with increasing methanamide conversion.

However at 260 °C, the increase was less impressive (approx. 8%) at all contact times. Increasing the ammonia to formic acid molar ratio from 0 to 12 at  $W/F = 2.4 \cdot 10^{-5} \text{ g s cm}^{-3}$ , led to an increase in conversion from 7% to 26% at 160 °C, and from 12% to 28% at 260 °C. This is reflected in an enhancement in the carbon dioxide yield from 7% to 23% at 160 °C and from 11% to 23% at 260 °C. Strikingly, at the highest ammonia to formic acid molar ratio of 12, the carbon dioxide yields achieved at 160 °C equaled the corresponding values at 260 °C at all

contact times. Using the intermediate contact time ( $W/F = 7.5 \cdot 10^{-5} \text{ g s cm}^{-3}$ ), the formic acid conversion increased from 12% to 48% and 36% to 62% at 160 °C and 260 °C, respectively. At  $W/F = 1.62 \cdot 10^{-4} \text{ g s cm}^{-3}$ , even though there existed considerable difference in the formic acid conversion ( $\sim 10\%$ ) at the two temperatures, the carbon dioxide yields again remarkably assumed closely identical values around 75% at the ammonia to formic acid molar ratio of 12. This implies an increase by more than 300% and 25% at 160 °C and 260 °C, respectively. Such a temperature-dependent influence of ammonia on formic acid reactivity went hand in hand with a drastic shift in the product selectivities at the two temperatures.

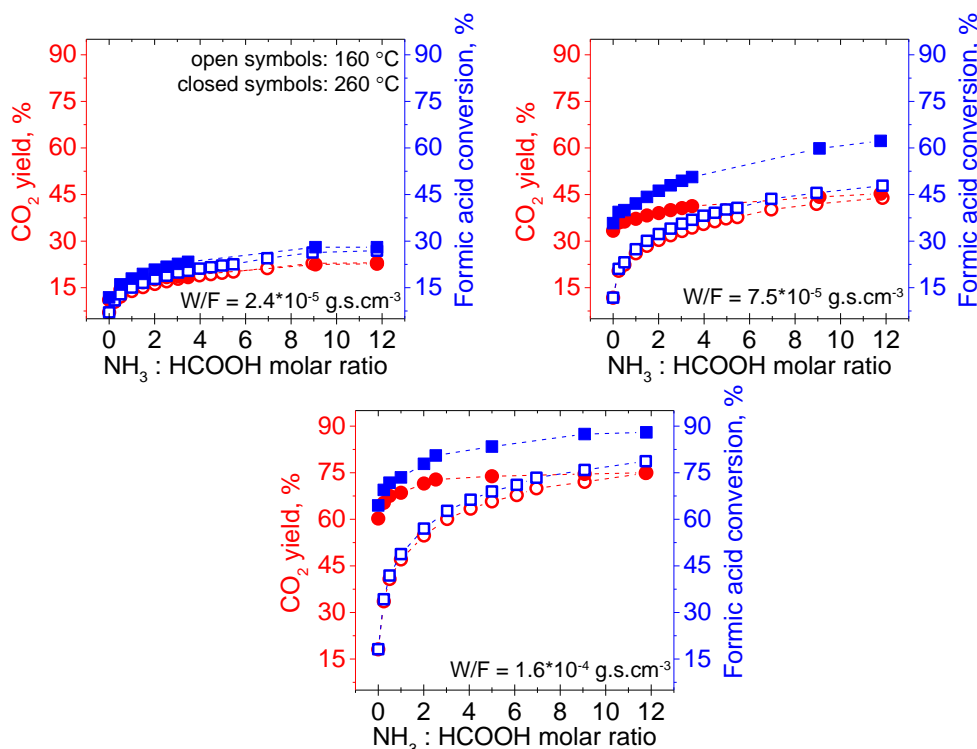


**Figure 4.6** Formic acid conversion and carbon dioxide yield over 0.5 wt% Au/TiO<sub>2</sub> with varying ammonia to formic acid molar ratio at different temperatures: 160 °C (open symbol) and 260 °C (closed symbol) and different contact times.

Figure 4.7 depicts the selectivity of carbon dioxide, carbon monoxide and methanamide selectivities as a function of ammonia concentration at three different contact times and temperatures. X denotes the conversion value attained at the highest ammonia to formic acid molar ratio specific to the contact time. The black crosses, indicating the corresponding product selectivities obtained from independent measurements using AmFo as the precursor coincided with those obtained using stoichiometric ammonia-formic acid mixture.

Clearly, for all contact times, the methanamide selectivities attained with increasing ammonia concentrations at 260 °C largely exceeded the corresponding values at 160 °C. In fact, at  $W/F = 1.62 \cdot 10^{-4} \text{ g s cm}^{-3}$ , the methanamide selectivity at the ammonia to formic acid molar ratio of 12 was only 4.8% at 160 °C, which is nearly 3 times lower than the value obtained at 260 °C. The

methanamide selectivity levelled off beyond two molar equivalents of ammonia when the reaction temperature was 160 °C. For instance, at the intermediate contact time ( $W/F = 7.5 \cdot 10^{-5} \text{ g s cm}^{-3}$ ), increasing the ammonia to formic acid ratio from 2 to 12 invoked only a limited increase in the methanamide selectivity from 6% to 8%. The difference was even lower at other contact times. This was not the case at 260 °C, where the methanamide selectivity almost doubled with further addition of ammonia from 2 to 12 molar equivalents at all contact times. This means that at 260 °C, more formic acid converts to methanamide rather than to carbon dioxide. This is in congruence with literature reports that suggest higher methanamide formation at higher temperatures,<sup>[23]</sup> thereby explaining the higher carbon dioxide yields at 160 °C even though the corresponding formic acid conversion value was lower.

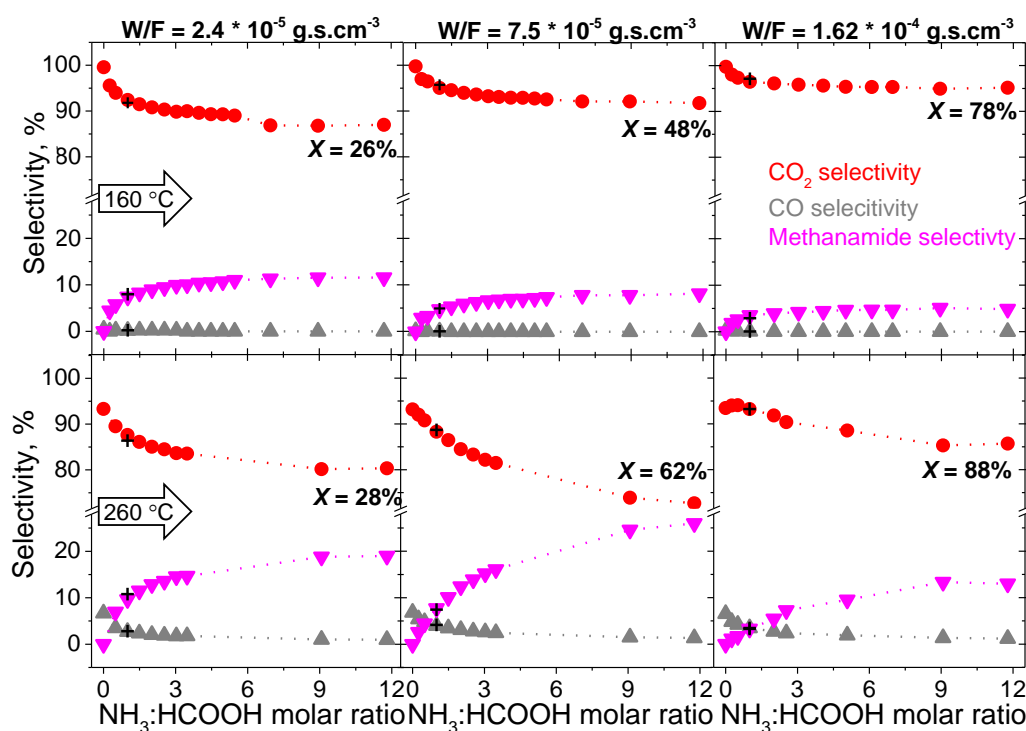


**Figure 4.7** Carbon dioxide, carbon monoxide and methanamide selectivities obtained over 0.5 wt% Au/TiO<sub>2</sub> with varying ammonia to formic acid molar ratio at different temperatures: 160 °C (top row) and 260 °C (bottom row), and different contact times, the (+) symbols represent the corresponding selectivities obtained during AmFo decomposition.

The maximum methanamide yield obtained at 160 °C was between 3% and 4% for all contact times. On the other hand, at 260 °C, the methanamide yields at 260 °C amounted 5% (at  $W/F = 2.4 \cdot 10^{-5} \text{ g s cm}^{-3}$ ), 16% (at  $W/F = 7.5 \cdot 10^{-5} \text{ g s cm}^{-3}$ ) and 12% (at  $W/F = 1.62 \cdot 10^{-4} \text{ g s cm}^{-3}$ ). Such a trend in the methanamide emissions can be reasoned by the effect of contact time. As discussed earlier, at lower contact times, with increasing ammonia concentration, formic acid may not have sufficient time to react to form methanamide; at the highest contact time, the formed methanamide may re-hydrolyze to ammonia and form formic acid ensuing further decomposition to carbon monoxide or carbon dioxide. However, at the intermediate contact

time, the formed methanamide may still be stable enough to be emitted as such resulting in higher selectivities/yields.<sup>[23]</sup>

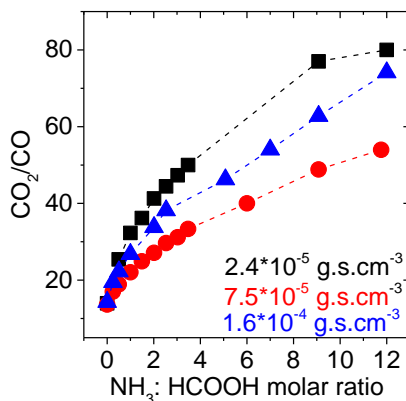


**Figure 4.8** Molar ratio of reaction products, namely, carbon dioxide and carbon monoxide as a function of ammonia to formic acid molar ratio.

Another interesting feature is the decrease in carbon monoxide selectivity with increasing ammonia concentration (Figure 4.7). At 260 °C, with the introduction of one stoichiometric equivalent of ammonia, the carbon monoxide selectivity is lowered by a magnitude of 3%, even when using the lowest contact time ( $W/F = 2.4 \cdot 10^{-5} \text{ g s cm}^{-3}$ ). Inclusion of additional 8 stoichiometric equivalents resulted in carbon monoxide selectivities below 1% for all contact times. This decline in carbon monoxide formation is proposed to originate from the influence of ammonia on the decomposition activity of bare titania, which will be discussed later. Figure 4.8 visualizes the effect of ammonia to formic acid molar ratio on the carbon dioxide to carbon monoxide molar ratio in the effluent gas at 260 °C using three contact times. A monotonic increase in the carbon dioxide to carbon monoxide molar ratio was observed with increasing ammonia concentration. In the absence of ammonia, the carbon dioxide to carbon monoxide ratio is around 14 for all contact times. Dosing 12 molar equivalents of ammonia resulted in an increase in the carbon dioxide/carbon monoxide molar ratios to 80, 54 and 75 at the lowest, intermediate and the highest contact times, respectively.

To delineate the influence of ammonia over the two components of the catalyst system: gold and titania, additional experiments over bare titania at identical temperature, and flow were performed. Figure 4.9 illustrates the effect of varying ammonia to formic acid molar ratios on formic acid conversion and product yield, respectively, over bare titania, at three temperatures: 300 °C, 260 °C and 160 °C and employing a  $W/F$  of  $1.62 \cdot 10^{-4} \text{ g s cm}^{-3}$ . To decouple the formic acid decomposition to carbon monoxide/carbon dioxide from the amidation reaction with ammonia to form methanamide/HCN, the legends, 'decomposition' and 'amidation' have been used, respectively. The 'total' encompasses both these components.

Evidently, under all conditions, bare titania displayed considerably lower activity compared to Au/TiO<sub>2</sub>. In the absence of ammonia, the conversion values, which essentially represent

decomposition, were 42%, 13.6 % and 2% at 300 °C, 260 °C and 160 °C, respectively. At 300 °C, the ‘total’ conversion was not greatly affected by the presence of ammonia. This can be clearly deduced from the two component curves which follow opposing trends, where the drop in conversion owing to inhibited decomposition is counterbalanced by the rise due to amidation reaction. With the addition of 8 molar equivalents of ammonia, conversion owing to decomposition to carbon monoxide fell from 42% to 22%, which was nearly compensated by an increase in conversion due to reaction with ammonia which amounted to 23%. At 260 °C, the inherent activity of bare titania for decomposition was already low, rendering a conversion value of only 13.6%. However, rapid reaction with ammonia led to an increase in total conversion to 33%, out of which the ‘decomposition’ accounted for 6%. At 160 °C, the activity of bare titania for decomposition was close to zero and the conversion owing to reaction was as low as 6% at ammonia to formic acid molar ratio of 10. The latter was expected, since, methanamide formation is not favored at lower temperatures.<sup>[23]</sup>

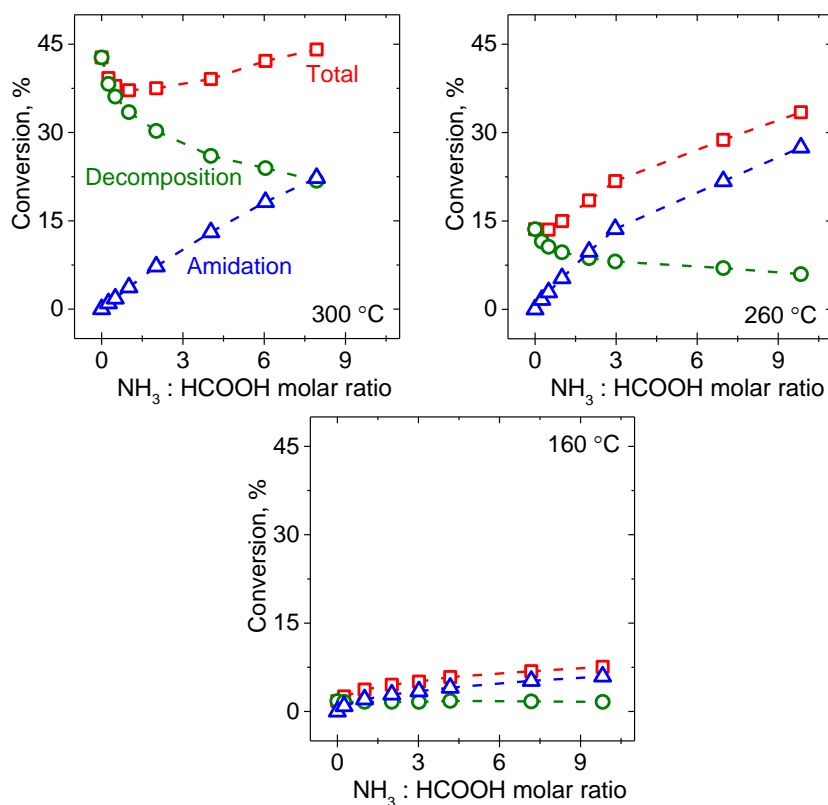


**Figure 4.9** Trends in formic acid conversion over bare titania as a function of ammonia gas dosed in the feed stream for temperatures between 160 °C and 300 °C. ‘Decomposition’: formic acid conversion only to carbon dioxide and carbon monoxide. ‘Amidation’: formic acid conversion to methanamide and hydrogen cyanide. ‘Total’: sum of ‘Decomposition’ and ‘Amidation’.

Methanamide production appeared to follow a volcano-like trend with respect to temperature, reaching a maximum at 260 °C (Figure 4.10). This can be explained by the higher reactivity of formic acid to form carbon monoxide at 300 °C instead of contributing towards amidation

reaction, which is reflected in the lower values of the rate constants for formic acid reaction with ammonia to form methanamide ( $k_a$ ) at 300 °C compared to the corresponding values at 260 °C. (Table 4.2). However, in the case of Au/TiO<sub>2</sub>, methanamide formation during AmFo decomposition is much less favored than over bare TiO<sub>2</sub> due to the significantly higher formic acid decomposition rate than the rate for amidation reaction at all temperatures (Table 4.3 and 4.4). Compared with the formic acid conversion obtained over Au/TiO<sub>2</sub> (Figure 4.1), the values observed for bare titania were lower by at least 2 orders of magnitude besides the preferred selectivity to carbon monoxide. This ascertains the pivotal role of gold in clean and efficient decomposition of formic acid. Additionally, it can be deduced that ammonia adversely affects formic acid decomposition to carbon monoxide since formic acid preferably reacted with ammonia to form amidation products.

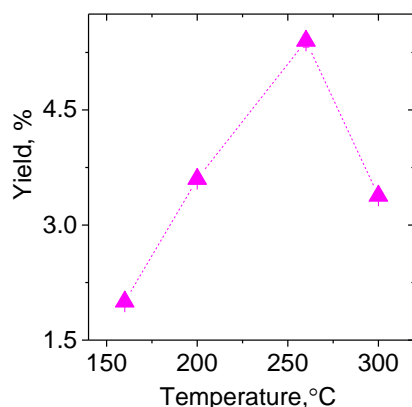


**Figure 4.10** Evolution of methanamide yield as a function of temperature during AmFo decomposition over bare titania revealing a volcano-like relationship.

Figure 4.11 shows product yield distribution obtained over bare titania as a function of ammonia to formic acid molar ratios. The crossed symbols represent the corresponding product yields obtained over 0.5 wt% Au/TiO<sub>2</sub> under identical GHSV and washcoat loadings for formic acid and AmFo decomposition. At all temperatures, there was an immediate decrease in carbon monoxide yield triggered by the introduction of ammonia. The low amounts of carbon dioxide yield (around 3%) detected over bare titania at 300 °C can be traced back to inherent activities in the gas phase (Table 4.1) and the blank (uncoated) monoliths. Hence, the high carbon dioxide yields amounting to 68% and 71% in the case of formic acid and AmFo, respectively, over Au/TiO<sub>2</sub>, can be clearly ascribed to the presence of gold.

In the absence of ammonia, titania selectively decomposed formic acid to carbon monoxide. The carbon monoxide yield decreased from 39% at 300 °C to 10% at 260 °C. At ammonia to formic acid molar ratio of 1, which is essentially the simulation of gas phase AmFo, the carbon monoxide yield decreased to 30%, while 3.3% methanamide was evolved at 300 °C. As discussed earlier, in the case of Au/TiO<sub>2</sub>, a decrease in the carbon monoxide yield from 14% to

9% was observed when switched between formic acid and AmFo. We speculate that this drop in carbon monoxide yield may have arisen from the reduced carbon monoxide production over titania in the presence of ammonia. At ammonia to formic acid molar ratio of 8, the methanamide yield rose to 20 % with a concomitant decrease in carbon monoxide yield to 18% which is a reduction by 20% relative to the yield obtained in the absence of ammonia. This suggests that the decomposition of formic acid to carbon monoxide and the amidation reaction to form methanamide are competitive. As denoted by the crossed symbols, the carbon dioxide yields achieved over Au/TiO<sub>2</sub> were significantly higher at all temperatures while the undesired products like carbon monoxide and methanamide were emitted at lower yields.

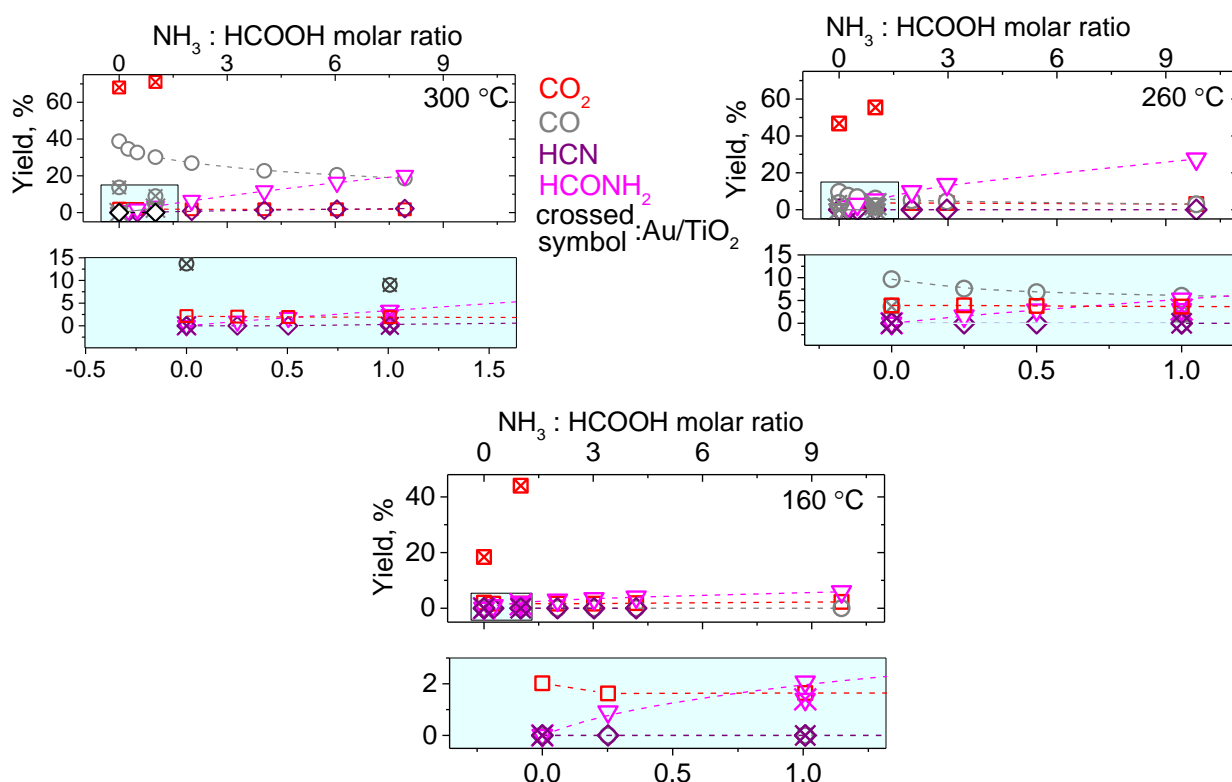


**Figure 4.11** Carbon dioxide, carbon monoxide and methanamide yields obtained over bare titania as a function of ammonia to formic acid molar ratio at  $W/F = 1.62 \cdot 10^{-4} \text{ g.s.cm}^{-3}$ , the crossed symbols of corresponding colors represent the corresponding yields obtained during formic acid/AmFo decomposition.

Small amounts of HCN, formed upon dehydration of methanamide at high temperatures, were also observed over bare titania at 300 °C amounting to a total of 2% yield at the highest ammonia concentration. At 260 °C, the carbon monoxide yield decreased from 10% to 7% upon addition of one molar equivalents of ammonia in the gas phase. Further addition of ammonia until ~10 molar equivalents diminished the carbon monoxide yield to less than 3%, while the methanamide yield rose to 24%. Methanamide yields were slightly higher at 260 °C than at 300 °C (Figure 4.10), which may be attributed to lower interaction of ammonia with the catalyst surface or an increased rate of hydrolysis of the formed methanamide at higher temperatures.<sup>[23]</sup>

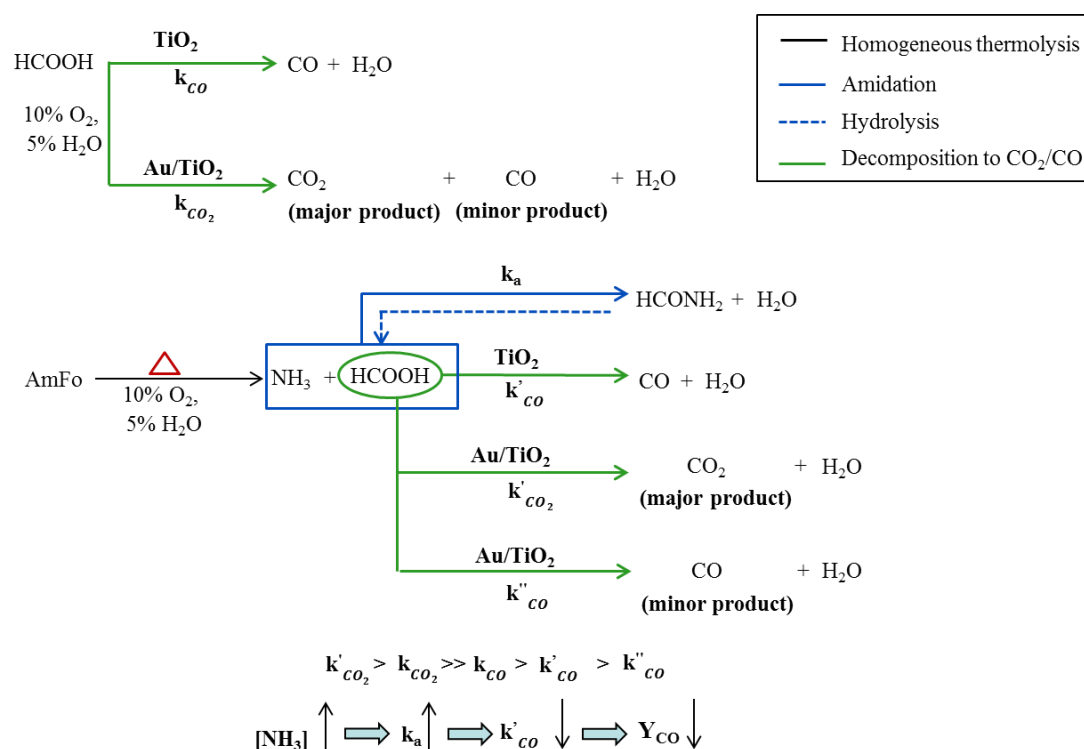
Formic acid was emitted practically undecomposed at 160 °C in the absence of ammonia and the observed conversion is almost exclusively accounted for by its reaction with ammonia to form methanamide. At ammonia to formic acid molar ratio of 10, methanamide yield reached a value of only 6% which is in stark contrast to the yield attained at higher temperatures. Hence, the temperature dictated the formation of methanamide over titania. Overall, it is clear that the positive influence of ammonia on formic acid decomposition is contingent on the presence of gold.

Table 4.3 and 4.4 list the product selectivities, fractional conversions and mass-based pseudo-first-order rate constants derived at different ammonia concentrations for formic acid decomposition over Au/TiO<sub>2</sub> and mass-based rate constants for bare titania at 260 °C and 160 °C, respectively, using  $W/F = 1.62 \cdot 10^{-4} \text{ g s cm}^{-3}$ .  $X_{CO_2}$ ,  $X_{CO}$  and  $X_{HCONH_2}$  represent the fractional formic acid conversion over Au/TiO<sub>2</sub> relevant in the formation of the respective products. For Au/TiO<sub>2</sub>, the fractional conversion corresponding to carbon dioxide and carbon monoxide formation decreased from 0.93 to 0.85 and from 0.07 to 0.01, respectively, with the addition of 12 molar equivalents of ammonia. This decrease manifested itself as an increase in the fractional conversion corresponding to methanamide formation up to 0.14. However, the mass-based rate constants for carbon dioxide production nearly doubled from 11.9 L g<sup>-1</sup> s<sup>-1</sup> to 21.5 L g<sup>-1</sup> s<sup>-1</sup>, while that for carbon monoxide declined by more than half from 0.8 to 0.3. Methanamide formation attained a rate constant equal to 3.4 L g<sup>-1</sup> s<sup>-1</sup>. As discussed earlier, formic acid decomposition to carbon dioxide was even more strongly influenced at lower temperature. At 160 °C, the rate constants for carbon dioxide formation doubled to 4.1 L g<sup>-1</sup> s<sup>-1</sup> with the addition of only 0.25 molar equivalents of ammonia in contrast to the 15% increase at 260 °C. With the stoichiometric ammonia-formic acid mixture, the rate constants underwent 225% and 22% increase at 160 °C and 260 °C, respectively.

At the highest ammonia concentration corresponding to 12 molar equivalents, the rate constant for carbon dioxide formation at 160 °C experienced 700% increase, reaching a value as high as 15.0 L g<sup>-1</sup> s<sup>-1</sup>, which is only a factor of 1.4 lower than the corresponding value at 260 °C. In contrast to the rate constants for methanamide formation at 260 °C (3.5 L g<sup>-1</sup> s<sup>-1</sup>), the highest value obtained using 12 molar equivalents of ammonia was 0.7 L g<sup>-1</sup> s<sup>-1</sup> which corresponded to a rise in the fractional conversion value to 0.05. Over bare titania, introduction of 0.25 molar equivalents of ammonia at 260 °C resulted in a 20% decrease in the rate constant for carbon monoxide formation, while the rate constants for methanamide formation experienced a 20% increase. Further increase in the ammonia to formic acid molar ratio up to 12 resulted in the suppression of the activity for carbon monoxide formation by greater than 73% which was outweighed by an increase in methanamide formation activity to 3.5 L g<sup>-1</sup> s<sup>-1</sup>. At 160 °C, there

was negligible decomposition activity and limited amidation reaction over bare titania as was evident from the corresponding rate constant equaling only  $0.8 \text{ L g}^{-1} \text{ s}^{-1}$ .

To put into perspective, the reactions taking place over bare titania and Au/TiO<sub>2</sub> have been depicted in Scheme 4.1. Formic acid decomposition over bare titania and Au/TiO<sub>2</sub> lead to the formation of carbon monoxide and carbon dioxide, respectively, as the preferentially formed products. If  $k_{CO}$  and  $k_{CO_2}$  were the corresponding rate constants, these experiments established  $k_{CO_2}$  to be significantly greater than  $k_{CO}$ . AmFo undergoes homogeneous thermolysis resulting in the instantaneous formation of ammonia and formic acid in the gas phase upstream of the catalyst (Table 4.1). Formic acid decomposition in the presence of ammonia ( $k'_{CO}$ ) is suppressed over bare titania owing to its increased reactivity towards ammonia to form amidation products ( $k_a$ ). With increasing ammonia concentration, the increase in  $k_a$  further offsets the amount of formic acid available to decompose to carbon monoxide ( $k_{CO}$ ) This leads to a depression in the carbon monoxide yield accompanied by increased methanamide yield. However, in the case of Au/TiO<sub>2</sub>, ammonia promotes the decomposition of formic acid ( $k'_{CO_2} > k_{CO_2}$ ) leading to higher carbon dioxide yields and lower carbon monoxide yields ( $Y_{CO}$ ) stemming from the response of bare titania.



**Scheme 4.1** Proposed reactions over bare titania and Au/TiO<sub>2</sub> during formic acid and AmFo decomposition.

**Table 4.3** Selectivity, fractional conversion and mass-based rate constants over Au/TiO<sub>2</sub> and mass-based rate constants over bare titania calculated at 260 °C using pseudo first order kinetics.\*

NH <sub>3</sub> : formic acid	Au/TiO <sub>2</sub>									TiO <sub>2</sub>		
	k <sub>mass</sub> (L.g <sup>-1</sup> .s <sup>-1</sup> )	S CO <sub>2</sub>	S CO	S HCONH <sub>2</sub>	X CO <sub>2</sub>	X CO	X HCONH <sub>2</sub>	k CO <sub>2</sub>	k CO	k HCONH <sub>2</sub>	k <sub>CO</sub>	k <sub>a</sub>
		S (%)			X			k (L g <sup>-1</sup> s <sup>-1</sup> )			k (L g <sup>-1</sup> s <sup>-1</sup> )	
0	12.7	93.5	6.5	0.0	0.93	0.07	0.00	11.9	0.8	0.0	1.5	0.0
0.25	14.6	94.0	4.8	1.1	0.94	0.05	0.01	13.7	0.7	0.2	1.2	0.2
0.5	15.6	94.1	4.2	1.7	0.94	0.04	0.02	14.7	0.7	0.3	1.1	0.3
1	16.4	93.2	3.5	3.3	0.93	0.03	0.03	15.3	0.6	0.5	1.0	0.6
2	18.6	91.8	2.7	5.4	0.92	0.03	0.05	17.1	0.5	1.0	0.9	1.0
3	20.7	89.8	2.3	7.9	0.90	0.21	0.08	18.6	0.5	1.6	0.8	1.5
5	22.1	88.5	1.9	9.5	0.89	0.02	0.10	19.6	0.4	2.1	0.7	2.5
9	25.6	85.3	1.4	13.3	0.08	0.02	0.13	21.4	0.4	3.4	0.6	3.2
12	25.3	84.8	1.7	13.5	0.85	0.01	0.14	21.5	0.3	3.4	0.4	3.5

\*Reaction temperature= 260 °C, W/F = 1.62\*10<sup>-4</sup> g.s.cm<sup>-3</sup>; 750 L.h<sup>-1</sup> flow, feed gas contained 10% oxygen, 5% water, 85% nitrogen to simulate exhaust gas composition, 0 to 7800 ppm NH<sub>3</sub> were dosed and 0.05 mL.min<sup>-1</sup> liquid spray of 30 wt% formic acid. k<sub>mass</sub> denotes the total mass-based pseudo-first-order rate constants for Au/TiO<sub>2</sub>, S<sub>i</sub>, X<sub>i</sub> and k<sub>i</sub> represent the selectivity, fractional formic acid conversion and mass-based pseudo first order rate constants relevant in the formation of the respective products. k<sub>a</sub> in the case of bare titania is used to designate the rate constant corresponding to the formation of methanamide and hydrogen cyanide.

**Table 4.4** Selectivity, fractional conversion and mass-based rate constants over Au/TiO<sub>2</sub> and mass-based rate constants over bare titania calculated at 160 °C using pseudo first order kinetics.\*

NH <sub>3</sub> : formic acid	Au/TiO <sub>2</sub>									TiO <sub>2</sub>		
	k <sub>mass</sub> (L.g <sup>-1</sup> .s <sup>-1</sup> )	S CO <sub>2</sub>	S CO	S HCONH <sub>2</sub>	X CO <sub>2</sub>	X CO	X HCONH <sub>2</sub>	k CO <sub>2</sub>	k CO	k HCONH <sub>2</sub>	k <sub>CO</sub>	k <sub>a</sub>
		S (%)			X			k (L g <sup>-1</sup> s <sup>-1</sup> )			k (L g <sup>-1</sup> s <sup>-1</sup> )	
0	2.0	100.0	0.0	0.0	1.00	0.00	0.00	2.0	0.0	0.0	0	0.0
0.25	4.2	98.2	0.0	1.8	0.98	0.00	0.02	4.1	0.0	0.1	0	0.2
0.5	5.4	97.4	0.0	2.6	0.97	0.00	0.03	5.3	0.0	0.1	0	0.3
1	6.7	96.5	0.0	3.5	0.97	0.00	0.03	6.5	0.0	0.2	0	0.4
2	8.4	96.1	0.0	3.9	0.96	0.00	0.04	8.1	0.0	0.3	0	0.4
3	9.9	95.8	0.0	4.2	0.96	0.00	0.04	9.5	0.0	0.4	0	0.5
5	11.7	95.4	0.0	4.6	0.95	0.00	0.05	11.2	0.0	0.5	0	0.6
9	14.2	95.3	0.0	4.7	0.95	0.00	0.05	13.6	0.0	0.7	0	0.8
12	15.7	95.2	0.0	4.8	0.95	0.00	0.05	15.0	0.0	0.7	0	0.8

\*Reaction temperature = 160 °C, W/F = 1.62\*10<sup>-4</sup> g.s.cm<sup>-3</sup>; 750 L.h<sup>-1</sup> flow, feed gas contained 10% oxygen, 5% water, 85% nitrogen to simulate exhaust gas composition, 0 to 7800 ppm NH<sub>3</sub> were dosed and 0.05 mL.min<sup>-1</sup> liquid spray of 30 wt% formic acid. k<sub>mass</sub> denotes the total mass-based pseudo-first-order rate constants for Au/TiO<sub>2</sub>, S<sub>i</sub>, X<sub>i</sub> and k<sub>i</sub> represent the selectivity, fractional formic acid conversion and mass-based pseudo first order rate constants relevant in the formation of the respective products. k<sub>a</sub> in the case of bare titania is used to designate the rate constant corresponding to the formation of methanamide and hydrogen cyanide.

#### 4.4 Conclusion

A systematic study investigating the influence of ammonia on formic acid decomposition over Au/TiO<sub>2</sub> under highly oxidizing conditions relevant to SCR has been carried out. Ammonium formate completely decomposes in the gas phase yielding 100% ammonia and ~99% formic acid, it exhibits starkly contrasting catalytic behavior compared to formic acid in the absence of ammonia. The profound influence of ammonia on formic acid conversion and products selectivities over Au/TiO<sub>2</sub> was mainly dictated by the reaction temperature, with lower temperatures showing significantly enhanced conversion and carbon dioxide yield, while, the carbon monoxide yield was adversely affected. Experiments investigating the activity of bare titania revealed that carbon monoxide was the selectively formed product from AmFo and formic acid decomposition. Moreover, ammonia suppressed carbon monoxide formation owing to competitive reaction with formic acid to form amidation products.

The promotional effect of ammonia on formic acid decomposition to carbon dioxide while suppressing carbon monoxide formation over Au/TiO<sub>2</sub> opens up new opportunities to develop efficient novel hydrolysis catalysts for decomposition of alternative ammonia precursors. Rapid enhancement of formic acid decomposition rate and carbon dioxide production was more predominant at lower temperature (160 °C) and higher contact times ( $W/F = 1.62 \times 10^{-4} \text{ g s cm}^{-3}$ ), since under these conditions, side product (methanamide) formation was curtailed to a minimum; thus, pointing to the pivotal role played by the optimal reaction conditions in achieving clean and complete decomposition.



# Chapter 5

## Promotion of ammonium formate and formic acid decomposition on Au/TiO<sub>2</sub> by support basicity

Based on: Sridhar, M.; Ferri, D.; Elsener, M.; van Bokhoven, J. A.; Kröcher, O. *ACS Catal.* **2015**, *5*, 4772–4782.

M.S. contributions: experiments, analysis and write-up.

## 5.1 Introduction

In Chapter 3, Au/TiO<sub>2</sub> was demonstrated to be a highly active and uniquely selective catalyst for AmFo decomposition. Chapter 4 showed that the activity of the catalyst is enhanced in the presence of excess ammonia. In this chapter, we investigate if such a promotional effect of a gas-phase reactant can be converted into a catalytic effect by support-modification with basic additives.

Base-promotion by alkali and alkaline-earth metals is frequently encountered in heterogeneous catalysis, particularly in water gas shift (WGS), methanol reforming reactions and catalysis by zeolites.<sup>[75,170,171]</sup> Panagiotopoulou et al. observed that the presence of sodium and cesium strengthened carbon monoxide adsorption on Pt/TiO<sub>2</sub> while facilitating hydrogen desorption making them promising candidates for application in WGS.<sup>[172]</sup> Ribeiro et al. observed an enhancement in the TOF for the low temperature WGS by a factor of ca. 100 and 4 upon addition of sodium to Pt/Al<sub>2</sub>O<sub>3</sub> and Pt/P25-TiO<sub>2</sub>, respectively.<sup>[57]</sup> Recently, Ross et al. observed improved vapor-phase formic acid decomposition rate over Pd/C doped by K.<sup>[173]</sup> In the context of catalysis over supported gold catalysts, Zhu et al. reported a steady increase in the activity of Au/C for selective alcohol oxidation with molecular oxygen in non-aqueous media upon addition of NaOH up to 1 molar equivalent. The higher activities in the presence of base was attributed to the formation of Au-OH<sup>-</sup>, which was speculated to participate in the hydrogen-abstraction from alcohol.<sup>[174]</sup> Lanthanum is a known structural and thermal stabilizer that improves sintering resistance and particle dispersion and an intrinsic activity-promoter due to its basic nature. In an earlier work, Jiang et al. showed that lanthana addition to CuO/γ-Al<sub>2</sub>O<sub>3</sub> resulted in superior activity for carbon monoxide and methane oxidation.<sup>[175]</sup> Borer and Prins also reported on lanthana-promoted Rh/SiO<sub>2</sub> catalyst for selective carbon monoxide hydrogenation to methanol.<sup>[176]</sup> In both the works, lanthana addition influenced the surface interaction with the adsorbates leading to improved oxygen-sorption kinetics and increased hydrogen availability at the catalyst interface.

This chapter shows that the previously observed promotional effect of the gas-phase basic-reactant (ammonia)<sup>[25]</sup> on formic acid decomposition over Au/TiO<sub>2</sub> can be transformed into a catalytic effect by the introduction of lanthanum to provide intrinsic basicity to the metal oxide support. Furthermore, the corollary, i.e. the inhibitory effect of acidity was achieved by tungsten-modification of the catalyst. Preliminary insights on the relation between formic acid coverages and the catalytic activity are offered.

## 5.2 Experimental

*Catalyst preparation, testing and characterization.* Au/TiO<sub>2</sub> was prepared by a modified incipient wetness impregnation technique as described in Chapter 2. The acid- and base-modified gold catalysts were prepared by the same procedure using commercial supports DT57 and DT52 (Cristal Global) both of which constituted 90 wt% anatase titania and 10 wt % each of lanthana and tungsten oxide, respectively. ICP-OES analysis indicated gold loadings between 0.47 % to 0.53 % for the acid-, base- and unmodified catalysts. The base- and acid-modified gold catalysts obtained after calcination will be henceforth designated as Au/La-TiO<sub>2</sub> and Au/W-TiO<sub>2</sub>. Au/La-TiO<sub>2</sub> was also aged at 600°C in air for 5 h in a static oven and will be hereupon referred to as Au/La-TiO<sub>2</sub>-aged. Each of the catalysts contained a nominal gold loading of 0.5 wt% unless otherwise stated. The catalysts were tested following the procedure reported in Chapter 2. The catalysts were analyzed by nitrogen physisorption, XRD and STEM. The details of the analysis are presented in Chapter 2. The *in situ* diffuse reflectance infrared Fourier transform spectroscopic (DRIFTS) analysis of carbon dioxide and formic acid adsorption was conducted using the procedures described in Chapter 2.

## 5.3 Results and Discussion

### 5.3.1 Catalyst characterization

The XRD patterns of Au/TiO<sub>2</sub>, Au/La-TiO<sub>2</sub>, Au/W-TiO<sub>2</sub> and Au/La-TiO<sub>2</sub>-aged catalysts revealed no reflections corresponding to gold, lanthanum, tungsten and any other mixed oxide suggesting that the gold and the additives may be present in a well-dispersed form (Figure 5.1). Modification by lanthanum and tungsten did not cause shifts of titania reflections indicating that, if present, introduction of these elements into the titania lattice is rather small. Owing to the large difference in the sizes of La<sup>3+</sup> (0.115 nm) and Ti<sup>4+</sup> (0.068 nm), there is very little probability of La<sup>3+</sup> entering into the lattice structure of titania, however insertion into the interstitial space can be expected.<sup>[177]</sup> On the other hand, in the case of gold and tungsten, in addition to the formation of surface-bound species, partial incorporation into the lattice induced by high-temperature calcination may not be ruled out.<sup>[178,179]</sup> While, the average anatase crystallite size is 25 nm in the case of Au/TiO<sub>2</sub>, the growth of anatase crystallites is restrained to 11.6 nm and 11.5 nm for Au/La-TiO<sub>2</sub> and Au/W-TiO<sub>2</sub>, respectively. Such an inhibition of the crystal growth of titania upon lanthanum- or tungsten-modification occurs because they occupy the defect sites which are involved in the particle growth and phase transformation.<sup>[177,180]</sup> The coverage of lanthana on the titania surface is proposed to increase the activation energy for nucleation and to reduce the number of nucleation sites.<sup>[181]</sup> The thermal treatment did not structurally modify the support apart from a modest growth in anatase crystallite size from 11.6 nm to 14 nm. The BET surface areas of Au/La-TiO<sub>2</sub> and Au/W-TiO<sub>2</sub> are 105 m<sup>2</sup> g<sup>-1</sup> and 90 m<sup>2</sup> g<sup>-1</sup>, respectively, while those for Au/TiO<sub>2</sub> and Au/La-TiO<sub>2</sub>-aged were 78 m<sup>2</sup> g<sup>-1</sup> and 81 m<sup>2</sup> g<sup>-1</sup>, respectively.

An *in situ* DRIFT study of carbon dioxide adsorption was performed to investigate the surface properties of the acid-, base-(fresh and aged) and un-modified catalysts. Figure 5.2 (left) compares the *in situ* DRIFT spectra obtained after 17 min of contact between the samples and 1000 ppm of carbon dioxide in nitrogen flow at 200 °C. Carbon dioxide adsorption on the un-modified and base-modified catalysts resulted in the formation of broad bands between 1600  $\text{cm}^{-1}$  and 1290  $\text{cm}^{-1}$  corresponding to unidentate and bidentate carbonate species,<sup>[182–184]</sup> while the acid-modified catalyst showed negligible adsorption. Bands centered around 1534  $\text{cm}^{-1}$  and 1421  $\text{cm}^{-1}$  can be assigned to the  $\nu_{\text{AS}}(\text{OCO})$  and  $\nu_{\text{S}}(\text{OCO})$  stretching modes of bidentate bicarbonate species.<sup>[185]</sup>

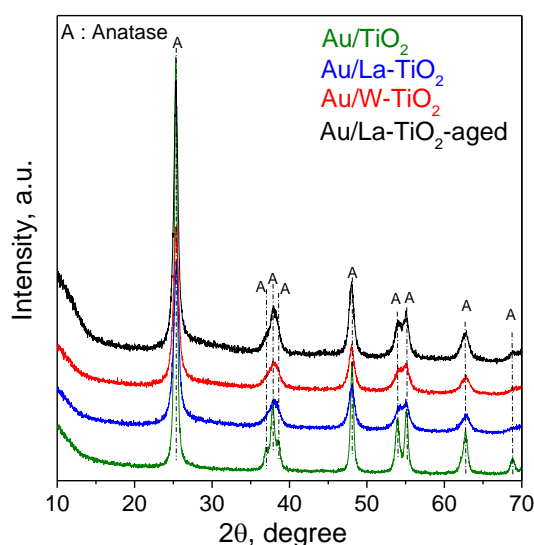


**Figure 5.1** XRD patterns of Au/TiO<sub>2</sub>, Au/La-TiO<sub>2</sub>, Au/W-TiO<sub>2</sub> and Au/La-TiO<sub>2</sub>-aged catalysts.

The lower frequency signals centered around 1570  $\text{cm}^{-1}$  and 1350  $\text{cm}^{-1}$  can arise from monodentate carbonate species. The high intensity of carbonate signals on the base-modified samples confirmed higher carbon dioxide uptake and thus an increased basicity relative to the other samples. An enhancement in the intensity of bands associated with different carbonate species was observed on the gold-loaded samples compared to their bare-support counterparts. The DRIFT spectra of adsorbed carbon dioxide on Au/La-TiO<sub>2</sub>-aged remained practically the same as Au/La-TiO<sub>2</sub>, indicating that the thermal treatment does not modify the surface basicity of the lanthanum-modified catalyst. The acid-modified samples showed very weak bands indicating low affinity towards carbon dioxide.

Complementary to the carbon dioxide adsorption studies, the extent of interaction between formic acid and the gold catalysts was also explored. The *in situ* DRIFT spectra obtained after 15 min of contact between the catalysts and 1120 ppm of formic acid in nitrogen flow at 200 °C are presented in Figure 5.2 (right). The spectra of the un- and base-modified catalysts are characterized by intense signals in the region 1700-1300  $\text{cm}^{-1}$  that are associated with the

$\nu_{AS}(\text{OCO})$  and  $\nu_S(\text{OCO})$  stretching modes of carboxyl groups of adsorbed formates.<sup>[186]</sup> Various shoulders on both signals indicate multiple adsorption geometries, namely mono-, bi-dentate and bridged configurations. The bands at 1690 and 1315 cm<sup>-1</sup> may originate from monodentate formate species.<sup>[187]</sup> The high frequency region (not shown) is also populated by characteristic signals of formate species at 2954, 2867 and 2731 cm<sup>-1</sup> corresponding to the combination band  $\nu_{AS}(\text{OCO})+\nu(\text{CH})$ ,  $\nu(\text{C-H})$  and the  $2\nu(\text{CH})$  overtone, respectively.

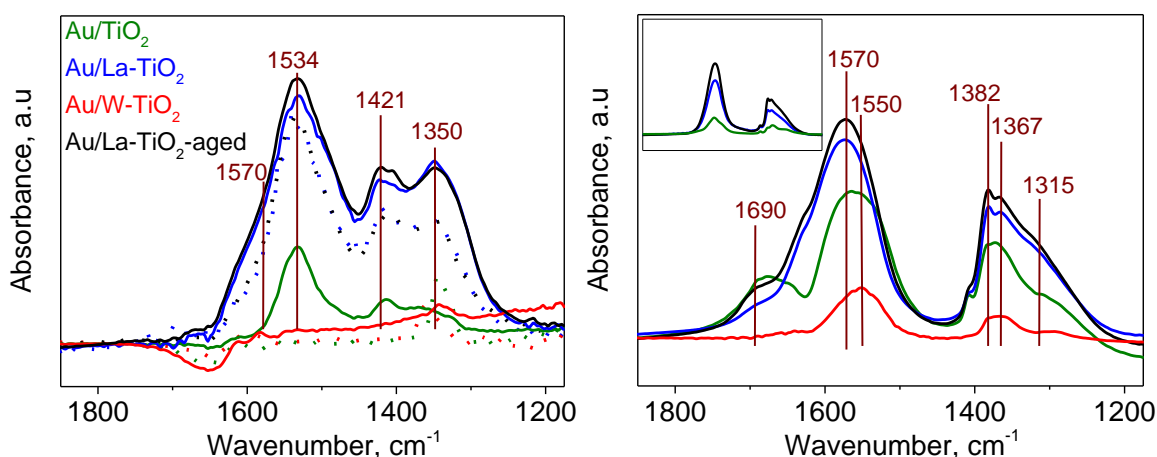


**Figure 5.2** In situ DRIFT spectra of 1000 ppm carbon dioxide adsorbed on Au/TiO<sub>2</sub>, Au/La-TiO<sub>2</sub>, Au/W-TiO<sub>2</sub> and Au/La-TiO<sub>2</sub>-aged and their corresponding supports (dotted spectra) at 200°C (left) and 1120 ppm formic acid adsorbed on Au/TiO<sub>2</sub>, Au/La-TiO<sub>2</sub>, Au/W-TiO<sub>2</sub> and Au/La-TiO<sub>2</sub>-aged at 200°C (right). Inset: In situ DRIFT spectra in the presence of 10% oxygen and 5% water in the same energy range (proportional XY scales).

It is evident that the overall intensity of signals on the base-modified catalysts is larger than that obtained on Au/TiO<sub>2</sub>, reflecting higher surface coverage of formate species. In line with the carbon dioxide adsorption results, there was no significant change in the overall density and position of the adsorbed formate species in the spectra after the thermal treatment of Au/La-TiO<sub>2</sub>, suggesting closely similar formic acid coverages on both the fresh and the aged base-modified catalysts. The acid-modified catalyst showed the weakest signals associated with formic acid adsorption. In order to observe the surface species under reaction conditions, formic acid adsorption was performed in the presence of 10 vol% oxygen and 5 vol% water and balance nitrogen, simulating the catalytic tests (Figure 5.2 right-inset, proportional XY scales). Clearly, the base-modified catalysts (both fresh and aged) exhibited the highest coverage of formate under reaction conditions. It is generally accepted that formate is the stable intermediate resulting from the first step in the formic acid decomposition mechanism on most oxide surfaces.<sup>[188]</sup> Osawa and co-workers employed surface-enhanced infrared adsorption spectroscopy (SEIRAS) and determined that formates adsorbed via two oxygen atoms are the reactive intermediates during formic acid oxidation over Pt electrode.<sup>[189]</sup> Similarly, for the investigated reaction, it is reasonable that a formate-based reactive intermediate participates in the decomposition mechanism.

The HAADF-STEM images of the three catalysts are presented in Figure 5.3. Lanthanum-modification of the support led to the formation of smaller gold particles in the size range of 2-4 nm, while the un- and acid-modified catalysts possessed similar gold particle sizes in the range of 5-7 nm. The structural effect causing stabilization of smaller gold particles on the support upon modification with rare-earth metal oxides was reported by Ma and co-workers.<sup>[190]</sup> Yu et al. also reported the formation of smaller gold particles on lanthanum-modified titania due to the possible presence of a large number of defects, such as oxygen vacancies, together with steps and adatoms on which gold immobilization could easily take place.<sup>[191]</sup> Thermal aging of Au/La-TiO<sub>2</sub> resulted in the growth of gold particles in the size range of those of Au/TiO<sub>2</sub>.

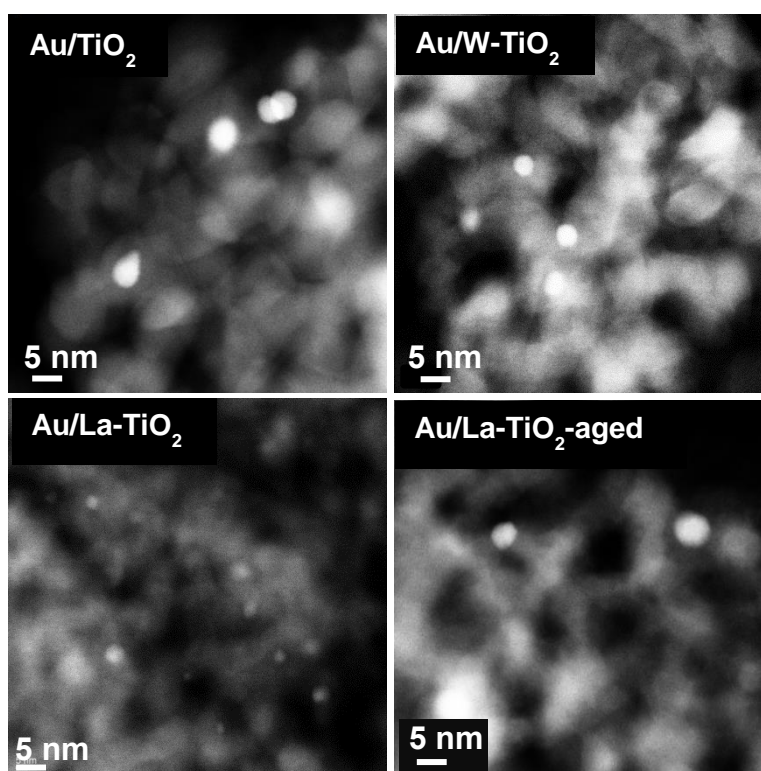


**Figure 5.3** HAADF-STEM images of Au/TiO<sub>2</sub>, Au/W-TiO<sub>2</sub>, Au/La-TiO<sub>2</sub> and Au/La-TiO<sub>2</sub>-aged catalysts.

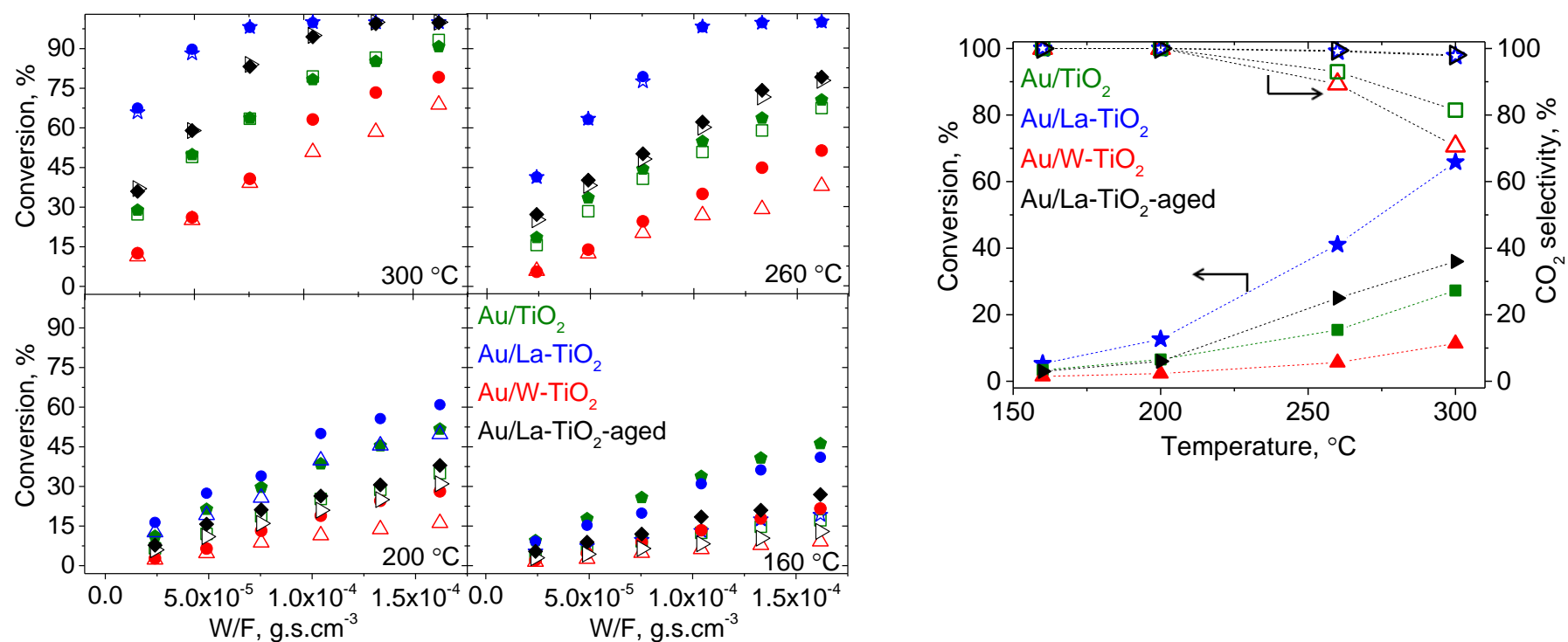
### 5.3.2 Activity for ammonium formate and formic acid decomposition

Au/TiO<sub>2</sub>, Au/La-TiO<sub>2</sub>, Au/W-TiO<sub>2</sub> and Au/La-TiO<sub>2</sub>-aged were tested for ammonium formate (AmFo) and formic acid decomposition in a simulated exhaust gas containing 10 vol% oxygen and 5 vol% water at different temperatures in the range 160 °C to 300 °C using various contact times ( $2.4 \cdot 10^{-5} \text{ g s.cm}^{-3} \leq W/F \leq 1.6 \cdot 10^{-4} \text{ g s.cm}^{-3}$ ) (Figure 5.4 left). These catalysts at identical gold loadings differ either by support modification at equal gold particle size (Au/TiO<sub>2</sub> versus Au/W-TiO<sub>2</sub> versus Au/La-TiO<sub>2</sub>-aged) or by gold particle size on the same support (Au/La-TiO<sub>2</sub> versus Au/La-TiO<sub>2</sub>-aged). In agreement with the previous studies,<sup>[25]</sup> the values for formic acid

conversion obtained at 300 °C over all the catalysts were identical for formic acid and AmFo. Ammonia was never oxidized.

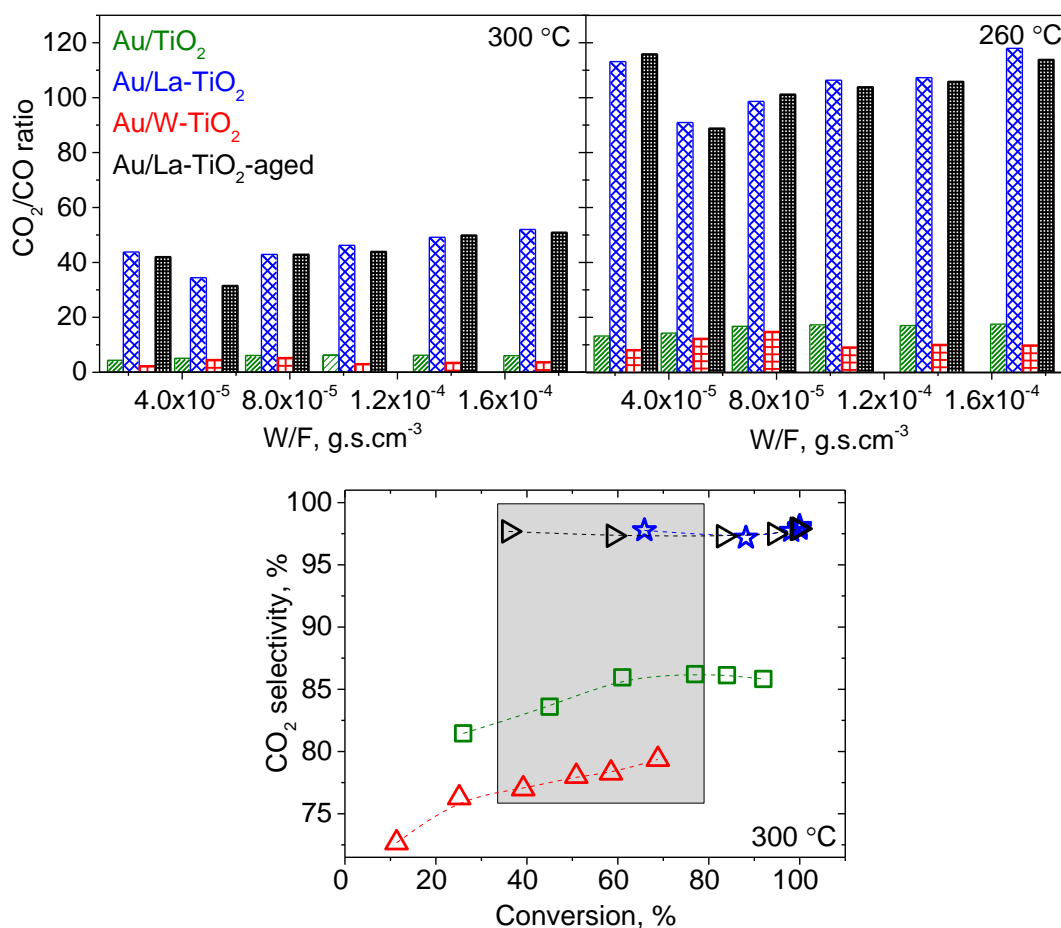
Clearly, at temperatures  $\geq 260$  °C, the lanthanum-modified catalysts, both fresh and aged, exhibited higher formic acid conversion, while Au/W-TiO<sub>2</sub> showed the lowest performance. Additionally, at these temperatures, the formic acid conversion obtained over the lanthanum-modified catalysts using formic acid as the precursor surpassed the corresponding values obtained over Au/TiO<sub>2</sub> using AmFo as the precursor. This observation implies that the promotional effect initiated by base modification surpasses the rate enhancement originating from the presence of a stoichiometric amount of ammonia in the feed gas.<sup>[25]</sup> At 300 °C, when formic acid was used as the precursor, Au/La-TiO<sub>2</sub> and Au/La-TiO<sub>2</sub>-aged exhibited close to 100% conversion at  $W/F = 7.5 \cdot 10^{-5}$  g s.cm<sup>-3</sup> and  $1 \cdot 10^{-4}$  g s.cm<sup>-3</sup>, respectively. In contrast, even at the highest contact time ( $W/F = 1.6 \cdot 10^{-4}$  g s.cm<sup>-3</sup>), Au/TiO<sub>2</sub> and Au/W-TiO<sub>2</sub> did not completely decompose formic acid, resulting in 92% and 69% conversion, respectively. Using the lowest contact time ( $W/F = 2.4 \cdot 10^{-5}$  g s.cm<sup>-3</sup>), the formic acid conversion obtained over the un-modified catalyst was <50% of that of Au/La-TiO<sub>2</sub> and more than twice that of Au/W-TiO<sub>2</sub>. Under these conditions, the Au/La-TiO<sub>2</sub>-aged still retained close to 60% of its original activity, thus, out-performing the fresh un-modified catalyst. At 260 °C and  $W/F \geq 1 \cdot 10^{-4}$  g s.cm<sup>-3</sup>, the formic acid conversion obtained over Au/La-TiO<sub>2</sub> using AmFo and formic acid as precursors reached close to 100% and any further increase in the contact time only led to increased carbon dioxide selectivity. Au/La-TiO<sub>2</sub>-aged suffered a decrease in conversion owing to the thermal treatment, reaching ~80% conversion at the highest contact time, still exceeding the performance of Au/TiO<sub>2</sub> by more than 15%. At 200 °C, when AmFo was used as the precursor, the formic acid conversion ranged from 70% over Au/La-TiO<sub>2</sub> to 50% and 28% over Au/TiO<sub>2</sub> and Au/W-TiO<sub>2</sub>, respectively.

At lower temperatures ( $\leq 200$  °C), the difference in the activities of the un-modified and the base-modified catalysts decreased when formic acid was used as the precursor and even turned in favor of the un-modified catalyst, when AmFo was used as the precursor. This has two implications: (i) base modification does not improve the formic acid decomposition activity at lower temperatures, and (ii) the promotional effects derived from the gas-phase and the base modification of the catalyst operate in complementary temperature regimes, wherein, at lower temperatures ( $\leq 200$  °C), the ammonia-induced rate enhancement<sup>[25]</sup> dominates. While, the interaction of ammonia is more favored at lower temperatures,<sup>[25]</sup> the catalytic effect prevails predominantly at higher temperatures, which reconciles with the higher  $E_a$  values stemming from the highly negative formic acid orders observed over the base-modified catalysts (See section 3.3). Under all the tested conditions, the acid-modified catalyst was the worst performing catalyst.



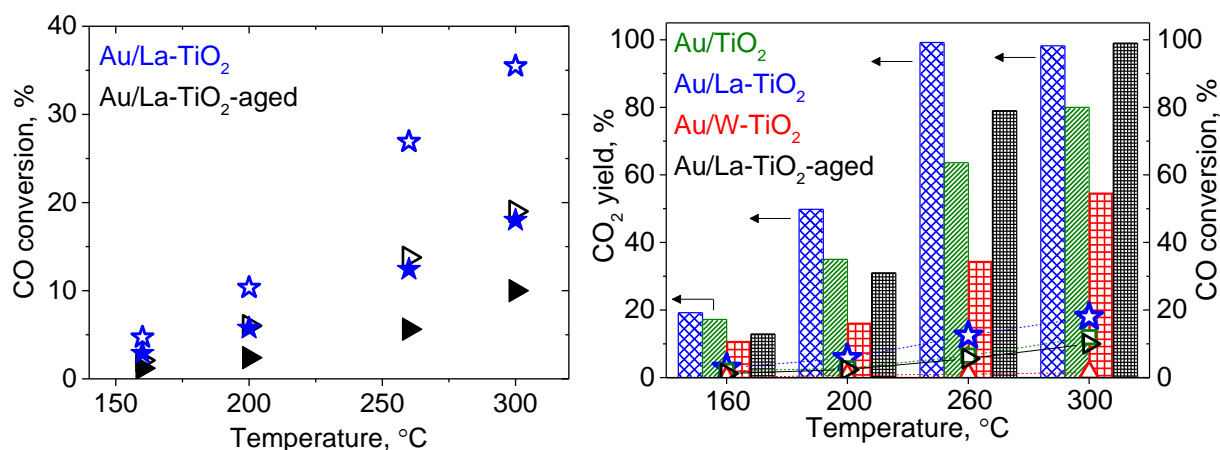
**Figure 5.4** Formic acid conversion as a function of contact time, expressed as  $W/F$  ( $\text{g s cm}^{-3}$ ), obtained using AmFo (closed symbols) and formic acid (open symbols) at different temperatures (left) and temperature dependence of formic acid conversion (closed symbols) and carbon dioxide selectivity (open symbols) at  $W/F = 2.4 \cdot 10^{-5} \text{ g s cm}^{-3}$  (right) over Au/TiO<sub>2</sub>, Au/W-TiO<sub>2</sub>, Au/La-TiO<sub>2</sub> and Au/La-TiO<sub>2</sub>-aged catalysts.

Figure 5.4 (right) depicts the temperature dependence of formic acid conversion and carbon dioxide selectivity over Au/TiO<sub>2</sub>, Au/La-TiO<sub>2</sub>, Au/W-TiO<sub>2</sub> and Au/La-TiO<sub>2</sub>-aged at W/F = 2.4\*10<sup>-5</sup> g s.cm<sup>-3</sup>. A progressive drop in carbon dioxide selectivity was evidenced over all the catalysts above 200 °C, with carbon monoxide being the only other (undesired) product of formic acid decomposition. Evidently, the low activity of the acid-modified catalyst is accompanied by the lowest carbon dioxide selectivity compared to the un- or base-modified catalysts. The thermal aging at 600 °C did not diminish the carbon dioxide selectivity, which remained >98% over the entire temperature window. At 300 °C, Au/TiO<sub>2</sub> exhibited 81% carbon dioxide selectivity, while Au/W-TiO<sub>2</sub> only 70%. At temperatures ≤ 200 °C, there was no carbon monoxide production over any of the catalysts. Figure 5.5 (top) compares the effect of support modification on the carbon dioxide/carbon monoxide ratio at 300 °C and 260 °C at different contact times. The carbon dioxide/carbon monoxide ratios observed with lanthanum-modification remained practically unaffected with aging.



**Figure 5.5** Evolution of CO<sub>2</sub>/CO ratio as a function of contact time obtained from formic acid decomposition over Au/TiO<sub>2</sub>, Au/W-TiO<sub>2</sub>, Au/La-TiO<sub>2</sub> and Au/La-TiO<sub>2</sub>-aged catalysts at 300 °C and 260 °C ( top) and formic acid conversion *versus* carbon dioxide selectivity obtained over Au/TiO<sub>2</sub>, Au/W-TiO<sub>2</sub>, Au/La-TiO<sub>2</sub> and Au/La-TiO<sub>2</sub>-aged catalysts at 300 °C (bottom).

There was a striking enrichment of carbon dioxide in the product gas, while the carbon monoxide formation remained suppressed over the base-modified catalysts. At the two temperatures and  $W/F = 2.4 \times 10^{-5} \text{ g s.cm}^{-3}$ , the carbon dioxide/carbon monoxide ratio experienced a  $\sim 10$ -fold increase upon base-modification, while acid-modification decreased the ratio by 50%. Hence, base-modification of the catalyst selectively promotes formic acid decomposition to carbon dioxide, reminiscent of the effect of ammonia.<sup>[25]</sup> Figure 5.5 (bottom) compares the carbon dioxide selectivity *versus* formic acid conversion obtained using formic acid at 300 °C over Au/TiO<sub>2</sub>, Au/La-TiO<sub>2</sub>, Au/W-TiO<sub>2</sub> and Au/La-TiO<sub>2</sub>-aged. The base- and the acid-modified catalysts exhibited the highest and the lowest carbon dioxide selectivity, respectively, over the whole conversion range. At all contact times, the carbon dioxide selectivity was  $>98\%$  for the base-modified catalysts, while it dropped to 80% and 70% over Au/TiO<sub>2</sub> and Au/W-TiO<sub>2</sub>, respectively, at  $W/F = 2.4 \times 10^{-5} \text{ g s cm}^{-3}$ . The shaded region shows that at similar conversion levels over the four catalysts, a marked difference exists in the carbon dioxide selectivity. This strongly suggests that base-modification increases the intrinsic propensity to produce carbon dioxide from formic acid decomposition.



**Figure 5.6** Oxidation of 650 ppm carbon monoxide (gas-phase) over Au/La-TiO<sub>2</sub> and Au/La-TiO<sub>2</sub>-aged in the presence (closed symbols) and absence of water (open symbols) (left) and comparison of carbon dioxide produced from formic acid decomposition (bars) and gas-phase carbon monoxide oxidation (scatters) as a function of temperature over Au/TiO<sub>2</sub>, Au/W-TiO<sub>2</sub>, Au/La-TiO<sub>2</sub> and Au/La-TiO<sub>2</sub>-aged catalysts using 650 ppm formic acid and 650 ppm carbon monoxide at  $W/F = 1.6 \times 10^{-4} \text{ g s cm}^{-3}$  (right).

Instead of direct formic acid oxidation to carbon dioxide, formic acid could alternatively first decompose to carbon monoxide as an intermediate, which subsequently oxidizes to carbon dioxide.<sup>[192,193]</sup> Gas-phase carbon monoxide oxidation experiments were performed to assess the contribution of this reaction pathway towards increased carbon dioxide production from formic acid decomposition over the base-modified catalysts. Figure 5.6 (left) plots carbon monoxide conversion as a function of temperature over the fresh and aged base-modified catalysts in the presence and absence of water at  $W/F = 1.6 \times 10^{-4} \text{ g s cm}^{-3}$ . The presence of

water adversely affected carbon monoxide conversion. Under realistic conditions involving 10 vol% water, the carbon monoxide conversion over both the fresh and aged base-modified catalysts was 50% of those when no water was present. Haruta et al. reported that the influence of water shifts from being positive to detrimental with increasing concentration.<sup>[194]</sup> They found that above 200 ppm, water suppressed the carbon monoxide oxidation activity of Au/TiO<sub>2</sub>. There was a conspicuous decline in carbon monoxide conversion with aging, which is expected to result from the sintering of gold during the high temperature treatment.<sup>[195,196]</sup>

Figure 5.6 (right) hypothetically compares the carbon dioxide production from decomposition of formic acid with the oxidation of isoconcentrations of carbon monoxide (650 ppm each) over the four catalysts under identical feed conditions ( $W/F = 1.6 \times 10^{-4} \text{ g s.cm}^{-3}$ ). At 300 °C, close to 100% carbon dioxide yield was obtained from formic acid decomposition over both the fresh and aged base-modified catalysts, while the carbon monoxide conversion under identical conditions was only 18% and 10%, respectively. The un-modified catalyst exhibited 80% carbon dioxide yield from formic acid, while converting 11% carbon monoxide. The acid-modified catalyst produced 54% carbon dioxide from formic acid decomposition and showed close to negligible conversion for carbon monoxide oxidation. At 160 °C, there was no carbon monoxide conversion over any of the catalysts. At the same temperature, Au/TiO<sub>2</sub>, Au/La-TiO<sub>2</sub> and Au/La-TiO<sub>2</sub>-aged produced 17%, 19% and 13% carbon dioxide, respectively, while Au/W-TiO<sub>2</sub> yielded 10% carbon dioxide. Since, the carbon monoxide conversion is significantly lower or negligible compared to the total carbon dioxide produced from formic acid decomposition over all the catalysts under the investigated conditions, there must exist an independent pathway for carbon dioxide formation directly from formic acid that precludes carbon monoxide formation and its subsequent oxidation. Therefore, it can be ascertained that base modification selectively promotes this direct formic acid conversion pathway responsible for carbon dioxide formation.

Figure 5.7 illustrates the relative percentage increase in the pseudo first order mass-based rate constants for formic acid decomposition upon introduction of a stoichiometric amount of ammonia as a function of temperature over Au/TiO<sub>2</sub>, Au/La-TiO<sub>2</sub>, Au/W-TiO<sub>2</sub> and Au/La-TiO<sub>2</sub>-aged. Au/TiO<sub>2</sub> exhibited the most pronounced effect of ammonia, followed by the base- and acid-modified catalysts. Aging did not alter the effect of ammonia. At 160 °C, in the presence of one molar equivalent of ammonia, the formic acid decomposition rate underwent close to 190% increase over the un-modified catalyst, while the base- and acid-modified catalysts showed ~80% and 45% increase, respectively. At 200 °C, the extent of enhancement reduced to 74%, ~23% and 21% over the un-, base-, and acid-modified catalysts, respectively. At 300 °C, the effect of ammonia on formic acid decomposition was negligible over the three catalysts. Dumesic and co-workers found that modification of alumina by lanthanum caused a decrease in the initial heat of ammonia adsorption by reducing the number of acid sites and simultaneously

increasing the number of basic sites whose strength increased with increasing loading of lanthana.<sup>[197]</sup> The lower extent of ammonia-induced-increase in rates over the base-modified catalysts can be rationally attributed to a lower level of interaction between ammonia and the basic surface of the catalysts. Even though the trend associated with the acid-modified catalyst appears counter-intuitive at first sight, it can be easily explained by taking into account the acidity of Au/W-TiO<sub>2</sub>, that is likely to result in very high ammonia coverages.<sup>[198]</sup> This in turn can be speculated to be detrimental causing unfavorable competition with formic acid, leading to the lowest degree of enhancement compared to un- and base-modified catalysts.

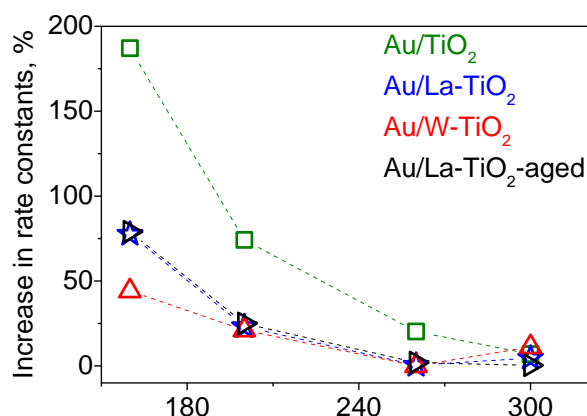


**Figure 5.7** Effect of 1 molar equivalent of ammonia on formic acid decomposition rate constants over Au/TiO<sub>2</sub>, Au/W-TiO<sub>2</sub>, Au/La-TiO<sub>2</sub> and Au/La-TiO<sub>2</sub>-aged at W/F = 2.4 \* 10<sup>-5</sup> g s cm<sup>-3</sup>.

### 5.3.3 Formic acid reaction orders and activation energy

To analyze the interaction between formic acid and the catalyst surface, experiments determining the apparent reaction orders were conducted using a wide range of formic acid concentrations (50-2500 ppm). Table 5.1 lists the reaction orders for formic acid at 300 °C and 200 °C on Au/TiO<sub>2</sub>, Au/La-TiO<sub>2</sub>, Au/W-TiO<sub>2</sub> and Au/La-TiO<sub>2</sub>-aged. On all the catalysts, negative orders for formic acid suggesting surface poisoning, were observed. Moreover, the formic acid orders tended to be more negative at low temperature than at high temperature, which arises from an increased surface coverage of formic acid-derived surface species at low temperature, while a lower coverage may be favored at high temperature. Aging did not affect the reaction order for formic acid. The base-modified catalysts exhibited more negative orders for formic acid at both low and high temperatures than the un- and acid-modified catalysts. Cui et al. found that lanthanum-modification of Ni/ $\alpha$ -Al<sub>2</sub>O<sub>3</sub> lowered the reaction order for carbon dioxide from ~-0.6 to 0 for carbon dioxide reforming of methane.<sup>[199]</sup> The ease of formation of La<sub>2</sub>O<sub>2</sub>CO<sub>3</sub> contributed to the decrease of the carbon dioxide order. Similarly, Leveles et al. observed negative orders as low as -0.5 for carbon dioxide for oxidative dehydrogenation of propane owing to the high basicity of lithium-promoted magnesia catalysts.<sup>[200]</sup> In the investigated system, as demonstrated by *in situ* DRIFTS results, there exists a higher affinity of formic acid for the highly basic catalyst

surface, which correlates with the most negative reaction orders for formic acid in the case of the lanthanum-modified catalysts. At 200 °C, the base-modified catalysts exhibited formic acid orders as low as -1.0 which signifies extensive blockage of the catalytic sites. Hence, the strong binding and arrested desorption of formic acid-derived surface species can explain the relatively lower performance of the base-modified catalysts at temperatures  $\leq 200$  °C.

Figure 5.8 (shaded area) compares the apparent activation energy ( $E_a$ , kJ.mol<sup>-1</sup>) and pre-exponential factor (A) for formic acid decomposition to carbon dioxide over the three catalysts using formic acid as the precursor. The unshaded area of the plot represents the Arrhenius curves determined using 650 ppm of formic acid. The un- and acid-modified catalysts exhibited similar  $E_a$  values in the range of 30-35 kJ.mol<sup>-1</sup> for formic acid decomposition, while, the base-modified catalyst showed a higher  $E_a$  of  $\sim 50$  kJ.mol<sup>-1</sup>. Concomitantly, lanthanum-modification increased A by two orders of magnitude compared to the un-modified catalyst. This sort of compensation is commonly observed when the surface concentration of the reactant species changes with temperature,<sup>[201,202]</sup> which is the case as confirmed by the more negative formic acid order at lower temperature. To assess the influence of the formic acid adsorption enthalpy on the  $E_a$  of the lanthanum-modified catalyst, a decomposition experiment was performed using lower formic acid concentration (120 ppm). The resulting  $E_a$  was  $\sim 15$  kJ.mol<sup>-1</sup> lower than the  $E_a$  obtained at higher formic acid concentration (650 ppm), while A remained unchanged (non-shaded area). Such a contribution of the enthalpy of formic acid adsorption to  $E_a$  was reported by Fein and Wachs for formic acid oxidation over metal oxides.<sup>[203]</sup> This supports the findings on the kinetic orders for formic acid, which assume smaller negative values at lower concentrations of formic acid (Table 5.1). Hence, a part of the thermal energy is utilized to desorb the strongly adsorbed formate species, resulting in an apparent activation energy higher than the intrinsic value.<sup>[201]</sup> The aged base-modified catalyst exhibited identical  $E_a$  as Au/La-TiO<sub>2</sub>, while A decreased by an order of magnitude (Table 5.1).

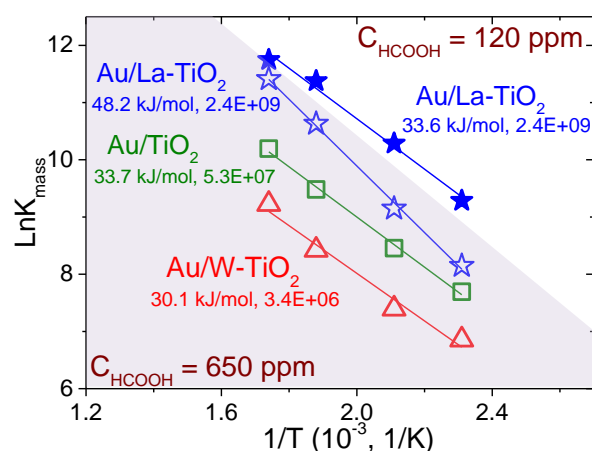


**Figure 5.8** Arrhenius plots for Au/TiO<sub>2</sub>, Au/W-TiO<sub>2</sub> and Au/La-TiO<sub>2</sub> for formic acid decomposition at  $W/F = 2.4 \times 10^{-5}$  g s cm<sup>-3</sup>.

**Table 5.1** Selectivity, fractional conversion, apparent activation energy, mass-based rate constants and formic acid orders over Au/TiO<sub>2</sub>, Au/W-TiO<sub>2</sub>, Au/La-TiO<sub>2</sub> and Au/La-TiO<sub>2</sub>-aged catalysts.

Temperature (°C)	$k_{\text{mass}}$ (L g <sup>-1</sup> s <sup>-1</sup> ) <sup>a</sup>	S CO <sub>2</sub>	S CO	X CO <sub>2</sub>	X CO	k CO <sub>2</sub>	k CO	E <sub>a</sub> (±3.0 kJ mol <sup>-1</sup> )		Formic acid order (±0.1)
		(%) <sup>b</sup>		(%) <sup>c</sup>		(L.g <sup>-1</sup> .s <sup>-1</sup> ) <sup>d</sup>		Formic acid	AmFo	
Au/TiO <sub>2</sub>										
300	26.8	81.0	19.0	0.81	0.19	21.7	5.1	33.7	14	-0.5 <sup>f</sup>
260	13.1	93.0	7.0	0.93	0.07	12.2	0.9			
200	4.7	100.0	0.0	1.00	0.00	4.7	0			
160	2.2	100.0	0.0	1.00	0.00	2.2	0			
Au/La-TiO <sub>2</sub>										
300	90.3	97.8	2.2	0.98	0.02	88.5	1.8	48.2, 34.9 <sup>e</sup>	37.6	-0.7 <sup>f</sup> , -0.4 <sup>g</sup>
260	41.4	99.1	0.9	0.99	0.01	40.9	0.4			
200	9.4	100.0	0.0	1.00	0.00	9.4	0			
160	3.4	100.0	0.0	1.00	0.00	3.4	0			
Au/W-TiO <sub>2</sub>										
300	10.1	70.7	29.3	0.71	0.29	7.1	2.9	30.1	22.5	-0.3 <sup>f</sup>
260	4.5	89.3	10.7	0.89	0.11	4.0	0.5			
200	1.6	100.0	0.0	1.00	0.00	1.6	0			
160	0.9	100.0	0.0	1.00	0.00	0.9	0			
Au/La-TiO <sub>2</sub> -aged										
300	37.5	98.2	2.1	0.98	0.02	36.7	0.8	48.9, 34.4 <sup>e</sup>	37.5	-0.6 <sup>f</sup> , -0.4 <sup>g</sup>
260	22.5	99.6	0.6	1.00	0.00	22.5	0			
200	4.3	100.0	0	1.00	0.00	4.3	0			
160	1.9	100.0	0	1.00	0.00	1.9	0			

<sup>a</sup> Total mass-based pseudo first order rate constant, <sup>b</sup> Selectivity, <sup>c</sup> Fractional formic acid conversion, <sup>d</sup> Mass-based pseudo first order rate constant, <sup>e</sup> Low concentration of formic acid (120 ppm), <sup>f</sup> Determined using formic acid concentrations in the range, 600-2200 ppm, with a step size of ~300 ppm, <sup>g</sup> Determined using formic acid concentrations in the range, 50-150 ppm, with a step size of 30 ppm, All values were determined using W/F = 2.4\*10<sup>-5</sup> g s cm<sup>-3</sup>; 750 L.h<sup>-1</sup> total flow with 10 vol.% oxygen, 5 vol.% water, 85 vol.% nitrogen to simulate exhaust gas composition, 650 ppm formic acid unless otherwise mentioned.

Table 5.1 lists the  $E_a$  for formic acid decomposition over Au/TiO<sub>2</sub>, Au/La-TiO<sub>2</sub>, Au/W-TiO<sub>2</sub> and Au/La-TiO<sub>2</sub>-aged catalysts determined in the temperature range of 160-260 °C when AmFo was used as the precursor. At 300 °C there was no effect of ammonia on formic acid decomposition (Figure 5.4 left). In the case of the un-modified catalyst, the activation energy was lowered by more than 50% in the presence of stoichiometric amounts of ammonia. The acid- and base-modified catalysts did not display such a pronounced ammonia-induced effect on the activation energies. This substantiates the occurrence of an optimum favorable interaction with ammonia over the un-modified catalyst, as demonstrated by the trend in the relative magnitudes of the ammonia-induced increase in the rate constants over the four catalysts (Figure 5.7). Table 5.1 also lists the product selectivity, fractional conversion and mass-based pseudo-first-order rate constants derived from formic acid decomposition in the temperature range of 160-300 °C.  $X_{CO_2}$  and  $X_{CO}$ , represent the fractional formic acid conversion, while  $k_{CO_2}$  and  $k_{CO}$  denote the pseudo-first-order mass based rate constants relevant for the formation of the respective products.

At 300 °C, Au/La-TiO<sub>2</sub> exhibited  $k_{CO_2}$  and  $k_{CO}$  of  $\sim 90 \text{ L.g}^{-1} \text{ s}^{-1}$  and  $\sim 2 \text{ L.g}^{-1} \text{ s}^{-1}$ , respectively, which are  $\sim 4$ -folds greater and  $\sim 2.5$  times lesser than the corresponding values obtained over Au/TiO<sub>2</sub>. On the other hand, tungsten-modification reduced  $k_{CO_2}$  by three times, while  $k_{CO}$  remained at more than 50% of the corresponding value obtained over Au/TiO<sub>2</sub>. This corresponded to fractional formic acid conversion to carbon monoxide of 19%, 2% and 29% over Au/TiO<sub>2</sub>, Au/La-TiO<sub>2</sub> and Au/W-TiO<sub>2</sub>, respectively. At 260 °C, formic acid decomposed to carbon dioxide with a selectivity of  $>99\%$  and 93% over the base-modified catalysts and Au/TiO<sub>2</sub>, respectively, while the acid-modified catalyst showed only 89% carbon dioxide selectivity. At temperatures  $\geq 260$  °C, the aged base-modified catalysts still exhibited close to two times higher  $k_{CO_2}$  compared to Au/TiO<sub>2</sub>. Concomitantly,  $k_{CO}$  varied from only  $0.8 \text{ L.g}^{-1} \text{ s}^{-1}$  at 300 °C to  $\sim 0$  at 260 °C over Au/La-TiO<sub>2</sub>-aged, which are significantly lower than the corresponding values over Au/TiO<sub>2</sub>. In agreement with the higher  $E_a$  values of the base-modified catalysts, the low temperature decomposition activity ( $k_{CO_2}$ ) of Au/La-TiO<sub>2</sub> and Au/La-TiO<sub>2</sub>-aged at 160 °C was  $3.3 \text{ L.g}^{-1} \text{ s}^{-1}$  and  $1.9 \text{ L.g}^{-1} \text{ s}^{-1}$ , respectively, which is similar to that of Au/TiO<sub>2</sub> ( $2.1 \text{ L.g}^{-1} \text{ s}^{-1}$ ). Overall, the rates on Au/La-TiO<sub>2</sub>-aged underwent close to 50% reduction upon five hours of thermal treatment at 600 °C, while the selectivity and the fractional conversion remained unchanged compared to the parent base-modified catalyst.

#### 5.3.4 Activity of the supports in the absence of gold

To delineate the influence of gold, formic acid decomposition experiments were conducted over the bare supports. Similar to the decomposition selectivity of bare titania as reported in Chapter 4,<sup>[25]</sup> carbon monoxide was the only product from formic acid decomposition over the acid- and the base-modified supports. Figure 5.9 compares the carbon monoxide yield obtained from

formic acid decomposition over  $\text{TiO}_2$ ,  $\text{La-TiO}_2$ ,  $\text{W-TiO}_2$  and  $\text{La-TiO}_2$ -aged at  $\text{W/F} = 1.6 \times 10^{-4} \text{ g s.cm}^{-3}$ . The aged base-modified support did not exhibit any significant change in the formic acid decomposition activity compared to the fresh  $\text{La-TiO}_2$ . Contrary to the activity trend in the gold catalysts, the supports displayed increasing activity with decreasing basicity suggesting that a different mechanism operates in the absence of gold.

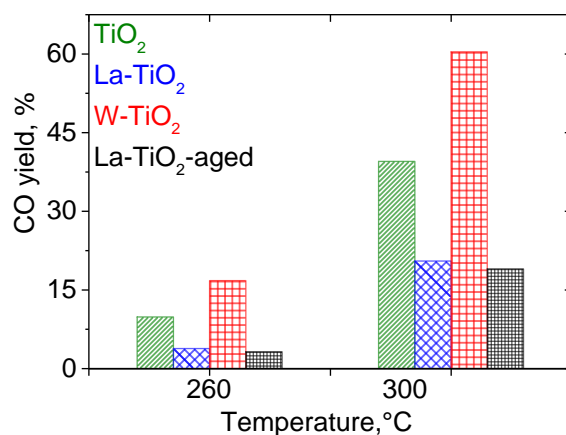


**Figure 5.9** Comparison of carbon monoxide yield from formic acid decomposition on titania, tungsten-modified titania and fresh and aged lanthanum-modified titania at  $\text{W/F} = 1.6 \times 10^{-4} \text{ g s cm}^{-3}$ .

At 300 °C,  $\text{W-TiO}_2$  and  $\text{TiO}_2$  produced 60% carbon monoxide and 40% carbon monoxide, respectively, while the base-modified catalysts yielded only ~20% carbon monoxide. At 260 °C, the base-modified supports (both fresh and aged) produced less than 25% carbon monoxide compared to  $\text{W-TiO}_2$ . Hence, the observed low carbon monoxide selectivity of  $\text{Au/La-TiO}_2$  may be associated with the inherent low formic acid decomposition activity of the support. Reports on such an ‘acid-promoted dehydration mechanism’ to form carbon monoxide from formic acid are prevalent in literature.<sup>[29,188]</sup> Ai has proposed a switch-over of formic acid decomposition pathway from oxidative dehydrogenation forming carbon dioxide to a dehydration mechanism yielding carbon monoxide with increasing acidity of the catalyst, further adding that an increased acidity correlated with increasing dehydration activity.<sup>[29]</sup> At temperatures  $\leq 200$  °C, we observed negligible carbon monoxide formation over all the supports, which correlates with negligible carbon monoxide yield observed over the gold catalysts at these temperatures. Furthermore, it is clear that even in the case of the best performing catalyst ( $\text{Au/La-TiO}_2$ ), the presence of gold is indispensable to realize high activity without which the support is virtually inactive for formic acid decomposition.

### 5.3.5 Effect of increased gold loading

Since bare supports selectively decompose formic acid to carbon monoxide, the pathway responsible for carbon dioxide production from formic acid must be associated with the presence of gold. Hence, an increase in the gold loading should be tantamount to increased

carbon dioxide formation. Figure 5.10 traces the evolution of carbon dioxide and carbon monoxide yield derived from formic acid decomposition as a function of gold loading at  $W/F = 4.9 \times 10^{-4} \text{ g s.cm}^{-3}$ . A systematic increase in the CO<sub>2</sub>/CO ratio was witnessed with increasing gold content over titania. At 300 °C, the carbon dioxide yield increased from 39% to 98% upon a four-fold increase in the gold content, while the carbon monoxide yield dropped from 8% to 2%. At 200 °C, no carbon monoxide production occurred over any of the catalysts; however, the carbon dioxide production experienced fourfold increase from 12% to 48%. These results in conjunction with the 100% carbon monoxide selectivity evidenced over bare supports imply that the active sites for carbon dioxide production must reside either on gold or at the interface between the gold particles and the support. The number of these sites increases with gold loading, which in turn manifests itself in the form of higher carbon dioxide production rates. Retrospectively, the CO<sub>2</sub>/CO ratios of the base-modified catalysts with 0.5 wt% gold loading are closely similar to those of the unmodified catalysts with 2 wt% gold, suggesting that lanthanum-modification preferentially influences the active sites associated with carbon dioxide production while those forming carbon monoxide remain disfavored.

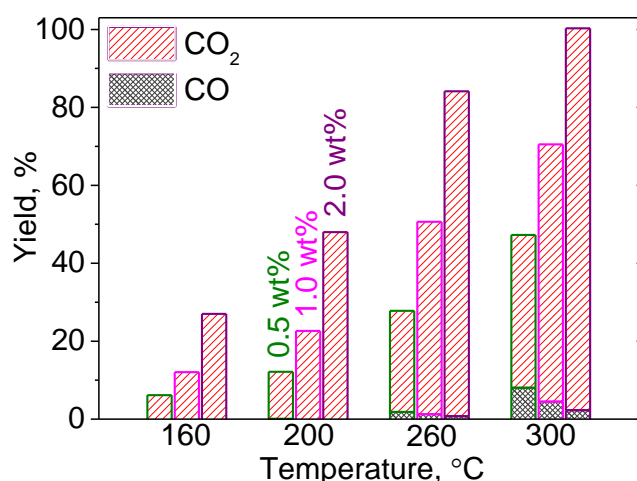
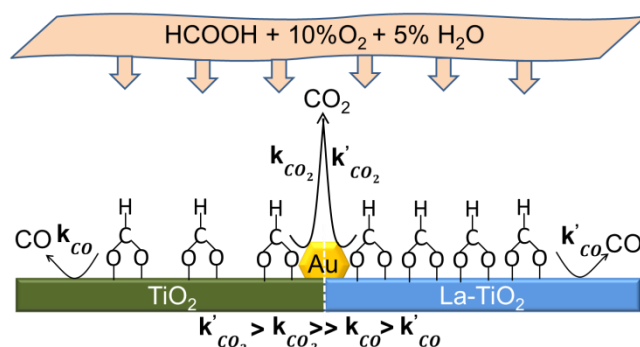


**Figure 5.10** Effect of gold loading on the product distribution during formic acid decomposition over the unmodified support as a function of temperature at  $W/F = 4.9 \times 10^{-5} \text{ g s cm}^{-3}$ .

### 5.3.6 Implications on the mechanism

Lanthanum-modification of titania resulted in two phenomena: stabilization of smaller gold particles and a substantial increase in the support basicity. Thermal-induced gold particle growth enabled the disentanglement of the two effects and comparison of the catalysts at identical gold loadings and gold particle sizes but on different supports. While the carbon monoxide oxidation activity, which is irrelevant to the decomposition mechanism, showed sensitivity to the gold particle size, the observed trend in the selectivity of formic acid decomposition towards carbon dioxide can be exclusively indexed as a consequence of basicity. The formic acid orders in

conjunction with the *in situ* DRIFTS results reveal that the catalytic activity is significantly influenced by formic acid adsorption which in turn is greatly augmented upon base-modification. High formic acid coverages is reflected in the crossing of the Arrhenius plots. This justifies the significantly higher activities of the lanthanum-modified catalysts compared to the un-modified catalysts at higher temperatures ( $\geq 260$  °C). The rate of carbon dioxide production increased proportionally with gold loading, with gold being indispensable for selective formic acid decomposition to carbon dioxide.



**Scheme 5.1** Preliminary mechanistic description of formic acid decomposition over the un-modified and lanthanum-modified catalysts.

Scheme 5.1 outlines these mechanistic insights: Formate is formed as a relevant reactive intermediate upon formic acid adsorption on both the un- and lanthanum-modified catalysts. The formate density is greatly enhanced upon lanthanum-modification which characterizes the higher rates for carbon dioxide production. The high formic acid coverages obviate the step of dissociative chemisorption of formic acid as the rate determining step (rds), meaning that the next step(s) involving the oxidative dehydrogenation of formate to carbon dioxide is likely to be the rds.<sup>[189]</sup> In the absence of gold, the formates selectively decompose to carbon monoxide over the bare supports, whose rates follow an opposite trend in relation to the support basicity.

### 5.3.7 Outlook on the use of AmFo as an alternative reducing agent

As outlined in the Introduction, applications reporting the use of AmFo as an additive to aqueous urea solution have demonstrated the existence of dual advantages in the form of freezing point depression and increased ammonia storage capacity.<sup>[204–207]</sup> Formulations containing AmFo and urea have been commercially employed, either under the name Denoxium®, or, in Canada, the USA and Mexico, under the name TerraCairPlus®, due to a license agreement between Denoxium® owner Kemira Oyj with Terra Environmental Technologies Inc.<sup>[21]</sup> Taking into account, the serious problems associated the usage of urea,<sup>[13,23]</sup> and the above stated benefits of AmFo, the latter by itself strikes as a promising candidate. AmFo thermolyzes in the hot exhaust to form ammonia and formic acid.<sup>[25]</sup> While, ammonia can be desirably consumed by the SCR reaction, there is a need to rapidly decompose the highly corrosive and reactive formic

acid. This study, which is in line with the alternative exhaust gas aftertreatment system conceived by Hammer et al. and Gerhart et al.,<sup>[18,24]</sup> envisages the independent operation of the gold-catalyst in a separate side stream reactor built in parallel to the SCR compartment. This way, complete and selective decomposition of ammonium formate to ammonia and carbon dioxide can be achieved circumventing the problems of side product formation and enabling the provision of clean stream of ammonia upstream of the SCR catalyst, thus resulting in enhanced DeNO<sub>x</sub> efficiency.

#### **5.4 Conclusion**

The activity of Au/TiO<sub>2</sub> for AmFo and formic acid decomposition could be significantly improved by translating the previously observed promotional effect (Chapter 4) of the basic gas-phase reactant (ammonia) into a catalytic effect by modification of the support with a basic additive. Such catalyst design for formic acid decomposition in the context of application in SCR is unique. Regardless of the high activity, the base-modified catalysts remained selective against ammonia oxidation which is a critical criterion for SCR-application. The lanthanum-modification of titania affected both the gold particle-size and the support-basicity. The observations in this chapter can be qualitatively explained with a mechanism where the density of formates, which are relevant reaction intermediates, is greatly increased upon base-modification. A more in-depth understanding of the base-effect is provided in Chapter 8. Carbon dioxide production increased systematically with increasing gold loading, while the bare supports exclusively produced carbon monoxide from formic acid decomposition, implying that the active site must be associated with the gold. It is speculated that the introduction of lanthanum culminates in the formation of a new type of sites that rapidly and selectively decomposes formic acid to carbon dioxide. On the other hand, acid modification with tungsten rendered the catalyst less active and less selective for carbon dioxide production.



# Chapter 6

## **Water-Assisted Oxygen Activation during Gold-Catalyzed Formic Acid Decomposition under SCR-Relevant Conditions**

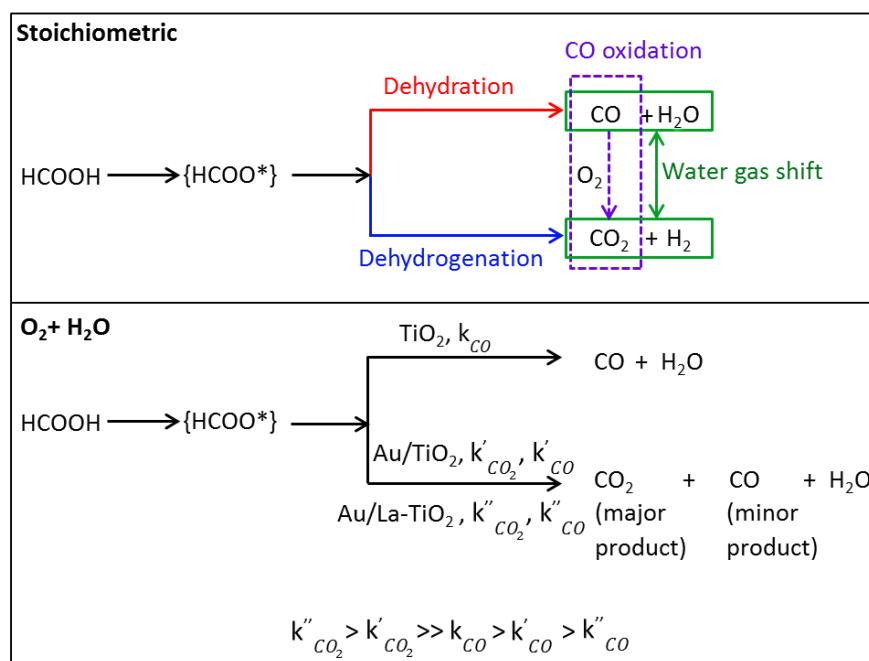
Based on:

Sridhar, M.; Ferri, D.; van Bokhoven, J.A.; Kröcher, O. 2016, (Under review).

M.S. contributions: experiments, analysis and write-up

## 6.1 Introduction

The scope of this chapter is to investigate the formic acid decomposition mechanism on the unmodified (Au/TiO<sub>2</sub>) and base-modified (Au/La-TiO<sub>2</sub>) gold catalysts under SCR-relevant conditions in which the feed contains excess oxygen and water. Scheme 6.1 compares the possible pathways for carbon dioxide and carbon monoxide formation from formic acid decomposition as reported in literature and observed in our studies. During formic acid decomposition in the simulated exhaust feed (composed of 10 vol% oxygen and 5 vol% water), Chapters 3-5 demonstrated that the gold catalysts predominantly produced carbon dioxide along with low yields of carbon monoxide (Scheme 6.1).<sup>[25,168,208]</sup> Even though the activity for hydrogen oxidation was negligible, no hydrogen was detected during formic acid decomposition suggesting that stoichiometric dehydrogenation does not take place under the investigated conditions. The presence of gas phase ammonia greatly improved the formic acid decomposition activity and carbon dioxide selectivity of Au/TiO<sub>2</sub>.<sup>[25]</sup> Chapter 5 showed that such a gas phase promotional effect can be realized as a catalytic effect by support modification with a basic additive (lanthanum). Gold supported on lanthanum-modified titania (Au/La-TiO<sub>2</sub>) exhibited significantly enhanced rates while carbon monoxide production was restricted to lower levels (Scheme 6.1).<sup>[208]</sup>



**Scheme 6.1.** Pathways for carbon dioxide and carbon monoxide formation from stoichiometric formic acid decomposition and decomposition in the presence of oxygen and water.

The promotional effect of lanthanum originated from dual phenomena: (i) a particle size effect leading to the stabilization of smaller gold particles and, (ii) a base-effect characterized by higher formate coverage under reaction conditions. By thermally aging the base-modified catalyst and growing the gold particle to the size range similar to that of the unmodified catalyst,

the base-induced increase in carbon dioxide production was disentangled from that arising from a decreased gold particle size. It is known from literature,<sup>[192,209]</sup> that instead of direct formic acid oxidation to carbon dioxide, formic acid could alternatively first decompose to carbon monoxide as an intermediate that subsequently oxidizes to carbon dioxide (Scheme 6.1). However, in the previous chapter,<sup>[208]</sup> it was found that the carbon dioxide production emerging from the oxidation of isoconcentration of carbon monoxide was significantly lower (by a factor of >five) than that from formic acid decomposition on both the unmodified and the base-modified catalysts. In fact, such an experiment assessed the maximum possible contribution from carbon monoxide oxidation activity since it assumes that all the formic acid decomposes to carbon monoxide (isoconcentration) prior to oxidation to carbon dioxide, which is not likely to be the case in reality. These findings establish that carbon monoxide oxidation is irrelevant in the formic acid decomposition mechanism operating on the two catalysts and instead a direct pathway leading from formic acid to carbon dioxide exists which in turn is accelerated upon base-modification.

With the elimination of carbon monoxide oxidation from the mechanistic picture, the next question that arises is on the very origin of carbon monoxide. In this regard, it was found that an exclusive dehydration-type reaction to carbon monoxide and water (Scheme 6.1) occurred in the absence of gold on the pristine metal oxide supports (Chapter 5).<sup>[25,168,208]</sup> In fact, the observed suppression in the carbon monoxide yield during formic acid decomposition over Au/La-TiO<sub>2</sub> compared with that of Au/TiO<sub>2</sub> correlated with the decreased carbon monoxide production on the base-modified support.<sup>[208]</sup> Experiments investigating the effect of gold loading revealed a selective increase in the carbon dioxide production proportional to an increase in the gold loading on titania. These findings suggest that the direct pathway responsible for carbon dioxide production is associated with the presence of gold and that the carbon monoxide exclusively arises from the activity of the bare supports. Furthermore, a spectroscopic investigation identified formates to be the kinetically-relevant intermediates in the decomposition mechanism operating on both the unmodified and the base-modified catalysts.<sup>[208]</sup>

Formates as the reaction intermediates have been widely proposed in mechanisms related to formic acid decomposition<sup>[27,29,210]</sup> and water gas shift. Several studies investigating stoichiometric formic acid dehydrogenation to hydrogen (and carbon dioxide) in the context of fuel cells have reported formates to be the kinetically relevant reaction intermediates and their C-H bond cleavage as the rate-determining-step.<sup>[61–66]</sup> The catalytic links between WGS and formic acid decomposition are well-established in literature and largely consent on C-H bond breakage as the rate-determining-step.<sup>[54,59,67,75,171,211–213]</sup>

In this chapter, the origin of the formic acid decomposition activity of gold supported on lanthanum-modified titania (Au/La-TiO<sub>2</sub>) and unmodified titania (Au/TiO<sub>2</sub>) is examined by

systematically investigating the consequences of SCR-relevant feed (oxygen and water) on the catalyst kinetics and the reactivity of the spectroscopically measured surface species. Using these findings, a mechanism is proposed that is consistent with the observed kinetics and reconciles with the different perspectives prevalent in literature. The findings from this chapter reveal that under the SCR-relevant feed conditions employing excess oxygen and water in the feed, an oxidative-dehydrogenation type reaction converting formic acid to carbon dioxide and water takes place which is in contrast to the stoichiometric formic acid dehydrogenation to hydrogen and carbon dioxide that is commonly encountered in literature.

## 6.2 Experimental

The preparation and testing of the titania and lanthana-modified titania supported gold catalysts was conducted following the procedures described in Chapter 2. For experiments determining the kinetic orders, the concentrations of formic acid, carbon monoxide, oxygen, carbon dioxide and water were varied in the range 0-2200 ppm, 0-750 ppm, 0.25-4.00 vol %, 0-750 ppm and 0.01-1.50 vol%, respectively. The in situ diffuse reflectance infrared Fourier transform spectroscopic (DRIFTS) study of formic acid adsorption under steady state and transient conditions was performed as described in Chapter 2.

## 6.3 Results

### 6.3.1 Catalytic roles of oxygen and water

#### 6.3.1.1 Feed-dependent activity

Figure 6.1 depicts the effect of oxygen and water on the activity of Au/La-TiO<sub>2</sub> and Au/TiO<sub>2</sub> for formic acid decomposition at 200 °C and 300 °C at different contact times. At 300 °C, stoichiometric formic acid decomposition in nitrogen led to maximum conversion of ~80% at the highest contact time. The highest formic acid conversion on Au/La-TiO<sub>2</sub> was obtained in oxygen-water mixture and oxygen, while the lowest conversion was obtained when only water was added to the formic acid feed. Au/TiO<sub>2</sub> exhibited similar trends in conversion except that the highest decomposition activity was observed in dry feed containing oxygen and only nitrogen. At 200 °C, the presence of both oxygen and water was essential to achieve high formic acid conversion on both the catalysts. When the feed contained only nitrogen or water, Au/La-TiO<sub>2</sub> exhibited less than ~3% formic acid conversion which falls within the range of homogenous (non-catalytic) gas phase conversion.<sup>[25]</sup> Au/TiO<sub>2</sub> displayed essentially similar trends irrespective of temperature except that the decomposition activity was slightly higher in nitrogen reaching ~10% conversion. The WGS activity of the two catalysts was examined in feed composed of 5 vol% water and 750 ppm carbon monoxide to maintain isoconcentrations with respect to formic acid decomposition experiments. The two catalysts showed negligible WGS activity as represented by carbon monoxide conversion (magenta triangles).

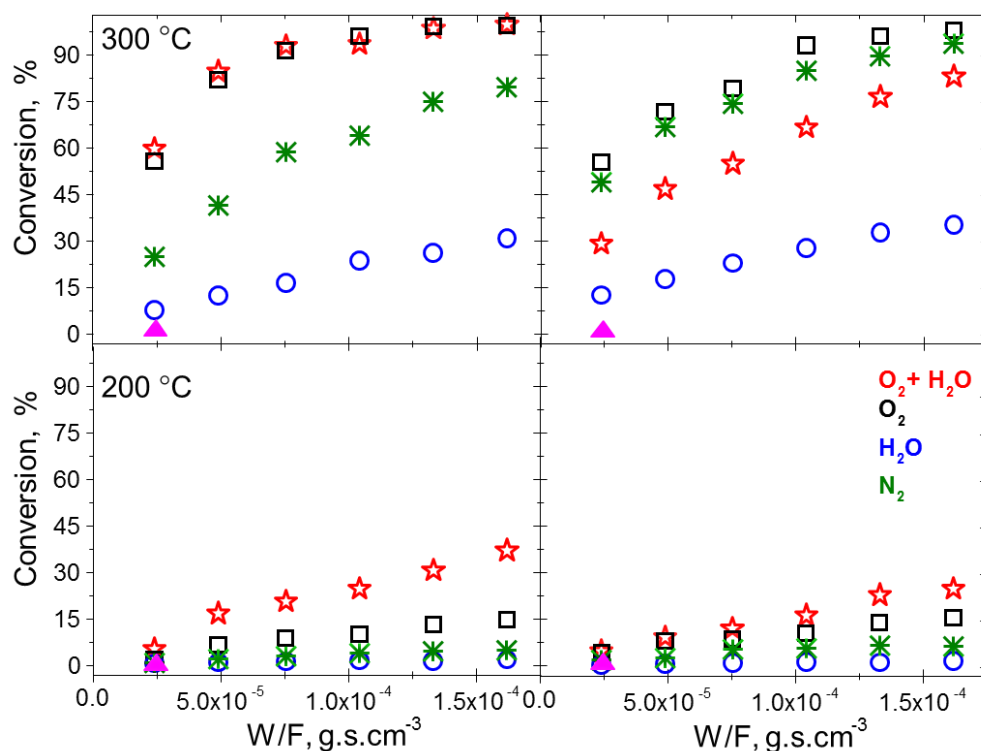
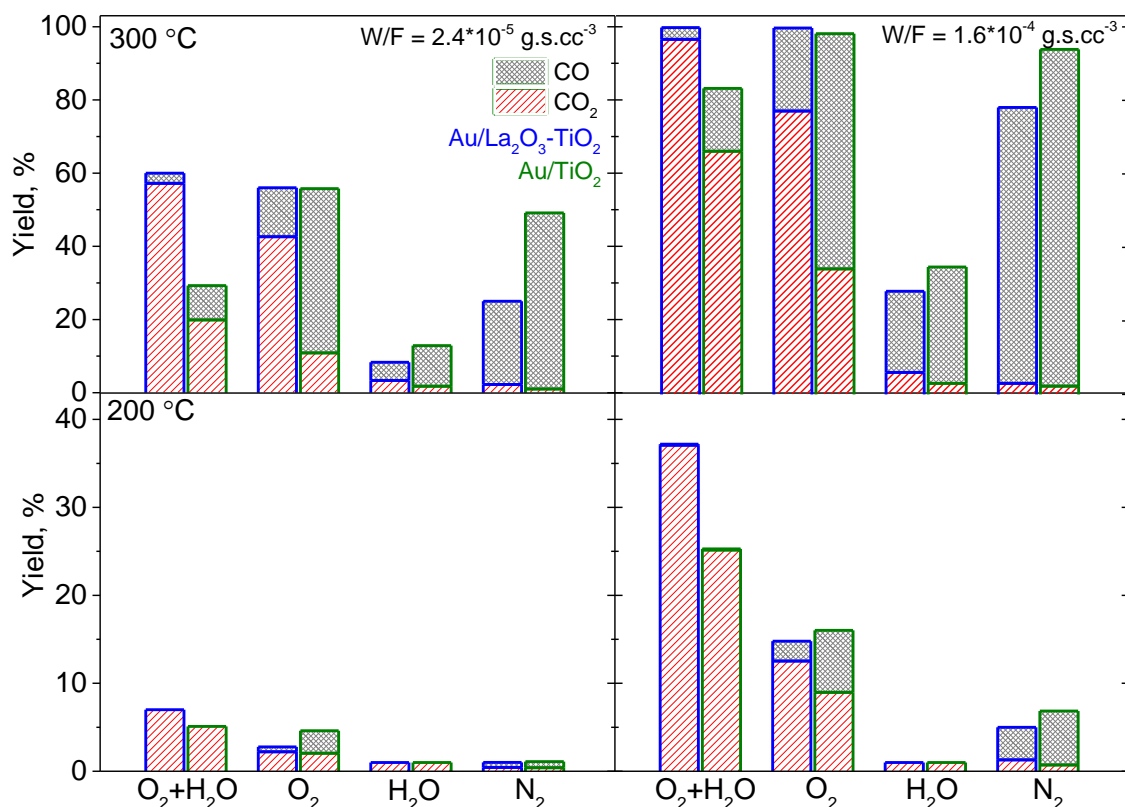


**Figure 6.1** Formic acid conversion on Au/La-TiO<sub>2</sub> and Au/TiO<sub>2</sub> at 200 °C and 300 °C as a function of contact time (W/F, g.s.cm<sup>-3</sup>) and feed composition. The WGS activity (▲) of the two catalysts was determined using isoconcentrations of carbon monoxide (750 ppm) and 5 vol% H<sub>2</sub>O using W/F= 2.4\*10<sup>-5</sup> g.s.cm<sup>-3</sup>.

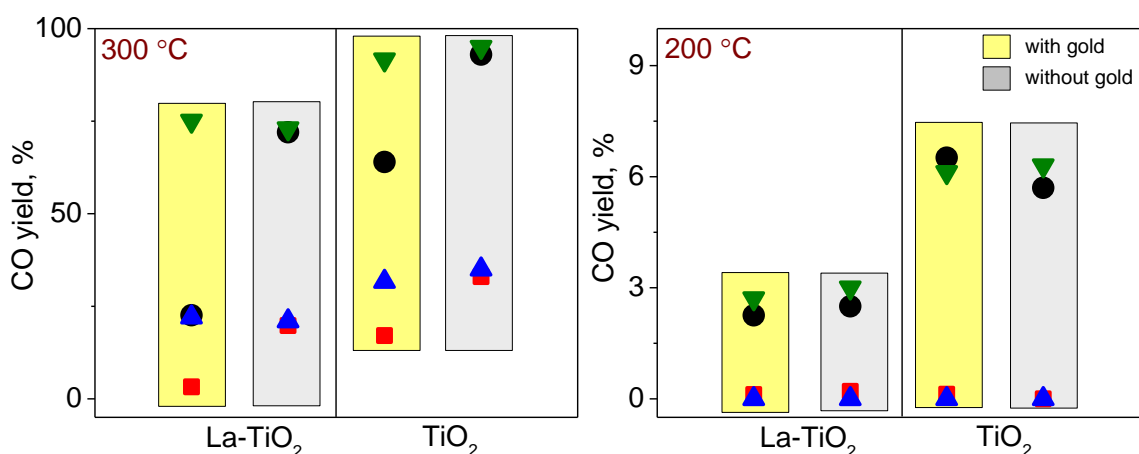
Figure 6.2 illustrates the influence of the feed composition on the product distribution from formic acid decomposition on Au/La-TiO<sub>2</sub> and Au/TiO<sub>2</sub>. The two catalysts exhibited a similar feed-dependent behavior. Carbon monoxide was the only other product besides carbon dioxide. At the highest contact time, stoichiometric formic acid decomposition in nitrogen led to 76% carbon monoxide yield over Au/La-TiO<sub>2</sub>. This reaction pathway was reduced by a factor of about three by the introduction of water to the nitrogen feed while the carbon dioxide yield underwent a modest increase by 2-3%. However, the carbon dioxide yield increased from ~77% to ca. 100% upon the addition of water to the oxygen feed. At 200 °C, the combined presence of oxygen and water was highly beneficial for formic acid decomposition. The carbon dioxide yield underwent close to three-fold increase on both the catalysts upon switching from oxygen to oxygen-water mixture, while carbon monoxide formation was fully suppressed.

Figure 6.3 compares the activity of titania and lanthanum-modified titania with that of the corresponding gold catalysts. Irrespective of the feed composition, the bare supports produced only carbon monoxide from formic acid decomposition. At 200 °C and 300 °C, the carbon monoxide yields over the gold catalysts matched well with that over the corresponding supports in case of formic acid decomposition in water and stoichiometric formic acid decomposition in nitrogen. However, at 300 °C, in oxygen and oxygen-water mixture, the carbon monoxide yields

obtained on the gold catalysts were considerably lower than those on the corresponding supports.



**Figure 6.2** Comparison of carbon dioxide and carbon monoxide yield obtained from decomposition of 750 ppm formic acid over  $\text{Au/La-TiO}_2$  and  $\text{Au/TiO}_2$  using different feed compositions at 200 °C and 300 °C and  $W/F = 2.4 \times 10^{-5} \text{ g.s.cm}^{-3}$  (left column) and  $1.6 \times 10^{-4} \text{ g.s.cm}^{-3}$  (right column).



**Figure 6.3** Comparison of carbon monoxide yield obtained from decomposition of 750 ppm formic acid over  $\text{Au/La-TiO}_2$ ,  $\text{Au/TiO}_2$  and the corresponding supports at 200 °C and 300 °C using different feed compositions: nitrogen ( $\blacktriangledown$ ), 10 vol % oxygen ( $\bullet$ ), 5 vol% water ( $\blacktriangle$ ) and mixture of 10 vol% oxygen and 5 vol % water ( $\blacksquare$ ) at  $W/F = 1.6 \times 10^{-4} \text{ g s cm}^{-3}$ .

**Table 6.1.** Reaction orders in formic acid, oxygen and water for carbon dioxide and carbon monoxide production over Au/TiO<sub>2</sub> and Au/La-TiO<sub>2</sub>

Feed condition	Catalyst	Temperature (°C)	CO <sub>2</sub> production				CO production			
			HCOOH (±0.05)	O <sub>2</sub> (±0.05)	H <sub>2</sub> O (±0.1)	CO <sub>2</sub> /CO (±0.05)	HCOOH (±0.05)	O <sub>2</sub> (±0.05)	H <sub>2</sub> O (±0.05)	CO <sub>2</sub> /CO (±0.05)
Wet	Au/TiO <sub>2</sub>	300	-0.59	0.26	0.17	0.00	-0.15,0.54 <sup>a</sup>	-0.09	-0.34	0.00
		200	-0.72	0.31	0.25	0.00	n.a.	n.a.	-0.64	0.00
	Au/La-TiO <sub>2</sub>	300	-0.74,-0.44 <sup>*</sup>	0.32	0.11	0.00	-0.16,0.52 <sup>a</sup>	-0.08	-0.41	0.00
		200	-0.95,-0.73 <sup>*</sup>	0.31	0.21	0.00	n.a.	n.a.	-0.62	0.00
Dry	Au/TiO <sub>2</sub>	300	-0.49	0.30	-	0.00	-0.38	-0.05	-	0.00
		200	-0.61	0.24	-	0.00	-0.60	-0.04	-	0.00
	Au/La-TiO <sub>2</sub>	300	-0.65	0.36	-	0.00	-0.31	-0.05	-	0.00
		200	-0.75	0.24	-	0.00	-0.69	-0.01	-	0.00

<sup>a</sup> Determined using formic acid concentrations in the range 40-150 ppm in 20 ppm increments.

All values were determined using W/F = 2.4\*10<sup>-5</sup> g s cm<sup>-3</sup>; 750 L h<sup>-1</sup> total flow.

The formic acid, carbon monoxide, oxygen, carbon dioxide and water concentrations were varied in the range 0-2200 ppm, 0-750 ppm, 0.25-4.00 vol %, 0-750 ppm and 0.1-1.50 vol%, respectively.

### 6.3.1.2 Reaction orders

Formic acid orders (Table 6.1) were found to be negative under all conditions for carbon dioxide production on both the catalysts. The change in the orders to less negative values in lower gas phase formic acid concentration regime and at higher temperatures along with the observation of coverage-dependent activation energies<sup>[208]</sup> are in line with the compensation phenomenon. In dry feed, the formic acid orders were slightly less negative. The reaction order in oxygen was ca. 0.3. The water orders were always positive ranging between 0.1 to 0.3 over both the catalysts. Zero orders in carbon monoxide and carbon dioxide were observed indicating the absence of kinetic inhibition by products.

The formic acid orders for carbon monoxide production (Table 6.1) in wet feed varied between weakly negative values of -0.1 to more positive values of ca. 0.5 depending on the gas phase formic acid concentration. Dry feed elicited negative formic acid orders in the range -0.7 to -0.4. The reaction orders in oxygen were always close to zero while those in water were negative (ca. -0.5).

**Table 6.2.** Apparent  $E_a$  and Arrhenius constants (A, in brackets) determined for carbon dioxide and carbon monoxide production from formic acid decomposition on Au/TiO<sub>2</sub> and Au/La-TiO<sub>2</sub> under different feed conditions

Feed composition	Au/La-TiO <sub>2</sub>		Au/TiO <sub>2</sub>	
	CO <sub>2</sub> production	CO production	CO <sub>2</sub> production	CO production
O <sub>2</sub> +H <sub>2</sub> O	53 (10 <sup>10</sup> )	89 (10 <sup>11</sup> )	34 (10 <sup>7</sup> )	90 (10 <sup>12</sup> )
O <sub>2</sub>	65 (10 <sup>10</sup> )	76 (10 <sup>11</sup> )	42 (10 <sup>7</sup> )	80 (10 <sup>11</sup> )
H <sub>2</sub> O	-	103 (10 <sup>12</sup> )	-	102 (10 <sup>12</sup> )
N <sub>2</sub>	-	79 (10 <sup>11</sup> )	-	83 (10 <sup>12</sup> )

<sup>a</sup> All values were determined using 750 ppm formic acid at W/F = 2.4\*10<sup>-5</sup> g s cm<sup>-3</sup> and 750 L h<sup>-1</sup> total flow.

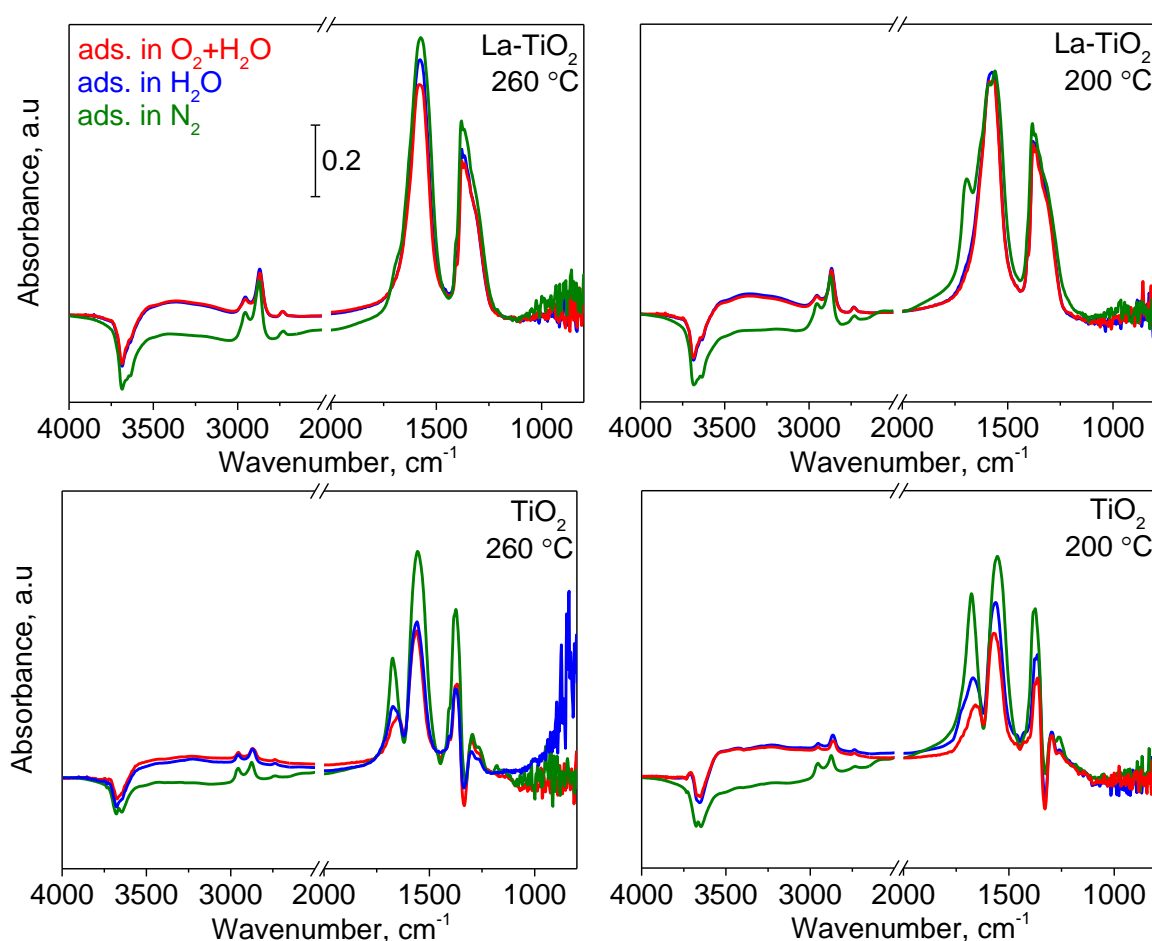
### 6.3.1.3 Effect of feed composition on the apparent activation energy ( $E_a$ )

The apparent activation energy ( $E_a$ ) and the Arrhenius constant (A) (Table 6.2) for carbon dioxide production on Au/La-TiO<sub>2</sub> were higher than on Au/TiO<sub>2</sub> in oxygen-water mixture. These values were a consequence of the compensation phenomenon as reported in Chapter 5.<sup>[208]</sup> The presence of water in the feed reflected in a decrease in  $E_a$  by ~10 kJ mol<sup>-1</sup> on both catalysts. The very low carbon dioxide production in the feed containing only water and only nitrogen (Figure 6.2) was in the range of homogeneous gas phase formic acid conversion (Chapter 4)<sup>[25]</sup> and hence, no  $E_a$  was determined. In agreement with the high values (~100 kJ mol<sup>-1</sup>) reported in literature for formic acid decomposition to carbon monoxide,<sup>[32,214]</sup> both the catalysts exhibited  $E_a$  of ~90 kJ mol<sup>-1</sup>. In water, the  $E_a$  for carbon monoxide formation increased by 10-20 kJ mol<sup>-1</sup>. The presence or absence of oxygen did not affect the  $E_a$ .

### 6.3.2 In situ DRIFTS study

#### 6.3.2.1 Steady state formic acid adsorption under different feed conditions

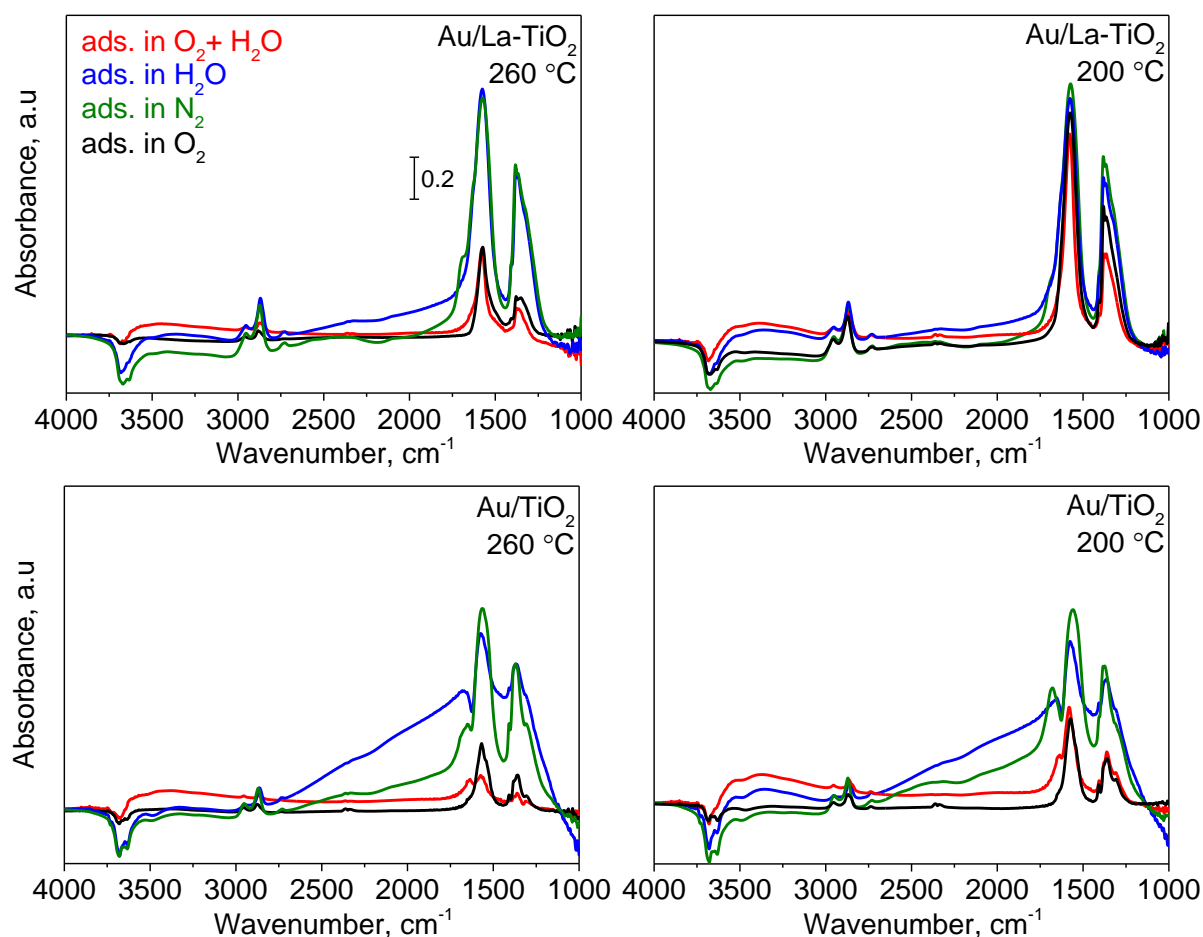
Figures 6.4 and 6.5 represent the in situ DRIFT spectra of formic acid adsorption at 200 °C and 260 °C in different feeds on the supports and the gold catalysts, respectively.<sup>[215]</sup> Both supports (Figure 6.4) exhibited signals in the region 1700-1300  $\text{cm}^{-1}$  which arise from the  $\nu_{\text{as}}(\text{OCO})$  and  $\nu_{\text{s}}(\text{OCO})$  stretching modes of the carboxyl groups of adsorbed formates, and the high frequency bands at 2954, 2869, and 2731  $\text{cm}^{-1}$  which are characteristic of the combination band  $\nu_{\text{as}}(\text{OCO}) + \delta(\text{CH})$ ,  $\nu(\text{C-H})$ , and the  $2\delta(\text{CH})$  overtone, respectively of the formates.<sup>[186]</sup> Various shoulders on both signals indicate multiple adsorption geometries, namely monodentate, bidentate and bridged configurations. Monodentate formate species contribute to the bands at ca. 1690 and 1320  $\text{cm}^{-1}$  on the two supports.<sup>[187]</sup> No signals corresponding to molecularly adsorbed formic acid species were observed.



**Figure 6.4** DRIFT spectra of formic acid adsorption on La-TiO<sub>2</sub> and TiO<sub>2</sub> obtained under different feed conditions at 200 °C and 260 °C.

The bridged/bidentate formates with  $\nu_{\text{as}}(\text{OCO})$  signals around 1590 and 1560  $\text{cm}^{-1}$  and  $\nu_{\text{s}}(\text{OCO})$  signals around 1380 and 1340  $\text{cm}^{-1}$  remained practically unaffected on lanthanum-modified titania upon altering the feed composition. Monodentate formates at 1690  $\text{cm}^{-1}$  fully disappeared

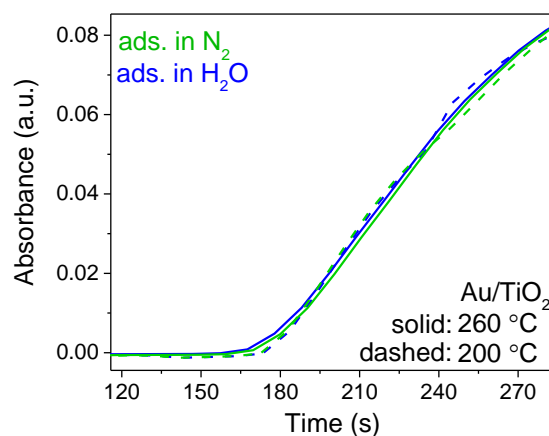
in wet feed. This was accompanied by a considerable decrease of gas phase carbon monoxide in the online FTIR spectra. Upon co-adsorption of formic acid and water on titania, the overall intensity of the formate signals was lowered along with a substantial suppression of the signals associated with monodentate formates. Water replenished the hydroxyls that were depleted during formic acid adsorption as evident from the partial restoration of the signals in the 3800-3500  $\text{cm}^{-1}$  region. Formic acid adsorption on the supports was not significantly affected by the presence of oxygen.



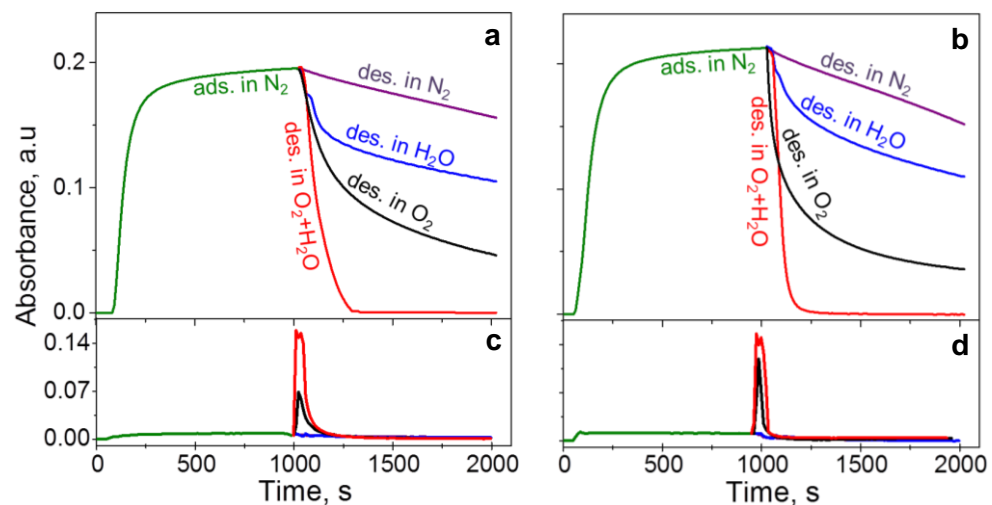
**Figure 6.5** Steady state DRIFT spectra of formic acid adsorption on Au/La-TiO<sub>2</sub> and Au/TiO<sub>2</sub> obtained under different feed conditions at 200 °C and 260 °C.

Figure 6.5 represents identical experiments on the two gold catalysts. Similar to the support counterparts, formates prevailed as the dominant surface species during formic acid adsorption in the different feeds. No vibrations could be ascribed to adsorbed carbon monoxide species on gold. In line with its higher basicity, Au/La-TiO<sub>2</sub> exhibited higher formate intensities compared to Au/TiO<sub>2</sub> under all feed conditions. Water exposure nearly eliminated the features corresponding to the monodentate formates. This was again complimented by the absence of carbon monoxide in the online FTIR spectra. The shoulder around 1635  $\text{cm}^{-1}$  in the spectra obtained in feed containing water and oxygen-water mixture can be attributed to physisorbed water on

titania.<sup>[216]</sup> The broad feature centered around  $3500\text{ cm}^{-1}$  is assigned to the  $\nu(\text{OH})$  of hydroxyl groups involved in hydrogen bonding.<sup>[217,218]</sup> The broad hump extending from  $\sim 1750\text{ cm}^{-1}$  to higher wavenumbers may signify a spectral signature indicative of delocalized shallow trap and conduction band electrons.<sup>[219,220]</sup> Introduction of water did not cause any significant displacement of bridged/bidentate formates on both the catalysts. Similar slopes for the rise of the formate signals (Figure 6.6) indicate that the rate of formate formation remained unaffected upon flowing water during formic acid decomposition. On both the catalysts, the co-presence of oxygen and water yielded comparable formate intensities as that obtained with only oxygen, but significantly higher carbon dioxide production was noted in the gas phase.



**Figure 6.6** Temporal evolution of the C-H stretch vibrational mode of formate at  $2873\text{ cm}^{-1}$  on  $\text{Au/TiO}_2$  at 200 and 260 °C during formic acid adsorption in the indicated feed.



**Figure 6.7** Temporal evolution of the C-H vibrational mode of formate at 2873 cm<sup>-1</sup> on Au/La-TiO<sub>2</sub> at (a) 200 and (b) 260 °C during formic acid adsorption in the indicated feed. (c, d) Corresponding carbon dioxide trace from gas phase FTIR analysis.

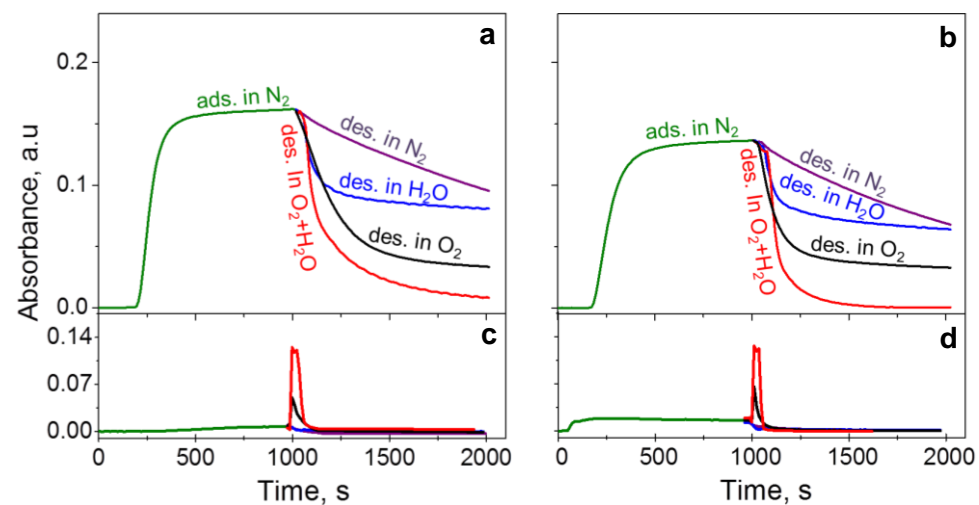


**Figure 6.8** Temporal evolution of the C-H stretch vibrational mode of formate at 2873 cm<sup>-1</sup> on Au/TiO<sub>2</sub> at (a) 200 and (b) 260 °C during formic acid adsorption in the indicated feed. (c, d) Corresponding carbon dioxide trace from gas phase FTIR analysis.

### 6.3.2.2 Transient response under different feed conditions

Figures 6.7 and 6.8 show the temporal evolution of the C-H stretching mode of bidentate formates at  $2873\text{ cm}^{-1}$  and the corresponding gas phase carbon dioxide traces obtained on the gold catalysts during different switches at  $200\text{ }^{\circ}\text{C}$  and  $260\text{ }^{\circ}\text{C}$ . On both the catalysts, a slow decay in the formate intensity was observed when desorption was performed in nitrogen feed. The switch to water slightly improved desorption. The carbon dioxide production was negligible during both the switches. The switch to water produced formic acid in the effluent gas. In marked contrast, switching to oxygen resulted in a greatly enhanced removal of the adsorbed formates. Desorption was in this case reactive in nature as revealed by the rise of the carbon dioxide signal. At the end of the switch, the DRIFT spectra showed unreacted formates still residing on the catalyst surfaces (Figure 6.9). The most rapid fall of the signals was evidenced upon switching to the oxygen-water mixture, which also coincided with the highest carbon dioxide production. The spectra recorded at the end of this switch showed that essentially all the surface formates had been consumed (Figure 6.9).

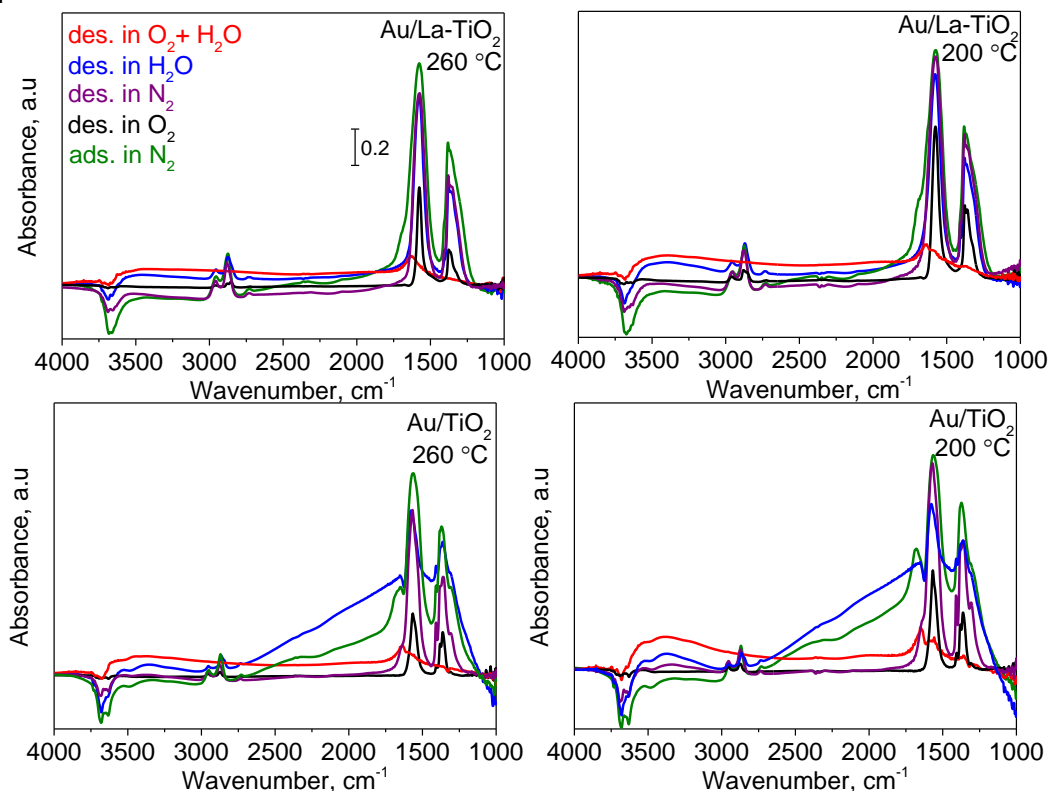


**Figure 6.9** DRIFTS spectra of formic acid adsorption in nitrogen and desorption in nitrogen, oxygen, water and oxygen-water mixture on Au/TiO<sub>2</sub> and Au/La-TiO<sub>2</sub> at  $200\text{ }^{\circ}\text{C}$  and  $260\text{ }^{\circ}\text{C}$ .

Figure 6.10 compares the ratios between the carbon dioxide produced in the feed containing oxygen-water mixture and oxygen obtained from the catalytic measurements ( $r_{\text{CO}_2, \text{catalytic}}$ , Eq. 6.1),

the slopes of the decrease of the signal at  $2869\text{ cm}^{-1}$  in oxygen-water mixture and oxygen ( $r_{\text{C-H,DRIFTS}}$ , Eq. 6.2) and the corresponding carbon dioxide peak areas measured by gas phase FTIR ( $r_{\text{CO}_2,\text{FTIR}}$ , Eq. 6.3). The estimated ratios closely matched. In agreement with the higher carbon dioxide yield on the gold catalysts in oxygen-water mixture (Figure 6.2), the ratios between the slopes of decrease of the C-H signal in oxygen-water mixture and oxygen were always  $>1$ , reaching values as high as  $\sim 3$  on both the catalysts at  $200\text{ }^\circ\text{C}$ .

$r_{\text{CO}_2,\text{catalytic}}$  is calculated from the catalytic formic acid decomposition experiments reported in Figure 6.2.

$$r_{\text{CO}_2,\text{catalytic}} = \frac{\text{CO}_2 \text{ yield obtained in O}_2 + \text{H}_2 \text{ mixture}}{\text{CO}_2 \text{ yield obtained in O}_2} \quad (6.1)$$

$r_{\text{C-H,DRIFTS}}$  is calculated from the transient in situ DRIFTS measurements (Figures 6.7 and 6.8)

$$r_{\text{C-H,DRIFTS}} = \frac{\text{slope of fall of C-H signal upon flushing with O}_2 + \text{H}_2 \text{ mixture}}{\text{slope of fall of C-H signal upon flushing with O}_2} \quad (6.2)$$

$r_{\text{CO}_2,\text{FTIR}}$  is calculated from the online FTIR measurements recorded during transient in situ DRIFTS experiments (Figures 6.7 and 6.8)

$$r_{\text{CO}_2,\text{FTIR}} = \frac{\text{CO}_2 \text{ peak area resulting upon flushing with O}_2 + \text{H}_2 \text{ mixture}}{\text{CO}_2 \text{ peak area resulting upon flushing with O}_2} \quad (6.3)$$

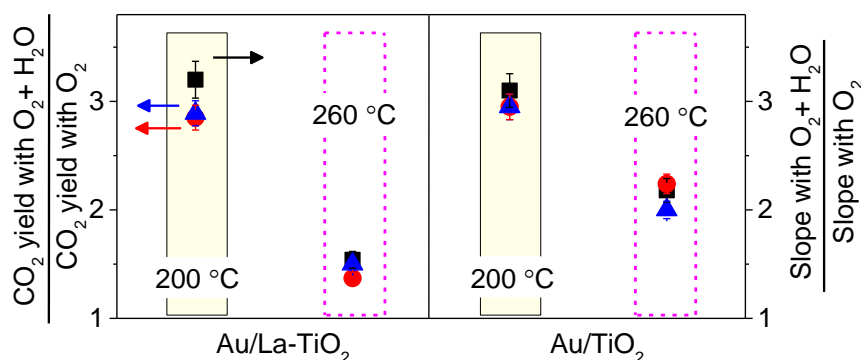


**Figure 6.10** Relative yields of the carbon dioxide produced from formic acid decomposition on Au/La-TiO<sub>2</sub> and Au/TiO<sub>2</sub> in oxygen-water mixture and only oxygen derived from the catalytic experiments (▲), the ratio of slopes of the decrease in the C-H signal ( $2873\text{ cm}^{-1}$ ) from transient DRIFTS experiments (■) and ratio of carbon dioxide peak areas obtained from formic acid decomposition in oxygen-water mixture to that in only oxygen derived from the gas phase FTIR analysis (●).

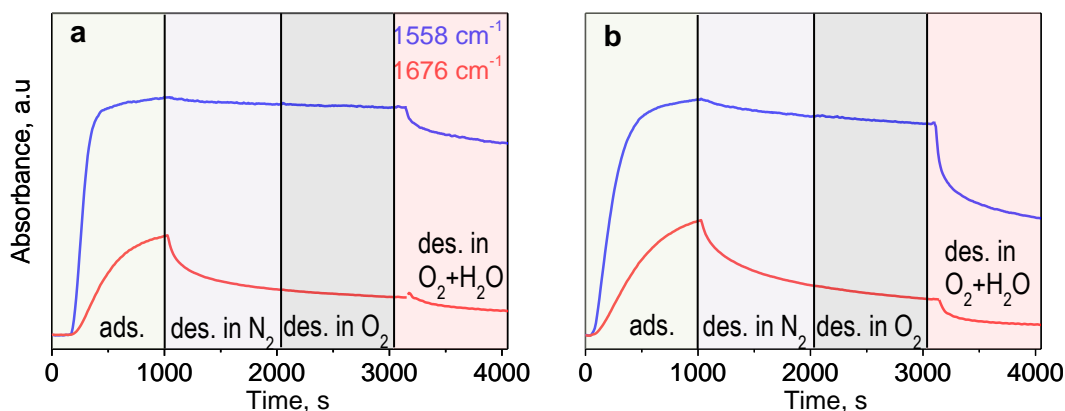


**Figure 6.11** Temporal evolution of the  $-(\text{OCO})-$  stretch signals at  $1558\text{ cm}^{-1}$  and  $1676\text{ cm}^{-1}$  on (a)  $\text{La-TiO}_2$  and (b)  $\text{TiO}_2$ , during formic acid adsorption in nitrogen and sequential desorption in feed containing only nitrogen, water, oxygen and an oxygen-water mixture at  $260\text{ }^\circ\text{C}$ .

Figure 6.11 illustrates the temporal evolution of the  $v_{\text{as}}(\text{OCO})$  of the bidentate and monodentate formates at  $1558\text{ cm}^{-1}$  and  $1676\text{ cm}^{-1}$ , respectively, during equivalent transient experiments on the supports at  $260\text{ }^\circ\text{C}$ . These bands were chosen to allow differentiation between the mono- and bidentate formates on the supports. In contrast to the gold catalysts, bidentate formates on the supports showed little reactivity in the presence of nitrogen and oxygen. In wet feed, titania exhibited greater extent of displacement of the bidentate formates than the more basic lanthanum-modified titania. The monodentate formates exhibited a sharper decline in nitrogen followed by a slower decay that was virtually independent of the feed composition on the two supports.

## 6.4 Discussion

### 6.4.1 Catalytic roles of gold and the support: Parallel pathways for carbon dioxide and carbon monoxide formation

Formic acid can decompose to carbon monoxide and/or carbon dioxide (Scheme 6.1). The bare supports exclusively produced carbon monoxide (Figure 6.3) while the gold catalysts catalyzed both (Figure 6.2). Carbon monoxide which was produced at close to 100% selectivity on the gold catalysts from stoichiometric formic acid decomposition in nitrogen and formic acid decomposition in water, entirely originated from the supports. Hence, gold does not catalyze formic acid decomposition to carbon monoxide. The very low carbon dioxide production (1-5%) on the gold catalysts under these feed conditions arose largely from the homogeneous gas phase formic acid conversion ( $\sim 3\%$ )<sup>[25]</sup> and a very small extent of stoichiometric formic acid dehydrogenation.<sup>[51,63,89]</sup> Thus, gold was practically inactive for formic acid decomposition in nitrogen and water. Consistent with the findings from Chapter 5, lanthanum-modification resulted in enhanced carbon dioxide production.

Unifying these results with the gold loading effect observed in Chapter 4, the inherent nature of gold to selectively produce carbon dioxide from formic acid decomposition is revealed.<sup>[106]</sup> Furthermore, we can distinguish the operation of two independent active sites/pathways responsible for carbon dioxide and carbon monoxide formation. On the one hand, carbon dioxide-producing sites are strictly related to gold, residing either on gold or at the interface between the gold particles and the support. On the other hand, the carbon monoxide producing sites are located exclusively on the support. The higher  $E_a$  values for carbon monoxide formation than for carbon dioxide production (Table 6.2) suggest that the latter pathway is more kinetically favored and that in the presence of active carbon dioxide-producing sites, a rapid transfer and consumption of the formic acid species to form carbon dioxide overtakes the slower turnover on the support-sites. This reconciles with the lower carbon monoxide yield on the gold catalysts compared to their support counterparts in the presence of oxygen (Figure 6.3).

#### **6.4.2 Effect of oxygen and oxygen-water synergy: Nature and reactivity of surface intermediates**

The activity of the gold-related sites was contingent on the presence of oxygen and was further promoted by water (Figure 6.2). Since the activities for carbon monoxide oxidation (reported in Chapter 5) and the WGS reaction (Figure 6.1) are virtually irrelevant for carbon dioxide production on the gold catalysts, carbon monoxide can be excluded as intermediate. Oxygen and water are most likely involved in a 'direct pathway' which in turn is accelerated in the case of the lanthanum-modified catalyst (Figure 6.2).

Formates were the only detectable surface intermediates on the catalysts whether gold was present or not under any feed conditions (Figures 6.4 and 6.5). Formic acid adsorption was always accompanied with the consumption of surface hydroxyls resulting in the formation of surface formates and release of water. Analogously, surface hydroxyls have been reported to deprotonate alcohol to alkoxide which in turn constituted the relevant reaction intermediate for alcohol oxidation.<sup>[120]</sup> Adding water during formic acid adsorption restored the depleted hydroxyls only to some extent. The high coverage of formate prevented further hydroxyl formation.<sup>[59]</sup>

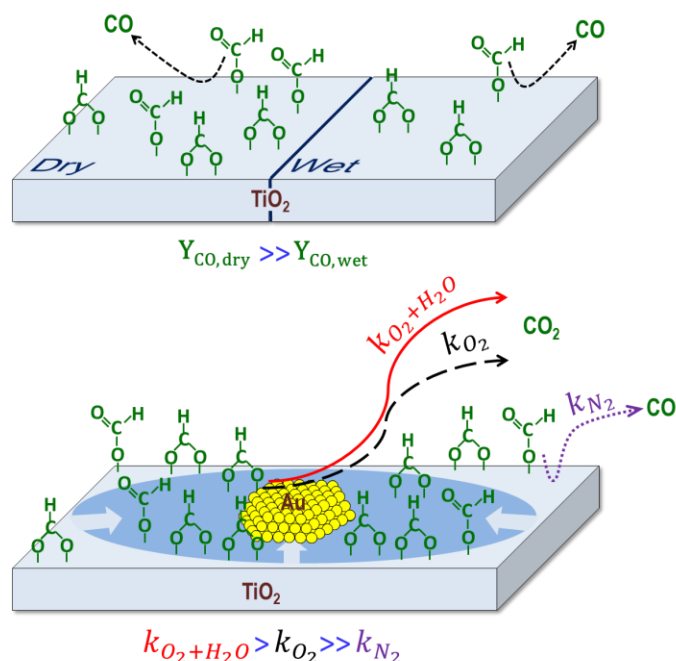
On supports free of gold, bidentate formates behaved as spectators showing very little reactivity to a change of feed composition (Figures 6.4 and 6.11). Monodentate formates were linked to carbon monoxide production in the gas phase. The higher intensities of the monodentate formate signals on titania concur with its higher carbon monoxide yield than lanthanum-modified titania (Figure 6.3). The presence of water suppressed the formation of monodentate formates on both these supports

lowering the carbon monoxide production. Formic acid adsorption on oxygen vacancies on titania, which are proposed to be the sites for the formation of monodentate formates, competes with water adsorption.<sup>[42,221]</sup> Such a competitive adsorption correlates well with the highly negative water orders (Table 6.1) and the increased  $E_a$  for carbon monoxide formation in wet feed (Table 6.2). The higher degree of suppression at the lower temperature (200 °C) is consistent with more negative water orders. These monodentate formates are proposed to undergo C-H bond scission over an adjacent oxygen anion to form carbon monoxide and a surface hydroxyl; condensation of two hydroxyls into water regenerates the surface vacancy.<sup>[42]</sup> In line with the oxygen-independent activity of the supports (Figure 6.2, Tables 6.1 and 6.2), oxygen did not induce any change in the nature or the reactivity of the formate species.

Gold catalysts exhibited higher formate signal intensities (Figure 6.5) than the corresponding supports suggesting that gold catalyzed the formation of formate species either directly, e.g. at the perimeter of the gold particles, by offering an alternative reaction pathway with lower activation barrier or indirectly as a consequence of modifying the oxide surface and/or increasing local reactant coverages by spillover processes.<sup>[59]</sup> Bridged/bidentate formates were the major surface species under all feed conditions (Figures 6.5 and 6.9). The highly negative formic acid orders (Table 6.1) along with the observation of only formates and absence of adsorbed carbon monoxide signals in the in situ DRIFT spectra under different feed conditions (Figures 6.5 and 6.9) indicate that the active sites associated with gold have higher affinity for formic acid than for carbon monoxide. Hence, high formate coverages render the active sites unavailable for the adsorption (and subsequent oxidation) of carbon monoxide which is present at much lower concentrations than formic acid (Figure 6.2).

Consistent with the lower carbon monoxide production on the gold catalysts (Figures 6.2 and 6.3), there was a lower density of monodentate formates than on the gold-free supports. In contrast to the trend on the supports, the reactivity of bidentate formates was highly contingent on the feed (Figures 6.5-6.9). The considerably lower formate concentration in oxygen and oxygen-water mixtures than in nitrogen and water (Figure 6.5) suggest higher rate of formate consumption to form carbon dioxide.<sup>[74]</sup> The surface formate concentration in the oxygen-water mixture was similar to that in oxygen though enhanced carbon dioxide production was observed. This indicates that in the presence of both oxygen and water, more formates turnover to carbon dioxide.<sup>[222]</sup> The decreased formate coverage with increased temperature (Figure 6.5) correlates well with the less negative orders in formic acid at higher temperature (Table 6.1) and support the experimentally observed compensation phenomenon.<sup>[208]</sup>

Switching the feed from formic acid to oxygen-water mixture caused all formates to disappear from the surface and water and carbon dioxide desorbed (Figures 6.7-6.9). Since all of these formates cannot be accommodated on gold, this suggests that the support acts as a reservoir of formates which in the presence of oxygen decompose to carbon dioxide after diffusion to the gold.<sup>[59,223,224]</sup> The relative rates of reactive clean-up of bidentate formates in oxygen and oxygen-water mixture correlated well with the relative rates of carbon dioxide production in the two feeds (Figure 6.10). This is consistent with a mechanism in which (bidentate) formates represent the relevant reaction intermediates for carbon dioxide formation on both the catalysts. Thus, the catalytic and the in situ DRIFTS experiments add complementary evidences to the feed-dependent kinetics of gold and the reactivity of the formate intermediate. Furthermore, the data of Figure 6.10 validates the comparison between the DRIFTS and the catalytic experiments and justifies the use of the spectroscopic measurements to derive mechanistic insights. In the absence of gold, most of these formates remain as inert spectators while minor portion (the monodentate formates) slowly decompose/react to carbon monoxide (Figure 6.11).



**Scheme 6.2** Illustration of the surface species and their reactivity under different feed conditions over the support and the gold catalyst.

Scheme 6.2 summarizes these mechanistic insights. Formates constitute the major surface species on the catalysts and the gold-free supports under all reaction conditions. Monodentate formates are the precursors for carbon monoxide and experience competitive adsorption with water, which lowers the carbon monoxide yield. The bidentate formates only react in the presence of gold and oxygen. The gold catalyst is more densely populated with bidentate formates. The darker region

adjoining the gold particle denotes the area on the support acting as a dynamic sink for these formates that decompose to carbon dioxide on the active sites associated with gold. Decomposition to carbon dioxide is enhanced in the presence of water. The rate of carbon dioxide production dominates the rate of carbon monoxide formation taking place separately but simultaneously on the support.

### 6.4.3 A hydroperoxy-mediated mechanism for oxidative dehydrogenation of formic acid: From elementary steps to global kinetics

The importance of oxygen and water with respect to carbon dioxide production is in line with their positive orders (Table 6.1). In such a water-assisted oxidative decomposition of formic acid to carbon dioxide, water may act as a co-catalyst offering an energetically-favorable pathway for oxygen activation similar to the hydroperoxy route proposed for carbon monoxide oxidation on supported gold catalysts.<sup>[129,225,226]</sup> The formation of such hydroperoxy species (HOO\*) by proton transfer between molecularly adsorbed water and oxygen bypasses the energy-intensive route involving O-O bond cleavage.<sup>[125,126]</sup> This is in line with the water-induced reduction of  $E_a$  (Table 6.2) for carbon dioxide production.

In contrast to the positive orders in oxygen and water, the highly negative formic acid orders for carbon dioxide production imply that the active sites are saturated by the bidentate formates (Figure 6.5).<sup>[208]</sup> These formates may undergo oxidative-dehydrogenation to carbon dioxide. The hydroperoxy species that compete for the same adsorption site cleaves the C-H bond of the formate in the rate-determining-step. Carbon dioxide desorbs and the hydrogen atom reacts with activated oxygen species to form water or hydroxyl. DFT calculations showed that the  $\alpha$  C-H bond of an alcohol can be easily cleaved by hydroperoxy species without involving atomic oxygen during the aerobic alcohol oxidation reaction under aqueous conditions.<sup>[123]</sup> Direct experimental evidence and reactivity of such species in the C-H bond activation during propylene epoxidation was established using in situ UV-Vis and electron paramagnetic resonance.<sup>[227]</sup> The catalytic and spectroscopic findings reported in this study clearly indicate that the same mechanism operates on the base-modified and unmodified catalysts. In view of the negative orders in formic acid, the promotional effect of basicity cannot result from an increased extent of deprotonation. The catalytic effect of the base may relate to C-H bond weakening of formate<sup>[74,75,212,213]</sup> or an increase in the stability of activated oxygen species<sup>[128,228,229]</sup> which is delved into in Chapter 8.

These mechanistic insights can be formulated by the following elementary steps:

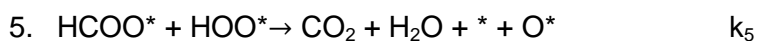
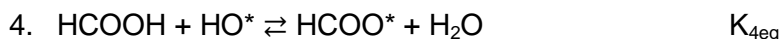




Steps 1 and 2 represent the quasi-equilibrated, non-dissociative adsorption steps for oxygen and water. \* denotes the active site. The carbon dioxide production rate increased with increasing oxygen and water concentrations in a manner consistent with Langmuir-Hinshelwood rate equations on surfaces with oxygen- and water-derived species present below saturation coverages. The absence of first-order kinetics in oxygen (Table 6.1) precludes irreversible oxygen adsorption. The formation of hydroperoxyls from water and oxygen is an energetically favorable bimolecular route for oxygen activation that has lower enthalpy barrier in the temperature range 30-330 °C.<sup>[230]</sup> Thus, its formation compensates for the entropic penalty owing to their transition state that is larger and more ordered than that for unimolecular dissociation. Step 3 describes the proton shift equilibrium responsible for the creation of the hydroperoxy species.



Step 4 is the dissociative adsorption of formic acid onto the active site where a surface hydroxyl abstracts the proton to form the surface formate and a water molecule. In step 5, HOO\* cleaves the C-H bond, leading to the release of carbon dioxide and water. The resulting atomically adsorbed oxygen species, O\*, are removed by reaction with another adsorbed formate (step 6).



The catalytic cycle is completed by kinetically irrelevant steps of recombination of the resulting hydroxyls to form water and O\* (step 7), adsorbed water dissociation into surface hydroxyl and proton (step 8) and reaction of O\* and surface proton to form surface hydroxyl (steps 9). Since water is regenerated in steps 4 and 5, the role of water is that of a co-catalyst and not of a stoichiometric reactant. In agreement with our study, Nijhuis and coworkers<sup>[231]</sup> showed that even though water was not consumed, its presence is critical for the formation of the active hydroperoxy species.



Steps 5 and 6 are the rate-determining-steps of the proposed mechanism. Because  $O^*$  is a transient species, i.e.  $d[O^*]/dt = 0$ , pseudo steady state approximation can be applied for these steps.  $HCOO^*$  is considered to be the most dominant surface species as justified by its negative order.

The overall stoichiometric equation is:



The overall reaction rate is the sum of the rates of steps (5) and (6), giving:

$$\text{Rate} = \frac{2(k_5 K_{2eq} K_{3eq})^{1/3} (k_6 K_{7eq})^2 (p_{H_2O})^{2/3} (p_{O_2})^{1/3} L}{(K_{1eq})^{1/3} K_{4eq} p_{HCOOH}}, \text{ where } L \text{ is the total number of sites.}$$

The rate expression derived from the proposed mechanism elicits orders that accurately matched the experimentally observed kinetic orders. The full mathematical derivation is provided in the Appendix of this chapter.

The predicted orders for water are higher than the experimentally observed values, which can have two plausible explanations. (i) The dehydration reaction occurring in parallel on the support and forming carbon monoxide and water is expected to increase the local water concentrations, thus lowering the water orders. Complementary to this argument, we observed a more positive water order for carbon dioxide production at 200 °C than at 300 °C (Table 6.2), which coincided with lower carbon monoxide production. (ii) Considering that the oxidative-dehydrogenation-type (ODH) pathway of formic acid is autocatalytic with respect to water, it is reasonable that the catalytic surface harbors much higher quantities of adsorbed water species with increasing water concentration, thus lowering the apparent water orders. Analogous to our findings, Chandler and coworkers<sup>[226]</sup> reported that the experimentally determined water orders (~0.3) during water-assisted carbon monoxide oxidation on Au/TiO<sub>2</sub> were lower by a factor of four, as compared to those based on the hydroperoxyl-mediated mechanism (1.3).

With respect to the formic acid orders, the proposed mechanistic model predicts a more negative value (-1) compared to the experimentally observed values (Table 6.1). This can be justified again considering that the model assumes only one kind of site (carbon dioxide-forming site associated with gold) that is binding formates. However, in reality, the sites on titania also adsorb formic acid as formates and convert them to carbon monoxide (Figure 6.3) and hence, in reality, the local formic acid concentrations are lower than that considered by the mechanistic model. Such an argument is

also consistent with the more negative formic acid orders for the base-modified catalysts (-0.7 to -1.0) which coincidentally produces lesser carbon monoxide, meaning that there is lesser formic acid turn over to carbon monoxide and hence the local formic acid concentrations are closer to that available in the gas phase. Also, the relatively less negative order of -0.4 for carbon dioxide production observed with the base-modified catalyst in the lower formic acid concentration regime (Table 6.1) is complimented by the positive order for carbon monoxide formation ( $\sim +0.5$ ) such that the carbon monoxide-producing sites on titania competitively consume a part of the gas phase formic acid, thus, resulting in lower local formic acid concentrations available for the carbon dioxide forming sites.

## 6.5 Conclusions

Mechanistic understanding of formic acid decomposition under conditions relevant to diesel exhaust marks an important step towards realizing formate-based ammonia precursors as alternatives to urea in the exhaust aftertreatment systems. This chapter provides fundamental understanding of the roles of oxygen and gold in selective carbon dioxide production from formic acid decomposition on titania-supported gold catalysts under SCR-relevant conditions. Gold is catalytically inactive in the absence of oxygen. The presence of water leads to higher carbon dioxide production rates originating from the promotional effect of water in oxygen activation. The activity of the gold catalysts for carbon monoxide oxidation and the water gas shift reaction was too low to account for the carbon dioxide formation. Carbon monoxide is therefore not a reaction intermediate and carbon dioxide is produced via a direct oxidative-dehydrogenation-type mechanism. Bidentate formates are the kinetically relevant intermediates to carbon dioxide. Steps for the direct participation of water as a co-catalyst in assisting oxygen-activation via formation of the active intermediate (hydroperoxy species) which cleaves the C-H bond of formate in a rate-determining-step are incorporated into a kinetically consistent mechanism.

Carbon monoxide production occurs autonomously on the metal oxide support and is unaffected by the presence of oxygen. Monodentate formates are the precursors for carbon monoxide and their formation is suppressed in the presence of water.

## 6.6 Appendix

Derivation of the rate expression:

Step (1) gives:

$$[\text{H}_2\text{O}^*] = (\text{K}_{1\text{eq}} p_{\text{H}_2\text{O}})[*] \quad (6.4)$$

Similarly, step (2) gives:

$$[\text{O}_2^*] = (\text{K}_{2\text{eq}} p_{\text{O}_2})[*] \quad (6.5)$$

From step (3):  $\text{K}_{3\text{eq}} = \frac{[\text{HOO}^*][\text{HO}^*]}{[\text{H}_2\text{O}^*][\text{O}_2^*]}$

Substituting the expressions for  $[\text{H}_2\text{O}^*]$  and  $[\text{O}_2^*]$  from Eq. 6.4 and 6.6, respectively:

$$[\text{HOO}^*] = \frac{\text{K}_{1\text{eq}} \text{K}_{2\text{eq}} \text{K}_{3\text{eq}} p_{\text{H}_2\text{O}} p_{\text{O}_2}}{[\text{HO}^*]} [*]^2 \quad (6.6)$$

Using Pseudo-steady state approximation for  $[\text{O}^*]$ , we have rate of step (5) = rate of step (6)

Using the above relation and Eq. 6.6:

$$[\text{O}^*] = \frac{k_5}{k_6} \frac{\text{K}_{1\text{eq}} \text{K}_{2\text{eq}} \text{K}_{3\text{eq}} p_{\text{H}_2\text{O}} p_{\text{O}_2}}{[\text{HO}^*]} [*]^2 \quad (6.7)$$

From step (7):  $\text{K}_{7\text{eq}} = \frac{[\text{H}_2\text{O}^*][\text{O}^*]}{[\text{HO}^*]^2}$

Substituting the expression for  $[\text{H}_2\text{O}^*]$  from (11) and  $[\text{O}^*]$  from Eq. 6.7:

$$[\text{HO}^*] = \left\{ \frac{k_5 (\text{K}_{1\text{eq}} p_{\text{H}_2\text{O}})^2 \text{K}_{2\text{eq}} \text{K}_{3\text{eq}} p_{\text{O}_2}}{k_6 \text{K}_{7\text{eq}}} \right\}^{1/3} [*] \quad (6.8)$$

Substituting Eq. 6.8 in Eq. 6.6:

$$[\text{HOO}^*] = \frac{\text{K}_{1\text{eq}} \text{K}_{2\text{eq}} \text{K}_{3\text{eq}} p_{\text{H}_2\text{O}} p_{\text{O}_2}}{\left\{ \frac{k_5 (\text{K}_{1\text{eq}} p_{\text{H}_2\text{O}})^2 \text{K}_{2\text{eq}} \text{K}_{3\text{eq}} p_{\text{O}_2}}{k_6 \text{K}_{7\text{eq}}} \right\}^{1/3}} [*] \quad (6.9)$$

From step (4):  $\text{K}_{4\text{eq}} = \frac{p_{\text{H}_2\text{O}} [\text{HCOO}^*]}{p_{\text{HCOOH}} [\text{HO}^*]}$

Substituting for  $[\text{HO}^*]$  from Eq. 6.8 in the above expression:

$$[\text{HCOO}^*] = \frac{\text{K}_{4\text{eq}} p_{\text{HCOOH}}}{p_{\text{H}_2\text{O}}} \left\{ \frac{k_5 (\text{K}_{1\text{eq}} p_{\text{H}_2\text{O}})^2 \text{K}_{2\text{eq}} \text{K}_{3\text{eq}} p_{\text{O}_2}}{k_6 \text{K}_{7\text{eq}}} \right\}^{1/3} [*] \quad (6.10)$$

Substituting Eq. 6.8 in Eq. 6.7:

$$[O^*] = \frac{k_5}{k_6} \frac{K_{1eq} K_{2eq} K_{3eq} p_{H_2O} p_{O_2}}{\left\{ \frac{k_5 (K_{1eq} p_{H_2O})^2 K_{2eq} K_{3eq} p_{O_2}}{k_6 K_{7eq}} \right\}^{1/3}} [*] \quad (6.11)$$

Performing site balance:

$$L = [*] + [H_2O^*] + [O_2^*] + [HCOO^*] + [HO^*] + [O^*] + [OOH^*] + [H^*] \quad (6.12)$$

Under reaction conditions: The coverage of  $[H^*]$  is assumed to be negligible, hence its contribution in Eq. 6.12 can be neglected.

Substituting from Eq. 6.4, 6.5, 6.8, 6.9, 6.10 and 6.11 in Eq. 6.12:

$$[\Delta] = \frac{L}{1 + (K_{1eq} p_{H_2O}) + (K_{2eq} p_{O_2}) + \frac{K_{4eq} p_{HCOOH}}{p_{H_2O}} \left\{ \frac{k_5 (K_{1eq} p_{H_2O})^2 K_{2eq} K_{3eq} p_{O_2}}{k_6 K_{7eq}} \right\}^{1/3} + \left\{ \frac{k_5 (K_{1eq} p_{H_2O})^2 K_{2eq} K_{3eq} p_{O_2}}{k_6 K_{7eq}} \right\}^{1/3}} + \frac{k_5 K_{1eq} K_{2eq} K_{3eq} p_{H_2O} p_{O_2}}{k_6 \left\{ \frac{k_5 (K_{1eq} p_{H_2O})^2 K_{2eq} K_{3eq} p_{O_2}}{k_6 K_{7eq}} \right\}^{1/3}} + \frac{K_{1eq} K_{2eq} K_{3eq} p_{H_2O} p_{O_2}}{k_6 \left\{ \frac{k_5 (K_{1eq} p_{H_2O})^2 K_{2eq} K_{3eq} p_{O_2}}{k_6 K_{7eq}} \right\}^{1/3}} \quad (6.13)$$

The overall rate is given by: rate (5) + rate (6), but since rate (5) = rate (6),

$$\text{Rate} = 2 \text{Rate (5)} = 2k_5 [\text{HCOO}^*][\text{OOH}^*]/L \quad (6.14)$$

Substituting for  $[\text{HCOO}^*]$ ,  $[\text{OOH}^*]$  and assuming that the coverage of  $[\text{HCOO}^*]$  is the highest (that is neglecting the coverages of all other

$$\text{species): } \frac{2k_5 K_{4eq} p_{HCOOH} K_{1eq} K_{2eq} K_{3eq} p_{H_2O} p_{O_2}}{L p_{H_2O}} \left\{ \frac{L}{\frac{K_{4eq} p_{HCOOH}}{p_{H_2O}} \left\{ \frac{k_5 (K_{1eq} p_{H_2O})^2 K_{2eq} K_{3eq} p_{O_2}}{k_6 K_{7eq}} \right\}^{1/3}} \right\}^2$$

Simplifying,

$$\text{Rate} = \frac{2(k_5 K_{2eq} K_{3eq})^{1/3} (k_6 K_{7eq})^2 (p_{H_2O})^{2/3} (p_{O_2})^{1/3} L}{(K_{1eq})^{1/3} K_{4eq} p_{HCOOH}} \quad (6.15)$$

Kinetic data used for the determination of orders and activation energies:

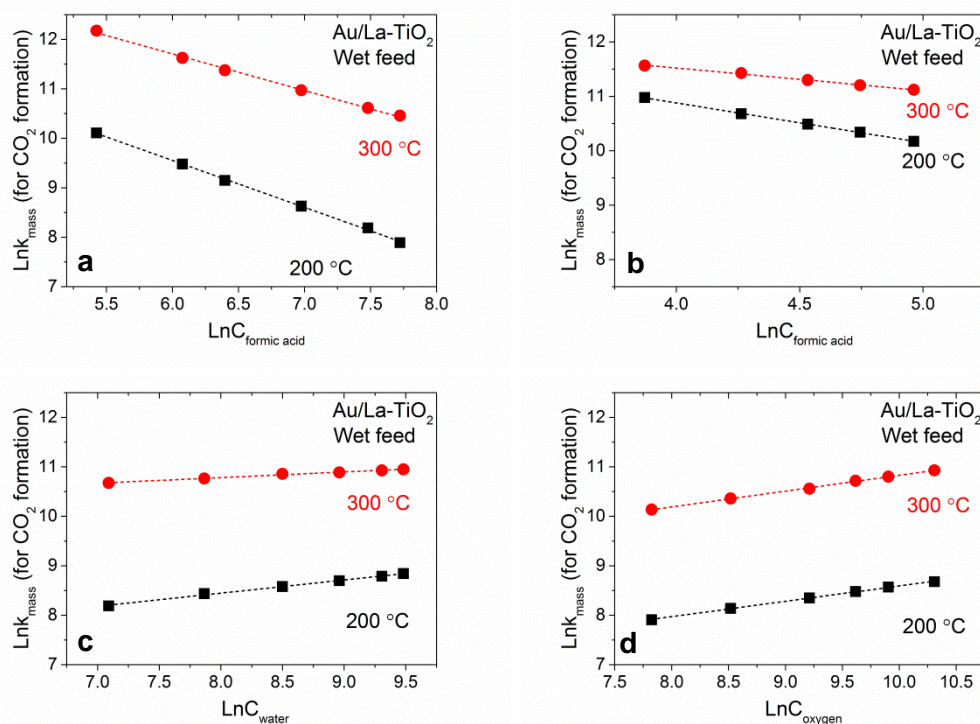


**Figure 6.12** Plots used to calculate the apparent reaction orders at 200 °C and 300 °C for  $\text{CO}_2$  formation from formic acid decomposition on Au/La-TiO<sub>2</sub> in wet feed by varying (a-b) formic acid concentration in the range 400-2,200 ppm and 50-150 ppm, respectively, (c) water concentration in the range 1000-10,000 ppm and (d) oxygen concentration in the range 2500-30,000 ppm.

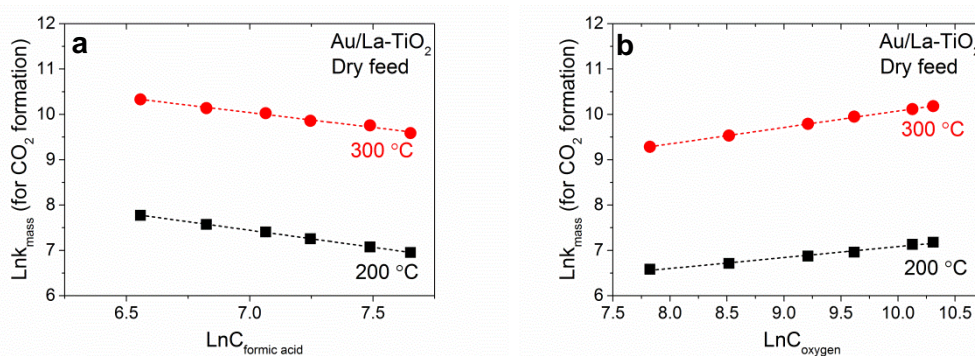


**Figure 6.13** Plots used to calculate the apparent reaction orders at 200 °C and 300 °C for  $\text{CO}_2$  formation from formic acid decomposition on Au/La-TiO<sub>2</sub> in dry feed by varying (a) formic acid concentration in the range 700-2,200 ppm and (b) oxygen concentration in the range 2500-30,000 ppm.

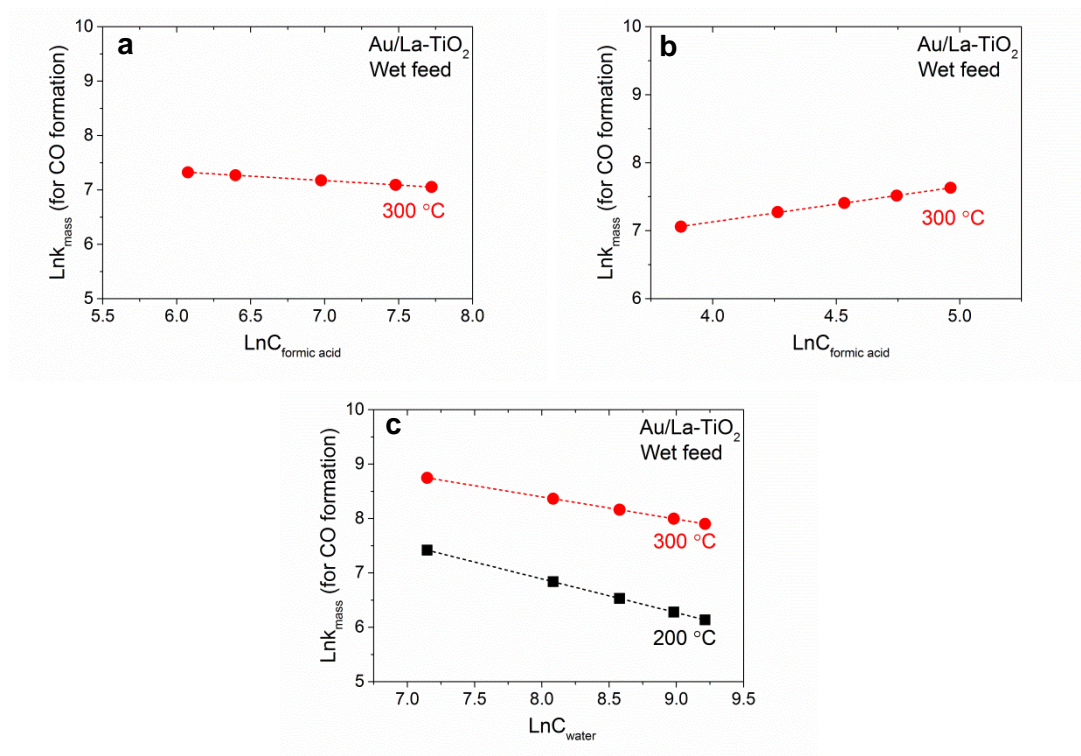


**Figure 6.14** Plots used to calculate the apparent reaction orders at 200 °C and 300 °C for CO formation from formic acid decomposition on Au/La-TiO<sub>2</sub> in wet feed by varying (a-b) formic acid concentration in the range 400-2,200 ppm and 50-150 ppm, respectively and (c) water concentration in the range 1000-10,000 ppm.

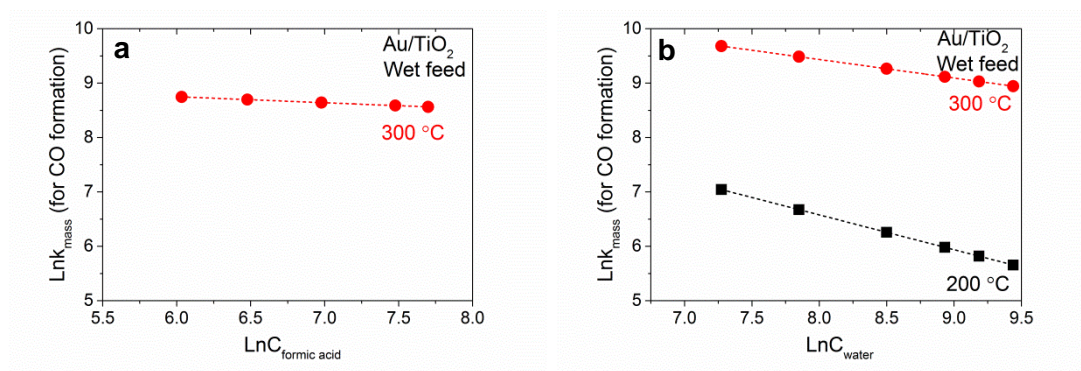


**Figure 6.15** Plots used to calculate the apparent reaction orders at 200 °C and 300 °C for CO formation from formic acid decomposition on Au/TiO<sub>2</sub> in wet feed by varying (a) formic acid concentration in the range 400-2,200 ppm and (b) water concentration in the range 1000-10,000 ppm.

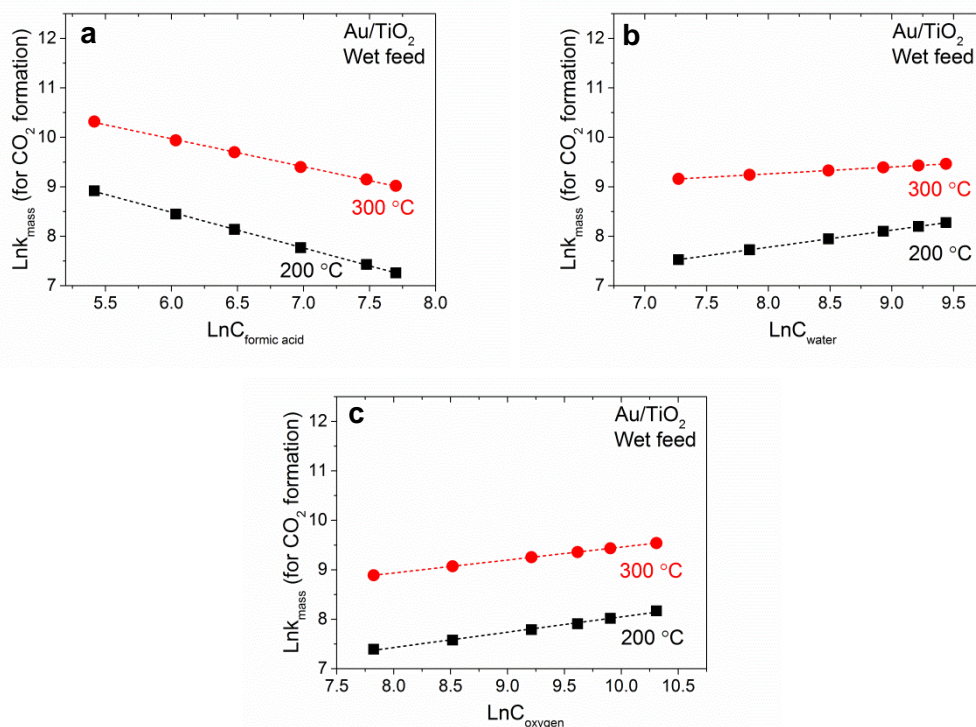


**Figure 6.16** Plots used to calculate the apparent reaction orders at 200 °C and 300 °C for  $\text{CO}_2$  formation from formic acid decomposition on  $\text{Au/TiO}_2$  in wet feed by varying (a) formic acid concentration in the range 400-2,200 ppm, (c) water concentration in the range 1000-10,000 ppm and (d) oxygen concentration in the range 2500-30,000 ppm.

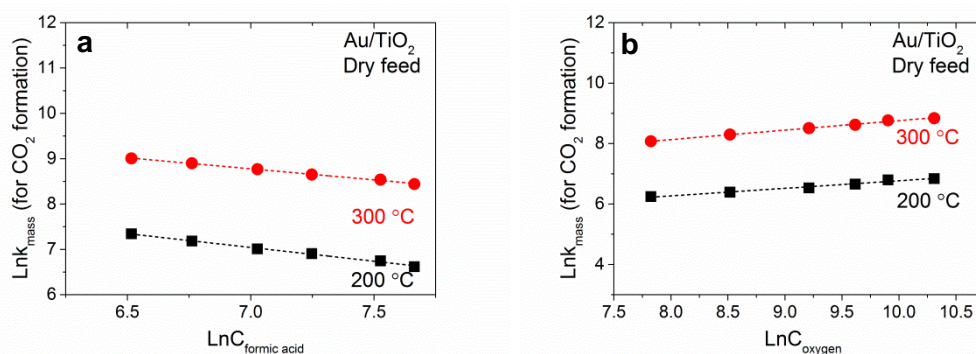


**Figure 6.17** Plots used to calculate the apparent reaction orders at 200 °C and 300 °C for  $\text{CO}_2$  formation from formic acid decomposition on  $\text{Au/TiO}_2$  in dry feed by varying (a) formic acid concentration in the range 700-2,200 ppm and (b) oxygen concentration in the range 2500-30,000 ppm.

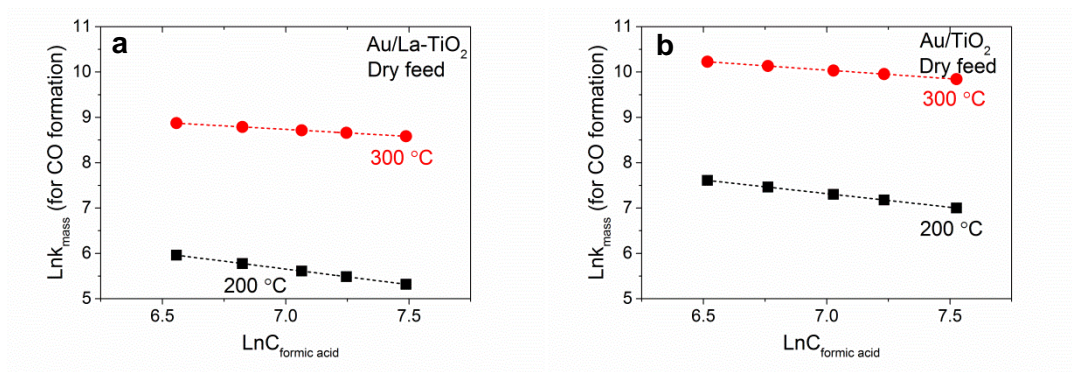


**Figure 6.18** Plots used to calculate the apparent reaction orders at 200 °C and 300 °C for CO formation from formic acid decomposition in dry feed by varying formic acid concentration in the range 700-2, 200 ppm and (a) on Au/La-TiO<sub>2</sub> and (b) Au/TiO<sub>2</sub>.

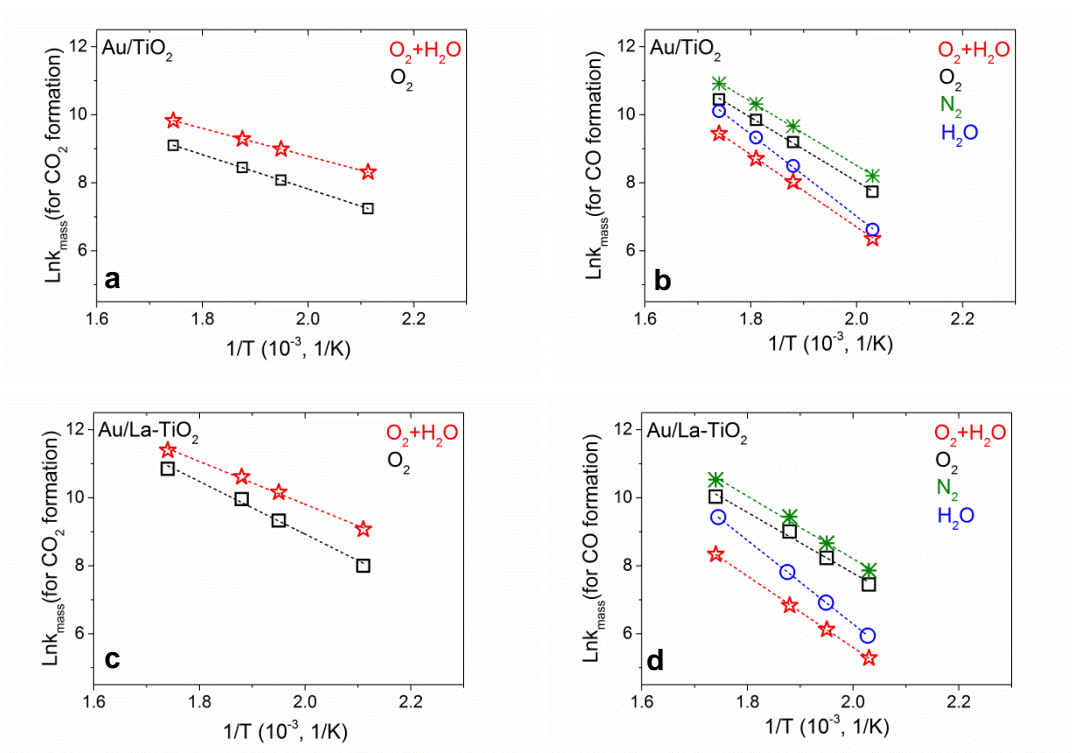


**Figure 6.19** Arrhenius plots for CO<sub>2</sub> (a,c) and CO (b,d) formation from formic acid decomposition on Au/La-TiO<sub>2</sub> (a,b) and Au/TiO<sub>2</sub> (c,d).



# Chapter 7

## Numerical modeling of hydroperoxyl-mediated oxidative dehydrogenation of formic acid

Based on:

Sridhar, M.; Mantzaras, J.; van Bokhoven, J. A.; Kröcher, O.; 2016, In preparation

M.S. contributions: experimental, analysis and write-up

J.M. contributions: numerical modelling

## 7.1 Introduction

Chapter 6 identified an oxidative-dehydrogenation (ODH) mechanism for formic acid conversion to carbon dioxide under SCR-relevant conditions. As a next step, it is highly interesting to numerically model this mechanism to test its applicability in predicting the observed catalytic performance. The surface perfectly stirred reactor (SPSR) has been a widely applied model to successfully simulate complex reaction networks involved in homogeneous fuel combustion as well as catalytic emission control.<sup>[232–242]</sup> For instance, Chaniotis and Poulikakos used an SPSR to validate the kinetic model describing the catalytic partial oxidation of methane in a fuel cell.<sup>[238]</sup> Mantzaras and coworkers performed sensitivity analysis in an SPSR to investigate the influence of surface chemistry on the oxidation of carbon monoxide/hydrogen/air mixtures<sup>[234]</sup> and on the gaseous combustion of methane/air<sup>[239]</sup> or ethane/air mixtures<sup>[236]</sup> over platinum, all under fuel-lean stoichiometries. SPSR offers simplified mixing while retaining full detailed chemistry. In the SPSR, the contents of the reactor are assumed to be nearly spatially uniform owing to high diffusion rates or forced turbulent mixing. Thus, the rate of conversion of reactants to products is considered to be controlled by chemical reaction rates (i.e reaction kinetics) and not by mixing processes. The crucial element of the SPSR is its underlying assumption that sufficient mixing allows it to be described well by spatially averaged or bulk properties. The main advantage of such an approximation lies in the relatively small computational demands of the mathematical model. In-depth information of the SPSR model can be found in the reference.<sup>[243]</sup> In this chapter, the validity of the proposed ODH mechanism is tested by comparing SPSR model predictions with the experiments on gold supported on lanthana–modified titania catalyst. Furthermore, an estimation of the relative coverages of the different reaction intermediates is provided and sensitivity analyses are performed to determine the dominant elementary steps controlling the conversion of reactants.

## 7.2 Experimental

*Catalyst synthesis and testing.* The preparation and testing of the titania-supported gold catalyst modified with lanthana can be found in Chapter 2. Concentrations of formic acid, oxygen, and water were varied in the range 227–1070 ppm, 0.1–3.0 vol %, and 0.5–1.30 vol%, respectively (Table 7.1). External and internal mass transfer limitations were ruled out under the investigated conditions.<sup>[208]</sup> The formulae used for the calculation of conversion, product selectivity and yield are described in our previous work.<sup>[208]</sup> The C–balance was closed within an accuracy of  $\pm 3\%$  by summing up carbon monoxide, carbon dioxide and formic acid. Temperature programmed oxidation and time on stream experiments revealed that no carbon deposition occurred on the catalysts.

*Mechanistic model.* The proposed mechanism for the ODH of formic acid under SCR-relevant conditions encompasses 16 reactions out of which 14 represent the forward and backward direction of seven fast and quasi-equilibrated elementary reactions (Chapter 6). The remaining two steps involve the slow and irreversible steps of hydrogen abstraction from the adsorbed formate with the aid of activated oxygen species. Table 7.2 lists the 16 surface reactions and the values for the Arrhenius pre-exponentials, temperature exponents and the activation energies.  $\text{HCOO}^*$ ,  $\text{HOO}^*$ ,  $\text{H}_2\text{O}^*$ ,  $\text{O}_2^*$ ,  $\text{O}^*$ ,  $\text{HO}^*$  and  $\text{H}^*$  describe the surface intermediates adsorbed on the active site '\*'. Coverage-dependent activation energies (COV) were introduced for the steps 9 and 10. This mechanistic scheme does not take into account the reactions concerning formic acid decomposition to carbon monoxide on titania and to carbon dioxide in the gas phase, because their contributions are very low.<sup>[208]</sup>

**Table 7.1** Experimental conditions.<sup>a</sup>

Case	Formic acid mol/mol	Oxygen mol/mol	Water mol/mol	Temperature (°C)
I	0.00065	0.1	0.05	160–300
II	0.000227–0.00107	0.1	0.05	200, 300
III	0.00065	0.025–0.03	0.05	200, 300
IV	0.00065	0.1	0.0049–0.013102	200, 300

<sup>a</sup> The feed was diluted with nitrogen to amount to a total flow of  $750 \text{ L h}^{-1}$ , contact time  $(W/F) = 2.4 \cdot 10^{-5} \text{ g s cm}^{-3}$ .

*Numerical model.* The numerical platform for the kinetic studies is the steady state SPSR.<sup>[243]</sup> The underlying assumption that perfect mixing of reactants in the SPSR ensures that the conversion of reactants to products is homogeneous in space and is completely determined by the chemical reaction rates, the reactor surface and the mass flow rate.<sup>[243]</sup> The salient features of this model include perfect mixing and spatially uniform temperatures and species compositions. In this zero-dimensional model, the inlet species undergo instantaneous homogeneous mixing upon reaction inside the reactor, such that only kinetic limitations are present.<sup>[243]</sup> Simulations are carried out at a fixed SPSR temperature (mimicking the present isothermal reactor experiments), thus negating solution of the energy equation. The gas-phase species governing equations for a steady state SPSR in the presence of catalytic and gas phase reactions are:

$$\dot{m}(Y_{k,OUT} - Y_{k,IN}) = V\dot{\omega}_k W_k + A\dot{s}_k W_k, \quad k = 1, 2, \dots, K_g, \quad (7.1)$$

where  $\dot{m}$  is the mass flow rate in the reactor in g/s,  $Y_{k,IN}$  and  $Y_{k,OUT}$  the mass fractions of the  $k$ -th gaseous species at the inlet and outlet, respectively,  $\dot{\omega}_k$  the volumetric molar production rate of  $k$ -th species via gaseous reactions in  $\text{mol}\cdot\text{cm}^{-3}\cdot\text{s}^{-1}$ ,  $\dot{s}_k$  the surface molar production rate of

$k$ -th species via catalytic reactions in  $\text{mol}\cdot\text{cm}^{-2}\cdot\text{s}^{-1}$ ,  $A$  and  $V$  the SPSR surface area ( $\text{cm}^2$ ) and volume ( $\text{cm}^3$ ), respectively,  $W_k$  the molecular weight of the  $k$ -th species in  $\text{g}\cdot\text{mol}^{-1}$ , and  $K_g$  the total number of gas phase species. In the present case  $K_g = 5$ , accounting for formic acid, oxygen, water, carbon dioxide and nitrogen. The gaseous reaction rates  $\dot{\omega}_k$  in Eq. 7.1 have quite small contributions at the present moderate temperatures and are thus neglected. The known variables are  $\dot{m}$ ,  $Y_{k,IN}$ ,  $A$ ,  $W_k$  and  $\dot{s}_k$ , where  $\dot{s}_k$  is calculated from Eq. 7.3.

**Table 7.2** Sequence of steps describing ODH of formic acid on Au/La-TiO<sub>2</sub> and their corresponding kinetic parameters.<sup>a</sup>

Step	Elementary steps	A (mol·cm·s)	B	E <sub>act</sub> (kJ mol <sup>-1</sup> )
1	$\text{H}_2\text{O} + * \rightarrow \text{H}_2\text{O}^*$	1.20E+18	0.0	52.0
2	$\text{H}_2\text{O}^* \rightarrow \text{H}_2\text{O} + *$	8.50E+14	0.0	110.0
3	$\text{O}_2 + * \rightarrow \text{O}_2^*$	1.04E+17	0.0	60.0
4	$\text{O}_2^* \rightarrow \text{O}_2 + *$	1.00E+15	0.0	120.0
5	$\text{H}_2\text{O}^* + \text{O}_2^* \rightarrow \text{HOO}^* + \text{HO}^*$	1.60E+21	0.0	50.0
6	$\text{HOO}^* + \text{HO}^* \rightarrow \text{H}_2\text{O}^* + \text{O}_2^*$	1.20E+22	0.0	50.0
7	$\text{HCOOH} + \text{HO}^* \rightarrow \text{HCOO}^* + \text{H}_2\text{O}$	1.42E+26	0.0	38.0
8	$\text{HCOO}^* + \text{H}_2\text{O} \rightarrow \text{HCOOH} + \text{HO}^*$	5.25E+18	0.0	30.0
9	$\text{HCOO}^* + \text{HOO}^* \rightarrow \text{CO}_2 + \text{H}_2\text{O} + * + \text{O}^*$	1.70E+13	0.0	$32.3 + 3.647 \cdot \theta_{\text{HCOO}^*}$
10	$\text{HCOO}^* + \text{O}^* \rightarrow \text{CO}_2 + \text{HO}^* + *$	2.50E+20	0.0	$25.8 + 1.459 \cdot \theta_{\text{HCOO}^*}$
11	$2\text{HO}^* \rightarrow \text{H}_2\text{O}^* + \text{O}^*$	2.00E+20	0.0	40.0
12	$\text{H}_2\text{O}^* + \text{O}^* \rightarrow 2\text{HO}^*$	2.00E+20	0.0	60.0
13	$\text{H}_2\text{O}^* + * \rightarrow \text{HO}^* + \text{H}^*$	1.55E+22	0.0	40.0
14	$\text{HO}^* + \text{H}^* \rightarrow \text{H}_2\text{O}^* + *$	2.40E+21	0.0	30.0
15	$\text{H}^* + \text{O}^* \rightleftharpoons \text{HO}^* + *$	2.30E+22	0.0	40.0
16	$\text{HO}^* + * \rightarrow \text{H}^* + \text{O}^*$	2000E+22	0.0	40.0

<sup>a</sup> The rate constant ( $k$ ) is given by  $k = A \times T^b \times e^{-\frac{E_{act}}{RT}}$ .  $\theta_{\text{HCOO}^*}$  is the surface coverage of adsorbed formate ( $\text{HCOO}^*$ ) species. The kinetic parameters of steps 1-4 have been adjusted based on values from references [244–246].

The coverage equations for the surface species are given by:

$$\frac{\partial \theta_m}{\partial t} = \sigma_m \frac{\dot{s}_m}{\Gamma}, \quad m = 1, \dots, K_s \quad (7.2)$$

The left-side in Eq. 7.2 is not a true transient term and is only introduced to facilitate numerical convergence to steady state; therein, limited time integrations are performed to bring the solution within the convergence domain of the employed Newton solver.<sup>[243]</sup> In Eq. 7.2,  $\sigma_m$  is the site occupancy (number of sites occupied by the  $m$ -th surface species),  $\Gamma$  the surface site

density,  $\theta_m$  the surface coverage of the  $m$ -th species and  $K_s$  the total number of surface species. In the present case  $K_s = 8$ , which accounts for  $\text{HCOO}^*$ ,  $\text{HO}_2^*$ ,  $\text{HOO}^*$ ,  $\text{O}_2^*$ ,  $\text{O}^*$ ,  $\text{HO}^*$ ,  $\text{H}^*$  and  $*$  (the latter denotes the available free sites). The value of  $\sigma_m$  is one since each surface species occupy only one site. Since the value of  $\Gamma$  for gold is unknown, the corresponding value for platinum<sup>[247]</sup> (equal to  $2.7 \cdot 10^{-9}$  mol  $\text{cm}^{-2}$ ) is employed. The surface reaction rates are given by:

$$\dot{s}_m = \sum_{\ell=1}^{N_s} \nu_{m\ell} k_{f\ell} \prod_{j=1}^{K_g+K_s} C_j^{\nu_{j\ell}}, \quad (7.3)$$

with  $N_s$  the number of surface reactions and  $\nu_{m\ell}$  the stoichiometric coefficient of species  $m$  in surface reaction  $\lambda$ . For the gas phase species ( $j = 1, 2, \dots, K_g$ ) the concentrations in Eq. 7.3 are  $C_j = \rho Y_j / W_j$  (mol/ $\text{cm}^3$ ), while for the surface species ( $j = 1, 2, \dots, K_s$ ) the surface concentrations are  $C_j = \Gamma \theta_j / \sigma_j$  (mol/ $\text{cm}^2$ ). The reaction rate coefficients  $k_{f\ell}$  in Eq. 7.3 are:

$$k_{f\ell} = A_\ell T^{\beta_\ell} \exp\left(\frac{-E_\ell}{RT}\right) \prod_{m=1}^{K_s} \theta_i^{\mu_{m\ell}} \exp\left(\frac{\varepsilon_{m\ell} \theta_m}{RT}\right), \quad (7.4)$$

with  $A_\ell$ ,  $\beta_\ell$  and  $E_\ell$  the pre-exponential, temperature exponent, and activation energy of surface reaction  $\lambda$ , respectively. The parameters  $\varepsilon_{m\ell}$  and  $\mu_{m\ell}$  introduce coverage dependencies on the reaction rate coefficient, which account for variation in the adsorption binding states due to changing surface coverage.<sup>[248]</sup> In the present mechanism  $\mu_{m\ell} = 0$  for all surface reactions, while  $\varepsilon_{m\ell}$  is non-zero only for reactions  $\lambda = 9$  and 10 for the surface species  $\text{HCOO}^*$ .

Equations 7.1 and 7.2 constitute a system of algebraic non-linear equations, solved by a modified Newton method for the unknown gas-phase species mass fractions  $Y_{k,OUT}$  and surface coverages  $\Theta_m$ <sup>[243]</sup>  $Y_{k,OUT}$  in turn gives the conversion value. In Newton's method, a sequence of iterations or approximate solutions is determined such that they approach the true solution. For the sake of brevity, these approximate solution vector is called as  $\varphi$ . When an arbitrary  $\varphi$  is substituted into the governing equation, the equation generally does not equal zero unless  $\varphi$  represents the true solution; the equation equals a residual vector  $F$ . The objective then is to find  $\varphi$  such that  $F(\varphi) = 0$ . A more detailed overview of this approach can be found in the reference.<sup>[243]</sup>

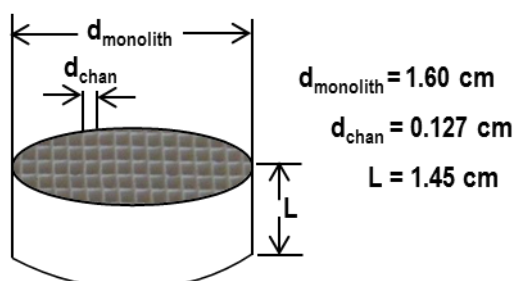
The sensitivity coefficients ( $SC_{i,k}$ ) for the conversion of species  $i$  = formic acid, oxygen and water on reaction  $k$  were calculated as follows:

$$SC_{i,k} = \frac{A}{C_{i,A_k}} \frac{C_{i,A_k+\delta A_k} - C_{i,A_k}}{\delta A_k} \quad (7.5)$$

where  $A_k$  is the pre-exponential of the  $k$ -th reaction,  $\delta A_k$  the change in the pre-exponential (always 2% increase of  $A_k$ ),  $C_{i,A_k}$  is the conversion of species  $i$  when the pre-exponential is  $A_k$ , and  $C_{i,A+\delta A_k}$  the conversion of species  $i$  when the pre-exponential is  $A+\delta A_k$ .

The SPSR simulates a single channel of the honeycomb reactor used in the experiments. The geometrical parameters of a single honeycomb channel yield an area  $A = 0.5786 \text{ cm}^2$ , while the mass flow rate  $\dot{m}$  in the SPSR is calculated by dividing the total honeycomb mass flow rate by the number of channels (159). Geometrical and flow properties of each channel are as follows:

- Honeycomb type: 400 cpsi
- Number of cells in honeycomb:  $400 \cdot (16/25.4)^2 = 158.7$  cells
- Total flow rate is 750 L/h at STP =  $208.33 \text{ cm}^3/\text{s}$  at STP. For each channel, the flow rate is:  $Q_{\text{chan}} = 1.313 \text{ cm}^3 \text{ s}^{-1}$  at STP.
- Density of feed mixture (mol: 0.1  $\text{O}_2$ , 0.05  $\text{H}_2\text{O}$ , 0.85  $\text{N}_2$ ) at STP is  $1.23 \times 10^{-3} \text{ g/cm}^3$ , such that the mass flow rate in each channel is in the range  $0.001680 \leq \dot{m} \leq 0.001682 \text{ g/s}$
- The equivalent diameter of each channel is  $d_{\text{chan}} = 0.127 \text{ cm}$ , such that the volume of each channel is  $V_{\text{chan}} = (\pi d_{\text{chan}}^2/4)L = 0.018368 \text{ cm}^3$ .
- Area of channel is  $A_{\text{chan}} = \pi d_{\text{chan}} L = 0.5786 \text{ cm}^2$

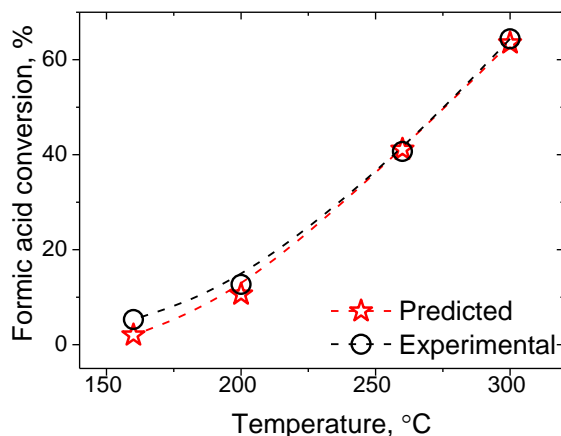


**Scheme 7.1** Sketch of a model monolith and its dimensions.

## 7.3 Results and Discussion

### 7.3.1 Case I: Effect of temperature at fixed feed composition

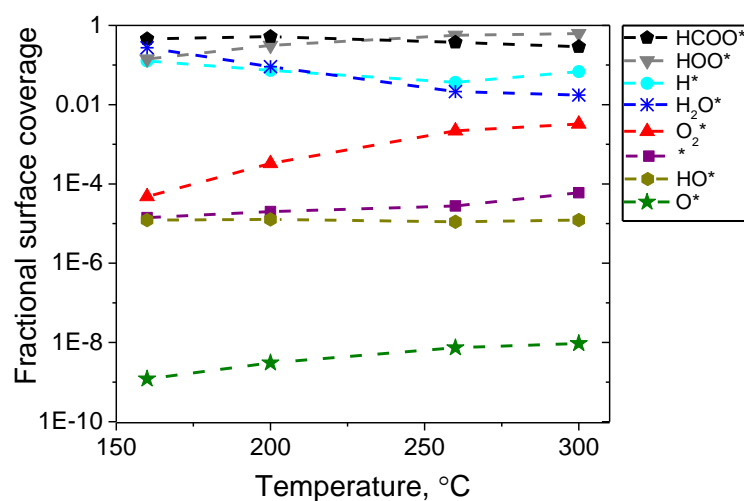
Figure 7.1 compares model predictions with the experimental formic acid conversions for Case 1 (Table 7.1). The catalyst exhibited typical Arrhenius behavior wherein formic acid conversion increased with increasing temperature. The proposed mechanistic model achieved good agreement between the experimental and predicted conversions. The small deviation in the predictions at low temperatures may be inherent to the homogeneous contribution<sup>[25]</sup> that is neglected in the proposed heterogeneous scheme.



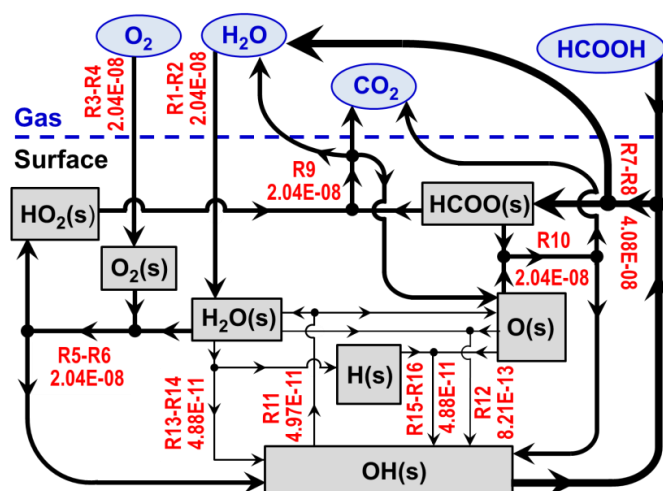
**Figure 7.1** Comparisons of predicted and measured formic acid conversions as a function of temperature for Case I, Table 7.1.

Figure 7.2 depicts surface coverages of the eight reaction intermediates involved in the ODH of formic acid as a function of reaction temperature. An increase in temperature entailed an increase in the surface coverages of molecularly as well as atomically adsorbed oxygen species. This agrees well with the strongly activated nature of these reactions.<sup>[116,249–251]</sup> Mantzaras and coworkers reported a similar behavior, wherein the coverage of the atomically adsorbed oxygen species increased monotonically with increasing wall temperature during platinum-catalyzed carbon monoxide oxidation in a channel-flow reactor.<sup>[234]</sup> Formates and hydroperoxyls which dominate the surface at all temperatures followed inverse trends. The lower formate coverages at higher temperature can stem from two phenomena: (a) increased availability of activated oxygen species which promote more rapid consumption of formates to produce carbon dioxide, (b) higher formic acid desorption rates. Complementary to the fall in the formate coverages, the proportion of free active sites experienced a slight increase with increasing temperature. Such a trend is in line with the in situ DRIFTS results reported in Chapters 5 and 6, which showed lower steady state formate coverages at higher temperature. The formation of hydroperoxyls (step 5, Table 7.2) is endothermic<sup>[229]</sup> and hence favored at higher temperatures as evident from an increased coverage of these species. The reduced coverage of adsorbed hydrogen species with increasing temperature up to 260 °C could arise from increased rates of reaction with atomically adsorbed oxygen species to form hydroxyl which in turn could scavenge more adsorbed hydrogen to form water (Figure 7.5). The adsorption-desorption equilibrium for water shifts towards desorption with increasing temperature leading to a decreasing trend in the water coverage.<sup>[252]</sup> Hydroxyls, which are involved in multiple reaction steps, undergo very little change with varying temperature. The low site occupancy of these species is in agreement with their high degree of depletion observed using in situ DRIFTS in Chapter 6.

Interestingly, the model predicts relatively higher coverages of hydroperoxy species than formates at higher temperature (300 °C) even though, formic orders were still negative and the oxygen/water orders were positive (Chapter 6). While, there is a small probability that the active sites are only 'kinetically saturated'<sup>[253]</sup> by formates and that they do not necessarily physically represent the majority of surface species on the active sites, it is also important to bear in mind that the predicted trends in the surface coverages may not represent the reality since the kinetic parameters of the mechanistic scheme offer much room to maneuver in terms of the various kinetic parameters to be optimized (Table 7.2). Within the timeframe of this study, the current predictions make up the best match to the experiments.



**Figure 7.2** Predicted surface coverages as a function of temperature for Case I, Table 7.1.



**Figure 7.3** Reaction flux diagram for case I (Table 7.1) at 300 °C. Thicker lines (not to scale) denote dominant reactions.

Figure 7.3 presents a reaction flux diagram for Case I (Table 7.1) computed at 300 °C. The initiating steps were molecular adsorption of oxygen (net of R3-R4), water (net of R1-R2) and

the Eley–Rideal–type reaction of formic acid with adsorbed hydroxyl to form surface formate (net of R7-R8). The main surface steps were the Langmuir–Hinshelwood type reactions of adsorbed oxygen and water to form the hydroperoxyl (net of R5-R6), which in turn reacted with adsorbed formate to form carbon dioxide and an atomically adsorbed oxygen species (R9). The latter reacted with another formate to form another carbon dioxide molecule and an adsorbed hydroxyl (R10). Other flux analyses indicated that the dominant pathways remained essentially the same at a lower temperature (200 °C, not shown) except that the net rates were ~an order of magnitude lower. The net rate of formate formation was about twice as high as that of oxygen and water adsorption, indicating that that former step is more favored leading to high formate coverages (Figure 7.2). Consequently, the catalytic rate was controlled by the hydroperoxyl–assisted decomposition of abundantly present formates. Similar trends were observed for CO oxidation on a platinum surface, where the high sticking coefficient of CO dominated the slower oxygen adsorption and activation steps and resulted in lower catalytic rates despite the abundance of oxygen in the gas phase.<sup>[234]</sup>

Figures 7.4 present the sensitivity coefficients (see Eq. 7.5) for the conversion of formic acid, oxygen and water at 300 °C and 200 °C. A positive coefficient indicates that a given step promotes the species conversion and, conversely, a negative coefficient signifies an inhibiting effect of the step. The three reactants showed similar trends in sensitivities, indicating that formic acid, oxygen and water react with one another in a common pathway to form carbon dioxide. At 300 °C, the rate–determining–step of hydroperoxyl–mediated dehydrogenation of formate to carbon dioxide and water (step 9, Table 7.2) predominantly controlled the conversion of all reactants (Figure 7.4, top row). However, a slightly different picture unfolded at 200 °C (Figure 7.4, bottom row). The high formate coverages at the low temperature (Figure 7.2) inhibited further consumption of the reactants, which was reflected in the form of highly negative coefficients for the step of formate formation (step 7, Table 7.2). Contrarily, formate desorption to molecular gas phase formic acid (step 8, Table 7.2), which frees up active sites, promoted the conversion of all reactant species. This is consistent with the observations of Zheng et al.<sup>[234]</sup> on platinum on which carbon monoxide adsorption was found to inhibit its own and the oxygen consumption for surface temperatures below 280 °C. Thus, the proposed single–site mechanism correctly describes the effects of competitive adsorption between formic acid, oxygen and water, where the rate of reactant consumption is impeded by the poisoning of active sites by formates.

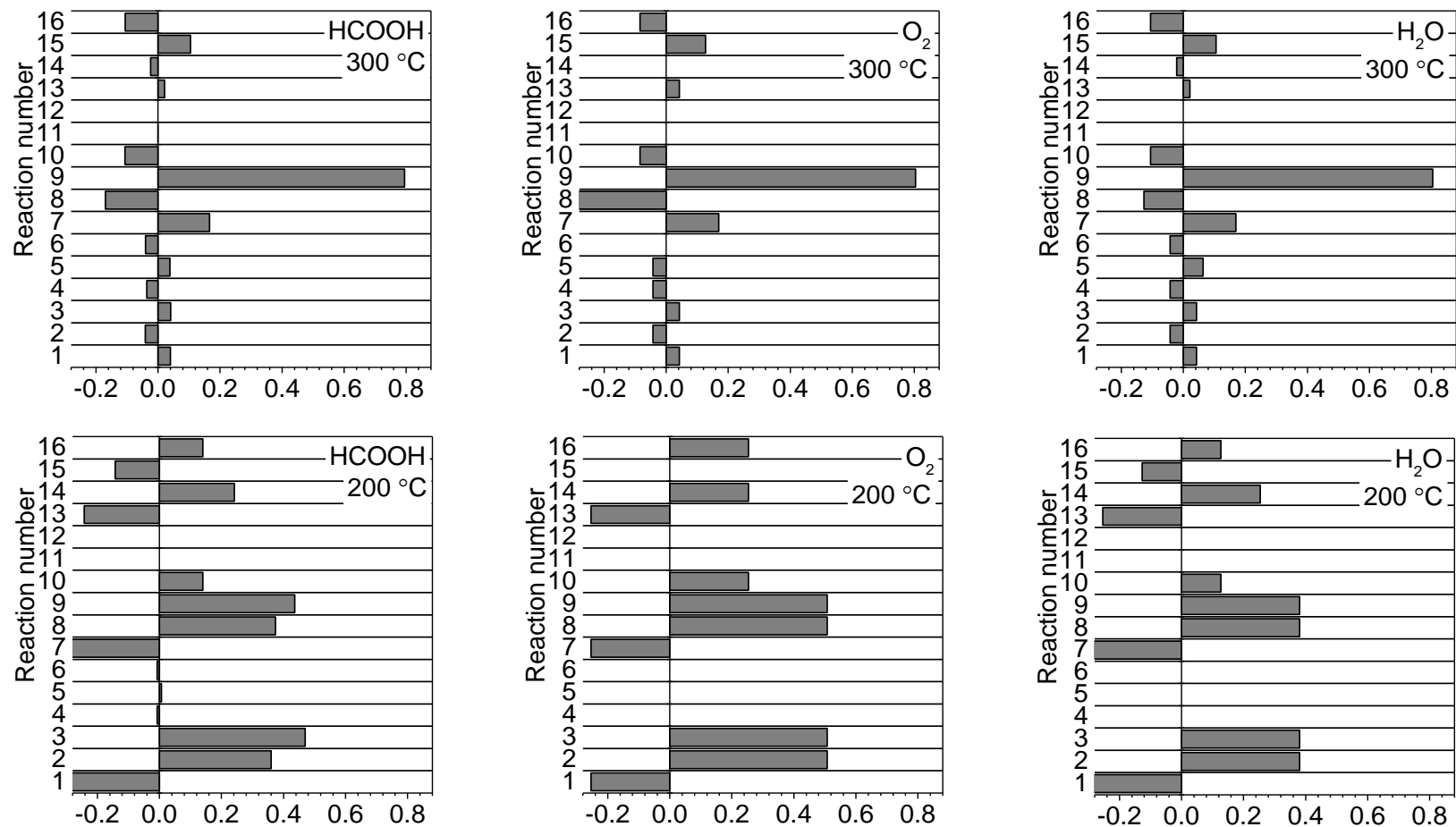


**Figure 7.4** Sensitivity analysis for conversion of formic acid, oxygen and water, in a surface perfectly stirred reactor (SPSR) for case I in Table 7.1 at 300 °C and 200 °C. Reaction numbering follows Table 7.2.

Water and oxygen adsorption exerted opposing effects, wherein the former (step 1, Table 7.2) inhibited and the latter (step 3, Table 7.2) promoted the conversion of reactants. Furthermore, water dissociation to adsorbed hydroxyl and hydrogen (step 13, Table 7.2) suppressed the conversion. This can be explained by considering that an increasing hydroxyl concentration may further promote the Eley-Rideal reaction with formic acid to form surface formate (step 7, Table 7.2), which in turn inhibits the conversion.

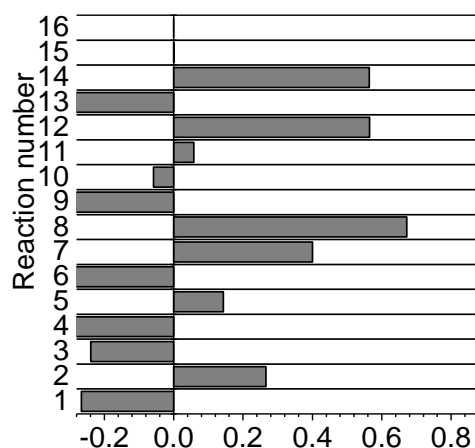


**Figure 7.5** Sensitivity analysis for  $H^*$  in a surface perfectly stirred reactor (SPSR) for oxygen concentration of 0.01 mol/mol at 300 °C. Reaction numbering follows Table 7.2.

### 7.3.2 Effect of feed composition on the catalytic activity and the relative surface coverages of intermediates

#### 7.3.2.1 Case II: Varying formic acid concentration

Figure 7.6 plots the trends in the measured and predicted formic acid conversion as a function of gas-phase formic acid concentration at 200 °C and 300 °C. By imposing coverage-dependent activation energies of the rate determining steps, the proposed mechanism was able to essentially capture the negative trend in conversion with increasing formic acid concentration. The coverage-dependent activation energies are supported by the experimentally observed increase in the activation energy with increasing formate coverage on the active sites.<sup>[208]</sup> In Chapter 6, the inhibitory effect on conversion was attributed to the strong surface poisoning by formates, which in turn reduced the availability of active sites for the adsorption and formation of the activated oxygen species necessary for formate decomposition.

The results from the numerical simulations indicate that there is room for improvement since there exists a noticeable difference from the measured values at 300 °C. One possible explanation for the deviation at 300 °C is that the proposed scheme considers only one type of active sites that can adsorb formic-derived species (formates) and produce carbon dioxide. However, as shown in Chapters 5 and 6, other sites exist on the support away from the gold, which deprotonate formic acid and decompose the formate to carbon monoxide. These carbon

monoxide-producing sites exhibited formic acid orders ranging between 0.0 and 0.5 suggesting that they harbor formate coverages equal to lower than the saturation coverage. Since this pathway is not integrated into the mechanistic model, higher formate coverages on the carbon dioxide-producing active sites are anticipated by the mechanistic model at a given formic acid concentration than that existing in reality. Hence a higher degree of surface poisoning by formates can account for lower predicted formic acid conversion to carbon dioxide. Such an explanation is in line with the close agreement observed at 200 °C in Figure 7.6. This is because, formate coverages at the carbon monoxide producing sites on the support were negligibly low at this temperature owing to competitive adsorption and site blockage by water as shown in Chapters 5 and 6. Thus at low temperature, the actual formate coverages on the carbon dioxide producing active sites can be expected to be close to those considered by the mechanistic scheme.

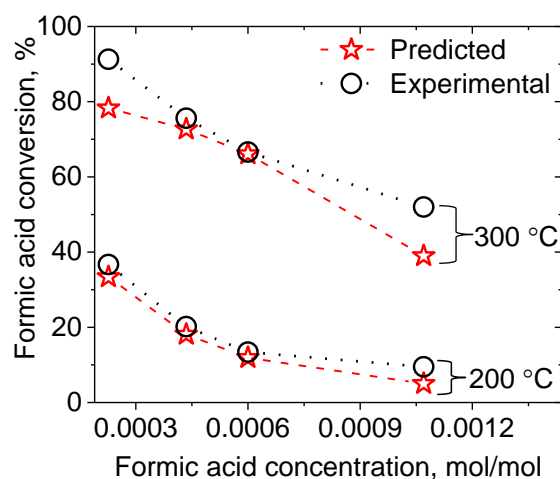


**Figure 7.6** Simulated and measured trends in formic acid conversion as a function of formic acid concentration (Case II, Table 7.1) at 200 °C and 300 °C.

Figures 7.7 (left and right) depict the surface species coverages determined at different formic acid concentrations at 300 °C and 200 °C. Concordant with the previously observed formic acid order change to more negative values when determined at a higher formic acid concentration regime,<sup>[208]</sup> the formate coverages increased with increasing gas phase formic acid concentration. This occurred at the expense of the molecularly adsorbed and activated oxygen species ( $O_2^*$ ,  $HOO^*$  and  $O^*$ ), which decreased with increasing formic acid concentrations. Such a reciprocal relationship between the formates and the activated oxygen species is characteristic for the competitive adsorption of these species on the active site. The relatively high coverage of hydroperoxy species at low formic acid concentrations is supported by experiments showing lower oxygen orders. The decreased availability of the activated oxygen species causes the lower conversion values at higher gas phase formic acid concentrations (Figure 7.6). The free sites (\*) underwent little change suggesting that a dynamic trade-off results from an increased formate formation and site regeneration upon formate decomposition.

The coverage of hydroxyls experienced only a modest decrease owing to competitive reactions contributing to their consumption and production (steps 5 to 8 and 10 to 16, Table 7.2). Coverage of adsorbed water decreased only marginally suggesting that it is not substantially displaced by formic acid. This is because formate formation (step 7, Table 7.2) consumes hydroxyls produced from water (steps 5 and 13, Table 7.2) as well as generates water that can be re-adsorbed on the active site.

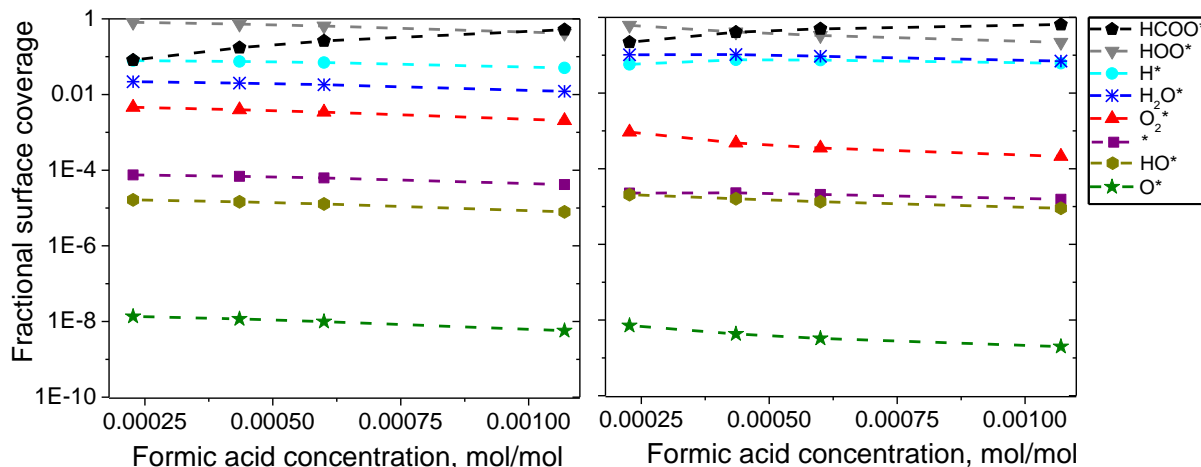


**Figure 7.7** Predicted surface coverages as a function of formic acid concentration (Case II, Table 7.1) at 300 °C (left) and 200 °C (right).

### 7.3.2.2 Case III: Varying oxygen concentration

Figure 7.8 plots the influence of oxygen on the experimentally and predicted formic acid conversion at 200 °C and 300 °C. Chapter 5 demonstrated that oxygen is indispensable for carbon dioxide production, without which gold does not catalyze formic acid decomposition. Additionally positive orders in oxygen dictate an increasing trend in conversion with increasing gas phase oxygen concentration.

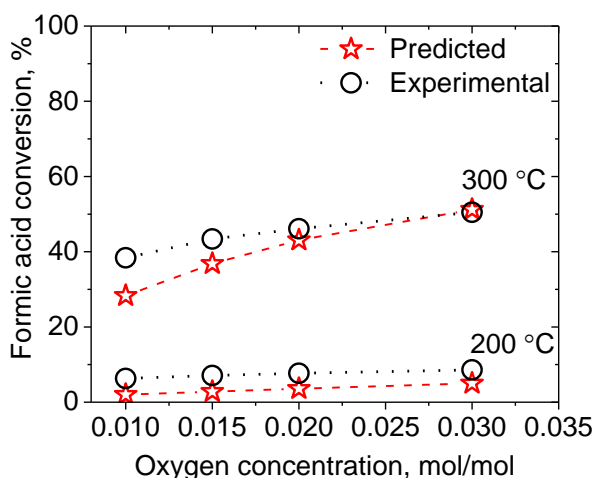


**Figure 7.8** Simulated and measured trends in formic acid conversion as a function of oxygen concentration (Case III, Table 7.1) at 200 °C and 300 °C.

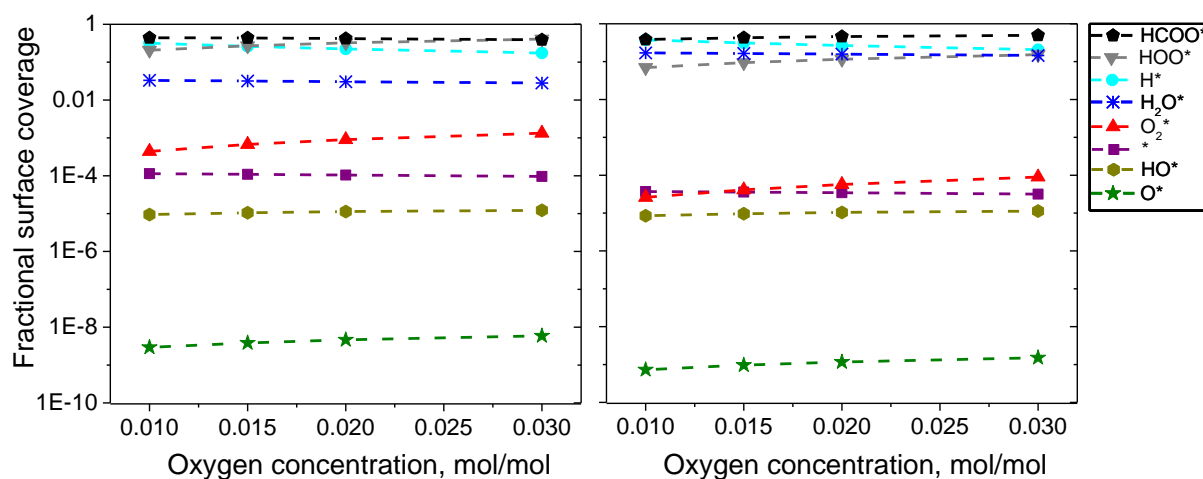


**Figure 7.9** Predicted surface coverages as a function of oxygen concentration (Case III, Table 7.1) at 300 °C (left) and 200 °C (right).

Though the predicted conversions increased, they lagged behind the experimental values at lower oxygen concentrations (1 and 1.5%). Such a deviation may arise from the intrinsic design of the experimental setup. In order to avoid pulsations in the water concentration, the experimental setup employed a water dosing system based on the catalytic oxidation of hydrogen by a slight stoichiometric excess of oxygen.<sup>[254]</sup> Hence, the higher measured conversion values at lower oxygen concentration  $\leq 0.02\%$  could be an artefact derived from the presence of a small excess of oxygen compared to the set value. At 200 °C, the observed difference ( $\leq 4\%$ ) can be partly accounted by the contribution of homogenous gas phase formic acid decomposition that manifest at low conversions.<sup>[25]</sup>

Figures 7.9 (left and right) present the fractional surface coverages calculated as a function of oxygen concentration at 300 °C and 200 °C. An increase in the oxygen concentration increased the oxygen-derived surface species (O<sub>2</sub>\*, HOO\* and O\*). The formate coverage remained practically unaffected with changing oxygen coverage. This was experimentally verified by determining the formic acid orders at different oxygen concentrations, which essentially remained constant irrespective of the oxygen concentrations. Such a trend can be explained by taking into account the ‘reservoir-effect’ reported in Chapter 6. The dynamic equilibrium between the adsorbed formates on titania and on the active sites (\*) can rapidly replenish the formates as they are increasingly decomposed with rising oxygen concentrations, consequently sustaining constant formate coverage at steady state. High coverage of adsorbed hydrogen may result from direct dehydrogenation of the C-H bond of formates on gold-related active sites (\*) at very low surface concentrations of activated oxygen species.<sup>[123]</sup> However, high Au-H bond energy disfavors their recombination to dihydrogen.<sup>[51,103]</sup> With increasing oxygen concentrations, adsorbed hydrogen are readily scavenged<sup>[122,123,226,231]</sup> (step 15, Table 7.2) leading to a rapid decrease in their coverage.

### 7.3.2.3 Case IV: Varying water concentration

Figure 7.10 depicts the influence of water concentration on the predicted and measured formic acid conversions at 200 °C and 300 °C. In Chapter 6, the mechanism elicits higher water orders (~0.6) compared to the experimentally determined value (0.1–0.3). Such a discrepancy can be explained by considering two phenomena. Since, water is also a product, ODH of formic acid can be regarded as being autocatalytic. Additionally, formic acid dehydration reaction taking place independently and simultaneously on titania rises the local water concentrations near the gold-related active sites (\*) producing carbon dioxide. Considering that water is not a stoichiometric reactant and it only acts as a co-catalyst, very small concentrations should be sufficient to realize the water-induced promotional effect. In fact, a significant rate enhancement for carbon monoxide oxidation on Au/TiO<sub>2</sub> was realized at ultralow water concentrations between 0.1–3000 ppm.<sup>[255,256]</sup> Furthermore, the promotional effect of water is proposed to depend on the amount of adsorbed water on the catalyst rather than on the gas-phase water concentration. Hence in our study, it can be hypothesized that the slower response and faster stabilization of the measured formic acid conversion reflects the higher actual water coverages that exceed the water coverages predicted by the idealistic model at identical gas phase water concentrations.

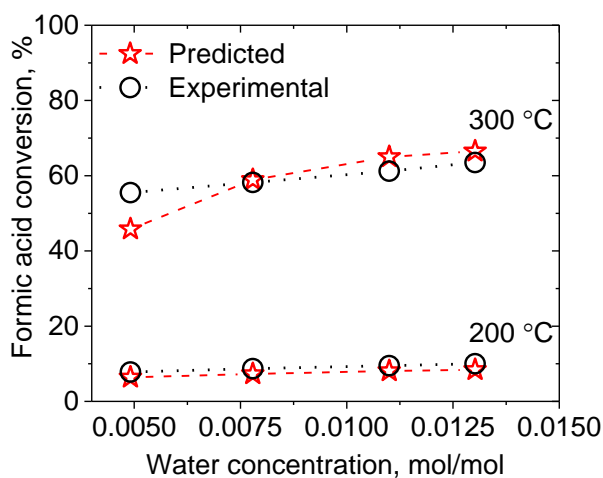


**Figure 7.10** Simulated and measured trends in formic acid conversion as a function of water concentration (Case IV, Table 7.1) at 200 °C and 300 °C.

Figures 7.11 (left and right) illustrate the trends in the predicted fractional surface coverages derived from increasing water concentration at 300 °C and 200 °C. Reasonably, the surface adsorbed water increased with increasing water concentration. This was accompanied by an increase in the hydroperoxyls and hydroxyls by approximately one order of magnitude. Such an increase is consistent with the findings from Chapter 6 showing the critical role of water in the generation of the active hydroperoxyls that are critical for formate decomposition in the RDS. Concomitantly, the formate coverage was reduced. Such a decrease can be triggered by two factors: increased consumption owing to increased availability of activated oxygen species

and/or displacement of formates by water. In situ DRIFTS study of formic acid adsorption under differential feed conditions in Chapter 6 revealed that, while formates adsorbing on bare titania were prone to non-reactive desorption, the formates on the gold catalyst displayed significantly higher stability. Hence, it can be deduced that the decrease in the formate coverage with increasing water concentration occurs due to accelerated rate of decomposition to form carbon dioxide.

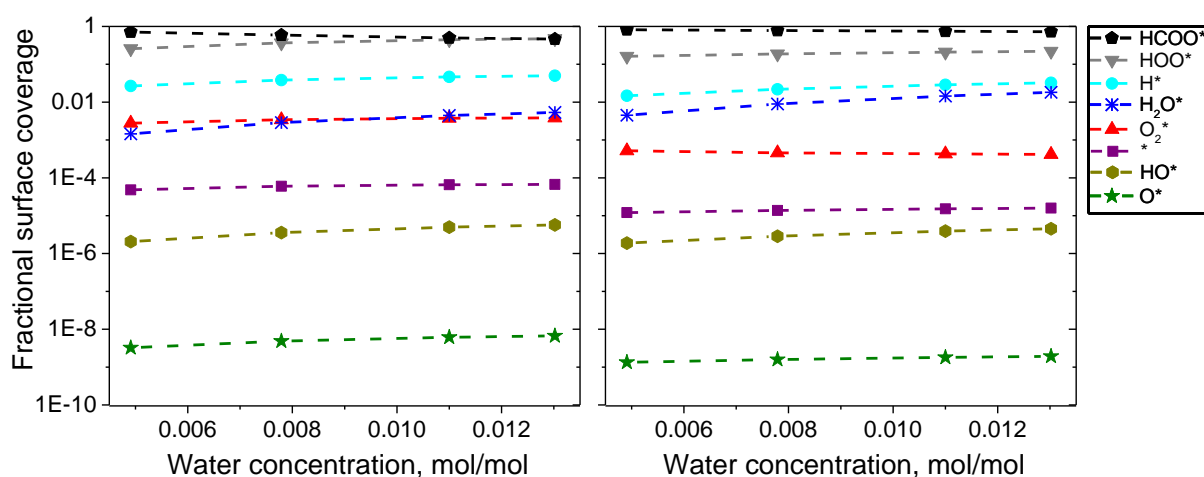


**Figure 7.11** Predicted surface coverages as a function of water concentration (Case III, Table 7.1) at 300 °C (left) and 200 °C (right).

#### 7.4 Conclusions

In this chapter, numerical modeling of the proposed ODH mechanism yielded satisfactory agreement with the experiments. The inhibiting effect of increasing formate coverage on the catalytic rates was accurately described by the model. On the other hand, adsorbed oxygen and water, which remained well below saturation coverages, promoted the rates by providing the active hydroperoxyls required for formate decomposition in the rate-determining step. The trends in fractional surface coverages, calculated using the surface perfectly stirred reactor model, were in agreement with previously reported kinetic and spectroscopic measurements. The good convergence between the model predictions and experiments might be further improved by integrating side processes related to carbon monoxide formation and homogeneous gas phase formic acid decomposition to carbon dioxide in the mechanistic scheme.

# Chapter 8

## From mechanism to catalyst design: Fine tuning the basicity for formic acid decomposition on Au/TiO<sub>2</sub>

Based on:

Sridhar, M.; Brose, S.; Siewert, D.; Ferri, D.; van Bokhoven, J. A.; Kröcher, O. 2016, In preparation.

M.S. contributions: kinetic measurements, analysis and write-up

S.B. contributions: experimental

## 8.1 Introduction

In this Chapter, the promotional effect of lanthanum-modification on the formic acid decomposition activity is optimized. Here, the effect of two preparation methods on the structure and activity of gold supported on lanthanum-modified titania catalysts is evaluated and the lanthanum content is systematically varied to identify the optimum of surface structure that leads to increased activity. By wet-impregnation, the desired amount of lanthana is precipitated on the surface of anatase titania (commercial DT51) while, by coprecipitation, titania and lanthana are precipitated together which yields a more intimate contact between the two components.

## 8.2 Experimental

The wet-impregnated and coprecipitated lanthanum-modified titania supports were synthesized in accordance with previously published procedures<sup>[134,135]</sup> as described in Chapter 2. The procedure for the synthesis of the gold catalysts and their testing is provided in Chapter 2. The gold catalysts prepared using wet-impregnated and coprecipitated supports will be henceforth referred to as AuXLT-WI and AuXLT-CP, respectively, where X denotes the weight loading of lanthana (wt%). The commercial anatase (DT51) and the pure lanthana supported catalysts are designated as AuT and AuL, respectively. The titania supported catalyst prepared from metatitanic acid will be referred to as AuT-MA. The catalysts were analyzed by nitrogen physisorption, XRD, STEM, XPS, ICP-OES and in situ formic acid and carbon dioxide adsorption following procedures presented in Chapter 2.

## 8.3 Results and Discussion

### 8.3.1 Catalyst characterization

Table 8.1 lists the theoretical lanthanum dispersion capacity (La atoms nm<sup>-2</sup>) of all materials calculated on the basis of a simple close-packed monolayer model describing the spontaneous dispersion of oxides and salts on the surfaces.<sup>[257]</sup> This model assumes that the dopant anions (O<sup>2-</sup>) form a close-packed layer on the support surface while the dopant cations (La<sup>3+</sup>) occupy the interstices. The ratio of theoretical lanthanum coverages of wet-impregnated and coprecipitated catalysts at a given lanthana loading ( $[La_{WI}/La_{CP}]_T$ ) is mostly larger than one suggesting that wet-impregnation generates higher lanthanum coverages compared to coprecipitation.

Figures 8.1 a and b present the XRD patterns of selected catalysts prepared by wet-impregnation and coprecipitation, respectively. The supports and the catalysts exhibited identical reflections originating primarily from the anatase phase; the very low loading (~0.5 wt%) and the high dispersion render the detection of gold nearly impossible.<sup>[258-260]</sup> Irrespective of the synthesis method, increasing lanthana content resulted in a gradual decrease in the intensity and a broadening of the anatase reflections. This is in agreement with the lanthanum-

induced decrease in anatase crystallite size.<sup>[261–266]</sup> With increasing lanthana loading, the anatase peaks slightly shifted towards higher  $2\theta$  values indicating a decrease of the lattice parameter,<sup>[267,268]</sup> which was more pronounced in the case of the coprecipitated catalysts. The large difference in the sizes of La<sup>3+</sup> (0.115 nm) and Ti<sup>4+</sup> (0.068 nm) prevents the La<sup>3+</sup> from entering the lattice structure of titania; however, at the interface, a partial substitution of lanthanum atoms in the lanthana lattice by titanium atoms may occur, resulting in the formation of a Ti-O-La bond.<sup>[268,269]</sup> The resulting charge deficiency can be compensated by the formation of surface hydroxyls (Figure 8.2). Mixed lanthanum-titanium phases of the form La<sub>2</sub>Ti<sub>2</sub>O<sub>7</sub><sup>[270,271]</sup> were present in the XRD patterns of the coprecipitated catalysts with lanthana loadings in the range  $50 \leq X \leq 85$  wt%. Comparison of the broad feature in the  $2\theta$  range of 25–33° in AuXLT-WI ( $X > 29$  wt%) with the peaks in the corresponding region of AuL indicates that the lanthanum phases in the wet-impregnated catalysts are present in amorphous and/or well-dispersed form. However, in the case of the coprecipitated catalysts, reflections indexed to lanthana and lanthanum hydroxide become evident for 85 wt% lanthana loading.<sup>[272,273]</sup> Lanthanum carbonates could not be identified in agreement with their high temperature of formation.<sup>[274,275]</sup>

**Table 8.1** Lanthana coverages computed on the basis of close-packed monolayer model.<sup>[257,270]</sup>

Lanthana loading (wt%)	Theoretical dispersion capacity <sup>a</sup> (La nm <sup>-2</sup> )		[La <sub>WI</sub> /La <sub>CP</sub> ] <sub>T</sub> <sup>b</sup>
	Coprecipitated	Wet-impregnated	
2.3	1.1	1.3	1.2
5	2.3	2.7	1.2
8	3.3	4.4	1.3
11	4.0	6.3	1.6
15	5.8	9.4	1.6
29	13.8	26.8	1.9
50	44.0	68.5	1.6
70	78.9	103.5	1.3

<sup>a</sup> Assumes a simple close-packed monolayer model.<sup>[257]</sup>

<sup>b</sup> [La<sub>WI</sub>/La<sub>CP</sub>]<sub>T</sub> is the ratio of the theoretical lanthanum dispersion capacity of the wet-impregnated catalyst to that of the coprecipitated catalyst at a given lanthanum loading.

Figure 8.3 shows the dependence of the anatase crystallite size on the lanthana content. With the introduction of only 2.3 wt% lanthana, which is equivalent to  $\sim 1$  La nm<sup>-2</sup> (Table 8.1), the impregnated catalysts exhibited 28% reduction in crystallite size from 25 nm to  $\sim 18$  nm. Further addition of lanthana did not induce significant reduction and the anatase crystallite size stabilized at  $\sim 14$  nm at 29 wt% lanthana content.

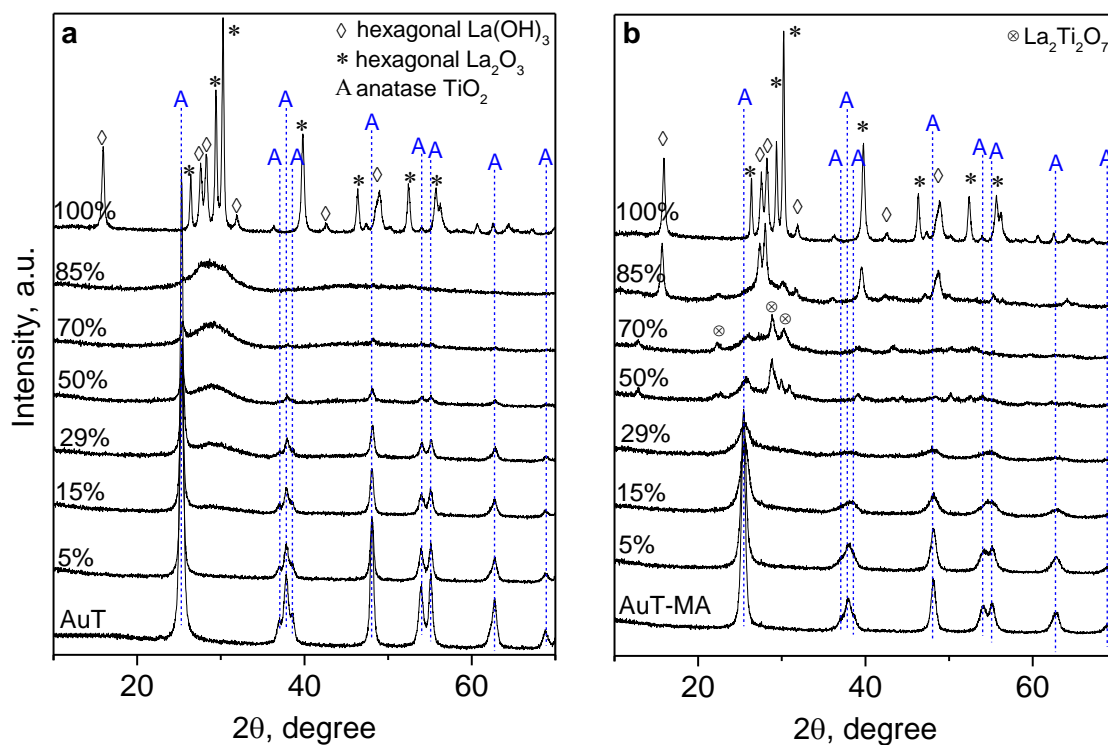


**Figure 8.1** XRD patterns of the lanthanum-modified catalysts prepared by (a) wet-impregnation and (b) coprecipitation.

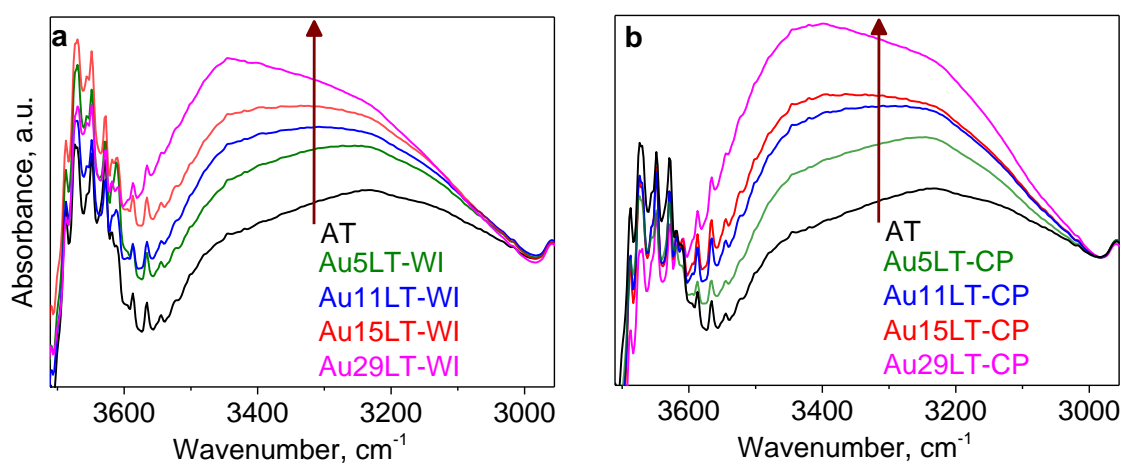


**Figure 8.2** Absorbance in the hydroxyl region of (a) wet-impregnated and (b) coprecipitated catalysts.

Introduction of lanthana by coprecipitation initiated a gradual decrease of the crystallite size from the value of  $\sim 15$  nm obtained for AuT-MA. At 29 wt% lanthana content (Au29LT-CP), the anatase crystallite size was  $\sim 4$  nm, which is  $\sim 70\%$  lower than the average crystallite size obtained for the corresponding wet-impregnated catalyst (Au29LT-WI). As a consequence, the coprecipitated catalysts possessed higher specific surface areas than their wet-impregnated counterparts (Figure 8.4). In agreement with several works<sup>[134,262,265]</sup> reporting the effect of lanthanum-modification at low loadings ( $<20$  wt%), the surface area of the coprecipitated

catalysts passed through a maximum at 15 wt%. This value corresponds to a lanthanum surface density of 5.8 La nm<sup>-2</sup>, which is lower than the reported monolayer coverage on titania (~9.4 La nm<sup>-2</sup>).<sup>[270]</sup> Below 10 La nm<sup>-2</sup>, the critical lanthanum dispersion, lanthana forms preferentially a sub-monolayer on titania, which prevents the coalescence of titania crystallites.<sup>[257]</sup> At higher loadings, multilayers of lanthana and eventually phase segregation cause a reduction in surface area. In the wet impregnated catalysts the surface area did not change significantly up to 11 wt% lanthana (65-70 m<sup>2</sup>/g), while it gradually dropped for higher loadings and reached ~25 m<sup>2</sup>/g at 50 wt% loading.

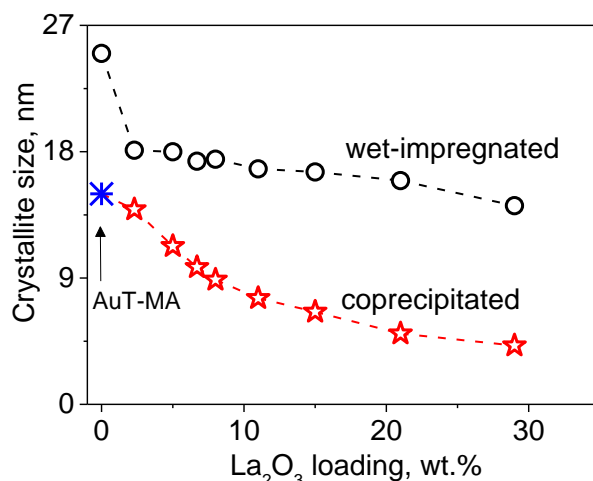


**Figure 8.3** Crystallite size (nm) as a function of lanthana loading in gold catalysts prepared by coprecipitation and wet impregnation. The blue star represents AuT-MA.

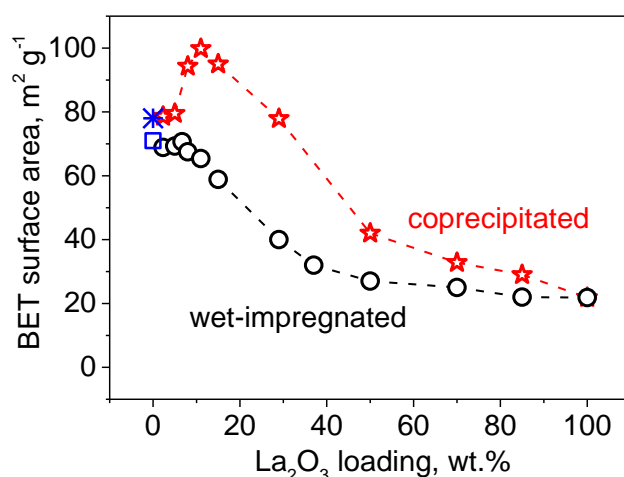


**Figure 8.4** BET surface area (m<sup>2</sup> g<sup>-1</sup>) as a function of lanthana loading in the gold catalysts prepared via coprecipitation and wet impregnation. The blue square and star represent AuT and AuT-MA, respectively.

The morphology and microstructure of selected lanthanum-modified catalysts prepared by wet-impregnation and coprecipitation were studied by high angle annular dark field scanning transmission electron microscopy (HAADF-STEM, Figure 8.5). AuT-MA exhibited gold particles in the same size range (5-7 nm) of those observed in AuT.<sup>[168,208]</sup> Lanthana caused a decrease in the gold particle size. The average gold particle size of Au5LT-WI and Au15LT-WI was

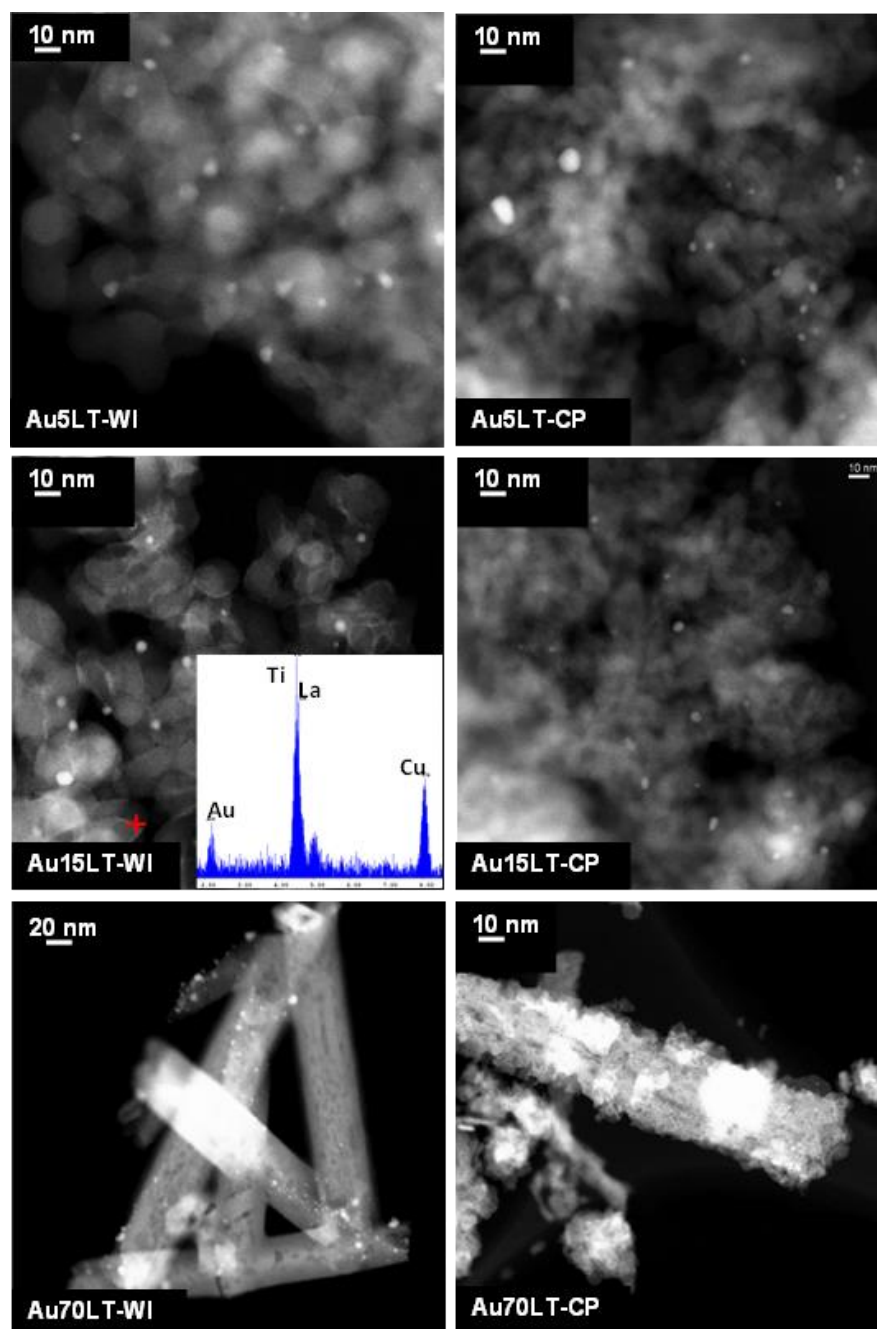
reduced to 2-3 nm despite the observation of few larger particles in the range 5-7 nm. A similar trend was observed in the coprecipitated catalysts. An increased density of surface hydroxyls with increasing lanthana loading (Figure 8.2) can greatly facilitate high dispersion of the gold precursor resulting in smaller gold particles (Figure 8.5).<sup>[161,276]</sup> For Au15LT-WI, the lanthana coverage was calculated to be  $\sim 9.4 \text{ La nm}^{-2}$ , which marks the onset of formation of lanthana multilayers on titania.<sup>[270]</sup> Energy-dispersive X-ray spectroscopy (EDXS, inset of Figure 8.5) confirmed that the bright rims encapsulating the titania particles in Au15LT-WI were indeed composed of lanthanum. This sort of coating was not discernable in the case of the coprecipitated analogue (Au15LT-CP). Irrespective of the synthesis methodology, rod-like morphologies formed at lanthana loadings  $\geq 70 \text{ wt}\%$ . For these samples, the poor contrast between the two heavier elements, gold and lanthanum hampers their precise identification. At these high loadings, lanthanum hydroxide and lanthana segregate to form distinct XRD phases that grow preferentially in the form of rods.<sup>[277-279]</sup>

The different distribution of the lanthanum component and the different morphology of impregnated and coprecipitated samples prompted us to use X-ray photoelectron spectroscopy (XPS) to measure the lanthanum surface concentrations accurately. Table 8.2 presents the atomic concentration of lanthanum measured on Au5LT and Au15LT prepared by wet-impregnation and coprecipitation. The nominal atomic percentage of lanthanum differed significantly from the values estimated by XPS. Clearly, the wet-impregnated catalysts exhibited higher degree of surface enrichment by lanthanum showing two-fold higher concentration compared to that of the nominal atomic percentage. Such a preferential distribution of species on the surface is commonly encountered in wet-impregnated catalysts.<sup>[280-282]</sup> In marked contrast, the coprecipitated catalysts possessed a surface lanthanum concentration that was roughly equivalent to half the nominal values. This suggests that lanthanum was dispersed more into the bulk such that there is a lesser extent of surface enrichment of titania.<sup>[283]</sup> Comparison of Table 8.1 and Table 8.2 demonstrates that  $[\text{La}_{\text{WI}}/\text{La}_{\text{CP}}]_{\text{XPS}}$  is considerably higher than  $[\text{La}_{\text{WI}}/\text{La}_{\text{CP}}]_{\text{T}}$ . The significant divergence between the XPS-derived values and the theoretical values estimated using the simple close-packed monolayer model demonstrates that the wet-impregnated catalysts engender more lanthanum on the surface compared to the coprecipitated analogues even at 5 wt% lanthana loading. At 15 wt% lanthana, though the theoretical lanthanum coverages are not largely different ( $[\text{La}_{\text{WI}}/\text{La}_{\text{CP}}]_{\text{T}} = 1.6$ ), the  $[\text{La}_{\text{WI}}/\text{La}_{\text{CP}}]_{\text{XPS}}$  value indicates more than three-fold higher lanthanum concentrations on the surface in the case of Au15LT-WI. These results are in agreement with the surface coating of titania particles by lanthana in this sample, which is absent in Au15LT-CP (Figure 8.5). Therefore, the simple close-packed monolayer model overestimates the lanthanum dispersion capacity of the coprecipitated catalysts.

**Table 8.2** Estimation of lanthanum surface composition by XPS

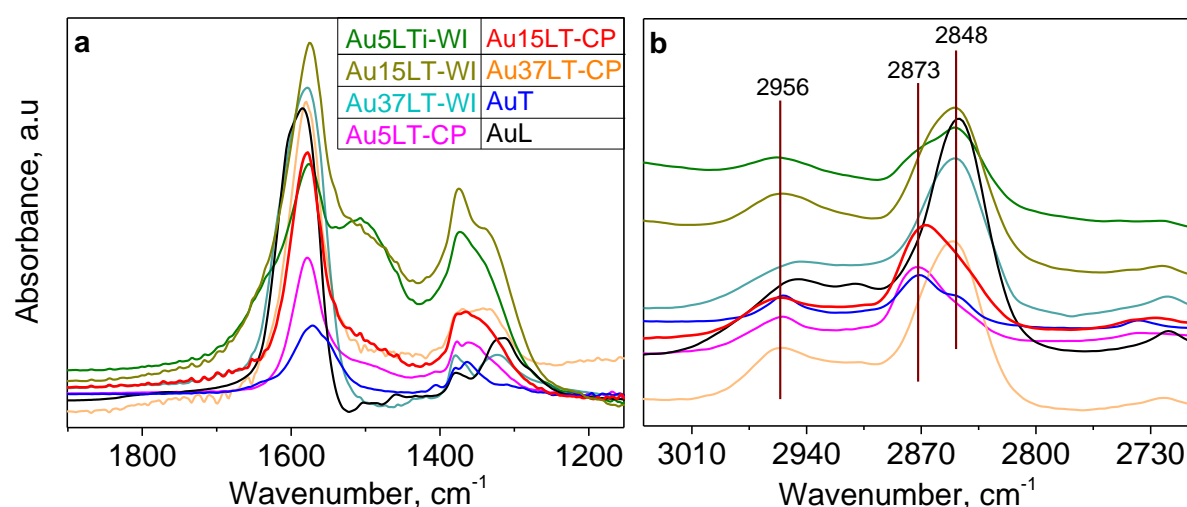
Lanthana loading (wt%)	Atomic % <sup>b</sup>		[La <sub>WI</sub> /La <sub>CP</sub> ] <sub>XPS</sub>
	Coprecipitated	Wet-impregnated	
5 (0.9) <sup>a</sup>	0.4	1.6	4.1
15 (2.6) <sup>a</sup>	1.3	4.4	3.2

<sup>a</sup> Theoretical atomic % calculated on the basis of nominal weight % of lanthana. <sup>b</sup> Calculated on the basis of total normalized peak area of La 3d. [La<sub>WI</sub>/La<sub>CP</sub>]<sub>XPS</sub> is the ratio of the lanthanum surface concentration of the AuLT-WI catalysts to that of AuLT-CP catalysts at a given lanthanum loading determined using XPS.

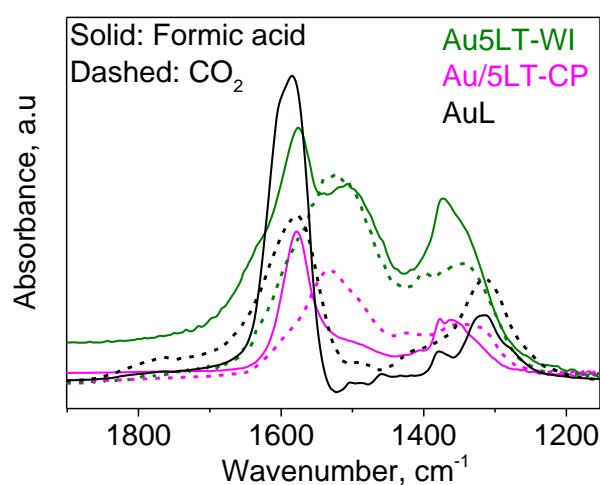


**Figure 8.5** HAADF-STEM images of gold catalysts of different lanthana content prepared by wet-impregnation and coprecipitation.

Figures 8.6 a and b present selected in situ DRIFT spectra obtained during formic acid adsorption under steady state reaction conditions (1120 ppm formic acid in 10 vol% oxygen and 5 vol% water) at 260 °C. The spectra of all the catalysts are characterized by signals in the region 1700-1300  $\text{cm}^{-1}$  that are associated with the  $\nu_{\text{AS}}(\text{OCO})$  and  $\nu_{\text{S}}(\text{OCO})$  stretching modes of carboxyl groups of adsorbed formates. Various shoulders on both signals can be ascribed to the presence of both bidentate and bridged configurations and of multiple adsorption sites. The shoulder at  $\sim 1670 \text{ cm}^{-1}$  is ascribed to the  $\nu_{\text{AS}}(\text{OCO})$  stretching mode of monodentate formate species.<sup>[187]</sup> Besides formates, the wet-impregnated catalysts exhibited features corresponding to uni- and bidentate carbonates<sup>[208]</sup> (Figure 8.7), which showed little contribution on the coprecipitated catalysts.



**Figure 8.6** In situ DRIFT spectra of formic acid adsorption on selected gold catalysts at 260°C. Conditions: 1120 ppm formic acid, 10 vol% oxygen and 5 vol% water. Spectral range showing the carboxyl and C-H bands of formates are presented in (a) and (b), respectively.



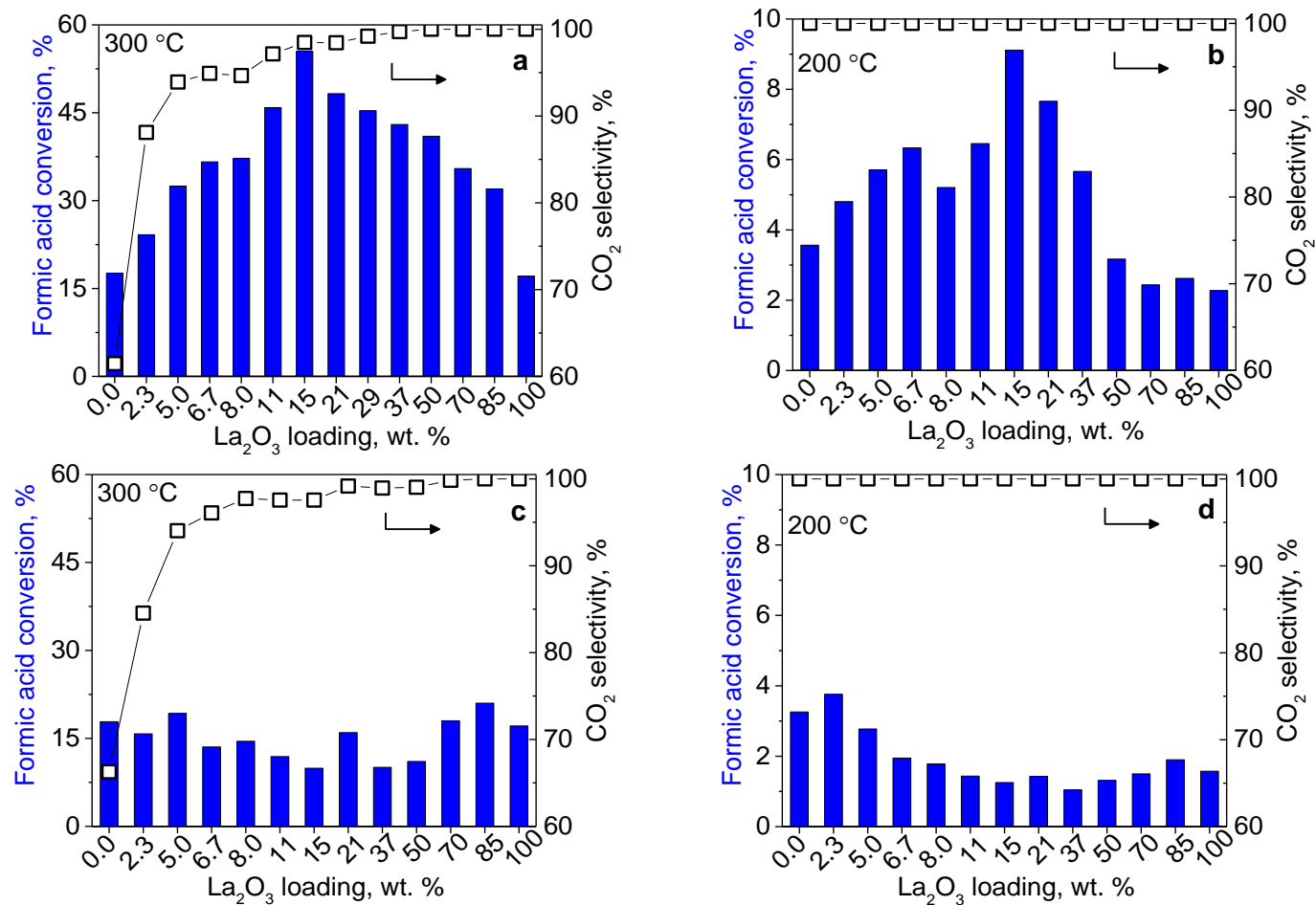
**Figure 8.7** Comparison of in situ DRIFTS spectra of formic acid and carbon dioxide adsorption on selected catalysts.

Figure 8.6 b depicts the spectral region of the characteristic signals of formate species corresponding to the  $\nu_{AS}(\text{CO}) + \delta(\text{CH})$  combination band and the  $\nu(\text{CH})$  band at 2956 cm<sup>-1</sup> and 2873 cm<sup>-1</sup>, respectively.<sup>[208]</sup> In both catalyst series, the signal intensified with increasing lanthana content up to 15 wt% in agreement with the increasing basicity of the material. The intensity gain was marginal with further loading increase. This is likely the result of the trade-off between increasing basicity and decreasing surface area. Owing to the difference in the mechanism of lanthana addition by the two synthesis methods and the resulting different structure, at identical lanthana contents, a higher density of formates and thus higher basicity was observed on the wet-impregnated catalysts exposing more lanthana on the surface (Table 8.1 and 8.2), compared to their coprecipitated analogues. Au5LT-WI and Au15LT-WI exhibited broader bands suggesting the presence of multiple adsorption geometries and thus of an heterogeneous distribution of adsorption sites. With increasing lanthana content, the  $\nu(\text{CH})$  band progressively red shifted by 25 cm<sup>-1</sup>, indicating a weakening of the C-H bond. The high frequency  $\nu(\text{CH})$  band at 2873 cm<sup>-1</sup> is very small in Au37LT-WI indicating that high lanthana content and basicity weakened the C-H bond. This observation is substantiated by similar shifts of formate bands observed on alkali-modified platinum catalysts<sup>[75,212,213]</sup> and of methoxy species coordinated to more reduced oxygen vacancy sites.<sup>[284]</sup>

### 8.3.2 Activity for formic acid decomposition

High activity and selectivity for formic acid decomposition to carbon dioxide are prerequisites for the design of dedicated hydrolysis catalysts for the decomposition of alternative formate-based ammonia precursor compounds in the SCR process. Figure 8.8 (a-d) present the formic acid conversion and carbon dioxide selectivity of all catalysts at 200 °C and 300 °C. Carbon monoxide was the only other product formed at 300 °C (Chapters 3-6). Irrespective of the synthesis method, lanthana caused a sharp increase in carbon dioxide selectivity.<sup>[208]</sup>

The coprecipitated catalysts exhibited significantly enhanced activities upon modification by lanthana (Figure 8.8 a and b). With the introduction of 2.3 wt% lanthana to AuT-MA, the formic acid conversion at 300 °C increased from ~18% to 24% along with an increase in the carbon dioxide selectivity from ~65% to ~88%. The formic acid conversion was the highest at 15 wt% lanthana loading (~56%) and the corresponding carbon dioxide selectivity was ~98%. The performance of this catalyst is similar to that of the gold catalyst prepared using commercial lanthanum-modified titania support (10 wt% lanthana), which showed ~60% formic acid conversion and ~98% carbon dioxide selectivity.<sup>[208]</sup> Interestingly, 15 wt% lanthana corresponds to 5.8 La nm<sup>-2</sup>, which is well below the critical loading for monolayer coverage (~10 La nm<sup>-2</sup>) on titania.<sup>[257,270]</sup>



**Figure 8.8** Effect of lanthana loading on the catalytic activity of gold catalysts prepared by (a,b) coprecipitation, and (c,d) wet-impregnation for formic acid decomposition at 200 °C and 300 °C and  $W/F = 2.4 \cdot 10^{-5} \text{ g s cm}^{-3}$

Beyond this optimal composition, a steady decline in formic acid conversion was observed although the carbon dioxide selectivity was close to 100%. These catalysts with lanthana loading exceeding 10 La nm<sup>-2</sup>, suffered surface area reduction and segregation and crystallization of lanthana as evidenced from the XRD measurements. At 200 °C, a similar trend in performance was observed with the highest conversion at 15 wt% lanthana content which was about three-fold higher than that of the unmodified catalyst. The carbon dioxide selectivity of the wet-impregnated catalysts showed a very similar pattern as that of the coprecipitated catalysts (Figure 8.8 c). This was however accompanied by marginal changes in formic acid conversion, which remained relatively constant. The catalytic activity data indicate that lanthanum addition to Au/TiO<sub>2</sub> catalysts suppresses carbon monoxide formation<sup>[208]</sup> and that coprecipitation is the method of choice for preparing highly active catalysts for oxidative formic acid decomposition to carbon dioxide under SCR-relevant conditions.

### 8.3.3 Carbon monoxide oxidation activity on the gold catalysts

The carbon monoxide oxidation activity was examined to determine if carbon monoxide is an intermediate to carbon dioxide (See Chapter 6). Figure 8.9 depicts the carbon monoxide conversion on selected catalysts in the presence and absence of water in the feed. In the presence of water, the carbon monoxide conversion remained below 5%. The carbon monoxide oxidation activity was higher by a factor of ~two in the absence of water in the feed. This observation is in line with reversible poisoning of the active sites by water-derived species reported in feed saturated with water vapor.<sup>[194,208]</sup> Although an increase in lanthana content modestly increased the conversion, it only amounted to about 1/6<sup>th</sup> the carbon dioxide production from formic acid decomposition on Au15LT-CP (Figure 8.8 a). Therefore, the carbon dioxide produced over the lanthanum-modified catalysts originates from the direct formic acid decomposition pathway (see Chapter 6).

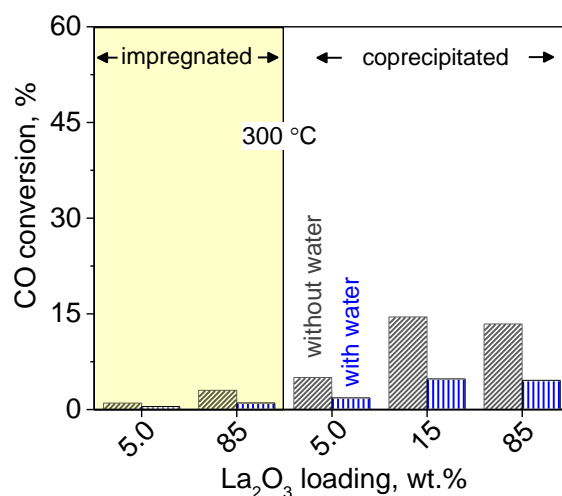


**Figure 8.9** Effect of lanthana loading on the carbon monoxide oxidation activity of the gold catalysts in the presence and absence of 5 vol% water at 300 °C and W/F = 7.5\*10<sup>-5</sup> g s cm<sup>-3</sup>.

### 8.3.4 Formic acid decomposition activity of the supports

Carbon monoxide is the only product of formic acid decomposition on the pristine supports. Figure 8.10 depicts the trend in carbon monoxide yield at 300 °C as a function of lanthana content ( $0 \leq X \leq 29$  wt%) in titania prepared by coprecipitation. A drop in carbon monoxide production was observed with increasing lanthana loading. The wet-impregnated catalysts behaved similarly (not shown). Hence, the decrease in carbon monoxide selectivity (Figure 8.8) observed on the gold catalysts with increasing lanthana content originates from the blockage of the sites on titania responsible for carbon monoxide formation.<sup>[29,210,285]</sup>

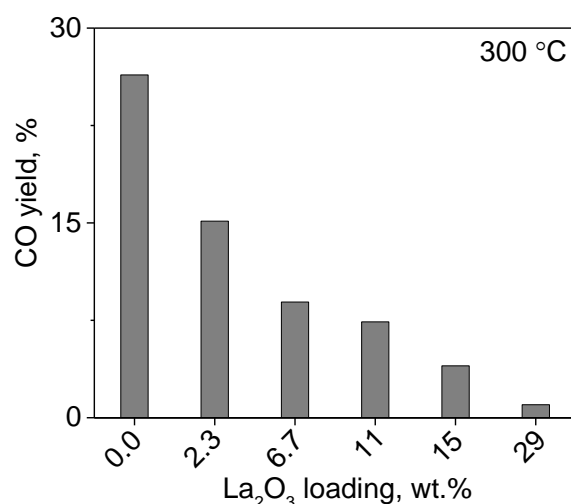


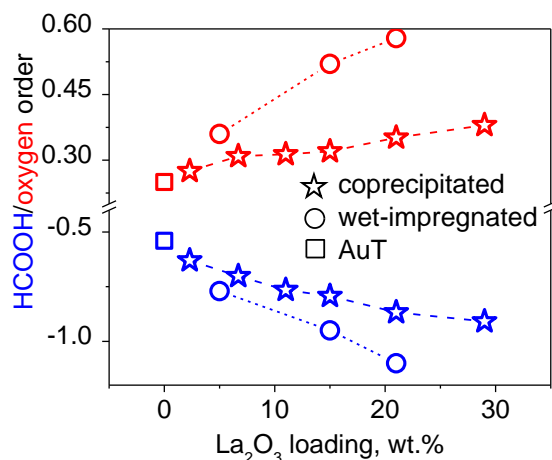
**Figure 8.10** Effect of lanthana loading on the performance of supports prepared by coprecipitation for formic acid decomposition at 300 °C and  $W/F = 2.4 \cdot 10^{-5} \text{ g s cm}^{-3}$ .

### 8.3.5 Kinetic study

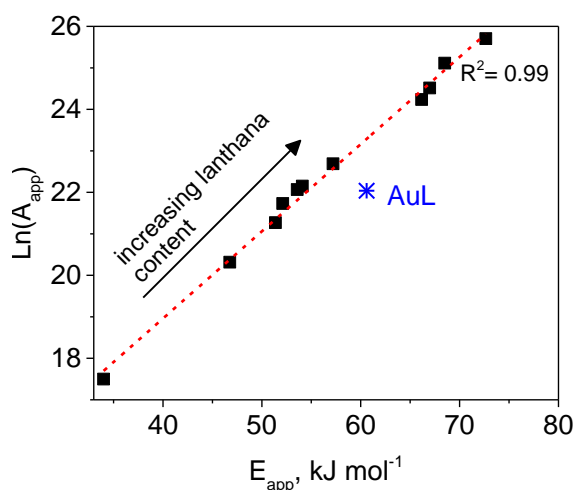
Figure 8.11 depicts the influence of lanthana loading on the reaction orders in formic acid and oxygen. Generally, with increasing lanthana content, the formic acid orders became more negative, while the oxygen orders became more positive. Increasingly negative formic acid orders support the activity trend at high lanthana loadings, wherein extensive poisoning of the active sites by formic acid-derived species prompts low activity. Inverse trends in formic acid and oxygen orders are consistent with a mechanism where the reaction intermediates derived from the two reactants compete for the same active site (Chapter 6). Reaction orders in carbon dioxide were zero. Hence, surface carbonates may exist only as spectator species.

Figure 8.12 presents the Constable plot<sup>[201,202]</sup> between the apparent activation energy ( $E_a$ ) and pre-exponential factor ( $A_{app}$ ) for formic acid decomposition on the gold catalysts of increasing lanthana content ( $0 \leq X < 100$ ) prepared by coprecipitation. The linear relationship suggests the occurrence of the compensation phenomenon originating from systematic changes in the adsorptive properties of the catalysts without any substantial change in the overall reaction mechanism.<sup>[201,202]</sup> This is in line with the systematic change in the orders in formic acid and

oxygen. The deviation of AuL indicates that a different mechanism may operate in the absence of titania.<sup>[286,287]</sup>



**Figure 8.11** Influence of lanthana content in the gold catalysts prepared by coprecipitation and wet-impregnation on reaction orders in formic acid and oxygen at 300 °C.



**Figure 8.12** Constable plot of pre-exponential factor ( $A_{app}$ ) and the apparent activation energy ( $E_{app}$ ) for formic acid decomposition over gold catalysts prepared by coprecipitation.

### 8.3.6 Activity for ammonium formate decomposition

In view of its advantages, ammonium formate (AmFo) is an attractive ammonia precursor (See Chapter 1).<sup>[204–207,288]</sup> Like other formate-based precursors, AmFo thermolyzes in the gas phase to form ammonia and formic acid (See Chapter 3).<sup>[23,25]</sup> Hence, selectivity against ammonia oxidation is a crucial aspect in the design of a dedicated hydrolysis catalyst. To examine this, the optimal catalyst, Au15LT-CP, was tested for AmFo decomposition. Figure 8.13 compares the carbon dioxide and ammonia yields from the decomposition of isoconcentrations of AmFo on the unmodified and the coprecipitated catalyst with optimal lanthana loading ( $X=15$  wt%) in the temperature window 160–300 °C. The trend in the activity of the two catalysts was retained for AmFo decomposition, wherein Au15LT-CP exhibited close to three-folds higher carbon dioxide yield compared with the unmodified catalyst. The high activity of the lanthanum-modified

catalyst was accompanied by nearly 100% yield of ammonia, suggesting the ability of the catalyst system to efficiently decompose formic acid to carbon dioxide without consuming ammonia.

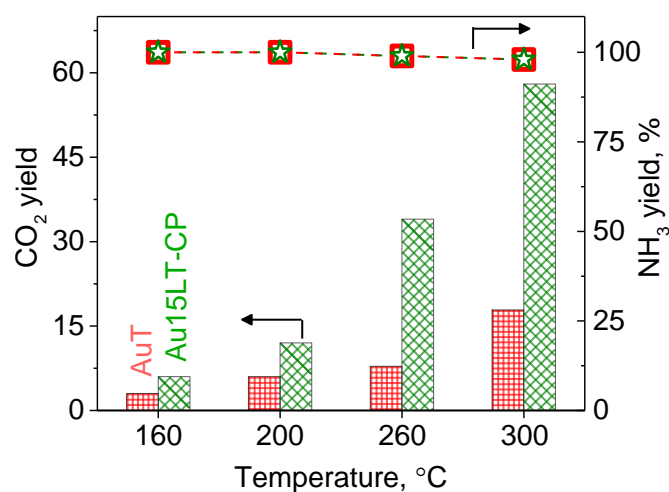


**Figure 8.13** Ammonium formate decomposition on AuT and Au15LT-CP.

### 8.3.7 Mechanistic implications of lanthana modification

In Chapter 5, gold supported on commercial lanthana-modified titania was found to exhibit a selective enhancement in formic acid decomposition to carbon dioxide. Base-modification by lanthana addition resulted in enhanced formation of bidentate formates (Figure 8.6 a) which are the kinetically relevant precursors for carbon dioxide formation (see Chapter 6). Another consequence of base-modification weakening of the C-H bond owing to the increased electron density of the catalyst, observable from the red-shifting of the  $\nu(\text{CH})$  band of formate (Figure 8.6 b).<sup>[289,290]</sup> Hence, the enhancement in the activity of the base-modified catalysts can be traced back to the acceleration of the rate limiting step involving C-H bond cleavage of the formate.

Catalysts prepared by wet-impregnation were less active than their co-precipitated analogues. The steadily increasing population of lanthanum on the surface (Tables 8.1 and 8.2) has mechanistic implications that can explain this behaviour. According to the proposed single-site mechanism for formic acid decomposition under the investigated conditions (Chapter 6), hydroperoxy species ( $\text{OOH}^*$ ) formed from the proton shift equilibrium between adsorbed oxygen and water are responsible for the decomposition of the abundantly present formates in the rate-determining-step (RDS) forming carbon dioxide. In the case of the wet-impregnated catalysts, a drastic increase in basicity triggered by high surface concentrations of lanthanum manifests itself in notably higher formate coverages compared to the coprecipitated catalysts (Figure 8.6). This entails an extensive blockage of the active sites by formates which in turn diminish their availability for the formation of the hydroperoxy species. This explanation is in line with the more negative orders in formic acid and more positive orders in oxygen.

Besides inducing a rapid increase in the surface basicity (Figure 8.6) and a decrease in the surface area (Figure 8.4), an increase in the surface lanthanum coverage (Tables 8.1 and 8.2) in the case of the wet-impregnated catalysts can additionally impede the catalytic rates by reducing the interaction between gold and titania. While gold is crucial for the formation of the hydroperoxy species, tetrahedrally coordinated Ti<sup>4+</sup> sites have been postulated to play a pivotal role in binding these species before transferring them to the active site (See Chapter 9).<sup>[125,227]</sup> Hence, the blanketing of titania particles by lanthana (inset of Au15LT-WI in Figure 8.5) can adversely affect the Au-Ti synergy that is responsible for the formation of hydroperoxy species.

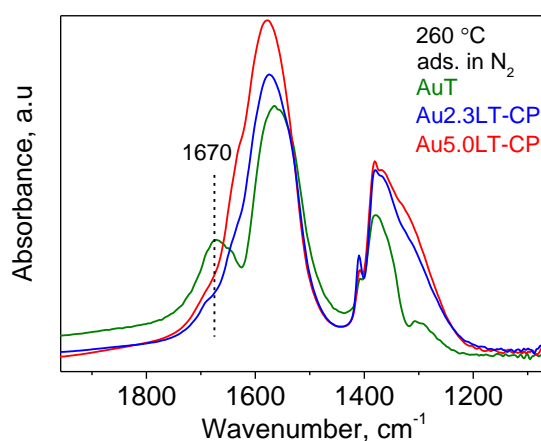


**Figure 8.14** In situ DRIFTS spectra of formic acid adsorption in nitrogen on gold catalysts of different lanthana loadings showing the inhibition of the band at 1670 cm<sup>-1</sup>.

In the proposed mechanism (Chapter 6), the dissociative chemisorption of formic acid as formate (HCOO\*) is an exothermic process while the formation of the active oxygen species (OOH\*) is an activated process. Hence, the formation of the former intermediate is favored at lower temperatures and the generation of the hydroperoxy species is accelerated at higher temperatures. In Chapters 5 and 6, the formic acid orders were found to change as a function of temperature and gas phase formic acid concentration, becoming less negative at lower temperature and lower formic acid concentration regime. This is a clear sign of the measured kinetic parameters being apparent and the activation energy bearing non-trivial contributions from the heats of adsorption of the reactants. In this study, the compensation phenomenon where an increase in the measured (apparent) activation energy,  $E_{app}$  is offset by an increase in the pre-exponential factor ( $A_{app}$ ) originates from a change in the relative surface coverages of formates and hydroperoxy species and thus, inherently linked to the differences in their heats of adsorption with increasing lanthana concentrations<sup>[202,291]</sup>. An increased basicity can be speculated to enhance the stability of adsorbed oxygen species required for the formation of active hydroperoxy species.<sup>[128,229]</sup> Bond et al. rigorously maintained that  $\Delta E_{app}$  should ideally be at least 50% of the smallest  $E_{app}$  measured.<sup>[202]</sup> In this study, this is ~52%, thus adding credence

to the observed compensation phenomenon. The compensation phenomenon can be described by the Constable–Cremer relation (Eq. 8.1).

$$\ln A_{\text{app}} = mE_{\text{app}} + c \quad (8.1)$$

Besides unifying the mechanisms operating on the Au/TiO<sub>2</sub> catalysts of different lanthana loadings, the observed obedience to the linearity of the Constable–Cremer relation can be mechanistically interpreted as the increase in the adsorption enthalpy of active-oxygen species with increasing lanthanum content, which in turn entails higher energy (barrier) for destabilization.<sup>[171]</sup> This is in line with the negative orders in formic acid and positive orders in oxygen. The decrease in the C-H bond strength does not cause significant reduction in the activation energy.<sup>[292,293]</sup> The pre-exponential factor represents the number as well as the strength of the active sites. Overall, the observed optimum in the basicity-induced rate enhancement can be attributed to a favorable combination of factors including decreased C-H bond strength of formates, increased probability of formation of hydroperoxy species arising from increased stability of adsorbed oxygen and increased number of active sites owing to the decreased gold particle size. The highly negative formic acid orders in the case of unmodified as well-as base-modified catalysts ascertain that the classical effect of basicity associated with an increased degree of formic acid deprotonation to formate does not entail higher activity. Thus, this study coupled with the mechanistic investigation performed in Chapter 6 offers clarity on the more realistic effect of basicity on the catalytic activity for formic acid decomposition.

Modification by lanthana also favorably suppressed the carbon monoxide production. The introduction of only 1 atomic % of lanthanum to the surface of titania (Au15LT-CP, Table 8.2) led to ~85% drop in formic acid conversion to carbon monoxide (Figure 8.10). With increasing lanthana content, the tendency to form monodentate formates which are the intermediates relevant for carbon monoxide formation (Chapter 6) was substantially decreased (Figure 8.14). Additionally, the increased density of surface hydroxyls (Figure 8.2) that are engendered on the surface of lanthanum-modified titania can disfavor the RDS involving the decomposition of monodentate formate to carbon monoxide and a hydroxyl at a bridging oxygen anion.<sup>[42]</sup> These results are consistent with reports on decreased formic acid dehydration activity with increasing basicity.<sup>[28,29]</sup>

#### 8.4 Conclusions

In this chapter, the basicity of titania supported gold catalysts was tailored by incremental addition of lanthana via wet-impregnation and coprecipitation. Irrespective of the synthesis method, introduction of lanthana to Au/TiO<sub>2</sub> favored smaller gold particle and anatase crystallite sizes and steered the selectivity towards higher carbon dioxide production from formic acid

decomposition. The rate-determining-step (RDS) involving the hydroperoxyl-mediated C-H bond cleavage of formate to form carbon dioxide is speculated to be accelerated as a consequence of progressive weakening of the C-H bond as well as an increased availability of hydroperoxy species with increasing lanthana content. However, very high surface basicity reduced the availability of active surface oxygen species owing to an extensive blockage of the active sites by formates, thus leading to poor performance of highly basic catalysts. The systematic changes in the relative coverages of formates and the hydroperoxy species leads to kinetic compensation between  $E_{app}$  and  $\ln(A_{app})$ . At an optimum surface lanthanum concentration of ~1.3 atomic %, gold supported on coprecipitated lanthanum-modified titania catalyst exhibited close to three-fold enhancement in carbon dioxide production while carbon monoxide selectivity and ammonia oxidation activity were restricted to negligible levels. Another effect of increasing basicity was the suppression of monodentate formates which are the precursors to carbon monoxide.



# **Chapter 9**

## **Conclusion and Outlook**

## 9.1 Conclusion

Catalysis is a key technology that has revolutionized the chemical industry. By improving the energetics, product selectivities and the turnovers, the use of catalysts has entailed the replacement of traditional environmentally and economically unfeasible processes by cleaner, cheaper and more efficient alternatives. The current energy crisis and the circumstances surrounding environmental degradation urge the development of innovative catalytic systems that can potentially serve as the technological breakthrough needed to drive truly sustainable industrial solutions. In this direction, the development of dedicated hydrolysis catalysts that can rapidly and selectively decompose formic acid to carbon dioxide can afford the replacement of urea with more efficient formate-based alternative ammonia precursors such as ammonium formate, guanidinium formate or methanamide in the selective catalytic reduction (SCR) process for diesel exhaust after-treatment. An important criterion to be fulfilled is that the prospective catalyst must remain inactive for the oxidation of ammonia that is co-evolved during the decomposition of these precursors so that the ammonia is made fully available for the downstream SCR process. In this regard, a titania-supported gold catalyst ( $\text{Au/TiO}_2$ ) exhibited high activity, stability and unique selectivity for ammonium formate decomposition to carbon dioxide and ammonia at close to 100% yield under the highly oxidizing conditions prevailing in the simulated exhaust feed.

With the discovery of the remarkable chemical activity of nanoparticulate gold, catalysis by gold has attracted immense research activity unveiling exciting chemistries involving numerous reactions. In this work, gold-catalyzed formic acid decomposition to carbon dioxide was studied in the light of SCR, where in the presence of oxygen and water dictated an oxidative dehydrogenation (ODH)-type mechanism which was markedly different from the traditional stoichiometric dehydrogenation to carbon dioxide and hydrogen that is commonly encountered in literature. However, some of these findings also reconciled with those from literature indicating that bidentate formates are the relevant reaction intermediates common amongst ODH of formic acid operating under SCR-relevant conditions, stoichiometric formic acid dehydrogenation and water gas shift reaction.

In this work, an oxygen-water synergy was revealed which was reminiscent of water-assisted oxygen activation. Hydroperoxy species form, which circumvent the energy-intensive step of oxygen activation on gold. These species aid in abstraction of hydrogen from the C-H bond of formate in the rate-determining-step (RDS). The findings from this work provide further evidence supporting the inherent selectivity of gold to produce carbon dioxide from formic acid while titania was predisposed to dehydrate formic acid to form carbon monoxide. Numerical modelling of the ODH mechanism yielded satisfactory agreement with the experimental results.

The mechanistic insights were applied towards gaining functional understanding of an optimal lanthanum-modified Au/TiO<sub>2</sub> catalyst. Although, the increased basicity resulted in a classical increase in the extent of formic acid deprotonation to formate, this does not cause the activity-enhancement. Instead, the changes in the electronic properties of the catalyst surface which in turn induce C-H bond weakening of formate and increase the stability of active oxygen species underlined the promotional effect of base-modification. An optimum in the surface basicity exists which marks the tradeoff between increasing formate coverage and decreasing number of sites available for the formation of hydroperoxy species required to scavenge hydrogen from the formate. Lanthanum also blocks the sites on titania that form monodentate formates, thus suppressing carbon monoxide formation.

The findings from this work advance the knowledge of gold-catalyzed formic acid decomposition chemistry by adding new mechanistic insights related to the influence of oxygen, water and structural-modification. Oxygen-activation on gold is an intensely researched area with several experimental and theoretical works reporting on the crucial role of water. This thesis supplements strong evidence on the promotional role of water, which is always present either as a trace impurity or as a feed component, in facilitating catalytic reactions involving molecular oxygen. The optimized lanthanum-modified Au/TiO<sub>2</sub> catalyst serves as a promising candidate for use as a dedicated hydrolysis catalyst for the decomposition of formate-based ammonia precursor compounds in the SCR process.

## 9.2 Outlook

An important question that remains to be answered is on the structure of the active site and the proof for the existence and reactivity of the hydroperoxy species. Using inelastic neutron scattering, the first spectroscopic evidence of hydroperoxy species was provided during hydrogen oxidation on Au/TiO<sub>2</sub>.<sup>[127]</sup> More recently, by coupling in situ ultraviolet-visible diffuse reflectance spectroscopy (UV-vis DRS) and in situ titanium K-edge X-ray absorption near-edge structure (XANES), the formation and the true intermediate nature of titanium-hydroperoxide species was revealed during the gas-phase epoxidation of propylene with hydrogen and oxygen under reaction conditions.<sup>[294,295]</sup> In the context of electrochemical oxidation, surface enhanced Raman spectroscopy (SERS) was applied to identify Au-OOH species as the reactive intermediates during oxygen evolution reaction on gold electrodes.<sup>[122]</sup> Theoretical calculations predict that these species can be facilely formed in the presence of oxygen and water on gold.<sup>[123,125]</sup>

In the proposed ODH mechanism, single site is active and involved in the formation of (bidentate) formate, the kinetically relevant reaction intermediate responsible for carbon dioxide formation as well as the formation of hydroperoxy species needed for the C-H bond scission of

the formate in the RDS. That single site is responsible is deduced from the poisoning effect of formate on the activity and is consistent with the inverse trends in oxygen and formic acid orders. Steady state DRIFTS revealed that the gold catalysts were covered with higher density of formates than the corresponding pristine metal oxide supports. While, it is clear that the formate formation is catalyzed in the presence of gold, it is also certain that all the formates cannot exist on gold considering that the gold loading was very low. The transient DRIFTS experiments showed that all the formates were consumed to produce carbon dioxide when the feed was switched to oxygen and water. Hence, there is reverse-spillover of formates to the 'active site' where decomposition occurs.

The active site must involve gold, since in its absence, formates remained merely as spectators and no carbon dioxide was formed. These findings along with the gold loading and particle size effect suggest that the active sites are likely the interfacial sites between the gold particle and the support. It is often cited that an intimate contact between gold and a support is needed to realize the exceptional catalytic abilities displayed by supported gold catalysts.<sup>[59,112-115,250,256,296,297]</sup> Active hydroperoxy species are proposed to form at interfacial Au-Ti<sup>4+</sup> sites by reaction with oxygen and hydrogen (Figure 9.1 top) or water (Figure 9.1 bottom).<sup>[294]</sup> The crucial role of gold is to facilitate oxygen adsorption.<sup>[125,128,294]</sup> In such a mechanism, it is reasonable to speculate that the electron-donating property of a base (like lanthanum) increases the stability of the molecularly adsorbed oxygen on gold which in turn increases the concentration of the hydroperoxy species.<sup>[229]</sup> Gold supported on titanasilicate has been well studied for the formation of these species.<sup>[124,294]</sup> It is believed that the hydroperoxy species are located on the isolated tetrahedral titanium sites at high Si/Ti ratio (>100). Hence, it would be of immense interests to apply such systems for studying the formation of hydroperoxy species during formic acid decomposition in oxygen and water. Moreover, the lower affinity of titanasilicate to formic acid should result in lower formate coverage than on titania or lanthanum-modified titania which in turn increases the chances of the detection of the hydroperoxy species. Another way to increase the relative coverage of these hydroperoxy species is to operate at higher temperature (higher activity). Besides static measurements, transient UV-Vis DRS and XANES experiments where the feed is switched in a manner similar to that reported in Chapter 6 are promising in revealing the reactivity of these species.

Isotope labelling studies employing DCOOH and HCOOH can confirm that the C-H bond activation is the RDS in the ODH mechanism. Ojeda and Iglesia observed normal kinetic isotope effect (KIE) values greater than one when switching the feed between HCOOH and DCOOH during stoichiometric formic acid dehydrogenation to carbon dioxide and hydrogen.<sup>[89]</sup> Similar effects have been reported during water gas shift reaction where surface formate decomposition constitutes the RDS.<sup>[71]</sup>

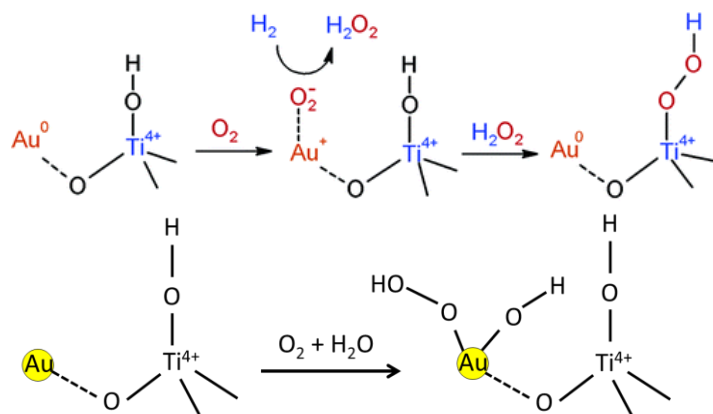


**Figure 9.1** Proposed mechanistic model for the formation of hydroperoxy species on gold supported on titanasilicate from oxygen and hydrogen (top) or water (bottom). Top figure adapted with permission from Reference<sup>[294]</sup>. Copyright 2006 American Chemical Society. Bottom figure adapted with permission from Reference<sup>[128]</sup>. Copyright 2009 John Wiley and Sons.

Another question is with regard to the effect of ammonia on formic acid decomposition. It is not clear how the basic gas phase reactant (ammonia) entails a selective increase in carbon dioxide production from formic acid decomposition as reported in Chapter 4. Loges and coworkers observed a linear correlation between the amine concentration and the volume of hydrogen produced from the decomposition of formic acid amine adducts using ruthenium-based homogeneous complexes.<sup>[81]</sup> Bi et al. demonstrated such a base-effect on a heterogeneous catalyst system using nanocrystalline Au/ZrO<sub>2</sub>. The proton scavenging ability of NEt<sub>3</sub> (triethylamine) was proposed to be responsible for the very high TOFs for dehydrogenation of formic acid amine mixtures.<sup>[66]</sup> In this study, the instantaneous formation of and kinetic saturation by formates on the active sites under reaction conditions as shown in Chapters 5 and 6 imply that increased rate of formate formation in the presence of ammonia cannot result in rate enhancement. Hence, ammonia must accelerate the RDS involving the formate decomposition to carbon dioxide. Another scenario that is also likely is that ammonia blocks the sites on titania which can explain the suppression in carbon monoxide formation in Chapter 4.

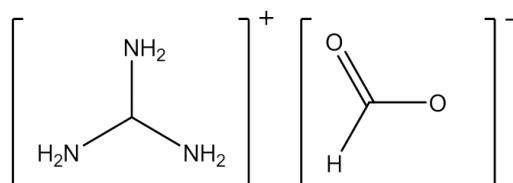


**Figure 9.2** Molecular structure of GuFo.

The final question that arises is can the mechanistic findings on formic acid and ammonium formate decomposition be extrapolated towards the understanding of more complex decomposition chemistry of guanidinium formate (GuFo, Figure 9.2) which can release up to

three molecules of ammonia per molecule that is fully decomposed. Based on the findings from Chapter 4 which revealed a gradual increase and decrease in carbon dioxide and carbon monoxide formation rates, respectively, with increasing gas phase ammonia concentration, it can be speculated that an increased formic acid decomposition rate can be obtained using GuFo as the precursor. However, such a promotional effect will be fully realized only at high catalyst loadings or high temperature, since, at low activity several side reactions occur between formic acid, ammonia and guanidine which result in the formation of methanamide, hydrogen cyanide and formoguanamin.<sup>[15,23,298]</sup>

---

## List of publications

### Journal articles

M. Sridhar, S. Brose, D. Siewert, D. Ferri, J. A. van Bokhoven, O. Kröcher, *From mechanism to catalyst design: Fine tuning the basicity of Au/TiO<sub>2</sub> for formic acid decomposition under SCR-relevant conditions*, 2016, *in preparation*.

Chapter 8

M. Sridhar, J. Mantzaras, J. A. van Bokhoven, O. Kröcher, *Numerical modeling of hydroperoxyl-mediated oxidative dehydrogenation of formic acid on Au/TiO<sub>2</sub> under SCR-relevant conditions*, 2016, *in preparation*.

Chapter 7

M. Sridhar, D. Ferri, J. A. van Bokhoven, O. Kröcher, *Water-Assisted Oxygen Activation over Au/TiO<sub>2</sub> during Formic Acid Decomposition under SCR-Relevant Conditions*, 2016, *in preparation*.

Chapter 6

M. Sridhar, D. Ferri, M. Elsener, J. A. van Bokhoven, O. Kröcher, *Promotion of Ammonium Formate and Formic Acid Decomposition over Au/TiO<sub>2</sub> by Support Basicity under SCR-Relevant Conditions*, **ACS Catal.** 2015, 5, 4772–4782.

Chapter 5

M. Sridhar, J. A. van Bokhoven, O. Kröcher, *Effect of ammonia on the decomposition of ammonium formate over Au/TiO<sub>2</sub> under oxidizing conditions relevant to SCR: Enhancement of formic acid decomposition rate and CO<sub>2</sub> production*, **Appl Catal. A Gen.** 2014, 486, 219-229.

Chapter 4

M. Sridhar<sup>\*</sup>, D. Peitz<sup>\*</sup>, J. A. van Bokhoven, O. Kröcher, *Ammonium formate decomposition over Au/TiO<sub>2</sub>: a unique case of preferential selectivity against NH<sub>3</sub> oxidation*, **Chem Commun.** 2014, 50, 6998–7000. <sup>\*</sup>equal contribution

Chapter 3

---

## Oral presentations

M. Sridhar, D. Ferri, J. A. van Bokhoven, O. Kröcher, *Base-promotion of selective decomposition of ammonium formate and formic acid over Au/TiO<sub>2</sub> under SCR-relevant conditions*, **European Congress on Catalysis (EUROPACAT)**, Kazan, Russia, 2015.

M. Sridhar, J. A. van Bokhoven, O. Kröcher, *NH<sub>3</sub> promoted formic acid decomposition over monolithic Au/TiO<sub>2</sub> catalyst: Rate enhancement without NH<sub>3</sub> oxidation*, **SCS Fall Meeting**, Zurich, Switzerland, 2014.

M. Sridhar, J. A. van Bokhoven, O. Kröcher, *Effect of NH<sub>3</sub> on formic acid decomposition over Au/TiO<sub>2</sub>: A unique case of rate enhancement without NH<sub>3</sub> oxidation*, **Nordic Symposium on Catalysis**, Oslo, Norway, 2014.

## Poster presentations

M. Sridhar, D. Ferri, J. A. van Bokhoven, O. Kröcher, *Water-assisted oxygen activation on Au/TiO<sub>2</sub> catalysts during formic acid decomposition*, **International Congress on Catalysis (ICC)**, Beijing, China, 2016.

M. Sridhar, D. Ferri, J. A. van Bokhoven, O. Kröcher, *Base-promoted formic acid decomposition over Au/TiO<sub>2</sub> catalysts under SCR-relevant conditions*, **Tenth International Congress on Catalysis and Automotive Pollution Control (CAPoC10)**, Brussels, Belgium, 2015.

M. Sridhar, D. Ferri, J. A. van Bokhoven, O. Kröcher, *From mechanism to catalyst design: Highly active formic acid decomposition catalysts under SCR-relevant conditions*, **SCS Fall Meeting**, Lausanne, Switzerland, 2015.

M. Sridhar, D. Ferri, M. Elsener, J. A. van Bokhoven, O. Kröcher, *Effect of basicity on formic acid decomposition over monolithic Au/TiO<sub>2</sub> catalysts under SCR-relevant conditions*, **Catalysis Fundamentals and Practice Summer School**, Liverpool, U.K, Jul 2015.

---

# Curriculum Vitae

## Personal information

**Name:** Manasa Sridhar

**Born:** 12.12.1987 in Hyderabad, India

**Place of Origin:** India

**Marital Status:** Married

## Education

- 2013 – 2016**      **Ph.D. in Chemical Engineering**  
ETH Zürich (CH) – Dept. of Chemistry and Applied Biosciences  
Group of Jeroen A. van Bokhoven
- 2009 – 2012**      **M.Sc. in Chemical Engineering**  
University of Cincinnati (U.S.A) – Dept. of Biomedical, Chemical and  
Environmental Engineering (BCEE) Engineering
- 01/2010 – 05/2012**      **Master thesis**  
University of Cincinnati (U.S.A)  
“Template Directed Synthesis and Characterization of Organic  
Mesoporous Polymers and their Adsorption Performance for Lysozyme” –  
Group of Panagiotis (Peter) G. Smirniotis
- 2005 – 2009**      **Bachelor in Technology in Chemical Engineering**  
Anna University, Sri Venkateswara College of Engineering, (India) – Dept.  
of Chemical Engineering

## Acknowledgements

Inspiring supervisors, exciting research topic, excellent infrastructure, wonderful colleagues and the incredible landscape of Switzerland are all the ingredients that made my PhD journey so pleasurable and memorable! The success of my PhD was highly dependent on the support of the following people.

Firstly, I would like to extend my utmost gratitude to Jeroen and Oliver for giving me the opportunity to pursue my doctoral research in their groups. I sincerely thank them for their guidance, helpful discussions, ideas and sharing their passion for science with me. I am indebted for their excellent mentoring which I believe has influenced me in a profound way. I would also like to thank Davide for many insightful discussions and his critical comments during manuscript revision. His great sense of humor made me laugh even during tense situations. Thank you Davide! I am sincerely thankful to Ioannis for the numerical modelling work. Thank you very much for taking your time to discuss with me during the many meetings we have had. I really appreciate it. I have now learnt a bit about numerical modelling and I hope to further improve my knowledge on this. I would like to express my sincere thanks to Prof. Christoph Müller for agreeing to be on my defense committee.

I am immensely grateful to Martin Elsener who was always there to help me when things went wrong with my reactor-setup and for sharing his expertly insight on automotive catalysis. I will always be in awe of his knowledge and expertise in SCR. Sometime in the near future, I hope to visit all the beautiful mountains of Switzerland that you have recommended.

I have been extremely lucky to have colleagues with whom it was an absolute joy to work with. Kasia, Tasos, Adrian, Andrey, Patrick, Valentina, Arnim and Christophe constituted the team at PSI and made the working atmosphere so lively and enjoyable. It is quite rare to have such an awesome group of people with amazing sense of humor and helpful nature as colleagues, but I was lucky to have that. I couldn't have asked for a better group! Thank you guys! I would also like to offer special thanks to Adrian for sharing his impeccably-built DRIFTS setup with me. I would like to thank Stefanie for her great work on the Master thesis with me. As a cross-PhD student, I was lucky to work with two groups, the second group being the 'Heterogeneous Catalysis' group from ETH. I would like to sincerely thank the present and past members including: Flavien, Vicky, Urs, Petr, Beata, Marco R., René, Waiz, Amaia, Kim, Ali, Rosh, Christian P., Martin, Matthäus, Marco T., Arno, Zhiqiang, Bahir, Sotiria, Piotr, Evalyn, Amy, Teng, Saeed, Jacinta, Jerick, Kanak, Charlotte and Daniela. Though I met you guys mostly during group meetings and group trips, it was great getting to know you.

Finally, I would like to express my deepest gratitude to my beloved parents- Sridhar and Jayashree. Thank you *Amma* and *Appa* for motivating me, standing by me and inspiring me all

---

along this journey. I am immensely grateful to my dear husband, Rajesh. You have made my life as happy and exciting as it can be. I am also thankful to my dear brother, Shreyas, who was the source of much needed cheer and laughter. Your jokes and light-heartedness surely helped me stay relaxed along the way. I am deeply thankful to the rest of my family members who encouraged and supported me in every way they could.



# Appendix

---

## References

- [1] K. Skalska, J. S. Miller, S. Ledakowicz, *Sci. Total Environ.* **2010**, *408*, 3976–3989.
- [2] M. Radojevic, *Environ. Pollut.* **1998**, *102*, 685–689.
- [3] K. Wark, C. F. Warner, in *Air Pollution*, Second Ed., **1981**.
- [4] J. Wright, *Environmental Chemistry*, Routledge, **2004**.
- [5] P. Forzatti, L. Lietti, E. Tronconi, in *Catal. Sustain. Energy Prod.*, Wiley-VCH Verlag GmbH & Co. KGaA, **2009**, 393–438.
- [6] T. Lee, J. Park, S. Kwon, J. Lee, J. Kim, *Sci. Total Environ.* **2013**, *461–462*, 377–385.
- [7] X. Wang, D. Westerdahl, J. Hu, Y. Wu, H. Yin, X. Pan, K. M. Zhang, *Atmos. Environ.* **2012**, *46*, 45–55.
- [8] M. Koebel, M. Elsener, M. Kleemann, *Catal. Today* **2000**, *59*, 335–345.
- [9] M. Koebel\*, E. O. Strutz, *Ind. Eng. Chem. Res.* **2003**, *42*, 2093–2100.
- [10] M. Koebel, M. Elsener, G. Madia, *Recent Advances in the Development of Urea-SCR for Automotive Applications*, SAE Technical Paper, **2001**.
- [11] M. Koebel, E. O. Strutz, *Ind. Eng. Chem. Res.* **2003**, *42*, 2093–2100.
- [12] I. A. Reşitoğlu, K. Altinişik, A. Keskin, *Clean Technol. Environ. Policy* **2014**, *17*, 15–27.
- [13] M. Eichelbaum, R. J. Farrauto, M. J. Castaldi, *Appl. Catal. B Environ.* **2010**, *97*, 90–97.
- [14] Handling, Diesel engines - NOx reduction agent AUS 32 - Part 3: Storage, transportation and storing, *International Standards ISO 22241-3*, **2008**.
- [15] D. Peitz, Investigations on the Catalytic Decomposition of Guanidinium Formate , Ammonium Formate and Methanamide as NH<sub>3</sub> -Precursors for the Selective Catalytic Reduction of NO<sub>x</sub>, ETH Diss., **2012**.
- [16] O. Kröcher, P. Daniel, *Catalyst for the conversion of liquid ammonia precursor solutions to gaseous ammonia avoiding the formation of undesired side products*, **2013**, WO2013110424 (A1).
- [17] O. Kröcher, P. Daniel, *Ammonia Generator Converting Liquid Ammonia Precursor Solutions to Gaseous Ammonia for Denox-Applications Using Selective Catalytic Reduction of Nitrogen Oxides*, **2012**, WO2012104205 (A1).
- [18] C. Gerhart, H.-P. Krimmer, B. Hammer, B. Schulz, O. Kröcher, D. Peitz, T. Sattelmayer, P. Toshev, G. Wachtmeister, A. Heubuch, et al., *SAE Int.J.Engines* **2012**, *5*, 938–946.
- [19] D. Peitz, A. M. Bernhard, M. Elsener, O. Kröcher, *Top. Catal.* **2013**, *56*, 19–22.
- [20] A. Solla, M. Westerholm, C. Söderström, K. Tormonen, T. Härmä, T. Nissinen, J. Kukkonen, *Catalytic process for reducing nitrogen oxides in flue gases and reducing agent composition*, **2005**, US7595034.
- [21] “Kemira and Terra Environmental Technologies Inc. signed license agreement of

- Kemira's Denoxium," can be found under <http://www.kemira.com/en/media/whatsup/Pages/KemiraTerra\Denoxium.aspx>.
- [22] T. Highfield, in *Present. Dir. Engine-Efficiency Emiss. Res. Conf. Detroit*, **2011**.
- [23] O. Kröcher, M. Elsener, E. Jacob, *Appl. Catal. B Environ.* **2009**, *88*, 66–82.
- [24] B. Hammer, H. P. Krimmer, B. Schulz, E. Jacob, *Use of Aqueous Guanidinium Formate Solutions for the Selective Catalytic Reduction of Nitrogen Oxides in Exhaust Gases of Vehicles*, **2014**, US8652426 B2.
- [25] M. Sridhar, J. A. van Bokhoven, O. Kröcher, *Appl. Catal. A Gen.* **2014**, *486*, 219–229.
- [26] P. Sabatier, A. Mailhe, *CR Hebd. Séanc. Acad. Sci., Paris C* **1911**, *152*, 1212–1215.
- [27] J. M. Trillo, G. Munuera, J. M. Criado, *Catal. Rev.* **1972**, *7*, 51–86.
- [28] J. M. Criado, F. Gonzalez, J. M. Trillo, *J. Catal.* **1971**, *23*, 11–18.
- [29] M. Ai, *J. Catal.* **1977**, *50*, 291–300.
- [30] G. Dalmai, A. Frachon de Pradel, B. Imelik, in *Proc. Second Int. Congr. Catal.*, Paris, **1960**, p. 890.
- [31] P. Mars, J. J. F. Scholten, P. Zwietering, *Adv. Catal* **1963**, *14*, 10–1016.
- [32] G. Munuera, *J. Catal.* **1970**, *18*, 19–29.
- [33] J. Fahrenfort, L. L. Van Reijen, W. M. H. Sachtler, J. H. deBoer, **1959**.
- [34] K. Goto, H. Ochi, T. Okura, *Bull. Chem. Soc. Jpn.* **1958**, *31*, 783–784.
- [35] B. Imelik, J. Francoisrossetti, P. Sigli, *J. Chim. Phys. Physico-Chimie Biol.* **1959**, *56*, 1048–1050.
- [36] Y. Noto, K. Fukuda, T. Onishi, K. Tamaru, *Trans. Faraday Soc.* **1967**, *63*, 2300–2308.
- [37] J. B. Peri, *J. Phys. Chem.* **1965**, *69*, 220–230.
- [38] J. B. Peri, A. L. H. Jr., *J. Phys. Chem.* **1968**, *72*, 2926–2933.
- [39] W. M. H. Sachtler, J. Fahrenfort, Paris, **1960**, 853–863.
- [40] Y. Tang, C. A. Roberts, R. T. Perkins, I. E. Wachs, *Surf. Sci.* **2016**, *650*, 103–110.
- [41] R. J. Madix, *Adv. Catal.* **1980**, *29*, 1–53.
- [42] M. Aizawa, Y. Morikawa, Y. Namai, H. Morikawa, Y. Iwasawa, *J. Phys. Chem. B* **2005**, *109*, 18831–18838.
- [43] \* Yoshitada Morikawa ‡, §. Ittetsu Takahashi ‡, §. Masaki Aizawa, §. Yoshimichi Namai, || Takehiko Sasaki, \* and Yashuhiro Iwasawa§, *J. Phys. Chem. B* **2004**, *108*, 14446–14451.
- [44] Q. Luo, M. Beller, H. Jiao, *J. Theor. Comput. Chem.* **2013**, *12*, 1330001.
- [45] H. Onishi, T. Aruga, Y. Iwasawa, *J. Catal.* **1994**, *146*, 557–567.
- [46] Y. Noto, K. Fukuda, T. Onishi, K. Tamaru, *Trans. Faraday Soc.* **1967**, *63*, 3081–3087.

- 
- [47] H. Onishi, T. Aruga, Y. Iwasawa, *J. Am. Chem. Soc.* **1993**, *115*, 10460–10461.
- [48] Y. Uemura, T. Taniike, M. Tada, Y. Morikawa, Y. Iwasawa, *J. Phys. Chem. C* **2007**, *111*, 16379–16386.
- [49] M. Bowker, R. J. Madix, *Surf. Sci.* **1981**, *102*, 542–565.
- [50] B. A. Sexton, R. J. Madix, *Surf. Sci.* **1981**, *105*, 177–195.
- [51] D. A. Outka, R. J. Madix, *Surf. Sci.* **1987**, *179*, 361–376.
- [52] A. A. Gokhale, J. A. Dumesic, M. Mavrikakis, *J. Am. Chem. Soc.* **2008**, *130*, 1402–1414.
- [53] T. Shido, Y. Iwasawa, *J. Catal.* **1991**, *129*, 343–355.
- [54] T. Shido, K. Asakura, Y. Iwasawa, *J. Catal.* **1990**, *122*, 55–67.
- [55] L. C. Grabow, A. A. Gokhale, S. T. Evans, J. a Dumesic, M. Mavrikakis, *J. Phys. Chem. C* **2008**, *112*, 4608–4617.
- [56] T. Shido, Y. Iwasawa, *J. Catal.* **1993**, *141*, 71–81.
- [57] J. H. Pazmiño, M. Shekhar, W. Damion Williams, M. Cem Akatay, J. T. Miller, W. Nicholas Delgass, F. H. Ribeiro, *J. Catal.* **2012**, *286*, 279–286.
- [58] G. Jacobs, P. M. Patterson, U. M. Graham, A. C. Crawford, A. Dozier, B. H. Davis, *J. Catal.* **2005**, *235*, 79–91.
- [59] R. Leppelt, B. Schumacher, V. Plzak, M. Kinne, R. J. Behm, *J. Catal.* **2006**, *244*, 137–152.
- [60] G. A. Filonenko, W. L. Vrijburg, E. J. M. Hensen, E. A. Pidko, *J. Catal.* **2015**, DOI 10.1016/j.jcat.2015.10.002.
- [61] T. C. Johnson, D. J. Morris, M. Wills, *Chem. Soc. Rev.* **2010**, *39*, 81–88.
- [62] R. H. Julian, *Chem. Commun.* **2012**, *48*, 4184–4186.
- [63] D. A. Bulushev, S. Beloshapkin, J. R. H. Ross, *Catal. Today* **2010**, *154*, 7–12.
- [64] Y. Huang, X. Zhou, M. Yin, C. Liu, W. Xing, *Chem. Mater.* **2010**, *22*, 5122–5128.
- [65] S. K. Hoekman, A. Broch, C. Robbins, R. Purcell, *Int. J. Greenh. Gas Control* **2010**, *4*, 44–50.
- [66] Q. Bi, X. Du, L. He, Y. Liu, Y. Cao, H. He, K. Fan, *J. Am. Chem. Soc.* **2012**, *134*, 8926–8933.
- [67] A. Ueno, T. Onishi, K. Tamaru, *Trans. Faraday Soc.* **1970**, *66*, 756.
- [68] T. van Herwijnen, W. A. de Jong, *J. Catal.* **1980**, *63*, 83–93.
- [69] T. van Herwijnen, R. T. Guuczalski, W. A. de Jong, *J. Catal.* **1980**, *63*, 94–101.
- [70] P. G. Gopal, R. L. Schneider, K. L. Watters, *J. Catal.* **1987**, *105*, 366–372.
- [71] G. Jacobs, P. M. Patterson, U. M. Graham, A. C. Crawford, B. H. Davis, *Int. J. Hydrogen Energy* **2005**, *30*, 1265–1276.
-

- [72] E. Chenu, G. Jacobs, A. C. Crawford, R. A. Keogh, P. M. Patterson, D. E. Sparks, B. H. Davis, *Appl. Catal. B Environ.* **2005**, *59*, 45–56.
- [73] G. Jacobs, *Appl. Catal. A Gen.* **2004**, *268*, 255–266.
- [74] J. M. Pigos, C. J. Brooks, G. Jacobs, B. H. Davis, *Appl. Catal. A Gen.* **2007**, *328*, 14–26.
- [75] H. N. Evin, G. Jacobs, J. Ruiz-Martinez, U. M. Graham, A. Dozier, G. Thomas, B. H. Davis, *Catal. Letters* **2008**, *122*, 9–19.
- [76] B. Loges, A. Boddien, F. Gärtner, H. Junge, M. Beller, *Top. Catal.* **2010**, *53*, 902–914.
- [77] M. Grasemann, G. Laurenczy, *Energy Environ. Sci.* **2012**, *5*, 8171–8181.
- [78] S. Enthaler, *ChemSusChem* **2008**, *1*, 801–804.
- [79] F. Joó, *ChemSusChem* **2008**, *1*, 805–808.
- [80] G. A. Olah, G. K. S. Prakash, A. Goeppert, *J. Am. Chem. Soc.* **2011**, *133*, 12881–12898.
- [81] B. Loges, A. Boddien, H. Junge, M. Beller, *Angew. Chemie Int. Ed.* **2008**, *47*, 3962–3965.
- [82] H. Junge, A. Boddien, F. Capitta, B. Loges, J. R. Noyes, S. Gladiali, M. Beller, *Tetrahedron Lett.* **2009**, *50*, 1603–1606.
- [83] S. Fukuzumi, T. Kobayashi, T. Suenobu, *ChemSusChem* **2008**, *1*, 827–834.
- [84] A. Boddien, B. Loges, H. Junge, F. Gärtner, J. R. Noyes, M. Beller, *Adv. Synth. Catal.* **2009**, *351*, 2517–2520.
- [85] A. Boddien, B. Loges, H. Junge, M. Beller, *ChemSusChem* **2008**, *1*, 751–758.
- [86] K. Tedsree, T. Li, S. Jones, C. W. A. Chan, K. M. K. Yu, P. A. J. Bagot, E. A. Marquis, G. D. W. Smith, S. C. E. Tsang, *Nat Nano* **2011**, *6*, 302–307.
- [87] N. Hoshi, M. Nakamura, K. Kida, *Electrochem. commun.* **2007**, *9*, 279–282.
- [88] H.-F. Wang, Z.-P. Liu, *J. Phys. Chem. C* **2009**, *113*, 17502–17508.
- [89] M. Ojeda, E. Iglesia, *Angew. Chemie - Int. Ed.* **2009**, *48*, 4800–4803.
- [90] X. Zhou, Y. Huang, W. Xing, C. Liu, J. Liao, T. Lu, *Chem. Commun.* **2008**, 3540–3542.
- [91] A. Gazsi, T. Bánsági, F. Solymosi, *J. Phys. Chem. C* **2011**, *115*, 15459–15466.
- [92] F. Solymosi, Á. Koós, N. Liliom, I. Ugrai, *J. Catal.* **2011**, *279*, 213–219.
- [93] Y. Zhao, L. Deng, S.-Y. Tang, D.-M. Lai, B. Liao, Y. Fu, Q.-X. Guo, *Energy & Fuels* **2011**, *25*, 3693–3697.
- [94] G. J. Hutchings, *J. Catal.* **1985**, *96*, 292–295.
- [95] G. J. Hutchings, *Catal. Today* **2005**, *100*, 55–61.
- [96] M. Haruta, T. Kobayashi, H. Sano, N. Yamada, *Chem. Lett.* **1987**, *16*, 405–408.
- [97] M. Haruta, *Nature* **2005**, *437*, 1098–9.
- [98] G. C. Bond, P. A. Sermon, G. Webb, D. A. Buchanan, P. B. Wells, *J. Chem. Soc. {,} Chem. Commun.* **1973**, 444b–445.

- 
- [99] C. W. Corti, R. J. Holliday, D. T. Thompson, *Gold Bull.*, **35**, 111–117.
- [100] A. S. K. Hashmi, G. J. Hutchings, *Angew. Chemie Int. Ed.* **2006**, *45*, 7896–7936.
- [101] D. T. Thompson, *Platin. Met. Rev.* **2004**, *48*, 169–172.
- [102] T. Keel, *Chem. Ind.* **2010**, 24–27.
- [103] D. A. Outka, R. J. Madix, *J. Am. Chem. Soc.* **1987**, *109*, 1708–1714.
- [104] P. Hauwert, R. Boerleider, S. Warsink, J. J. Weigand, C. J. Elsevier, *J. Am. Chem. Soc.* **2010**, *132*, 16900–16910.
- [105] S. Fukuzumi, T. Kobayashi, T. Suenobu, *J. Am. Chem. Soc.* **2010**, *132*, 1496–1497.
- [106] G. L. Beltramo, T. E. Shubina, M. T. M. Koper, *ChemPhysChem* **2005**, *6*, 2597–2606.
- [107] S. Singh, S. Li, R. Carrasquillo-Flores, A. C. Alba-Rubio, J. A. Dumesic, M. Mavrikakis, *AIChE J.* **2014**, *60*, 1303–1319.
- [108] T. Barakat, J. C. Rooke, E. Genty, R. Cousin, S. Siffert, B.-L. Su, *Energy Environ. Sci.* **2013**, *6*, 371–391.
- [109] G. Bond, *Gold Bull.*, *42*, 337–342.
- [110] D. Andreeva, *Gold Bull.*, *35*, 82–88.
- [111] Q. Fu, H. Saltsburg, M. Flytzani-Stephanopoulos, *Science (80-. )*. **2003**, *301*, 935–938.
- [112] M. Flytzani-Stephanopoulos, *Acc. Chem. Res.* **2014**, *47*, 783–792.
- [113] R. Burch, *Phys. Chem. Chem. Phys.* **2006**, *8*, 5483–5500.
- [114] M. Yang, L. F. Allard, M. Flytzani-Stephanopoulos, *J. Am. Chem. Soc.* **2013**, *135*, 3768–3771.
- [115] J. A. Rodriguez, S. D. Senanayake, D. Stacchiola, P. Liu, J. Hrbek, *Acc. Chem. Res.* **2014**, *47*, 773–782.
- [116] D. Widmann, R. J. Behm, *Angew. Chemie - Int. Ed.* **2011**, *50*, 10241–10245.
- [117] R. Y. N. Ho, J. F. Liebman, V. J. Selverstone, *Active Oxygen in Chemistry*, Springer Netherlands, **1995**.
- [118] B. N. Zope, D. D. Hibbitts, M. Neurock, R. J. Davis, *Science (80-. )*. **2010**, *330*, 74–78.
- [119] J. Liu, X.-M. Cao, P. Hu, *Phys. Chem. Chem. Phys.* **2014**, *16*, 4176–4185.
- [120] M. S. Ide, R. J. Davis, *Acc. Chem. Res.* **2014**, *47*, 825–833.
- [121] T. Fujitani, I. Nakamura, *Angew. Chemie Int. Ed.* **2011**, *50*, 10144–10147.
- [122] B. S. Yeo, S. L. Klaus, P. N. Ross, R. a Mathies, A. T. Bell, *Chemphyschem* **2010**, *11*, 1854–1857.
- [123] C. Shang, Z.-P. Liu, *J. Am. Chem. Soc.* **2011**, *133*, 9938–9947.
- [124] J. J. Bravo-Suarez, K. K. Bando, J. Lu, M. Haruta, T. Fujitani, T. Oyama, *J. Phys. Chem. C* **2008**, *112*, 1115–1123.
-

- 
- [125] C. R. Chang, Y. G. Wang, J. Li, *Nano Res.* **2011**, *4*, 131–142.
- [126] A. Bongiorno, U. Landman, *Phys. Rev. Lett.* **2005**, *95*, 1–4.
- [127] C. Sivadinarayana, T. V Choudhary, L. L. Daemen, J. Eckert, D. W. Goodman, *J. Am. Chem. Soc.* **2004**, *126*, 38–39.
- [128] J. Huang, T. Akita, J. Faye, T. Fujitani, T. Takei, M. Haruta, *Angew. Chemie Int. Ed.* **2009**, *48*, 7862–7866.
- [129] M. Ojeda, B. Z. Zhan, E. Iglesia, *J. Catal.* **2012**, *285*, 92–102.
- [130] I. Nova, E. Tronconi, *Urea-SCR Technology for deNOx after Treatment of Diesel Exhausts*, Springer, **2014**.
- [131] L. Delannoy, N. El Hassan, A. Musi, N. N. Le To, J.-M. Krafft, C. Louis, *J. Phys. Chem. B* **2006**, *110*, 22471–22478.
- [132] A. Cybulski, J. A. Moulijn, *Structured Catalysts and Reactors*, CRC Press, **2005**.
- [133] O. H. Laguna, M. I. Domínguez, M. A. Centeno, J. A. Odriozola, in (Ed.: E.B.T.-N.M. for C.A. Kemnitz), Elsevier, Amsterdam, **2016**, 81–120.
- [134] J. Zhang, Q. Xu, S. Yan, S. Zhao, C. Li, *Mater. Res. Bull.* **2014**, *53*, 3–4.
- [135] X. Quan, H. Tan, Q. Zhao, X. Sang, *J. Mater. Sci.* **2007**, *42*, 6287–6296.
- [136] M. Devadas, O. Kröcher, A. Wokaun, *React. Kinet. Catal. Lett.* **2005**, *86*, 347–354.
- [137] A. V Neimark, K. S. W. Sing, M. Thommes, in *Handb. Heterog. Catal.*, Wiley-VCH Verlag GmbH & Co. KGaA, **2008**.
- [138] J. B. Condon, Elsevier Science, Amsterdam, **2006**, pp. 1–27.
- [139] W. G. McMillan, E. Teller, *J. Phys. Chem.* **1951**, *55*, 17–20.
- [140] D. D. Perovic, C. J. Rossouw, A. Howie, *Ultramicroscopy* **1993**, *52*, 353–359.
- [141] S. Utsunomiya, R. C. Ewing, *Environ. Sci. Technol.* **2003**, *37*, 786–791.
- [142] P. D. Nellist, in (Eds.: P.W. Hawkes, J.C.H. Spence), Springer New York, New York, NY, **2007**, 65–132.
- [143] C. C. Chusuei, D. W. Goodman, *Encycl. Phys. Sci. Technol.* **2002**, *17*, 921–938.
- [144] J. Sharma, B. C. Beard, in (Ed.: S.N. Bulusu), Springer Netherlands, Dordrecht, **1990**, 569–585.
- [145] E. Taillandier, J. Liquier, J. A. Taboury, **1985**.
- [146] M. P. Fuller, P. R. Griffiths, *Anal. Chem.* **1978**, *50*, 1906–1910.
- [147] M. B. Mitchell, in *Struct. Relations Polym.*, 351–375.
- [148] D. Peitz, A. Bernhard, M. Elsener, O. Kröcher, *Rev. Sci. Instrum.* **2011**, *82*, 084101.
- [149] A. M. Bernhard, D. Peitz, M. Elsener, O. Kröcher, *Top. Catal.* **2013**, *56*, 130–133.
- [150] S. Y. Joshi, M. P. Harold, V. Balakotaiah, *Chem. Eng. Sci.* **2010**, *65*, 1729–1747.

- 
- [151] More, Hayes, Liu, Votsmeier, Checkel, *Top. Catal.* **2006**, 37, 155–159.
- [152] A. M. Bernhard, D. Peitz, M. Elsener, T. Schildhauer, O. Kröcher, *Catal. Sci. Technol.* **2013**, 3, 942.
- [153] L. T. Gibson, B. G. Cooksey, D. Littlejohn, N. H. Tennent, *Anal. Chim. Acta* **1997**, 341, 1–10.
- [154] M. Kleemann, M. Elsener, M. Koebel, A. Wokaun, *Ind. Eng. Chem. Res.* **2000**, 39, 4120–4126.
- [155] H. S. Han, J. W. Kim, E. S. Kim, J. U. Han, *Catalyst for Selective Catalytic Reduction, with Improved Durability*, **2013**.
- [156] A. . Harinath, *Catalytic Devices for Converting Urea to Ammonia*, **2011**.
- [157] A. Luengnarumitchai, S. Osuwan, E. Gulari, *Int. J. Hydrogen Energy* **2004**, 29, 429–435.
- [158] W.-Y. Yu, W.-S. Lee, C.-P. Yang, B.-Z. Wan, *J. Chinese Inst. Chem. Eng.* **2007**, 38, 151–160.
- [159] G. K. Bethke, H. H. Kung, *Appl. Catal. A Gen.* **2000**, 194, 43–53.
- [160] L. H. Chang, N. Sasirekha, Y. W. Chen, *Catal. Commun.* **2007**, 8, 1702–1710.
- [161] R. Zanella, S. Giorgio, C. R. Henry, C. Louis, *J. Phys. Chem. B* **2002**, 106, 7634–7642.
- [162] R. J. Farrauto, R. M. Heck, *Catal. Today* **1999**, 51, 351–360.
- [163] L. Gang, B. G. Anderson, J. Van Grondelle, R. A. Van Santen, *Appl. Catal.* **2003**, 40, 101–110.
- [164] L. Gang, B. G. Anderson, J. van Grondelle, R. A. van Santen, W. J. H. van Gennip, J. W. Niemantsverdriet, P. J. Kooyman, A. Knoester, H. H. Brongersma, *J. Catal.* **2002**, 206, 60–70.
- [165] J. L. Yu, P. E. Savage, *Ind. Eng. Chem. Res.* **1998**, 37, 2–10.
- [166] N. Akiya, P. E. Savage, *Aiche J.* **1998**, 44, 405–415.
- [167] P. G. Blake, C. Hinshelwood, *Proc. R. Soc. London. Ser. A. Math. Phys. Sci.* **1960**, 255, 444–455.
- [168] M. Sridhar, D. Peitz, J. A. van Bokhoven, O. Kröcher, *Chem. Commun. (Camb)*. **2014**, 50, 6998–7000.
- [169] O. Kröcher, M. Elsener, E. Jacob, in *5th Int. Exhaust Gas Part. Emiss. Forum*, **2008**, 19–20.
- [170] X. Zhu, M. Shen, L. L. Lobban, R. G. Mallinson, *J. Catal.* **2011**, 278, 123–132.
- [171] Y. Zhai, D. Pierre, R. Si, W. Deng, P. Ferrin, A. U. Nilekar, G. Peng, J. a. Herron, D. C. Bell, H. Saltsburg, et al., *Science (80-. )*. **2010**, 329, 1633–1636.
- [172] P. Panagiotopoulou, D. I. Kondarides, *J. Catal.* **2008**, 260, 141–149.
- [173] D. A. Bulushev, L. Jia, S. Beloshapkin, J. R. H. Ross, *Chem. Commun.* **2012**, 48, 4184.

- 
- [174] J. Zhu, J. L. Figueiredo, J. L. Faria, *Catal. Commun.* **2008**, *9*, 2395–2397.
- [175] X. Jiang, R. Zhou, P. Pan, B. Zhu, X. Yuan, X. Zheng, *Appl. Catal. A Gen.* **1997**, *150*, 131–141.
- [176] A. L. Borer, R. Prins, *J. Catal.* **1993**, *144*, 439–451.
- [177] J. Zhang, Q. Xu, Z. Feng, C. Li, in *Environ. Benign Photocatal. SE - 6* (Eds.: M. Anpo, P. V Kamat), Springer New York, **2006**, p. 116023.
- [178] A. G. Shastri, A K. Datye, J. Schwank, *J. Catal.* **1984**, *87*, 265–275.
- [179] D.-S. Kim, J.-H. Yang, S. Balaji, H.-J. Cho, M.-K. Kim, D.-U. Kang, Y. Djaoued, Y.-U. Kwon, *CrystEngComm* **2009**, *11*, 1621.
- [180] G. Ramis, G. Busca, C. Cristiani, L. Lietti, P. Forzatti, F. Bregani, *Langmuir* **1992**, *8*, 1744–1749.
- [181] Y.-S. Lin, C.-H. Chang, R. Gopalan, *Ind. Eng. Chem. Res.* **1994**, *33*, 860–870.
- [182] G. Busca, V. Lorenzelli, *Mater. Chem.* **1982**, *7*, 89–126.
- [183] S. E. Collins, M. a Baltanas, A. L. Bonivardi, *J. Phys. Chem. B* **2006**, *110*, 5498–5507.
- [184] C. Li, Y. Sakata, T. Arai, K. Domen, K. Maruya, T. Onishi, *J. Chem. Soc. Faraday Trans. 1* **1989**, *85*, 1451.
- [185] C. Morterra, N. A. Chiorino, G. Ghiotti, *J. Chem. Soc. Faraday Trans. 1* **1982**, *78*, 2649–2659.
- [186] G. Busca, J. Lamotte, J. Lavalley, V. Lorenzelli, C. Erba, *J. Am. Chem. Soc.* **1987**, *109*, 5197.
- [187] L. F. Liao, W. C. Wu, C. Y. Chen, J. L. Lin, *J. Phys. Chem. B* **2001**, *105*, 7678–7685.
- [188] J. M. Criado, F. Gonzalez, J. M. Trillo, *J. Catal.* **1971**, *23*, 11–18.
- [189] G. Samjeské, M. Osawa, *Angew. Chemie - Int. Ed.* **2005**, *44*, 5694–5698.
- [190] Z. Ma, H. Yin, S. Dai, *Catal. Letters* **2009**, *136*, 83–91.
- [191] J. Yu, G. Wu, G. Lu, D. Mao, Y. Guo, *RSC Adv.* **2014**, *4*, 16985.
- [192] Y.-X. Chen, M. Heinen, Z. Jusys, R. J. Behm, *Langmuir* **2006**, *22*, 10399–408.
- [193] M. Neurock, M. Janik, A. Wieckowski, *Faraday Discuss.* **2008**, *140*, 363–378.
- [194] M. Haruta, *J. Catal.* **2001**, *224*, 221–224.
- [195] R. Grisel, K.-J. Weststrate, A. Gluhoi, B. E. Nieuwenhuys, *Gold Bull.* **2002**, *35*, 39–45.
- [196] M. Mavrikakis, P. Stoltze, J. K. Nørskov, *Catal. Letters* **2000**, *64*, 101–106.
- [197] J. Shen, R. Cortright, Y. Chen, J. Dumesic, *Catal. Letters* **1994**, *26*, 247–257.
- [198] M. Kleemann, *Appl. Catal. B Environ.* **2000**, *27*, 231–242.
- [199] Y. Cui, H. Zhang, H. Xu, W. Li, *Appl. Catal. A Gen.* **2007**, *331*, 60–69.
- [200] L. Leveles, K. Seshan, J. a. Lercher, L. Lefferts, *J. Catal.* **2003**, *218*, 296–306.
-

- 
- [201] G. C. Bond, *Catal. Rev.* **2008**, *50*, 532–567.
- [202] G. Bond, M. A. Keane, H. Kral, J. A. Lercher, *Catal. Rev.* **2000**, *42*, 323–383.
- [203] D. Fein, *J. Catal.* **2002**, *210*, 241–254.
- [204] A. Solla, M. Westerholm, C. Söderström, K. Tormonen, *Effect of Ammonium Formate and Mixtures of Urea and Ammonium Formate on Low Temperature Activity of SCR Systems*, SAE Technical Paper, **2013**.
- [205] T. Nissinen, J. Kukkonen, *Catalytic Process for Reducing Nitrogen Oxides in Flue Gases and Reducing Agent Composition*, **2006**, US7595034 B2.
- [206] M. Armin, T. Wahl, A. Ulrich, F. Brenner, M. Bareis, H. Horst, *Verfahren Und Vorrichtung Zur Selektiven Katalytischen NO<sub>x</sub>-Reduktion Method and Apparatus for Selective Catalytic NO<sub>x</sub> Reduction*, **2013**, DE19728343 C5.
- [207] M. Koebel, M. Elsener, *Ind. Eng. Chem. Res.* **1998**, *37*, 3864–3868.
- [208] M. Sridhar, D. Ferri, M. Elsener, J. A. van Bokhoven, O. Kröcher, *ACS Catal.* **2015**, *5*, 4772–4782.
- [209] M. Neurock, M. Janik, A. Wieckowski, *Faraday Discuss.* **2009**, *140*, 363–378.
- [210] J. M. Criado, F. Gonzalez, J. M. Trillo, *J. Catal.* **1971**, *23*, 11–18.
- [211] S. D. Senanayake, D. Stacchiola, J. Evans, M. Estrella, L. Barrio, M. Pérez, J. Hrbek, J. A. Rodriguez, *J. Catal.* **2010**, *271*, 392–400.
- [212] G. Jacobs, B. H. Davis, *Int. J. Hydrogen Energy* **2010**, *35*, 3522–3536.
- [213] J. M. Pigos, C. J. Brooks, G. Jacobs, B. H. Davis, *Appl. Catal. A Gen.* **2007**, *319*, 47–57.
- [214] H. Onishi, T. Aruga, Y. Iwasawa, *J. Catal.* **1994**, *146*, 557–567.
- [215] K. L. Miller, C. W. Lee, J. L. Falconer, J. W. Medlin, *J. Catal.* **2010**, *275*, 294–299.
- [216] M. Kantcheva, M. U. Kucukkal, S. Suzer, *J. Catal.* **2000**, *190*, 144–156.
- [217] K. Tanaka, J. M. White, *J. Phys. Chem.* **1982**, *86*, 3977–3980.
- [218] K. Hadjiivanov, V. Bushev, M. Kantcheva, D. Klissurski, *Langmuir* **1994**, *10*, 464–471.
- [219] D. A. Panayotov, S. P. Burrows, J. T. Yates, J. R. Morris, *J. Phys. Chem. C* **2011**, *115*, 22400–22408.
- [220] D. A. Panayotov, J. T. Yates, *J. Phys. Chem. C* **2007**, *111*, 2959–2964.
- [221] E. A. Ivanov, G. Y. Popova, Y. A. Chesalov, T. V. Andrushkevich, *J. Mol. Catal. A Chem.* **2009**, *312*, 92–96.
- [222] B. B. Chen, C. Shi, M. Crocker, Y. Wang, A. M. Zhu, *Appl. Catal. B Environ.* **2013**, *132-133*, 245–255.
- [223] O. S. Joo, K. D. Jung, S. H. Han, S. J. Uhm, D. K. Lee, S. K. Ihm, *Appl. Catal. A Gen.* **1996**, *135*, 273–286.
- [224] S. L. Silva, R. M. Lemor, F. M. Leibsle, *Surf. Sci.* **1999**, *421*, 135–145.
-

- 
- [225] G. M. Mullen, J. Gong, T. Yan, M. Pan, C. B. Mullins, *Top. Catal.* **2013**, *56*, 1499–1511.
- [226] J. Saavedra, H. a. Doan, C. J. Pursell, L. C. Grabow, B. D. Chandler, *Science (80-. )*. **2014**, *345*, 1599–1602.
- [227] B. Chowdhury, J. J. Bravo-Suarez, N. Mimura, J. Lu, K. K. Bando, S. Tsubota, M. Haruta, *J. Phys. Chem. B* **2006**, *110*, 22995–9.
- [228] J. Huang, T. Takei, T. Akita, H. Ohashi, M. Haruta, *Appl. Catal. B Environ.* **2010**, *95*, 430–438.
- [229] J. Huang, T. Takei, H. Ohashi, M. Haruta, *Appl. Catal. A Gen.* **2012**, *435-436*, 115–122.
- [230] D. Hibbitts, E. Iglesia, *Acc. Chem. Res.* **2015**, *48*, 1254–1262.
- [231] D. M. Perez Ferrandez, I. Herguedas Fernandez, M. P. G. Teley, M. H. J. M. de Croon, J. C. Schouten, T. A. Nijhuis, *J. Catal.* **2015**, *330*, 396–405.
- [232] D. I. Pineda, J.-Y. Chen, *Int. J. Hydrogen Energy* **2015**, *40*, 6059–6071.
- [233] M. K. Kim, P. S. Kim, H. J. Kwon, I.-S. Nam, B. K. Cho, S. H. Oh, *Chem. Eng. J.* **2012**, *209*, 280–292.
- [234] X. Zheng, J. Mantzaras, R. Bombach, *Combust. Flame* **2014**, *161*, 332–346.
- [235] C. Appel, J. Mantzaras, R. Schaeren, R. Bombach, B. Kaeppli, A. Inauen, *Proc. Combust. Inst.* **2002**, *29*, 1031.
- [236] X. Zheng, J. Mantzaras, R. Bombach, *Proc. Combust. Inst.* **2013**, *34*, 2279–2287.
- [237] Y. F. Tham, J. Y. Chen, R. W. Dibble, *Proc. Combust. Inst.* **2009**, *32 II*, 2827–2833.
- [238] A. K. Chaniotis, D. Poulikakos, *J. Power Sources* **2005**, *142*, 184–193.
- [239] M. Reinke, J. Mantzaras, R. Schaeren, R. Bombach, A. Inauen, S. Schenker, *Combust. Flame* **2004**, *136*, 217–240.
- [240] G. Vourliotakis, G. Skevis, M. A. Founti, Z. Al-Hamamre, D. Trimis, *Int. J. Hydrogen Energy* **2008**, *33*, 2816–2825.
- [241] C.-P. Chou, J.-Y. Chen, G. H. Evans, W. S. Winters, *Combust. Sci. Technol.* **2000**, *150*, 27–57.
- [242] S. Karagiannidis, J. Mantzaras, K. Boulouchos, *Proc. Combust. Inst.* **2011**, *33*, 3241–3249.
- [243] H. K. Moffat, P. Glarborg, R. J. Kee, J. F. Grcar, J. A. Miller, *Sandia Natl. Lab. Rep. SAND91-8001* **1991**.
- [244] J. Kim, E. Samano, B. E. Koel, *Surf. Sci.* **2006**, *600*, 4622–4632.
- [245] X. Deng, B. K. Min, A. Guloy, C. M. Friend, *J. Am. Chem. Soc.* **2005**, *127*, 9267–9270.
- [246] R. L. Wells, T. Fort Jr., *Surf. Sci.* **1972**, *32*, 554–560.
- [247] O. Deutschmann, L. I. Maier, U. Riedel, A. H. Stroemman, R. W. Dibble, *Catal. Today* **2000**, *59*, 141–150.

- [248] M. E. Coltrin, R. J. Kee, F. M. Rupley, *Surface Chemkin-iii: A Fortran Package for Analyzing Heterogeneous Chemical Kinetics At a Solid-Surface— Gas-Phase Interface*, Sandia National Labs., Albuquerque, NM (United States), **1996**.
- [249] M. Okumura, Y. Kitagawa, M. Haruta, K. Yamaguchi, *Chem. Phys. Lett.* **2001**, *346*, 163–168.
- [250] Z. Duan, G. Henkelman, *ACS Catal.* **2015**, *5*, 1589–1595.
- [251] Y. Xu, M. Mavrikakis, *J. Phys. Chem. B* **2003**, *107*, 9298–9307.
- [252] M. A. Henderson, *Langmuir* **1996**, *12*, 5093–5098.
- [253] C. G. Long, J. D. Gilbertson, G. Vijayaraghavan, K. J. Stevenson, C. J. Pursell, B. D. Chandler, *J. Am. Chem. Soc.* **2008**, *130*, 10103–10115.
- [254] D. Peitz, A. Bernhard, M. Elsener, O. Kröcher, *Rev. Sci. Instrum.* **2011**, *82*, 084101.
- [255] M. Daté, M. Haruta, *J. Catal.* **2001**, *201*, 221–224.
- [256] T. Fujitani, I. Nakamura, M. Haruta, *Catal. Letters* **2014**, *144*, 1475–1486.
- [257] Y.-C. Xie, Y.-Q. Tang, in *Adv. Catal.* (Ed.: H.P. and P.B.W.B.T.-A. in C. D.D. Eley), Academic Press, **1990**, 1–43.
- [258] T. Sakwarathorn, A. Luengnaruemitchai, S. Pongstabodee, *J. Ind. Eng. Chem.* **2011**, *17*, 747–754.
- [259] X. Zhang, H. Shi, B. Xu, *Catal. Today* **2007**, *122*, 330–337.
- [260] M. Ousmane, L. F. Liotta, G. Di Carlo, G. Pantaleo, A. M. Venezia, G. Deganello, L. Retailleau, A. Boreave, A. Giroir-Fendler, *Appl. Catal. B Environ.* **2011**, *101*, 629–637.
- [261] Y. Zhang, H. Zhang, Y. Xu, Y. Wang, *J. Solid State Chem.* **2004**, *177*, 3490–3498.
- [262] Y. Liu, S. Zhou, J. Li, Y. Wang, G. Jiang, Z. Zhao, B. Liu, X. Gong, A. Duan, J. Liu, et al., *Appl. Catal. B Environ.* **2015**, *168-169*, 125–131.
- [263] J. Zhang, M. Li, Z. Feng, J. Chen, C. Li, *J. Phys. Chem. B* **2006**, *110*, 927–935.
- [264] C. P. Sibui, S. R. Kumar, P. Mukundan, K. G. K. Warriar, *Chem. Mater.* **2002**, *14*, 2876–2881.
- [265] K. V. Baiju, C. P. Sibui, K. Rajesh, P. Krishna Pillai, P. Mukundan, K. G. K. Warriar, W. Wunderlich, *Mater. Chem. Phys.* **2005**, *90*, 123–127.
- [266] M.-Y. Xing, D.-Y. Qi, J.-L. Zhang, F. Chen, *Chem. - A Eur. J.* **2011**, *17*, 11432–11436.
- [267] A. M. Ruiz, A. Cornet, J. R. Morante, *Sensors Actuators B Chem.* **2005**, *111–112*, 7–12.
- [268] F. Li, X. Li, M. Hou, *Appl. Catal. B Environ.* **2004**, *48*, 185–194.
- [269] Z. Hu, B. Li, X. Sun, H. Metiu, *J. Phys. Chem. C* **2011**, *115*, 3065–3074.
- [270] R. Gopalan, Y. S. Lin, *Ind. Eng. Chem. Res.* **1995**, *34*, 1189–1195.
- [271] S. D. Škapin, D. Kolar, D. Suvorov, *J. Eur. Ceram. Soc.* **2000**, *20*, 1179–1185.
- [272] Q. Mu, Y. Wang, *J. Alloys Compd.* **2011**, *509*, 396–401.

- 
- [273] S. Bernal, J. A. Diaz, R. Garcia, J. M. Rodriguez-Izquierdo, *J. Mater. Sci.* **1985**, *20*, 537–541.
- [274] B. Bakiz, F. Guinneton, M. Arab, A. Benlhachemi, S. Villain, P. Satre, J.-R. Gavarri, *Adv. Mater. Sci. Eng.* **2010**, *2010*, 1–6.
- [275] P. Fleming, R. a. Farrell, J. D. Holmes, M. A. Morris, *J. Am. Ceram. Soc.* **2010**, *93*, 1187–1194.
- [276] P. Ganesh, P. R. C. Kent, G. M. Veith, *J. Phys. Chem. Lett.* **2011**, *2*, 2918–2924.
- [277] C. Li, H. Liu, J. Yang, *Nanoscale Res. Lett.* **2015**, *10*, 1–6.
- [278] H. Zhuang, S. Zhang, X. Zhang, C. Xue, B. Li, D. Wang, J. Shen, *Appl. Surf. Sci.* **2008**, *254*, 3057–3060.
- [279] J. Ding, Y. Wu, W. Sun, Y. Li, *J. Rare Earths* **2006**, *24*, 440–442.
- [280] J. A. Navío, G. Colón, M. Macías, C. Real, M. I. Litter, *Appl. Catal. A Gen.* **1999**, *177*, 111–120.
- [281] P. G. Savva, K. Goundani, J. Vakros, K. Bourikas, C. Fountzoula, D. Vattis, A. Lycourghiotis, C. Kordulis, *Appl. Catal. B Environ.* **2008**, *79*, 199–207.
- [282] G. Li, L. Hu, J. M. Hill, *Appl. Catal. A Gen.* **2006**, *301*, 16–24.
- [283] B. M. Reddy, I. Ganesh, *J. Mol. Catal. A Chem.* **2001**, *169*, 207–223.
- [284] J. S. Chung, R. Miranda, C. O. Bennett, *J. Catal.* **1988**, *114*, 398–410.
- [285] X. Guo, D. Mao, G. Lu, S. Wang, G. Wu, *J. Mol. Catal. A Chem.* **2011**, *345*, 60–68.
- [286] J. D. Lessard, I. Valsamakis, M. Flytzani-Stephanopoulos, *Chem. Commun.* **2012**, *48*, 4857–4859.
- [287] M. Mihaylov, E. Ivanova, Y. Hao, K. Hadjiivanov, H. Knözinger, B. C. Gates, *J. Phys. Chem. C* **2008**, *112*, 18973–18983.
- [288] D. Peitz, A. Bernhard, O. Kröcher, in *Urea-SCR Technol. deNO<sub>x</sub> After Treat. Diesel Exhausts*, Springer, **2014**, 485–506.
- [289] C. Choong, Z. Zhong, L. Huang, A. Borgna, L. Hong, L. Chen, J. Lin, *ACS Catal.* **2014**, *4*, 2359–2363.
- [290] J. Lin, K. G. Neoh, W. koon Teo, *J. Chem. Soc. {,} Faraday Trans.* **1994**, *90*, 355–362.
- [291] G. Bond, *Gold Bull.* **2010**, *43*, 88–93.
- [292] P. Panagiotopoulou, D. I. Kondarides, *J. Catal.* **2009**, *267*, 57–66.
- [293] M. Zboray, A. T. Bell, E. Iglesia, *J. Phys. Chem.* **2009**, *113*, 12380–12386
- [294] B. Chowdhury, J. J. Bravo-Suárez, N. Mimura, K. K. Bando, S. Tsubota, M. Haruta, *J. Phys. Chem. B* **2006**, *110*, 22995–22999.
- [295] J. J. Bravo-Suárez, K. K. Bando, J. Lu, M. Haruta, T. Fujitani, S. T. Oyama, *J. Phys. Chem. C* **2008**, *112*, 1115–1123.

- [296] B.-Z. Zhan, M. Ojeda, E. Iglesia, *J. Catal.* **2012**, *285*, 92–102.
- [297] I. X. Green, W. Tang, M. Neurock, J. T. Yates, *Faraday Discuss.* **2013**, *162*, 247–265.
- [298] T. Todorova, D. Peitz, O. Kröcher, A. Wokaun, B. Delley, *J. Phys. Chem. C* **2011**, *115*, 1195–1203.